



applied sciences

Light Beams in Liquid Crystals

Edited by

Gaetano Assanto and Noel F. Smyth

Printed Edition of the Special Issue Published in *Applied Sciences*

Light Beams in Liquid Crystals

Light Beams in Liquid Crystals

Editors

Gaetano Assanto

Noel F. Smyth

MDPI • Basel • Beijing • Wuhan • Barcelona • Belgrade • Manchester • Tokyo • Cluj • Tianjin



Editors

Gaetano Assanto
NooEL, Industrial Electronic
and Mechanical Engineering
University Roma Tre
Rome
Italy

Noel F. Smyth
School of mathematics
University of Edinburgh
Edinburgh
United Kingdom

Editorial Office

MDPI
St. Alban-Anlage 66
4052 Basel, Switzerland

This is a reprint of articles from the Special Issue published online in the open access journal *Applied Sciences* (ISSN 2076-3417) (available at: www.mdpi.com/journal/applsci/special_issues/Light_Beams_in_Liquid_Crystals).

For citation purposes, cite each article independently as indicated on the article page online and as indicated below:

LastName, A.A.; LastName, B.B.; LastName, C.C. Article Title. <i>Journal Name</i> Year , <i>Volume Number</i> , Page Range.
--

ISBN 978-3-0365-5124-1 (Hbk)

ISBN 978-3-0365-5123-4 (PDF)

© 2022 by the authors. Articles in this book are Open Access and distributed under the Creative Commons Attribution (CC BY) license, which allows users to download, copy and build upon published articles, as long as the author and publisher are properly credited, which ensures maximum dissemination and a wider impact of our publications.

The book as a whole is distributed by MDPI under the terms and conditions of the Creative Commons license CC BY-NC-ND.

Contents

About the Editors	vii
Gaetano Assanto and Noel F. Smyth Special Issue on Light Beams in Liquid Crystals Reprinted from: <i>Appl. Sci.</i> 2022 , <i>12</i> , 3668, doi:10.3390/app12073668	1
Saleh Baqer, Dimitrios J. Frantzeskakis, Theodoros P. Horikis, Côme Houdeville, Timothy R. Marchant and Noel F. Smyth Nematic Dispersive Shock Waves from Nonlocal to Local Reprinted from: <i>Appl. Sci.</i> 2021 , <i>11</i> , 4736, doi:10.3390/app11114736	5
Panayotis Panayotaros Discrete Nonlinear Schrödinger Systems for Periodic Media with Nonlocal Nonlinearity: The Case of Nematic Liquid Crystals Reprinted from: <i>Appl. Sci.</i> 2021 , <i>11</i> , 4420, doi:10.3390/app11104420	35
Marcel G. Clerc, Gregorio González-Cortés, Paulina I. Hidalgo, Lucciano A. Letelier, Mauricio J. Morel and Jorge Vergara Light-Induced Ring Pattern in a Dye-Doped Nematic Liquid Crystal Reprinted from: <i>Appl. Sci.</i> 2021 , <i>11</i> , 5285, doi:10.3390/app11115285	53
Guo Liang, Jinlong Liu, Wei Hu and Qi Guo Unique Features of Nonlocally Nonlinear Systems with Oscillatory Responses Reprinted from: <i>Appl. Sci.</i> 2022 , <i>12</i> , 2386, doi:10.3390/app12052386	69
Antonio d’Alessandro and Rita Asquini Light Propagation in Confined Nematic Liquid Crystals and Device Applications Reprinted from: <i>Appl. Sci.</i> 2021 , <i>11</i> , 8713, doi:10.3390/app11188713	91
Giovanna Palermo, Rossella Grillo, Luigia Pezzi, Thomas Bürgi, Nelson Tabiryan and Luciano De Sio et al. Photo-Aligned Nematic Liquid Crystals Enable the Modulation of Thermoplasmonic Heating Reprinted from: <i>Appl. Sci.</i> 2021 , <i>11</i> , 6272, doi:10.3390/app11146272	109

About the Editors

Gaetano Assanto

Gaetano Assanto is a Professor who currently teaches “Optoelectronics” and “Optics and Photonics of Solitons” for graduate students in Electronic Engineering. He is the founder and leader of “NooEL- the Nonlinear Optics and OptoElectronics Lab” in Roma Tre and a worldwide renowned expert in guided-wave nonlinear optics, including Kerr, quadratic and reorientational effects in both local and nonlocal optical materials.

Noel F. Smyth

Noel F. Smyth is a Professor of Nonlinear Waves and a worldwide expert in applied mathematics, particularly the use of Witham’s Modulation Theory in fluids and soft matter, including dispersive waves, undular bores, solitary and shock waves.

Special Issue on Light Beams in Liquid Crystals

Gaetano Assanto ^{1,*}  and Noel F. Smyth ^{2,3} ¹ NooEL—Nonlinear Optics and OptoElectronics Laboratory, University “Roma Tre”, 00146 Rome, Italy² School of Mathematics, University of Edinburgh, Edinburgh EH9 3FD, UK; n.smyth@ed.ac.uk³ School of Mathematics and Applied Statistics, University of Wollongong, Wollongong, NSW 2522, Australia

* Correspondence: gaetano.assanto@uniroma3.it

1. Introduction

The study of propagating light beams in liquid crystals, i.e., soft-matter encompassing optical birefringence, nonlocality, anisotropy and all-optical, as well as electro-optic, magneto-optic and thermo-optic responses, has been the subject of extensive experimental and theoretical investigations. These studies encompass light beams in liquid crystals, with applications including imaging, modulation, signal processing, display architectures, lasers, sensors and so on [1]. Owing to such wide-ranging importance, comprehensive papers are available in the literature on the optics and photonics of liquid crystals with reference to solitary waves, random lasing, topological and spin–orbit interactions of light, to cite just a few [2–5]. This Special Issue collates articles of theoretical and applied relevance to liquid crystals in the nematic phase, including one- and two-dimensional waveguides, bulk and periodic geometries and electro-optic and opto-optical phenomena. A brief summary is provided below.

1.1. Guided Waves and Integrated Optics

D’Alessandro and Asquini take up the important issue of tunable optical circuits [6]. Among the applications of liquid crystals in their nematic mesophase, the propagation of guided light waves in confined structures is one of the most promising and, therefore, most investigated. D’Alessandro et al. present an overview of recent achievements in this area, from materials to models and devices in various waveguide configurations, employing substrates such as silicon, glass and photo-dimerized monolayers (PDML) [6]. The authors include all-optical switching and tunable filtering, routers and attenuators, reporting performances competitive with similar integrated optical devices in other materials.

1.2. Self-Localized Wavepackets

The article by Liang et al. [7] concerns the nonlinear optics of reorientational nematic liquid crystals, in particular, light self-localization in unconfined samples. A theoretical review of the nonlocality-controlled transition between self-focusing and defocusing is provided, with a discussion of modulational instability and solitary waves [7]. The authors explore features of the model even beyond available regimes in materials currently known, presenting novel mathematical solutions.

1.3. Nonlinear Propagation in Discrete Arrays

A relatively unexplored area of the nonlinear optics of soft-matter is light propagation in waveguide arrays based on a liquid crystal substrate. The article by P. Panayotaros [8] is a comprehensive theoretical treatment detailing how a Wannier function basis associated with the periodic Schrödinger operator can describe stable light beams propagating in discrete arrays of waveguides, the latter encompassing nonlinearity in the presence of nonlocality, such as in nematic liquid crystals.

Citation: Assanto, G.; Smyth, N.F. Special Issue on Light Beams in Liquid Crystals. *Appl. Sci.* **2022**, *12*, 3668. <https://doi.org/10.3390/app12073668>

Received: 30 March 2022

Accepted: 2 April 2022

Published: 6 April 2022

Publisher’s Note: MDPI stays neutral with regard to jurisdictional claims in published maps and institutional affiliations.



Copyright: © 2022 by the authors. Licensee MDPI, Basel, Switzerland. This article is an open access article distributed under the terms and conditions of the Creative Commons Attribution (CC BY) license (<https://creativecommons.org/licenses/by/4.0/>).

1.4. Light Undular Bores

In line with the previous mathematical study of the nonlinear optics of liquid crystals, Baqer et al. [9] investigate dispersive shock waves in the nematic phase of the medium. Such shock waves, also termed undular bores, are the dispersive equivalent of shock waves in compressible flow. Undular bores in nematic liquid crystals are resonant, and six regimes are identified in this paper, each associated with a range of input beam powers. The authors specifically address the nonlocal, nonlinear response based on Whitham modulation theory. The modulation theory solutions are verified using full numerical solutions.

1.5. Ring Pattern Formation

Clerc et al. [10] investigate the amplified coupling of two coherent light beams in dye-doped liquid crystals. The authors experimentally study how light is able to induce ring patterns through the photo-isomerization of specific samples with photosensitive dopants. This process is modeled by a Swift–Hohenberg-type equation. An analysis of this model shows that the rings arise as a trans-critical bifurcation of the isotropic liquid phase. The article characterizes the bifurcation diagram of this complex opto-topological system.

1.6. Tunable Thermoplasmonic Heating

Palermo and coauthors [11] experimentally show that plasmonic heating delivered by a light-illuminated layer of nanoparticles can be adjusted based on the polarization-dependent refractive index change of nematic liquid crystals. A hybrid system consisting of gold nanoparticles immobilized on a glass substrate and layered with photo-aligned liquid crystals is developed, with the photo-aligning material providing molecular reorientation and tunability.

Author Contributions: G.A. and N.F.S. have read and agreed to the published version of this editorial, as they both contributed equally to it in their roles as Guest Editors. All authors have read and agreed to the published version of the manuscript.

Funding: Not applicable.

Informed Consent Statement: Not applicable.

Data Availability Statement: Not applicable.

Acknowledgments: This his Special Issue would not have been possible without the various authors and reviewers. Congratulations are due to all authors, despite the final editorial decisions on the submitted manuscripts. Thanks to the numerous hardworking and professional referees for their feedback, comments and suggestions.

Conflicts of Interest: The authors declare no conflict of interest.






References

1. Khoo, I.C. *Liquid Crystals*; Wiley: New York, NY, USA, 2022.
2. Assanto, G.; Smyth, N.F. Self confined light waves in nematic liquid crystals. *Phys. D Nonlinear Phenom.* **2020**, *402*, 132182. [CrossRef]
3. Jisha, C.P.; Alberucci, A.; Marrucci, L.; Assanto, G. Interplay between diffraction and the Pancharatnam-Berry phase in inhomogeneously twisted anisotropic media. *Phys. Rev. A* **2017**, *95*, 023823. [CrossRef]
4. Hess, A.J.; Poy, G.; Tai, J.-S.B.; Zumer, S.; Smalyukh, I.I. Control of light by topological solitons in soft chiral birefringent media. *Phys. Rev. X* **2020**, *10*, 031042. [CrossRef]
5. Perumbilavil, S.; Piccardi, A.; Barboza, R.; Buchnev, O.; Strangi, G.; Kauranen, M.; Assanto, G. Beaming random lasers with soliton control. *Nat. Commun.* **2018**, *9*, 3863. [CrossRef] [PubMed]
6. d'Alessandro, A.; Asquini, R. Light Propagation in Confined Nematic Liquid Crystals and Device Applications. *Appl. Sci.* **2021**, *11*, 8713. [CrossRef]
7. Liang, G.; Liu, J.; Hu, W.; Guo, Q. Unique Features of Nonlocally Nonlinear Systems with Oscillatory Responses. *Appl. Sci.* **2022**, *12*, 2386. [CrossRef]
8. Panayotaros, P. Discrete Nonlinear Schrödinger Systems for Periodic Media with Nonlocal Nonlinearity: The case of Nematic Liquid Crystals. *Appl. Sci.* **2021**, *10*, 4420. [CrossRef]

9. Baqer, S.; Frantzeskakis, D.J.; Horikis, T.P.; Houdeville, C.; Marchant, T.R.; Smyth, N.F. Nematic Dispersive Shock Waves from Nonlocal to Local. *Appl. Sci.* **2021**, *11*, 4736. [CrossRef]
10. Clerc, M.G.; González-Cortés, G.; Hidalgo, P.I.; Letelier, L.A.; Morel, M.J.; Vergara, J. Light-Induced Ring Pattern in a Dye-Doped Nematic Liquid Crystal. *Appl. Sci.* **2021**, *11*, 5285. [CrossRef]
11. Palermo, G.; Grillo, R.; Pezzi, L.; Bürgi, T.; Tabiryan, N.; Sio, L.D.; Umeton, C. Photo-aligned Nematic Liquid Crystals Enable the Modulation of Thermoplasmonic Heating. *Appl. Sci.* **2021**, *11*, 6272. [CrossRef]

Article

Nematic Dispersive Shock Waves from Nonlocal to Local

Saleh Baqer ^{1,†}, Dimitrios J. Frantzeskakis ^{2,†}, Theodoros P. Horikis ^{3,†}, Côme Houdeville ^{4,†},
Timothy R. Marchant ^{5,6,†} and Noel F. Smyth ^{7,*,†}

¹ Department of Mathematics, Faculty of Science, Kuwait University, Kuwait City 13060, Kuwait; saleh.baqer@ku.edu.kw

² Department of Physics, National and Kapodistrian University of Athens, 157 84 Athens, Greece; dfrantz@phys.uoa.gr

³ Department of Mathematics, University of Ioannina, 451 10 Ioannina, Greece; horikis@uoi.gr

⁴ Ecole Nationale Supérieure de Techniques Avancées, 828 Boulevard des Maréchaux, Palaiseau, 91120 Paris, France; come.houdeville@ensta-paris.fr

⁵ Australian Mathematical Sciences Institute, University of Melbourne, Melbourne, VIC 3052, Australia; t.marchant@uow.edu.au

⁶ School of Mathematics and Applied Statistics, University of Wollongong, Northfields Avenue, Wollongong, NSW 2522, Australia

⁷ School of Mathematics, University of Edinburgh, Edinburgh EH9 3FD, UK

* Correspondence: N.Smyth@ed.ac.uk

† All authors contributed equally to this work.

Abstract: The structure of optical dispersive shock waves in nematic liquid crystals is investigated as the power of the optical beam is varied, with six regimes identified, which complements previous work pertinent to low power beams only. It is found that the dispersive shock wave structure depends critically on the input beam power. In addition, it is known that nematic dispersive shock waves are resonant and the structure of this resonance is also critically dependent on the beam power. Whitham modulation theory is used to find solutions for the six regimes with the existence intervals for each identified. These dispersive shock wave solutions are compared with full numerical solutions of the nematic equations, and excellent agreement is found.

Keywords: nematic liquid crystal; dispersive shock wave; solitary wave; soliton; modulation theory

Citation: Baqer, S.; Frantzeskakis, D.J.; Horikis, T.P.; Houdeville, C.; Marchant, T.R.; Smyth, N.F. Nematic Dispersive Shock Waves from Nonlocal to Local. *Appl. Sci.* **2021**, *11*, 4736. <https://doi.org/10.3390/app11114736>

Academic Editor: Andrés Márquez

Received: 4 May 2021

Accepted: 18 May 2021

Published: 21 May 2021

Publisher's Note: MDPI stays neutral with regard to jurisdictional claims in published maps and institutional affiliations.



Copyright: © 2021 by the authors. Licensee MDPI, Basel, Switzerland. This article is an open access article distributed under the terms and conditions of the Creative Commons Attribution (CC BY) license (<https://creativecommons.org/licenses/by/4.0/>).

1. Introduction

Nematic liquid crystals form an ideal medium to study nonlinear optics due to their “huge” nonlinearity, which is orders of magnitude larger than that of optical fibers, so that nonlinear effects can be observed over millimeter distances [1–4]. In particular, the refractive index of nematic liquid crystals increases with optical intensity, so that they form a focusing medium. When a light beam propagates through a nematic liquid crystal, the electric field of the electromagnetic wave induces dipoles in the nematic molecules, which then rotate, changing the refractive index. In addition, nematic liquid crystals have a nonlocal response to an optical beam in that the elastic response of the nematic extends far beyond the optical forcing [4]. An optical beam propagating through a nematic medium can then form its own waveguide, resulting in a self-guided beam, an optical solitary wave, termed a “nematicon” [2,3,5,6], which was first experimentally generated and observed in 2000 [6]. Since this first observation, nematicons, and related solitary-type waves, such as optical vortices, have become a theme of intense experimental and theoretical research effort, driven both by interest in the nonlinear optics of nematic liquid crystals and also by their potential applications in optical devices [7–10]; see Refs. [2,3,5,11] for general reviews on the nonlinear optics of nematic liquid crystals.

Solitary waves are generic wave forms for nonlinear dispersive wave equations [12], first observed and studied in the context of water waves [12,13] and fluid dynamics [12], but are widespread in nature arising, e.g., in solid mechanics [14], biology [15], ecology [16],

and the aforementioned context of nonlinear optics [2,17,18], for instance. One of the appealing features of solitary waves, in addition to their widespread occurrence in nature, is that they are localized waves with steady profiles, which makes them easier to study theoretically. In addition to this, many generic nonlinear dispersive wave equations, such as the Korteweg-de Vries (KdV), nonlinear Schrödinger (NLS), and Sine-Gordon equations, are completely integrable systems via the Inverse Scattering Transform method [12,18]. Thus, a general initial condition for these equations will form a finite number of solitary waves, plus dispersive radiation. In addition, solitary wave solutions of integrable nonlinear dispersive wave equations, solitons, interact “elastically”, i.e., they emerge unscathed out of the interaction without any change in their form; hence, due to this particle-like behavior, solitary waves are termed solitons for such equations.

Another generic wave form supported by nonlinear dispersive wave equations are dispersive shock waves (DSWs), also termed undular bores; these structures are as widespread in nature as solitary waves, with well known examples being tidal bores and tsunamis [19]. In contrast to a solitary wave, a DSW is a non-steady wave form which continuously expands. A DSW is a dispersive regularization of a discontinuity and is a modulated periodic wavetrain with solitary waves at one edge and linear, dispersive waves at the other—see Reference [19] for a general review of DSWs. Since DSWs are non-steady waveforms, their study is more difficult than that for solitary waves. The development of DSW solutions of nonlinear dispersive wave equations relies chiefly on Whitham modulation theory [12,20–22], which is a version of the asymptotic method of multiple scales that is used to analyze slowly varying periodic wavetrains. Whitham modulation equations are a system of partial differential equations which govern the parameters of a slowly varying wavetrain, such as its amplitude, wavenumber, frequency, and mean height. If this system is hyperbolic, then the underlying wavetrain is modulationally stable, while, if it is elliptic, the wavetrain is unstable [12]. A major achievement of Whitham modulation theory was the development of the modulation equations for the KdV equation [12,21]. These modulation equations form a hyperbolic system, so that the cnoidal wave solution of the KdV equation is modulationally stable. It was subsequently realized that a simple wave solution of the KdV modulation equations is a DSW [23], even though the initial condition is a step, which is not slowly varying. This DSW solution is in excellent agreement with numerical solutions of the KdV equation [24]. The key to the determination of the simple wave DSW solution is the ability to set the modulation equations in Riemann invariant form. If the nonlinear dispersive wave equation governing the DSW is integrable, then its Whitham modulation equations can be automatically set in Riemann invariant form [25], so that the DSW solution can easily be found.

As mentioned above, the standard DSW form, termed of KdV type [19], is a modulated periodic wave with solitary waves at one edge and linear dispersive waves at the other. A non-standard DSW type is a resonant DSW [26,27], for which the waves of the DSW are in resonance with (linear) dispersive waves, resulting in a resonant wavetrain being emitted from the DSW. Resonant DSWs also occur for the KdV equation with next higher-order dispersion, i.e., fifth-order dispersion, namely for the Kawahara equation [28], and the NLS equation with next order, third-order dispersion [29–32]. If the emitted resonant wavetrain is of large enough amplitude, the KdV-type DSW structure can be destroyed; this results in the so-called traveling dispersive shock wave (TDSW) regime [26,27], consisting of a resonant wavetrain with a negative polarity solitary wave, which is the remnant of the DSW, linking this to the level behind [26]— see Figure 2d below for an example of such a TDSW. A nematic liquid crystal is a focusing medium; thus, optical waves are modulationally unstable; as a result, an optical DSW is not supported. However, the addition of azo dyes to the nematic medium changes its response so that it becomes defocusing [33]; in this case, nematics can support DSWs [34–36]. A nematic DSW is an example of a resonant DSW [34–36]. In these works, the nematic DSW was studied in the highly nonlocal limit, for which the nematic elastic response extends far beyond the light beam, with the nematic DSW generated by a step jump in the optical intensity. While the nematic equations are

of NLS-type [2], in the highly nonlocal limit the nematic bore is of KdV-type and is well described by the DSW solution of the KdV equation. The nematic DSW structure is highly dependent on the size of the jump of the optical electric field intensity generating it, with six distinct DSW types identified [36].

As stated above, in the highly nonlocal limit the nematic DSW is of KdV-type with the DSW having positive polarity. However, in the limit of weak nonlocality, the nematic equations reduce to the NLS equation [2,4], and the nematic DSW becomes the NLS DSW, which is non-resonant. The degree of nonlocality of the optical response of a nematic is inversely proportional to the power of the optical beam, with the response being highly nonlocal for lower power beams, transitioning to local as the beam power increases [2,4], as will be detailed in Section 2. In this work, the evolution of the nematic DSW structure as the degree of nonlocality ranges from highly nonlocal (low power beams) [34–36] to local (high power beams) will be studied. As the nonlocality decreases, the changes in the DSW structure from those previously found [36] in the limit of high nonlocality to the standard NLS DSW [37] will be identified, and the solutions for these will be derived. It is found that there exist two additional DSW regimes over those for large nonlocality, including the NLS DSW for zero nonlocality. The new DSW regime is a transition between the KdV DSW behavior for large nonlocality and the NLS DSW behavior for very small nonlocality. In this regime, the DSW structure consists of a resonant wavetrain headed by a partial DSW which takes the solution to the initial level ahead, similar to the resonant DSW for the KdV equation with fifth-order dispersion [27,38]. As the nonlocality decreases, the optical power increases, the resonant wavetrain contracts with the leading partial DSW expanding and becoming a full NLS DSW. The analytical solutions for the various DSW types will be compared with full numerical solutions of the nematic equations.

2. Nematic Equations

Let us consider the propagation of a linearly, extra-ordinarily polarized, coherent light beam of wavenumber k_0 , wavelength $\lambda_0 = 2\pi/k_0$, through a planar cell filled with nematic liquid crystals. The optical beam is assumed to propagate down the cell along in the Z direction, with its electric field E polarized in the Y direction. The coordinate X then completes the coordinate system. Nematic liquid crystals are a uniaxial medium consisting of elongated molecules, with the long axis termed the molecular director. The refractive index of the medium is n_{\parallel} for optical beams polarized along the molecular director and n_{\perp} for fields polarized orthogonal to the director. A fundamental property of nematic liquid crystals is the so-called Freédericksz threshold, whereby a minimum optical power is needed to rotate the nematic molecules, thus changing the refractive index of the medium [1]. However, high optical powers lead to heating of the nematic medium, which can cause the loss of the nematic state if the temperature change is high enough [1,6]. One method to overcome this is to pre-tilt the nematic molecules at an angle θ_0 with respect to the Z -direction upon the application of an external static electric field E_{LF} , so that milli-Watt power beams can rotate the nematic molecules [6]. Let us denote the optically induced rotation of the nematic by ϕ , so that, in the presence of an optical beam, the total angle of the nematic director to the Z direction is $\theta = \theta_0 + \phi$. This configuration of the nematic cell is illustrated in Figure 1. The dimensional equations governing the propagation of the optical beam in the nematic cell are then of the following form:

$$2ik_0n_e\frac{\partial E}{\partial Z} + \nabla^2 E + k_0^2\left[n_{\perp}^2\cos^2\theta + n_{\parallel}^2\sin^2\theta - n_{\perp}^2\cos^2\theta_0 - n_{\parallel}^2\sin^2\theta_0\right]E = 0, \quad (1)$$

for the electric field of the beam, and

$$K\nabla^2\phi + \left[\frac{1}{4}\epsilon_0\Delta\epsilon|E|^2 + \frac{1}{2}\Delta\epsilon_{LF}E_{LF}^2\right]\sin 2(\theta_0 + \phi) = 0, \quad (2)$$

for the nematic response [2–5]. Here, the extraordinary refractive index of the nematic is:

$$n_e^2 = \frac{n_{\perp}^2 n_{\parallel}^2}{n_{\parallel}^2 \cos^2 \theta + n_{\perp}^2 \sin^2 \theta}. \quad (3)$$

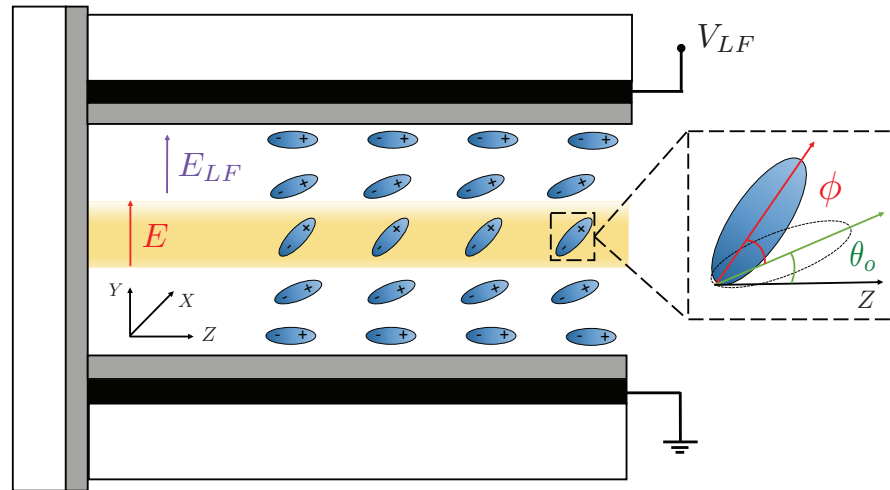


Figure 1. Sketch of nematic cell. A coherent light beam (yellow region) in which the electric field E is polarized in the Y direction propagates in the Z direction through a cell filled with a dye-doped nematic liquid crystal. Thin film electrodes (black) are deposited on the upper and lower cell walls (grey). An external low frequency voltage bias V_{LF} creates an electric field E_{LF} to pre-tilt the molecules at an angle θ_0 to Z . The nematic molecules which are located at the boundaries are held tightly by the virtue of the anchoring films. The far right inset (black) dashed box exhibits the angular rotation of a nematic molecule with respect to the propagation direction Z in the absence (θ_0) and presence ($\theta_0 + \phi$) of the optical beam.

In the above equations, $\Delta\epsilon = n_{\parallel}^2 - n_{\perp}^2$ is the optical anisotropy, $\Delta\epsilon_{LF}$ is the low-frequency dielectric anisotropy, and ϵ_0 is the electrical permittivity of free space. In addition, the constant K is the elastic medium constant in the one constant approximation for which the elastic constants of bend, twist, and splay are taken equal [1,2].

The nematic Equations (1) and (2) are highly nonlinear and difficult to analyze. However, for milli-Watt power beams, the optically induced rotation ϕ is small, $|\phi| \ll \theta_0$, so that these equations can be expanded in Taylor series around θ_0 . In addition, these equations can be put in dimensionless form using typical scales L_Z down the cell and W transverse to the down cell direction, as well as a typical scale A_b for the electric field of the optical beam, so that

$$Z = L_Z z, \quad X = Wx, \quad Y = Wy, \quad E = A_b u. \quad (4)$$

Here, (x, y, z) is the non-dimensional coordinate system, and u is the non-dimensional electric field of the optical beam. The electric field scale is obtained by assuming that the input optical beam is a Gaussian beam of power P_b , amplitude A_b , and width W_b , so that

$$A_b^2 = \frac{2P_b}{\pi\Gamma W_b^2}, \quad \Gamma = \frac{1}{2}\epsilon_0 c n_e, \quad n_e^2 = \frac{n_{\parallel}^2 n_{\perp}^2}{n_{\parallel}^2 \cos^2 \theta_0 + n_{\perp}^2 \sin^2 \theta_0}. \quad (5)$$

Substituting these into the nematic Equations (1) and (2), and expanding in Taylor series for small $|\phi|$, we find [5,39] that suitable scalings are

$$L_Z = \frac{4n_e}{\Delta\epsilon k_0 \sin 2\theta_0}, \quad W = \frac{2}{k_0 \sqrt{\Delta\epsilon \sin 2\theta_0}}, \quad (6)$$

and the resulting non-dimensional equations read

$$i \frac{\partial u}{\partial z} + \frac{1}{2} \nabla^2 u + 2\phi u = 0, \quad (7)$$

$$\nu \nabla^2 \phi - 2q\phi = -2|u|^2. \quad (8)$$

Here, the dimensionless elasticity and pre-tilting parameters, ν and q , are given by

$$\nu = \frac{8K}{\epsilon_0 \Delta \epsilon A_b^2 W^2 \sin 2\theta_0} = \frac{\pi K \Gamma k_0^2 W_b^2}{\epsilon_0 P_b}, \quad q = \frac{4 \Delta \epsilon_{LF} E_{LF}^2 \cos 2\theta_0}{\epsilon_0 \Delta \epsilon A_b^2 \sin 2\theta_0}. \quad (9)$$

Typical experimental beam parameter values are power $P_b = 2$ mW and half-width $W_b = 1.5$ μm , with a wavelength $\lambda_0 = 2\pi/k_0 = 1.064$ μm in the near infrared [2,5]. For the liquid crystal E7, a typical elastic constant is $K = 1.2 \times 10^{-11}$ N. These parameter values give the elasticity parameter $\nu = O(100)$, as found in other studies [5,40,41]. This high value of ν means that the nematic is operating in the highly nonlocal regime, in that the elastic response of the nematic extends far beyond the waist of the optical beam [2–4]. However, ν is inversely proportional to the beam power P_b . Note that, for $\nu = 0$, the nematic Equations (7) and (8) reduce to the standard NLS equation

$$i \frac{\partial u}{\partial z} + \frac{1}{2} \nabla^2 u + \frac{2}{q} |u|^2 u = 0. \quad (10)$$

This is the local response limit for the nematic. Note that, in $(2 + 1)$ -dimensions, beams governed by this equation are unstable and can show catastrophic collapse above a critical power [17]. It is known that a nonlocal response, ν large, stabilizes $(2 + 1)$ -dimensional optical beams [2–5]. This is because the nematic response Equation (2) is elliptic, so its solution depends on u in the entire domain, the origin of the physical concept of nonlocality. Hence, by adjusting the beam power P_b , the response of the medium can be adjusted from nonlocal to local, as long as the induced heating does not destroy the nematic phase at high power.

The nematic system (7) and (8) is a focusing NLS-type system, that is the refractive index in the dimensional Equation (1) increases with beam intensity $|u|^2$. Since focusing NLS equations do not possess (stable) DSW solutions, the equation needs to be defocusing; in such a case, the refractive index decreases with beam intensity, and DSW solutions do exist [19]. The nematic medium can feature a defocusing response through the addition of azo-dyes [33]. The change in the nematic response due to the addition of the azo-dye is physically complicated, with the “order parameter” change being opposite to that in the absence of the dye. A simple model of this response change is to modify the electric field Equation (7) from focusing to defocusing. In addition, the analysis of DSWs is simplest in $(1 + 1)$ -dimensions as then there are no geometric spreading effects. With these assumptions and simplifications, the nematic equations become

$$i \frac{\partial u}{\partial z} + \frac{1}{2} \frac{\partial^2 u}{\partial x^2} - 2\phi u = 0, \quad (11)$$

$$\nu \frac{\partial^2 \phi}{\partial x^2} - 2q\phi = -2|u|^2. \quad (12)$$

The same system of equations also describes optical beam propagation in thermal optical media for which the refractive index depends on the temperature of the medium [42]. Such thermal optical media typically have a defocusing response. For these defocusing nematic equations, a suitable initial condition which will generate a DSW is the intensity jump initial condition

$$u = \begin{cases} u_-, & x < 0 \\ u_+, & x > 0 \end{cases}, \quad \phi = \begin{cases} \frac{u_-^2}{q}, & x < 0 \\ \frac{u_+^2}{q}, & x > 0 \end{cases}. \quad (13)$$

The DSW solution of the defocusing nematic Equations (11) and (12) has been studied in the highly nonlocal limit $\nu \gg 1$ in previous work [34–36]. As stated above, in the local limit $\nu \ll 1$, this system reduces to a perturbed defocusing NLS equation and becomes the defocusing NLS equation for $\nu = 0$. The DSW solution of the defocusing NLS equation is known [37], so that the perturbed local DSW solution can be found using perturbed Whitham modulation theory [43]. Before studying the behavior of the nematic DSW as ν varies from large to small, some previously derived results [34–36] will be briefly summarized.

The analytical DSW solutions derived in this work will be compared with full numerical solutions of the nematic Equations (11) and (12) with the initial condition (13). The electric field Equation (11) was solved using the pseudo-spectral method of Fornberg and Whitham [24], as extended [44,45] to improve the stability for high wavenumbers through the use of an integrating factor. The x derivatives were calculated using the Fast Fourier Transform (FFT), and the solution was advanced in z in Fourier space employing the fourth-order Runge-Kutta method, as detailed in previous work [36,46]. The step initial condition (13) was smoothed using the hyperbolic tangent function, as detailed in Reference [36,46]. The director Equation (12) was also solved using the FFT, as the equation does not have a singularity at zero wavenumber due to the $2q\theta$ term.

Figure 2 displays a summary of the nematic DSW types as the nonlocality ν varies from large ν , corresponding to a highly nonlocal response for low beam power, to small ν , pertinent to a local medium response for high beam power. The terminology for the DSW regimes will be taken from previous work on radiating DSWs [26,36]. In particular, the DSW regimes from nonlocal to local response will now be detailed, for $u_- = 1$ and $u_+ = 0.8$, with the existence intervals for the various DSW types given in Table 1.

- PDSW (perturbed DSW): This regime is illustrated in Figure 2a. The nematic DSW is essentially a KdV DSW governed by the Kawahara Equation (44) and its solution can be found as a perturbed KdV DSW [36,47]. This DSW regime is non-resonant and there is no resonant wavetrain attached to the leading edge of the DSW.
- RDSW (radiating DSW): As the nonlocality ν decreases, the DSW becomes resonant with a resonant wavetrain attached to the leading edge of the DSW, as illustrated in Figure 2b. As all individual waves in the DSW are resonant, resonant waves are emitted from the DSW, which results in the DSW not being rank ordered [36].
- CDSW (crossover DSW): As the nonlocality decreases and the amplitude of the resonant wavetrain grows, the DSW becomes unstable with a total loss of the rank ordering of the waves of the DSW [26,36]. This regime is illustrated in Figure 2c.
- TDSW (traveling DSW): As the amplitude of the resonant wavetrain grows, the shedding of conserved quantities into resonant radiation eventually destroys the DSW, leaving a high amplitude resonant wavetrain with a negative polarity solitary wave linking this wavetrain to the intermediate level [26] as seen in Figure 2d. While there is a solitary wave linking the resonant wavetrain to the intermediate level, this linking can be conveniently treated as a Whitham shock [48], a shock wave in the Whitham modulation equation variables. The resonant wavetrain is brought down to the level u_+ ahead by a partial DSW [36]. This partial DSW has linear dispersive waves at its leading edge but has a finite wavelength wave at its trailing edge, that is, it is not bounded by solitary waves at the trailing edge [38,49], as for a standard DSW.
- RNLS DSW (radiating NLS DSW): Further decrease in the nonlocality results in the amplitude of the linking solitary wave becoming negligible, so that the wave form consists of a (stable) resonant wavetrain headed by a partial DSW which brings the wavetrain down to the level u_+ ahead, as seen in Figure 2e. This DSW regime does not occur in the high nonlocality limit as it is a “bridge” to the local NLS DSW for $\nu = 0$.

- NLS DSW: As the nonlocality ν decreases to $\nu = 0$ and the nematic Equations (11) and (12) reduce to the NLS equation, the resonant wavetrain length contracts and the leading partial DSW evolves to a full DSW, with linear dispersive waves at the leading edge and solitary waves at the trailing edge. The resonant wavetrain then disappears and the leading DSW bringing the wavetrain down to the level u_+ ahead attaches to the intermediate level with $|u| = u_i$, as in Figure 2f. The resulting DSW is essentially an NLS DSW, which completes the transition from the KdV-type DSW for high nonlocality, that is for low power beams, to a NLS DSW for low nonlocality, that is for high power beams.

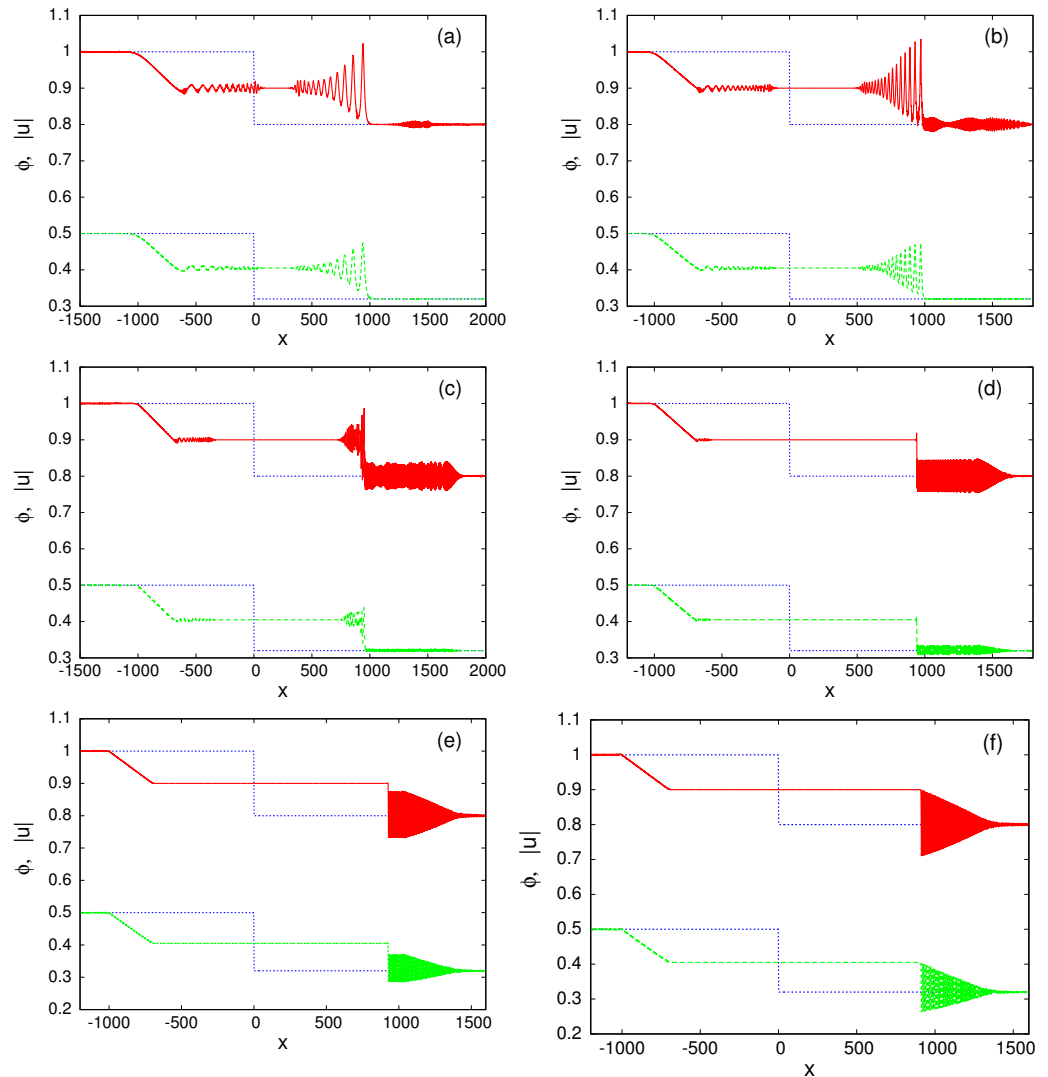


Figure 2. Numerical solutions of nematic Equations (11) and (12) for initial condition (13) with $u_+ = 0.8$ and $u_- = 1.0$. Red (solid) lines: $|u|$ at $z = 1000$; green (dashed) lines: ϕ at $z = 1000$; blue (dotted) lines: $|u|$ at $z = 0$ (upper) and ϕ at $z = 0$ (lower). (a) PDSW with $\nu = 200$, (b) RDSW with $\nu = 40$, (c) CDSW with $\nu = 10$, (d) TDSW with $\nu = 3.0$, (e) resonant NLS type DSW with $\nu = 1.0$, (f) NLS type DSW with $\nu = 0.5$. Here, $q = 2$.

In addition to these six DSW types, when $u_- - u_+$ is large enough as $u_+ \rightarrow 0$, there is an additional DSW type which is a sub-case of the TDSW regime, the vacuum DSW (VDSW) [37], for which the electric field u of the resonant radiation vanishes at a point [35,36]. As the solution for this DSW type has been previously analyzed [36], and it is a sub-case of the TDSW regime, it will not be considered here. In addition,

the analytical work of this manuscript is based on $u_- - u_+$ being small, which is not valid in the VDSW regime.

Table 1 shows that the transition regimes of the TDSW and RNLS DSWs which evolve the DSW from the KdV-type DSW for high nonlocality to the NLS-type DSW for weak nonlocality exist for very restricted ranges of ν , so that this transition is rapid. Over most of the range of ν the DSW is of KdV-type, one of the PDSW, RDSW, and CDSW types. As noted, the first four DSW regimes also occur for the Kawahara equation and the nematic equations in the low power, high nonlocality limit.

Table 1. Regime boundaries for type classifications of Figure 2. Here, $u_- = 1.0$, $u_+ = 0.8$ and $q = 2$.

PDSW	$88 < \nu$
RDSW	$34 < \nu < 88$
CDSW	$4.1 < \nu < 34$
TDSW	$1.53 < \nu < 4.1$
RNLS DSW	$0.60 < \nu < 1.53$
NLS DSW	$0 \leq \nu < 0.60$

The standard method to analyze DSW solutions of nonlinear dispersive wave equations of defocusing NLS-type is to transform the equation into hydrodynamic form using the Madelung transformation [19]

$$u = \sqrt{\rho}e^{i\psi}, \quad v = \psi_x, \tag{14}$$

where the real functions ρ and ψ denote the density and phase of the field u , while v is the fluid velocity. Upon substituting, it is found that the nematic Equations (11) and (12) become

$$\frac{\partial \rho}{\partial z} + \frac{\partial}{\partial x}(\rho v) = 0, \tag{15}$$

$$\frac{\partial v}{\partial z} + v \frac{\partial v}{\partial x} + 2 \frac{\partial \phi}{\partial x} - \frac{\partial}{\partial x} \left(\frac{\rho_{xx}}{4\rho} - \frac{\rho_x^2}{8\rho^2} \right) = 0, \tag{16}$$

$$v \frac{\partial^2 \phi}{\partial x^2} - 2q\phi = -2\rho. \tag{17}$$

The nematic equations are characterized by the linear dispersion relation [34,35]

$$\omega = k\bar{v} + \frac{\sqrt{\bar{\rho}k}}{\sqrt{\nu k^2 + 2q}} \left[\frac{\nu k^2 + 2q}{4\bar{\rho}} k^3 + 4k \right]^{1/2}, \tag{18}$$

for waves around the mean level $\bar{\rho}$ for ρ and \bar{v} for v . In the short wave and high nonlocality limit, $\nu k^2 \gg 1$, this dispersion relation can be approximated by

$$\omega = k\bar{v} + \frac{1}{2}k^2 + \dots \tag{19}$$

In the opposite local limit with ν small, the dispersion relation can be expanded as

$$\omega = k\bar{v} + k^2 \left[\frac{1}{4}k^2 + \frac{2}{q}\bar{\rho} \right]^{1/2} - \frac{\nu \bar{\rho} k^3}{2q^2} \left[\frac{1}{4}k^2 + \frac{2}{q}\bar{\rho} \right]^{-1/2} + \dots \tag{20}$$

As expected, at the leading-order, $O(1)$, this dispersion relation is the same as that for the NLS equation [19,50]. These dispersion relations are needed for the determination of the resonant wavetrain generated by the nematic DSW by which the linear phase velocity is matched to the velocity of the DSW front.

As seen from Figure 2, the solution outside of the DSW and the resonant wavetrain is non-dispersive. On neglecting dispersion, the nematic Equations (15)–(17) become the

shallow water equations [12], with ρ playing the role of fluid depth and v the (horizontal) fluid velocity. In Riemann invariant form, the dispersionless nematic equations read:

$$v + \frac{2\sqrt{2}}{\sqrt{q}}\sqrt{\rho} = R_+ = \text{constant} \quad \text{on} \quad C_+ : \frac{dx}{dz} = V_+ = v + \frac{\sqrt{2}}{\sqrt{q}}\sqrt{\rho}, \quad (21)$$

$$v - \frac{2\sqrt{2}}{\sqrt{q}}\sqrt{\rho} = R_- = \text{constant} \quad \text{on} \quad C_- : \frac{dx}{dz} = V_- = v - \frac{\sqrt{2}}{\sqrt{q}}\sqrt{\rho}. \quad (22)$$

The initial level behind u_- is linked to the intermediate shelf by a simple wave on the characteristic C_- . This simple wave solution has been derived previously [34–36] and is of the form:

$$|u| = \sqrt{\rho} = \begin{cases} u_-, & \frac{x}{z} < -\frac{\sqrt{2}u_-}{\sqrt{q}} \\ \frac{\sqrt{q}}{3\sqrt{2}} \left[\frac{2\sqrt{2}u_-}{\sqrt{q}} - \frac{x}{z} \right], & -\frac{\sqrt{2}u_-}{\sqrt{q}} \leq \frac{x}{z} \leq \frac{\sqrt{2}}{\sqrt{q}}(2u_- - 3\sqrt{\rho_i}), \\ \sqrt{\rho_i}, & \frac{\sqrt{2}}{\sqrt{q}}(2u_- - 3\sqrt{\rho_i}) < \frac{x}{z} \leq s_i \end{cases} \quad (23)$$

with $v = 2\sqrt{2}(u_- - \sqrt{\rho})/\sqrt{q}$, where s_i is the velocity of the trailing edge of the DSW which lies on the intermediate level u_i . This level can be determined by the requirement that the Riemann invariant along the characteristics C_- , that is, R_- , is conserved across the nematic DSW [34], giving

$$u_i = \frac{1}{2}(u_- + u_+). \quad (24)$$

We can see from the above calculations that the phase gradient on the intermediate level v_i is then

$$v_i = \frac{2\sqrt{2}}{\sqrt{q}}(u_- - \sqrt{\rho_i}). \quad (25)$$

In the small jump limit $|u_- - u_+| \ll 1$, the nematic Equations (11) and (12) can be reduced—in the high nonlocality regime ($v \gg 1$) under consideration—to a KdV equation with fifth-order dispersion [35,51]. This will be justified below upon employing a multiscale expansion method.

2.1. Derivation of the Extended KdV and Kawahara Equations

We seek solutions of Equations (15)–(17) in the form of the following asymptotic expansions in the formal small parameter $\varepsilon \equiv \sqrt{u_i - u_+}$ (with $0 < \varepsilon \ll 1$):

$$|u|^2 = \rho = \rho_+ + \varepsilon^2\rho_1(\xi, \eta) + \varepsilon^4\rho_2(\xi, \eta) + \dots, \quad (26)$$

$$v = \varepsilon^2V_1 + \varepsilon^4V_2 + \varepsilon^6V_3 + \dots, \quad (27)$$

$$\phi = \frac{\rho_+}{q} + \varepsilon^2\phi_1 + \varepsilon^4\phi_2 + \varepsilon^6\phi_3 + \dots, \quad (28)$$

where $\rho_+ = u_+^2$, and the unknown functions ρ_j , V_j , and ϕ_j ($j = 1, 2, 3, \dots$) depend on the stretched variables

$$\xi = \varepsilon(x - Uz), \quad \eta = \varepsilon^3z. \quad (29)$$

Here, U will be treated as an unknown velocity, which will be determined self-consistently.

Substituting the expansions (26)–(28) into Equations (15)–(17), and using the stretched coordinates (29), we obtain a set of equations at the different orders in ε . In particular, at the leading order, we derive the following linear equations:

$$O(\varepsilon^2) : \quad \rho_1 - q\phi_1 = 0, \quad (30)$$

and

$$O(\varepsilon^3) : \quad UV_{1\xi} - 2\phi_{1\xi} = 0 \quad \text{and} \quad U\rho_{1\xi} - u_+^2 V_{1\xi} = 0, \tag{31}$$

where subscripts denote partial derivatives. The compatibility of the above equations suggests that the squared velocity U^2 is given by $U^2 = 2u_+^2/q$. Next, Equations (15)–(17) yield a set of nonlinear equations, namely:

$$O(\varepsilon^4) : \quad 2\rho_2 - 2q\phi_2 + v\phi_{1\xi\xi} = 0, \tag{32}$$

and

$$O(\varepsilon^5) : \quad -u_+^2 V_{1\eta} + 3U\rho_1 V_{1\xi} - u_+^2 V_1 V_{1\xi} + Uu_+^2 V_{2\xi} - 6\rho_1 \phi_{1\xi} - 2u_+^2 \phi_{2\xi} + \frac{1}{4}\rho_{1\xi\xi\xi} = 0$$

$$\rho_{1\eta} + (\rho_1 V_1)_\xi - U\rho_{2\xi} + u_+^2 V_{2\xi} = 0 \tag{33}$$

The compatibility condition at this order can be found upon eliminating the fields ρ_2 , V_2 , and ϕ_2 upon using Equations (32) and (33) and the definition of the velocity U . This yields the following KdV equation:

$$\rho_{1\eta} + \frac{3}{2u_+} \sqrt{\frac{2}{q}} \rho_1 \rho_{1\xi} + \left(\frac{1}{q}\right)^{3/2} \frac{4vu_+^2 - q^2}{8\sqrt{2}u_+} \rho_{1\xi\xi\xi} = 0. \tag{34}$$

To the next order of approximation, we obtain:

$$O(\varepsilon^6) : \quad 2\rho_3 - 2q\phi_3 + v\phi_{2\xi\xi} = 0, \tag{35}$$

and

$$O(\varepsilon^7) : \quad -3u_+^4 \rho_1 V_{1\eta} - u_+^6 V_{2\eta} + 3Uu_+^2 (\rho_1^2 + u_+^2 \rho_2) V_{1\xi} - 3u_+^4 \rho_1 V_1 V_{1\xi}$$

$$- u_+^6 V_2 V_{1\xi} + 3Uu_+^4 \rho_1 V_{2\xi} - u_+^6 V_1 V_{2\xi} + Uu_+^6 V_{3\xi} - 6u_+^2 \rho_1^2 \phi_{1\xi}$$

$$- 6u_+^4 \rho_2 \phi_{1\xi} - 6u_+^4 \rho_1 \phi_{2\xi} - 2u_+^6 \phi_{3\xi} - \frac{1}{2}u_+^2 \rho_{1\xi} \rho_{1\xi\xi} + \frac{1}{2}u_+^2 \rho_1 \rho_{1\xi\xi\xi}$$

$$+ \frac{1}{4}u_+^4 \rho_{2\xi\xi\xi} = 0, \quad \text{and} \tag{36}$$

$$\rho_{2\eta} + (\rho_1 V_2 + \rho_2 V_1)_\xi - U\rho_{3\xi} + u_+^2 V_{3\xi} = 0. \tag{37}$$

It is now possible to follow the procedure used at the previous order and eliminate the fields ρ_3 , V_3 and ϕ_3 from Equations (35)–(37). Indeed, solving Equation (35) for ϕ_3 , Equation (37) for $\rho_{3\xi}$ and substituting into Equation (36) eliminates every term with index 3 (recall $U^2 = 2u_+^2/q$). Furthermore, employing the equations obtained at the previous orders, we can express the fields $\phi_{1,2}$ and $V_{1,2}$ in terms of the amplitudes ρ_1 and ρ_2 , which yields

$$\frac{1}{2U} \int \rho_{1\eta\eta} d\xi + \rho_{1\xi} \int \rho_{1\eta} d\xi + \frac{5}{2}\rho_1 \rho_{1\eta} + \rho_{2\eta} + 3U\rho_1^2 \rho_{1\xi} + \frac{3c}{2}(\rho_1 \rho_2)_\xi + \frac{Uv}{2q} \rho_{1\xi} \rho_{1\xi\xi}$$

$$- \frac{q-2U^2v}{8U^2q} \rho_{1\xi\xi\eta} - \frac{q-3U^2v}{4Uq} \rho_1 \rho_{1\xi\xi\xi} - \frac{q-2U^2v}{8Uq} \rho_{1\xi\xi\xi} + \frac{Uv^2}{8q^2} \rho_{1\xi\xi\xi\xi} = 0. \tag{38}$$

To this end, we multiply Equation (38) by ε^2 and add it to the KdV equation Equation (34). Then, introducing the combined amplitude function

$$P = \rho_1 + \varepsilon^2 \rho_2, \tag{39}$$

we solve for $\rho_1 = P - \varepsilon\rho_2$ and substitute the result into the above Equation (38). We, hence, obtain the nonlinear evolution equation for the field $P(\xi, \eta)$

$$P_\eta + \frac{3}{2u_+} \sqrt{\frac{2}{q}} P P_\xi + \left(\frac{1}{q}\right)^{3/2} \frac{4vu_+^2 - q^2}{8\sqrt{2}u_+} P_{\xi\xi\xi} + \varepsilon^2 \left(b_1 P^2 P_\xi + b_2 P_\xi P_{\xi\xi} + b_3 P P_{\xi\xi\xi} + b_4 P_{\xi\xi\xi\xi} \right) = 0. \tag{40}$$

The coefficients b_j ($j = 1, 2, 3, 4$) appearing in Equation (40) are given by

$$b_1 = -\frac{3}{8u_+^3} \sqrt{\frac{2}{q}}, \quad b_2 = -\left(\frac{1}{q}\right)^{3/2} \frac{20vu_+^2 - 13q^2}{32\sqrt{2}u_+^3},$$

$$b_3 = \left(\frac{1}{q}\right)^{3/2} \frac{4vu_+^2 + q^2}{16\sqrt{2}u_+^3}, \quad b_4 = \left(\frac{1}{q}\right)^{5/2} \frac{48v^2u_+^4 + 8vq^2u_+^2 - q^4}{256\sqrt{2}u_+^3}.$$

Then, we seek an asymptotic expansion in the optical beam intensity $|u|$ as

$$|u| = u_+ + \varepsilon^2 Q + \dots \tag{41}$$

and use the relation $|u| = \sqrt{\rho}$. This asymptotically gives $P = 2u_+Q$. The reductive nonlinear Equation (40) can now be written in terms of the field $Q(\xi, \eta)$ as

$$Q_\eta + 3\sqrt{\frac{2}{q}} Q Q_\xi + \left(\frac{1}{q}\right)^{3/2} \frac{4vu_+^2 - q^2}{8\sqrt{2}u_+} Q_{\xi\xi\xi} + \varepsilon^2 \left(c_1 Q^2 Q_\xi + c_2 Q_\xi Q_{\xi\xi} + c_3 Q Q_{\xi\xi\xi} + c_4 Q_{\xi\xi\xi\xi} \right) = 0. \tag{42}$$

The coefficients c_j ($j = 1, 2, 3, 4$) appearing in Equation (42) are given by

$$c_1 = 4u_+^2 b_1, \quad c_2 = 2u_+ b_2, \quad c_3 = 2u_+ b_3, \quad c_4 = b_4.$$

Notice that Equation (42) is the so-called extended KdV equation (eKdV), which can model the evolution of steeper waves, with shorter wavelengths, than those governed by the KdV equation. As such, the eKdV equation has been used to describe solitary waves in plasmas [52] and shallow water waves [53] in the presence of higher order effects. We note that the coefficient of the third derivative dispersive term changes sign when

$$v = \frac{q^2}{4u_+^2}. \tag{43}$$

Hence, in the high nonlocality, low power, limit, such that $v > q^2/(4u_+^2)$, the coefficient of the third derivative in eKdV equation is positive, so that its DSW (and solitary wave) solutions have positive polarity, with solitary waves at its leading edge and linear dispersive waves at its trailing edge. On the other hand, in the local limit, $v < q^2/(4u_+^2)$, the coefficient of the third derivative is negative and the DSW has negative polarity, with linear dispersive waves at its leading edge and solitary waves at its trailing edge, so that it resembles the standard NLS DSW [37]. The nematic DSW then undergoes a change of form from a KdV-type DSW to an NLS-type DSW as v decreases at the value of the nonlocality parameter given by (43).

At this point, it is useful to make the following remarks. First, in the highly nonlocal limit, the dominant higher-order coefficient is the one of the fifth-order dispersion term,

namely $c_4 \propto \nu^2$. Thus, in this limit, the eKdV Equation (40) may be approximated by the Kawahara equation

$$P_\eta + \frac{3}{2u_+} \sqrt{\frac{2}{q}} P P_\xi + \left(\frac{1}{q}\right)^{3/2} \frac{(4u_+^2 \nu - q^2)}{8\sqrt{2}u_+} P_{\xi\xi\xi} + \varepsilon^2 \frac{3}{16\sqrt{2}} \left(\frac{1}{q}\right)^{5/2} u_+ \nu^2 P_{\xi\xi\xi\xi\xi} = 0, \quad (44)$$

as was done in previous work [35,36].

3. Nonlocal to Local Nematic DSWs

The form and details of the DSW solution of the defocusing nematic Equations (11) and (12) will be found as the nonlocality ν changes from $O(100)$ to 0, that is from the nematic having a highly nonlocal response to a local response as the optical power increases. For high nonlocality, the DSW is of KdV type, with the leading edge of the DSW consisting of solitary waves of elevation [34–36]. The reason for this can be seen from the eKdV Equation (42) as for $\nu > q^2/(4u_+^2)$ the coefficient of the third derivative is positive, so that the DSW is of KdV type and has positive polarity. For $0 \leq \nu < q^2/(4u_+^2)$, the sign of the third derivative is negative, and the DSW has negative polarity, with solitary waves at the trailing edge and linear dispersive waves at the leading edge, as for the NLS DSW [37]. A nematic DSW of NLS type is illustrated in Figure 2e for $\nu = 0.5$. Indeed, for $\nu = 0$, the nematic Equations (11) and (12) reduce to the standard NLS equation on substituting for ϕ from (12) into (11). The DSW solution of the NLS equation is well known [37] as the NLS equation is integrable and so the solution is completely determined. Hence, the solution for this regime will not be considered here.

The existence regions for the various nematic DSW types as the nonlocality parameter ν varies (optical power varies), found from full numerical solutions of the nematic Equations (11) and (12) are shown in Figure 3 as the initial level ahead u_+ varies. The range $0.3 \leq u_+ \leq 0.9$ was chosen as this encompassed all six of the DSW types studied here. In addition, most of the theoretical expressions for the boundaries between these regions and the solutions within each region were based on $u_- - u_+$ small, for example, the boundary (43), which is based on the eKdV Equation (42). It can be seen that, over most of the (u_+, ν) domain, the nematic DSW is of CDSW or TDSW type, so that it is typically unstable. In addition, it is deduced that the nematic DSW is of NLS-type only for small values of the nonlocality parameter ν of 2 and below. The nematic DSW is then nonlocal, except for high enough optical powers for which ν is small. The nonlocality parameter ν is given by (9). For the nematic liquid crystal 4-(trans-4-n-hexylcyclohexyl)-isothiocyanato-benzene (6CHBT), the parameter values are $K \sim 10^{-11} N$, $n_{\parallel} = 1.6335$ and $n_{\perp} = 1.4967$ [54]. Let us take the pre-tilt angle θ_0 to be $\pi/4$ so that the nematic response is maximized [2]. A typical beam wavelength is 1064 nm, and a typical half width W_b is 1.5 μm [54]. With these parameter values, it is found that $\nu = 2$ when the beam power P_b is 288 mW, far in excess of typical beam powers of a few milliWatts to a few tens of milliWatts [2,54]. Such a large optical power can result in the nematic medium being heated enough so that its temperature goes above the critical temperature, 43 °C for 6CHBT [54], so that it undergoes a phase change out of the nematic state. In this regard, it should be noted that experimental nematic cells are small, of the order of 1 mm in the down cell propagation direction of the beam and 100 $\mu\text{m} \times 10 \text{ mm}$ in cross-section. The thin cross-section is the direction in which the pre-tilting electric field is applied, which results in a stable and uniform molecular pre-tilt. We then deduce that, for experimental beam powers, the nematic bore will be in the nonlocal response regime with ν large, which is low optical power.

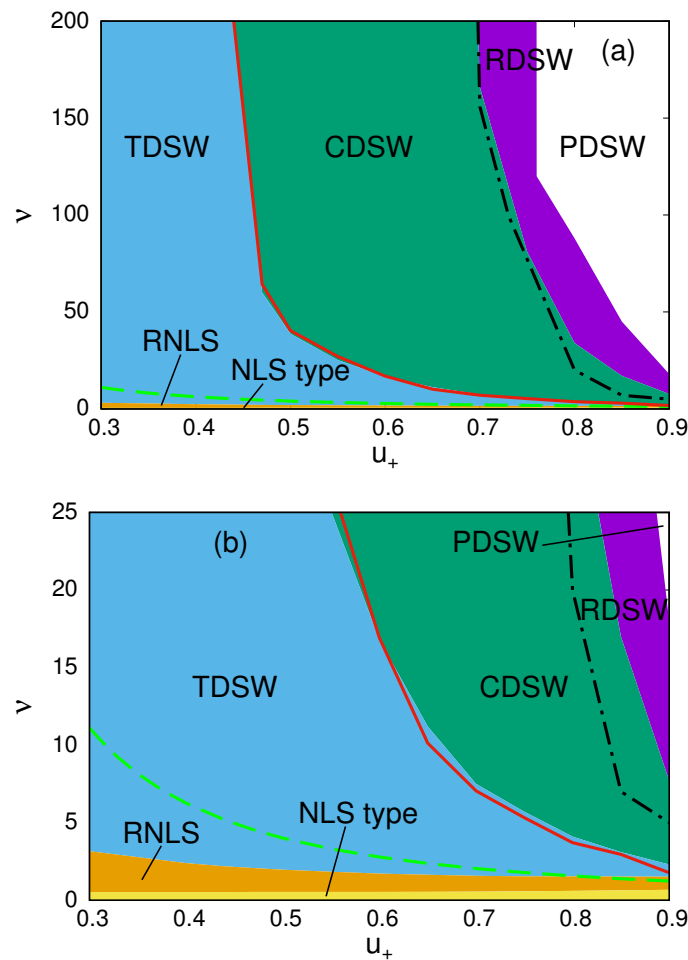


Figure 3. Numerical existence regions for nematic DSWS types in terms of the nonlocality parameter ν as the initial level u_+ varies. (a) Full existence regions from highly nonlocal $\nu = 200$ to local $\nu = 0$, (b) Detail of (a) for the transition to an NLS-type DSWS. Theoretical boundary (72) between RDSW and CDSW regimes: black (dot-dash) line; theoretical boundary $U_s = c_g$, (95), between CDSW and TDSW regimes: red (solid) line; theoretical boundary (43) between KdV-type and NLS-type DSWS: green (dashed) line. Here, $u_- = 1.0$ and $q = 2$.

4. PDSW and RDSW Regimes

Typical PDSW and RDSW solutions are illustrated in Figure 2a,b. In the PDSW regime, the DSWS is not in resonance with linear diffractive radiation, so that the DSWS is of KdV type, as seen in the boundary (43), and is a perturbed KdV-type DSWS. In the RDSW regime, the DSWS is in resonance with diffractive radiation, so that it consists of a KdV-type DSWS with resonant radiation propagating ahead of it. This resonant radiation is not large enough, however, as to destroy the KdV-type DSWS structure, as in the CDSW regime; see Figure 2c. As the DSWS in the PDSW and RDSW regimes are perturbed KdV DSWSs [36], the solutions in these two regimes can be found using the perturbed KdV DSWS solution of Reference [47]. In this previous work, the general eKdV equation, a particular case of which is (42), was asymptotically transformed to the KdV equation, in which the known DSWS solution [19,23] was then used to find the asymptotic DSWS solution of the original eKdV equation. This asymptotic DSWS solution can be used here based on the eKdV equation reduction (42) of the full nematic equations in the limit $u_- - u_+$ small. The work [47] then gives the following PDSW and RDSW nematic DSWS solutions. The amplitude of the DSWS is

$$a = 2m(u_i - u_+) + \frac{1}{3}(u_i - u_+)^2 \{m(1 - m)C_1 + m(m - 2)C_2 + mC_3 + 2m(8 - 3m)C_4\}, \tag{45}$$

its wavenumber is

$$k = \frac{\pi\sqrt{2\{u_i-u_+\}}}{K(m)\sqrt{u_+}\sqrt{\frac{v-q}{4u_+^2}}} \left\{ 1 + \frac{(u_i-u_+)}{12}C_1 + \frac{(u_i-u_+)(4m^2-8m+3)}{12}C_3 - \frac{(u_i-u_+)(8m^2-14m+11)}{3}C_4 \right\}, \tag{46}$$

and its mean level is

$$\begin{aligned} |\bar{u}| = & 2u_+ - u_i + (u_i - u_+) \left\{ m + \frac{2E(m)}{K(m)} \right\} \\ & - (u_i - u_+)^2 C_1 \left\{ \frac{3m^2K(m)+4mE(m)-5mK(m)-2E(m)+2K(m)}{18K(m)} \right\} \\ & - (u_i - u_+)^2 C_3 \left\{ \frac{(2-m-m^2)K^2(m)+(4m-10)E(m)K(m)+8E^2(m)}{6K^2(m)} \right\} \\ & + 2(u_i - u_+)^2 C_4 \left\{ \frac{(m^2-7m+6)K^2(m)+2(6m-11)E(m)K(m)+16E^2(m)}{3K^2(m)} \right\}. \end{aligned} \tag{47}$$

Here, $K(m)$ and $E(m)$ are complete elliptic integrals of the first and second kinds of modulus squared m , respectively. The modulus squared m is a parameter in these amplitude, wavelength, and mean height expressions. It is determined in terms of the simple wave (similarity) variable x/z by

$$\begin{aligned} \frac{x}{z} = & \frac{\sqrt{2}}{\sqrt{q}}u_+ + \frac{\sqrt{2}(u_i-u_+)}{\sqrt{q}} \left\{ 1 + m - \frac{2m(1-m)K(m)}{E(m)+(m-1)K(m)} \right\} \\ & + \frac{(u_i-u_+)^2}{3\sqrt{2q}}C_1 \left\{ 1 + m - \frac{2m(1-m)K(m)}{E(m)+(m-1)K(m)} \right\} \\ & + \frac{(u_i-u_+)^2}{3\sqrt{2q}}C_3 \left\{ 2m - 1 - m^2 - \left(1 + m - \frac{2m(1-m)K(m)}{E(m)+(m-1)K(m)} \right) \right. \\ & \left. - \frac{4m(1-m)(2E(m)+(m-1)K(m))}{E(m)+(m-1)K(m)} \right\} + \frac{4(u_i-u_+)^2}{3\sqrt{2q}}C_4 \\ & \times \left\{ -1 - m + \frac{2m(1-m)K(m)}{E(m)+(m-1)K(m)} + \left(1 + m - \frac{2m(1-m)K(m)}{E(m)+(m-1)K(m)} \right)^2 \right. \\ & \left. - 2(2m - m^2 - 1) + 4 \frac{m(1-m)[(m-1)K(m)+2E(m)]}{E(m)+(m-1)K(m)} \right\}. \end{aligned} \tag{48}$$

This expression for x/z derives from the characteristic of the KdV modulation equations on which the simple wave DSW solution occurs [23,24,47]. The coefficients C_j ($j = 1, 2, 3, 4$) in the above solutions are connected to c_j ($j = 1, 2, 3, 4$) through the relations

$$C_1 = \sqrt{2q}c_1, \quad C_2 = \frac{8\sqrt{2}q^{3/2}u_+}{(4u_+^2v - q^2)}c_2, \quad C_3 = \frac{8\sqrt{2}q^{3/2}u_+}{(4u_+^2v - q^2)}c_3, \quad C_4 = \frac{64\sqrt{2}q^{5/2}u_+^2}{(4u_+^2v - q^2)^2}c_4. \tag{49}$$

At the leading, solitary wave edge of the DSW $m \rightarrow 1$ and at the trailing, harmonic wave edge of the DSW $m \rightarrow 0$. It can then be found from the characteristics (48) that the DSW lies in the range

$$\begin{aligned} s_i = & \sqrt{\frac{2}{q}} \left\{ 4u_+ - 3u_i - (u_i - u_+)^2 \left(\frac{1}{2}C_1 + C_3 - \frac{64}{3}C_4 \right) \right\} \\ & \leq \frac{x}{z} \leq \sqrt{\frac{2}{q}} \left\{ 2u_i - u_+ + \frac{1}{3}(u_i - u_+)^2(C_1 - C_3 + 4C_4) \right\} = s_+, \end{aligned} \tag{50}$$

where s_i and s_+ are the harmonic and solitary wave edge velocities of the DSW, respectively.

Comparisons between the lead solitary wave amplitude a_+ as given by the asymptotic DSW solution (45), with $m = 1$, and numerical solutions are given in Figure 4 as the nonlocality parameter v varies. The existence regions for the PDSW and RDSW types depend on both u_+ and v , as shown in Figure 3, so that the comparison curves for each u_+ were stopped at the boundary between the RDSW and CDSW regimes. Figure 4 shows the lead solitary wave amplitude for the full eKdV Equation (42) and the Kawahara equation,

which is (42) with $c_1 = c_2 = c_3 = 0$. Previous work on the nematic bore [35,36] was based on the Kawahara equation, that is only the higher order fifth derivative was included in the asymptotic eKdV equation, so the lead wave amplitude based on this equation is given in the figure to determine the effect of the extra higher order terms in the full eKdV Equation (42). A key observation is that the height of the lead wave of the DSW depends very weakly on the strength of the nonlocality, with little variation even down to $\nu = O(10)$ from the high nonlocality amplitudes with $\nu = O(100)$. In some sense, the nematic DSW is then nonlocal down to small values of ν in the PDSW and RDSW regimes, which was also deduced above from Figure 3. It can also be seen that the inclusion of the extra higher order terms in the eKdV Equation (42) over the Kawahara equation improves the agreement with numerical solutions on the whole, especially as the nonlocality parameter ν decreases, but the effect of these extra terms is small, with the Kawahara equation giving good agreement over the whole range of ν and for all values of u_+ , except near the RDSW/CDSW borderline at $u_+ = 0.7$. This is expected as the weak dependence on the nonlocality parameter ν means that the DSW is nonlocal, so that ν can be taken as large. The dominant higher order term in the eKdV equation is $\varepsilon^2 c_4 Q_{\zeta\zeta\zeta\zeta\zeta}$ in this limit, as noted in (44). As $u_+ = 0.7$ is approached the resonant radiation shed by the DSW is of relatively large amplitude as in this limit the RDSW/CDSW boundary is approached. This results in oscillations in the lead wave amplitude as the resonant radiation moves through the DSW and is shed. In these cases, the numerical amplitude shown in Figure 4 was calculated as an average in z over the last few amplitude oscillations in the numerical solution. It is noted that except for $u_+ = 0.75$ and 0.7 the amplitude grows as ν decreases. This change in behavior is due to the DSW changing form as it transitions from the RDSW to the CDSW regime, for which the resonant radiation has a major effect on the DSW with its amplitude decreasing markedly due to the large amount of mass being shed as resonant radiation [36].

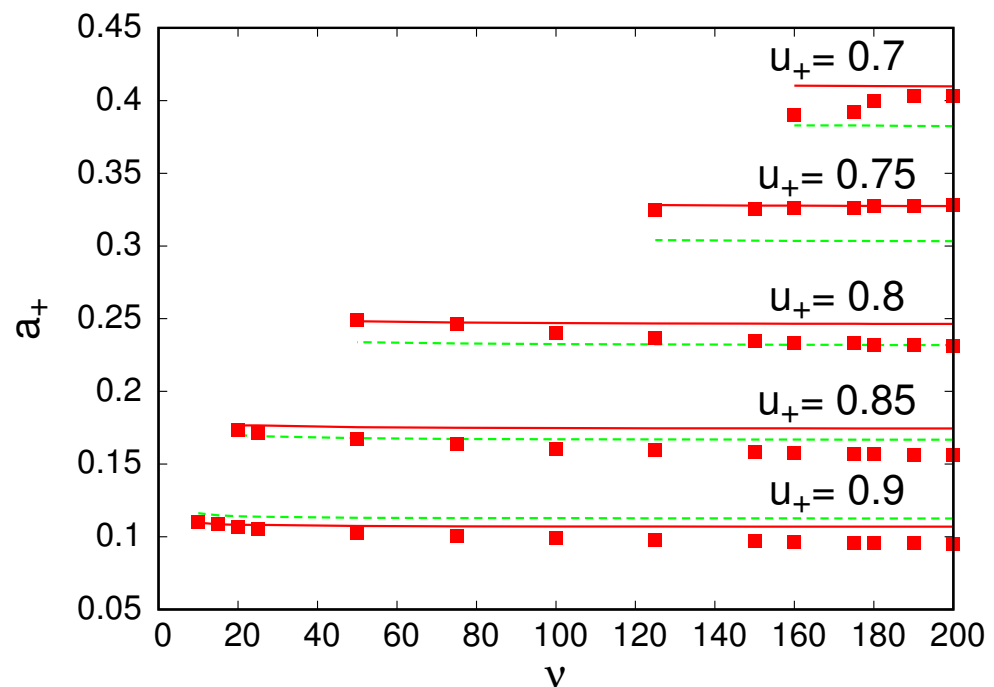


Figure 4. Comparison between lead wave amplitude a_+ of PDSW and RDSW with numerical solutions of the nematic Equations (11) and (12) with the initial condition (13). Numerical amplitude: red squares; amplitude (45) with $m = 1$ given by undular bore solution of eKdV Equation (42): red (solid) line; amplitude given by undular bore solution of Kawahara equation (Equation (42) with $c_1 = c_2 = c_3 = 0$): green (dashed) line. Here, $u_- = 1.0$ and $q = 2$.

The full linear dispersion relation (18) for the nematic Equations (11) and (12) is

$$\omega = k\bar{v} + \frac{\sqrt{\bar{\rho}}k}{\sqrt{\nu k^2 + 2q}} \left[\frac{\nu k^2 + 2q}{4\bar{\rho}} k^2 + 4 \right]^{1/2} + \frac{2\bar{\rho}}{q} \tag{51}$$

when the mean $2\bar{\rho}/q$ is added. This mean term arises on integrating $v = \psi_x$ to obtain the dispersion relation for ψ from that for v [35]. In the limit νk^2 large, this dispersion relation becomes (19)

$$\omega = k\bar{v} + \frac{1}{2}k^2 + \frac{2\bar{\rho}}{q} + \dots, \tag{52}$$

again with the carrier wave phase shift $2\bar{\rho}/q$ added to obtain the dispersion relation for ψ . In the RDSW regime, the resonant wavetrain has low amplitude; see Figure 2b. In addition, this wavetrain has high frequency relative to the DSW; again, see Figure 2b. So, the appropriate dispersion relation for the resonant wavetrain is (52). In the RDSW regime, the resonance condition for the resonant wavetrain ahead of the DSW has been set by matching the phase velocity of the resonant wavetrain to the velocity of the lead wave of the DSW [34–36], giving

$$s_+ = c_r, \quad c = \bar{v} + \frac{1}{2}k + \frac{2\bar{\rho}}{qk}, \tag{53}$$

so that

$$k_r = s_+ + \left[s_+^2 - \frac{4}{q}u_+^2 \right]^{1/2} \tag{54}$$

on setting $\bar{\rho} = \sqrt{u_+}$ and $\bar{v}_+ = 0$ as the resonant wavetrain propagates on the level ahead. This gives the wavenumber of the resonant wavetrain based on this criterion. The resonant wavetrain then exists if $s_+ \geq 2u_+/\sqrt{q}$, so that the borderline between the PDSW and RDSW regimes is $s_+ = 2u_+/\sqrt{q}$. Previous work [35,36] has shown that this theoretical borderline is in excellent agreement with numerical solutions in the high nonlocality limit ν large. For fixed u_+ , as ν decreases, a PDSW changes to an RDSW, then to a CDSW; see Figure 3. For instance, for $u_+ = 0.8$, the DSW changes from PDSW to RDSW at $\nu = 88$, then to CDSW at $\nu = 34$. However, the resonance condition (53), or (54), gives that the DSW changes from PDSW to RDSW at $\nu = 3$, which is the TDSW regime according to Table 1. This resonance condition is based on the limit $\nu k^2 \gg 1$, but, even if the full dispersion relation (51) were used for the resonance condition (53), the predicted PDSW/RDSW borderline is $\nu = 2.38$, which is still far from the numerical value and close to that for $\nu k^2 \gg 1$. The resonance condition (53) is based on resonance between the lead wave of the DSW and diffractive radiation. However, as pointed out previously [36], a DSW is modulated periodic wave so that all waves of the DSW can resonant with diffractive radiation, not just the lead wave, as seen in Figure 5 for a PDSW. Internal resonance will be discussed in detail in Section 5. The phase velocity of a component wave of the DSW is (72). Equating this bore component phase velocity with the nematic diffractive radiation phase velocity determined from the dispersion relation (18) determines the internal resonance. However, even using this internal resonance does not result in a borderline between the PDSW and RDSW regimes in any reasonable accord with numerical solutions; see Figure 3. A resonant wavetrain will then exist if the internally resonant waves can propagate out of the DSW, that is their group velocity is greater than the velocity of the lead solitary wave of the DSW. However, even this condition does not give the correct boundary between the PDSW and RDSW regimes as the nonlocality parameter ν decreases. The issue of internal resonance and its relation to the existence of the PDSW and RDSW regimes merits further study. In this regard, the recent work [55] on the interaction of linear wavepackets and DSWs could be relevant.

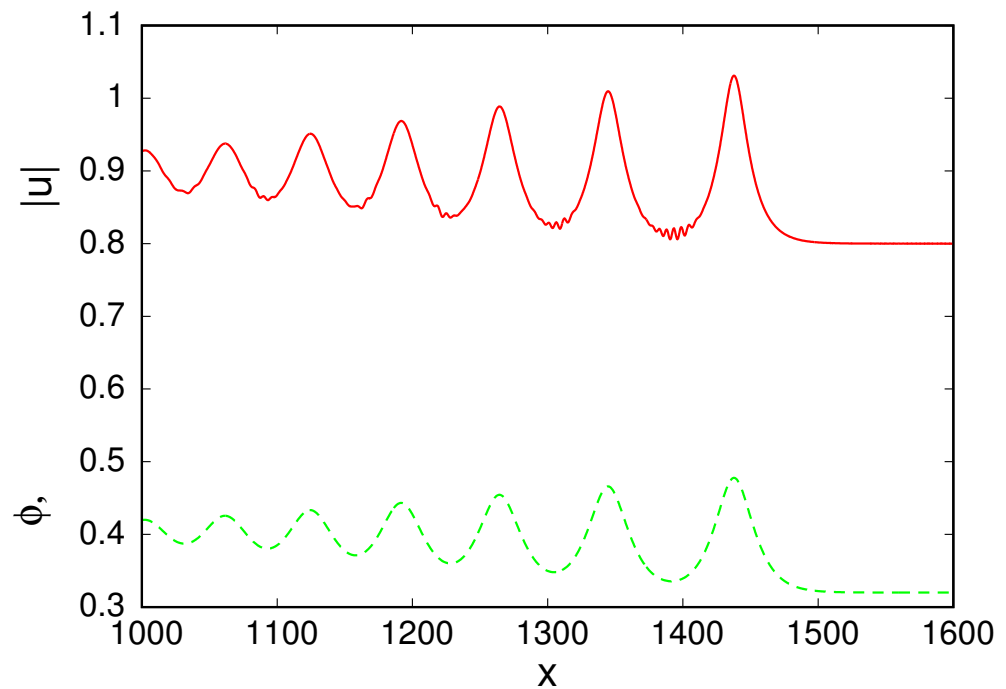


Figure 5. Numerical solution of nematic Equations (11) and (12) in PDSW regime at $z = 1500$ for initial condition (13) with $u_+ = 0.8$ and $u_- = 1.0$. Red (solid) line: $|u|$; green (dashed) line: ϕ . Here, $\nu = 200$ and $q = 2$.

5. CDSW Regime

For fixed a nonlocality parameter ν , as u_+ decreases, the jump height $u_- - u_+$ increases, the nematic DSW changes from RDSW to CDSW form; see Figure 3b. The reason for this is that, as the amplitude of the resonant wavetrain grows, it takes more conserved quantities from the DSW, so that its amplitude is reduced. In addition, the DSW becomes unstable in the CDSW regime, as for the Kawahara equation DSW [26], noting that, in the small jump height limit, the nematic equations reduce to the eKdV Equation (42), which becomes the Kawahara Equation (44) in the limit of large nonlocality ν . Figure 2c shows a typical nematic DSW in the CDSW regime. It can be seen that the DSW has changed from a modulated wavetrain with a monotonically decreasing amplitude from front to rear to a disordered wavetrain with an essentially uniform amplitude on average, except at its rear. This structure is in agreement with unstable DSW structure for the focusing NLS equation [56]. The unstable DSW can then be approximated by a train of equal amplitude solitary waves, which has been found to give good results for DSW solutions [57], particularly unstable DSWs, and for the particular case of the nematic CDSW in the high nonlocality, low optical power, regime [36]. The amplitude of the solitary waves of the CDSW is determined from mass and energy conservation equations for the underlying nonlinear dispersive wave equation [57].

If we set

$$B_2 = 3\sqrt{\frac{2}{q}}, \quad B_3 = \frac{4\nu u_+^2 - q^2}{8\sqrt{2}q^{3/2}u_+} \tag{55}$$

for simplicity, the eKdV Equation (42) has the mass conservation equation

$$\begin{aligned} \frac{\partial}{\partial \eta} Q + \frac{\partial}{\partial \xi} \left[\frac{1}{2} B_2 Q^2 + B_3 Q_{\xi\xi} + \frac{1}{3} \varepsilon^2 c_1 Q^3 + \frac{1}{2} \varepsilon^2 (c_2 - c_3) Q_{\xi}^2 + \varepsilon^2 c_3 Q Q_{\xi\xi} \right. \\ \left. + \varepsilon^2 c_4 Q_{\xi\xi\xi\xi} \right] = 0. \end{aligned} \tag{56}$$

The derivation of the energy conservation for the eKdV Equation (42) is not as straightforward. Multiplying the eKdV equation by Q and integrating by parts gives

$$\frac{\partial}{\partial \eta} \frac{1}{2} Q^2 + \frac{\partial}{\partial \xi} \left[\frac{1}{3} B_2 Q^3 + B_3 Q Q_{\xi\xi} - \frac{1}{2} B_3 Q_{\xi}^2 + \frac{1}{4} \varepsilon^2 c_1 Q^4 + \frac{1}{2} \varepsilon^2 c_2 Q^2 Q_{\xi\xi} + \varepsilon^2 c_4 Q Q_{\xi\xi\xi\xi} - \varepsilon^2 c_4 Q_{\xi} Q_{\xi\xi\xi} + \frac{1}{2} \varepsilon^2 c_4 Q_{\xi\xi}^2 \right] + \varepsilon^2 \left(c_3 - \frac{1}{2} c_2 \right) Q^2 Q_{\xi\xi\xi} = 0. \tag{57}$$

The final term on the right hand side of this equation cannot be expressed as a perfect derivative. However, it can be approximately expressed in this form on noting that ε is small, so that, at first order, the eKdV Equation (42) is the KdV equation

$$\frac{\partial Q}{\partial \eta} + B_2 Q \frac{\partial Q}{\partial \xi} + B_3 \frac{\partial^3 Q}{\partial \xi^3} = 0. \tag{58}$$

We then have at leading order that

$$\frac{\partial}{\partial \eta} Q^3 = -3Q^2 (B_2 Q Q_{\xi} + B_3 Q_{\xi\xi\xi}) = -\frac{\partial}{\partial \xi} \frac{3}{4} B_2 Q^4 - 3B_3 Q^2 Q_{\xi\xi\xi}. \tag{59}$$

This expression may now be used to eliminate the term in $Q Q_{\xi\xi\xi}$ in Equation (57) to give the final energy conservation equation

$$\frac{\partial}{\partial \eta} \left[\frac{1}{2} Q^2 - \varepsilon^2 \frac{c_3 - \frac{1}{2} c_2}{3B_3} Q^3 \right] + \frac{\partial}{\partial \xi} \left[\frac{1}{3} B_2 Q^3 + B_3 Q Q_{\xi\xi} - \frac{1}{2} B_3 Q_{\xi}^2 + \frac{1}{4} \varepsilon^2 c_1 Q^4 + \frac{1}{2} \varepsilon^2 c_2 Q^2 Q_{\xi\xi} + \varepsilon^2 c_4 Q Q_{\xi\xi\xi\xi} - \varepsilon^2 c_4 Q_{\xi} Q_{\xi\xi\xi} + \frac{1}{2} \varepsilon^2 c_4 Q_{\xi\xi}^2 - \varepsilon^2 \frac{B_2}{4B_3} \left(c_3 - \frac{1}{2} c_2 \right) Q^4 \right] = 0, \tag{60}$$

which is accurate to $O(\varepsilon^2)$.

To obtain an approximation to the nematic CDSW, let us assume that, at position η , the CDSW consists of N equal solitary waves of amplitude \tilde{a}_s and width \tilde{w}_s [57], where we shall use tildes to denote scaled variables in the moving and stretched coordinates (ξ, η) . It is also assumed that the CDSW sheds a uniform downstream resonant wavetrain of (scaled) amplitude \tilde{a}_r . Then, as $\xi \rightarrow -\infty$, $Q \rightarrow 1$ and as $\xi \rightarrow \infty$, $Q \rightarrow \tilde{a}_r \cos(\tilde{k}_r \xi - \tilde{\omega}_r \eta)$, since $|u| = u_+ + \varepsilon^2 Q$ with $\varepsilon^2 = u_i - u_+$. As the CDSW is approximated by a train of solitary waves, the solitary wave solution of the eKdV Equation (42) is also needed. While there is no known exact solitary wave solution of this equation, there is an asymptotic solution for $\varepsilon \ll 1$ [58]. To use this solution, the eKdV Equation (42) needs to be rescaled to conform with the eKdV scaling of Reference [58]. Performing this, we find that the asymptotic solitary wave solution of the eKdV Equation (42) is

$$Q = \gamma_1 \operatorname{sech}^2 \frac{\xi - V_s \eta}{W} + \gamma_2 \operatorname{sech}^4 \frac{\xi - V_s \eta}{W}, \quad V_s = \frac{1}{3} B_2 A \left(1 + 2\varepsilon^2 C_4 A \right), \tag{61}$$

where

$$W = \frac{\sqrt{12B_3}}{\sqrt{B_2 A}}, \quad \gamma_1 = A + \varepsilon^2 C_6 A^2, \quad \gamma_2 = \varepsilon^2 C_7 A^2. \tag{62}$$

The rescaled coefficients c_i , $i = 1, \dots, 4$, of the eKdV Equation (42), denoted by C_i , $i = 1, \dots, 4$, are given by

$$\begin{aligned} C_1 &= \frac{6}{B_2} c_1, & C_2 &= \frac{1}{B_3} c_2, & C_3 &= \frac{1}{B_3} c_3, & C_4 &= \frac{B_2}{6B_3^2} c_4, \\ C_6 &= \frac{2}{3} C_3 - \frac{1}{6} C_1 + \frac{1}{6} C_2 - 5C_4, & C_7 &= \frac{15}{2} C_4 - \frac{1}{2} C_3 + \frac{1}{12} C_1 - \frac{1}{4} C_2. \end{aligned} \tag{63}$$

It is noted that these scaled C_i , $i = 1, \dots, 4$, are the same as the C_i (49) used for the perturbed DSW solution (45)–(48) due to the same rescaling from the eKdV Equation (42) being used for this solution.

The mass and energy conservation Equations (56) and (60) can now be used to determine the amplitude of the solitary waves in the nematic CDSW in the equal amplitude approximation. The mass and energy conservation equations are integrated in ζ from $-\infty$ to ∞ . The integral of the mass and energy densities are approximated by N times these for a single solitary wave (61). The flux terms are calculated using the boundary conditions stated above, $Q = 1$ at $\zeta = -\infty$ and $Q = \tilde{a}_r \cos(\tilde{k}_r \zeta - \tilde{\omega}_r \eta)$ at $\zeta = \infty$. The resonant radiation flux at $\zeta = \infty$ is calculated by averaging the periodic radiation over a period [36]. In this manner, integrating the mass conservation equation gives

$$N \left[2\gamma_1 + \frac{4}{3}\gamma_2 \right] W = \left\{ \frac{1}{2}B_2 + \frac{1}{3}\varepsilon^2 c_1 - \left[\frac{1}{4}B_2 + \frac{1}{4}\varepsilon^2 (c_2 - 3c_3)\tilde{k}_r^2 \right] \tilde{a}_r^2 \right\} \eta \tag{64}$$

and integrating the energy conservation equation gives

$$\begin{aligned} N \left[\frac{2}{3}\gamma_1^2 + \frac{16}{15}\gamma_1\gamma_2 - \varepsilon^2 \frac{16}{45} \frac{c_3 - \frac{1}{2}c_2}{B_3} \gamma_1^3 \right] W &= \left\{ \frac{1}{3}B_2 + \frac{1}{4}\varepsilon^2 c_1 \right. \\ &- \varepsilon^2 \frac{B_2}{4B_3} \left(c_3 - \frac{1}{2}c_2 \right) - \frac{1}{4} \left[-3B_3\tilde{k}_r^2\tilde{a}_r^2 + \frac{3}{8}\varepsilon^2 c_1\tilde{a}_r^4 + 5\varepsilon^2 c_4\tilde{k}_r^2\tilde{a}_r^2 \right. \\ &\left. \left. - \varepsilon^2 \frac{3B_2}{8B_3} \left(c_3 - \frac{1}{2}c_2 \right) \tilde{a}_r^4 \right] \right\} \eta \\ &\sim \left\{ \frac{1}{3}B_2 + \frac{1}{4}\varepsilon^2 c_1 - \varepsilon^2 \frac{B_2}{4B_3} \left(c_3 - \frac{1}{2}c_2 \right) - \frac{1}{4}\tilde{c}_g\tilde{a}_r^2 \right\} \eta \end{aligned} \tag{65}$$

since \tilde{a}_r is small. In addition, this neglect of quartic terms in \tilde{a}_r is consistent with the radiation being determined by a linear WKB analysis [35]. Here, \tilde{c}_g is the scaled group velocity of the resonant radiation based on (29). Dividing the mass and energy Equations (64) and (65) gives an equation for A

$$\frac{\gamma_1^2 + \frac{8}{5}\gamma_1\gamma_2 - \varepsilon^2 \frac{8}{15} \frac{c_3 - \frac{1}{2}c_2}{B_3} \gamma_1^3}{\gamma_1 + \frac{2}{3}\gamma_2} = 4 \frac{B_2 + \frac{3}{4}\varepsilon^2 c_1 - \varepsilon^2 \frac{3B_2}{4B_3} \left(c_3 - \frac{1}{2}c_2 \right) - \frac{3}{4}\tilde{c}_g\tilde{a}_r^2}{2B_2 + \frac{4}{3}\varepsilon^2 c_1 - [B_2 + \varepsilon^2 (c_2 - 3c_3)\tilde{k}_r^2] \tilde{a}_r^2} \tag{66}$$

in terms of \tilde{a}_r . Once A is determined, the unscaled amplitude a_s of the solitary waves of the CDSW is given by

$$a_s = \varepsilon^2 \left[A + \varepsilon^2 (C_6 + C_7) A^2 \right] = (u_i - u_+) \left[A + (u_i - u_+) (C_6 + C_7) A^2 \right], \tag{67}$$

on using the solitary wave solution (61). Transforming back from the scaled eKdV variables to the original variables, the relation (66) becomes

$$\begin{aligned} &\frac{\gamma_1^2 + \frac{8}{5}\gamma_1\gamma_2 - \frac{8}{15}(u_i - u_+) \frac{c_3 - \frac{1}{2}c_2}{B_3} \gamma_1^3}{\gamma_1 + \frac{2}{3}\gamma_2} \\ &= 4 \frac{B_2 + \frac{3}{4}(u_i - u_+)c_1 - \frac{3B_2}{4B_3}(u_i - u_+) \left(c_3 - \frac{1}{2}c_2 \right) - \frac{3}{4} \frac{(c_g - \sqrt{\frac{2}{q}}u_+)a_r^2}{(u_i - u_+)^3}}{2B_2 + \frac{4}{3}(u_i - u_+)c_1 - [B_2 + (c_2 - 3c_3)k_r^2] \frac{a_r^2}{(u_i - u_+)^2}} \end{aligned} \tag{68}$$

on using the scalings (63) for the eKdV equation. Substituting for the higher order solitary wave coefficients γ_1 and γ_2 given by (62) gives the final equation determining the amplitude of the CDSW solitary waves as

$$A \frac{1 + 2(u_i - u_+) \left(C_6 + \frac{4}{5} C_7 \right) A - \frac{8}{15} (u_i - u_+) \left(C_3 - \frac{1}{2} C_2 \right) A}{1 + (u_i - u_+) \left(C_6 + \frac{2}{3} C_7 \right) A} = 4 \frac{B_2 + \frac{1}{8} (u_i - u_+) B_2 (C_1 + 3C_2 - 6C_3) - \frac{3}{4} \frac{(c_8 - \sqrt{\frac{2}{q}} u_+) a_r^2}{(u_i - u_+)^3}}{2B_2 + \frac{2}{9} (u_i - u_+) B_2 C_1 - [B_2 + (c_2 - 3c_3) k_r^2] \frac{a_r^2}{(u_i - u_+)^2}}. \tag{69}$$

The final quantity to determine is the amplitude of a_r of the resonant radiation, which is related to the scaled amplitude \tilde{a}_r by $a_r = \varepsilon^2 \tilde{a}_r = (u_i - u_+) \tilde{a}_r$. This resonant radiation was determined as a WKB solution of the nematic Equations (11) and (12) by linearizing about the mean level u_+ of the resonant radiation [35]. This WKB solution gives the amplitude of the resonant radiation as

$$a_r = \frac{1}{2} \frac{u_- - u_+}{1 + \frac{2u_+ k_r a_s}{q s_+ (k_r - s_+)^2}}. \tag{70}$$

Here, s_+ is the unscaled velocity of the CDSW, which is [36]

$$s_+ = \sqrt{\frac{2}{q}} u_+ + \frac{1}{3} B_2 a_s (1 + 2C_4 a_s). \tag{71}$$

The resonant radiation wavenumber k_r is determined by the resonance condition (54) and the group velocity of the resonant radiation is given by the k derivative of the short wave dispersion relation (52). The resonant radiation is a solution of the nematic equations in the limit $\nu k^2 \gg 1$, so that the appropriate group velocity for it is that from the dispersion relation (52), not the linearized KdV group velocity of the eKdV Equation (42) [36].

Figure 6 displays comparisons of the nematic DSW amplitude a_s and resonant wave amplitude a_r in the CDSW regime as given by (68) and (70) and numerical solutions. A typical CDSW is shown in Figure 2c, with details of the actual CDSW of this figure shown in Figure 7a. It can be seen that the lead waves of the DSW have an approximately uniform amplitude, with a rapid decrease of the amplitude towards the trailing edge of the CDSW, as also illustrated in Figure 7b. This solution, and that of Figure 7a, are typical structures for an unstable DSW [56]. The numerical DSW amplitude for the comparisons of this figure was calculated as an average over the approximately uniform waves at the leading edge, which is the same assumption on which the equal amplitude approximation used to calculate the solitary wave amplitude a_s was based. Figure 6a shows comparisons for the amplitude a_r of the resonant wavetrain leading the CDSW; see Figure 2c. It can be seen that there is excellent agreement between the theoretical amplitude and the numerical amplitude for the larger values of the level ahead u_+ , with the increase of a_r as the nonlocality parameter ν decreases being correctly given. This agreement is much improved through the inclusion of the all the higher order terms in the eKdV Equation (42) than that of previous work [36] based on the Kawahara equation, for which $c_1 = c_2 = c_3 = 0$, as given by the green dashed line in the figure. As u_+ decreases and the TDSW regime is approached, the agreement between theory and numerical solutions decreases. This is shown particularly in the final comparison of Figure 6a for $u_+ = 0.5$, which is near the TDSW boundary; see Figure 3. The reason for this decreasing agreement is that, as the TDSW regime is approached, the number of waves in the CDSW decreases so that only one lead wave is left; see Figure 7c. The approximation that an average can be taken over an equal amplitude wavetrain then breaks down.

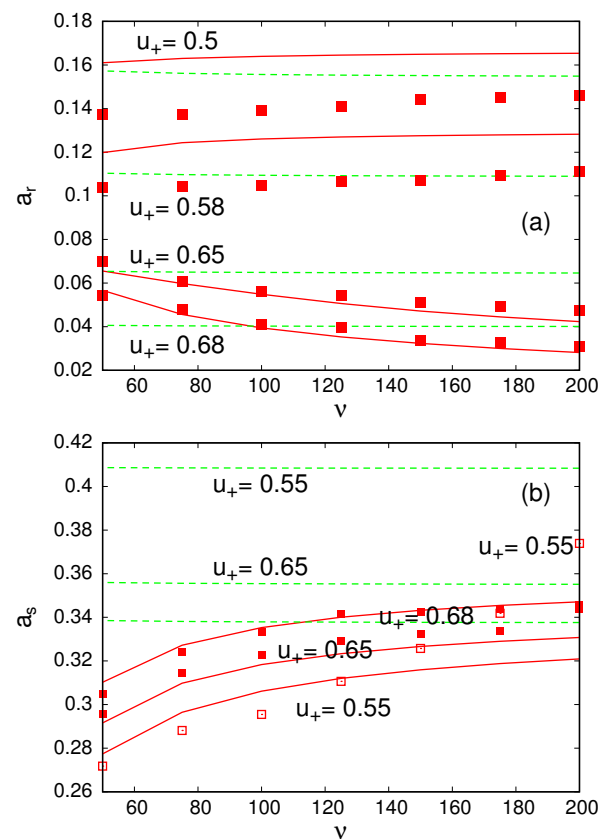


Figure 6. Comparison between theory and numerical solutions of the nematic Equations (11) and (12) with the initial condition (13) for the nematic CDSW. Numerical amplitude: red squares; amplitude (70): red (solid) line; amplitude given by the Kawahara equation (equation (42) with $c_1 = c_2 = c_3 = 0$): green (dashed) line. (a) Resonant wave amplitude a_r , (b) CDSW solitary wave amplitude a_s (67). Note that, for clarity, the numerical DSW amplitude for $u_+ = 0.55$ is denoted by red open squares. Here, $u_- = 1.0$ and $q = 2$.

Figure 6b displays similar comparisons for the amplitude a_s of the nematic CDSW with numerical solutions. It can be seen that the comparison for the DSW amplitude is similar to that for the resonant wave amplitude. It should be noted that different values of u_+ have been chosen for the DSW amplitude comparisons for the sake of clarity. The inclusion of all the higher order terms in the eKdV Equation (42) results in a significant improvement in the agreement with numerical solutions over that based on the Kawahara equation with $c_1 = c_2 = c_3 = 0$ when the level ahead u_+ is away from the TDSW/CDSW boundary of Figure 3. As u_+ approaches the TDSW/CDSW boundary, the DSW amplitude as given by the eKdV equation differs significantly from the numerical amplitude. The reason for this is that discussed in the previous paragraph for the resonant wave amplitude, the fact that the CDSW ceases to be a train of equal amplitude solitary waves, but reduces to a few waves.

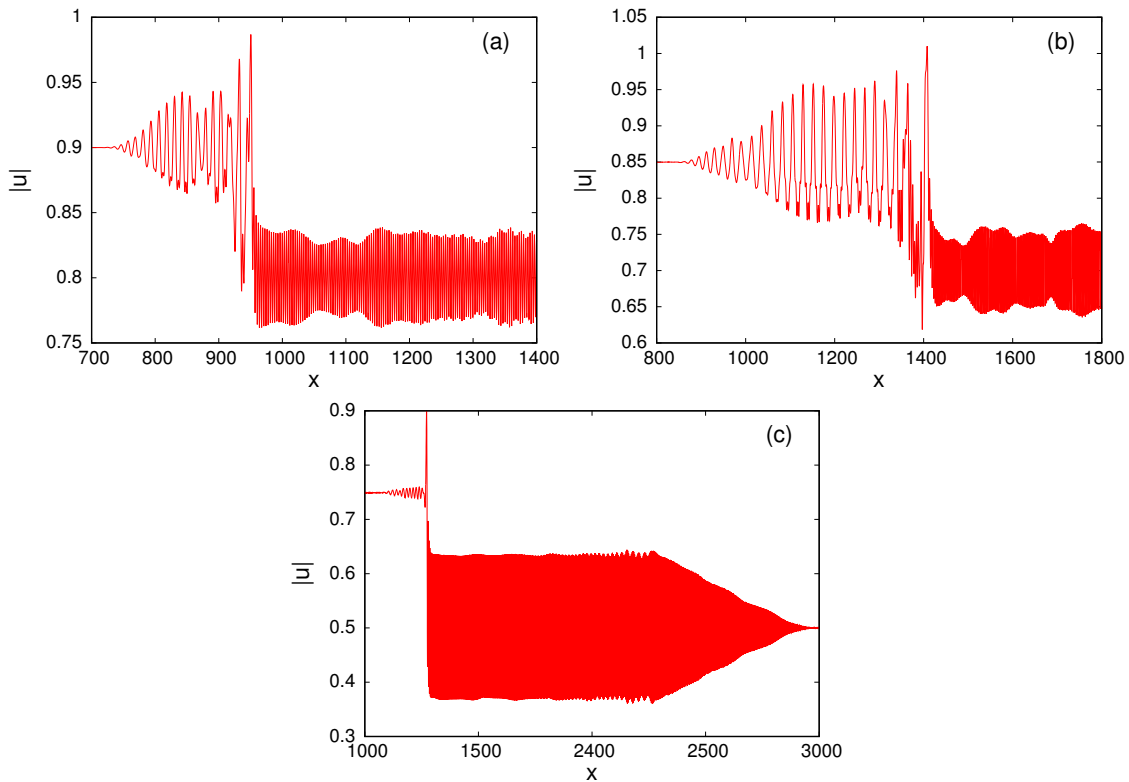


Figure 7. Numerical solution of nematic Equations (11) and (12) in the CDSW regime for the initial condition (13). (a) $u_+ = 0.8$ at $z = 1000$, (b) $u_+ = 0.7$ at $z = 1500$, (c) $u_+ = 0.5$ at $z = 1500$. Here, $u_- = 1.0$ and $q = 2$.

The next thing that we discuss is the analytical borderline between the nematic CDSW and RDSW regimes. This borderline can be found by determining when the resonant amplitude (70) approaches zero or approaches a minimum as a function of the nonlocality parameter ν . The determination of this borderline is similar to that of previous work [36] in which the resonant amplitude was found as a function of the initial state u_+ , rather than ν . This approach gave a borderline for $u_+ \leq 0.73$ for large ν , with the CDSW regime not existing above this value of u_+ for large ν . Above this limit, the resonance condition (53) ceases to work as a function of ν and an alternative method needs to be found to determine the borderline. To determine the borderline in this case, we exploit the fact that the (interior) structure of the nematic DSW is resonant, as evidenced in Figure 5, not only the leading, solitary wave edge. A DSW is an extended modulated periodic wavetrain, so that all its component waves can resonant, not just the leading edge. To verify this internal resonance, the phase velocity of the modulated cnoidal waves forming the DSW needs to be matched with the nematic linear phase velocity on the local mean level of the DSW. By way of illustration, we equate the DSW phase velocity [47]

$$c_p = \sqrt{\frac{2}{q}}u_+ + \frac{(u_i - u_+)}{\sqrt{2q}} \left\{ 2 + 2m - \frac{1}{7}(u_i - u_+)(8C_4 - C_3)(2m - m^2 - 1) \right. \\ \left. + \frac{1}{3}(u_i - u_+)C_4(2 + 2m)^2 - \frac{1}{6}(u_i - u_+)(C_3 - C_1 + 4C_4)(2 + 2m) \right\}, \quad (72)$$

where C_1 , C_3 , and C_4 are given in (49), with the nematic phase velocity from the full linear dispersion relation (51) on the DSW background (47) and solved for internal resonant wavenumbers, which are always positive and real, as the modulus m varies from near zero to near one. As the DSW parameter expressions (47) and (72) are only valid for a well-ranked DSW (stable DSW), such as the PDSW and the RDSW, and the CDSW is an ill-ranked DSW (unstable DSW), then a borderline exists when these wave parameter

expressions result in imaginary internal resonant wavenumbers, which are unphysical, at a borderline value of ν . The mean flow \bar{v} in the dispersion relation (51) was determined from the extended KdV reduction of the nematic equations of Section 4. Substituting the $O(\varepsilon^2)$ mean flow v_1 given by (31) into the mean flow perturbation expansion (27) for v and then averaging gives

$$\bar{v} = \frac{2\sqrt{2}}{\sqrt{q}} (|\bar{u}| - u_+). \tag{73}$$

This then completes the determination of the CDSW/RDSW borderline. A comparison between the theoretical and numerical borderlines between the RDSW and CDSW regimes is shown in Figure 3. It can be seen that the theoretical borderline is in excellent agreement with the numerical borderline for large values of the nonlocality parameter ν down to around $\nu = 50$, with poorer agreement towards the local limit with ν small for which the DSW is changing form from KdV type to NLS type.

6. TDSW Regime

Figure 2d displays a typical DSW in the TDSW regime. There is (almost) a constant amplitude resonant wavetrain which, at its trailing edge, is connected to the intermediate level u_i . At its leading edge there is a modulated wavetrain which takes u down to the level u_+ ahead. This wavetrain leading the resonant wave is a partial DSW [27,36,49]. A partial DSW differs from a standard DSW in that it connects a uniform state to a periodic wavetrain, unlike a standard DSW which links two different levels. While there is a negative polarity solitary wave connecting the resonant wavetrain to the intermediate level [26], this connection can be approximated by a Whitham shock [36,48], a shock, a jump, in the modulation parameters of the wavetrain, wavelength, frequency, amplitude, and mean level, of the Whitham modulation equations for the modulated periodic wavetrain [12]. A Whitham shock is determined from the Whitham modulation equations. As noted above, the nematic DSW is in the nonlocal regime, so the appropriate Whitham modulation equations are those for ν large.

The Whitham modulation equations in the highly nonlocal limit $\nu \gg 1$ (low optical power) have previously been determined [36], so these modulation equations will just be quoted here. These modulation equations determine the mean level $\bar{\rho}$ of ρ , the amplitude a and the wavenumber k of the Stokes' wave solution of the nematic Equations (15)–(17). As there is no known general periodic wave solution of the nematic equations, the highly nonlocal Whitham modulation equations are derived based on the weakly nonlinear Stokes wavetrain for the nematic equations [36]. It can be seen from Figure 2d that the resonant wavetrain has small amplitude, so the weakly nonlinear limit is appropriate. In the highly nonlocal limit $\nu \gg 1$, the Stokes' wave solution of the nematic Equations (15)–(17) is

$$\rho = \bar{\rho} + a \cos \varphi + \dots, \tag{74}$$

$$v = \bar{v} + av_1 \cos \varphi + \dots, \tag{75}$$

$$\phi = \frac{\bar{\rho}}{q} + a\phi_1 \cos \varphi + \dots, \tag{76}$$

$$\omega = \omega_0 + a\omega_1 + a^2\omega_2 + \dots, \tag{77}$$

where the uniform phase is $\varphi = kx - \omega z$, and the over bar, $\bar{\rho}$ and \bar{v} , denotes the mean value of a wave parameter [36]. The amplitude a of the (Stokes) wave is assumed to be

small. The work of Reference [36] gives that, at $O(a)$, the nematic Stokes coefficients and the $O(a^2)$ correction to the dispersion relation are

$$\omega_0 = k\bar{v} + \frac{k^2}{2} + \frac{4\bar{\rho}}{\nu k^2} - \frac{8\bar{\rho}q}{\nu^2 k^4} - \frac{16\bar{\rho}^2}{\nu^2 k^6} + \dots, \tag{78}$$

$$v_1 = \frac{k}{2\bar{\rho}} + \frac{4}{\nu k^3} - \frac{8q}{\nu^2 k^5} - \frac{16\bar{\rho}}{\nu^2 k^7} + \dots, \tag{79}$$

$$\phi_1 = \frac{2}{\nu k^2} - \frac{4q}{\nu^2 k^4} + \dots, \tag{80}$$

$$\omega_2 = -\frac{k^2}{8\bar{\rho}^2} - \frac{3}{\bar{\rho}\nu k^2} + \frac{6q}{\bar{\rho}\nu^2 k^4} - \frac{20}{\nu^2 k^6} + \dots \tag{81}$$

The coefficient ω_1 is set to zero, $\omega_1 = 0$, to eliminate secular terms. The weakly nonlinear Whitham modulation equations can then be derived by averaging conservation laws deduced from Nöther’s Theorem [59]. The Lagrangian for the hydrodynamic form of the nematic Equations (15)–(17) is

$$L = -2\rho\psi_z - \frac{1}{4} \frac{\rho_x^2}{\rho} - \rho\psi_x^2 - 4\rho\phi + \nu\phi_x^2 + 2q\phi^2. \tag{82}$$

Applying Nöther’s Theorem we have that translation invariance with respect to the phase ψ gives the mass conservation law

$$\frac{\partial}{\partial z} \frac{\partial L}{\partial \psi_z} + \frac{\partial}{\partial x} \frac{\partial L}{\partial \psi_x} = 0, \tag{83}$$

translation invariance with respect to space x yields the momentum conservation law

$$\frac{\partial}{\partial z} \left(\frac{\partial L}{\partial \rho_z} \frac{\partial \rho}{\partial x} + \frac{\partial L}{\partial \psi_z} \frac{\partial \psi}{\partial x} + \frac{\partial L}{\partial \phi_z} \frac{\partial \phi}{\partial x} \right) + \frac{\partial}{\partial x} \left(\frac{\partial L}{\partial \rho_x} \frac{\partial \rho}{\partial x} + \frac{\partial L}{\partial \psi_x} \frac{\partial \psi}{\partial x} + \frac{\partial L}{\partial \phi_x} \frac{\partial \phi}{\partial x} - L \right) = 0, \tag{84}$$

and translation invariance with respect to time-like z gives the energy conservation law

$$\frac{\partial}{\partial z} \left(\frac{\partial L}{\partial \rho_z} \frac{\partial \rho}{\partial z} + \frac{\partial L}{\partial \psi_z} \frac{\partial \psi}{\partial z} + \frac{\partial L}{\partial \phi_z} \frac{\partial \phi}{\partial z} - L \right) + \frac{\partial}{\partial x} \left(\frac{\partial L}{\partial \rho_x} \frac{\partial \rho}{\partial z} + \frac{\partial L}{\partial \psi_x} \frac{\partial \psi}{\partial z} + \frac{\partial L}{\partial \phi_x} \frac{\partial \phi}{\partial z} \right) = 0. \tag{85}$$

Substituting the Stokes expansions (74)–(76) into these conservation laws and averaging by integrating in φ from 0 to 2π [12] yields the modulation equations, truncated to $O(1/\nu)$,

$$\frac{\partial k}{\partial z} + \frac{\partial}{\partial x} \left(k\bar{v} + \frac{k^2}{2} + \frac{2\bar{\rho}}{q} + \frac{4\bar{\rho}}{\nu k^2} - \frac{k^2 a^2}{8\bar{\rho}^2} - \frac{3a^2}{\nu \bar{\rho} k^2} \right) = 0, \tag{86}$$

$$\frac{\partial \bar{\rho}}{\partial z} + \frac{\partial}{\partial x} \left(\bar{\rho}\bar{v} + \frac{ka^2}{4\bar{\rho}} + \frac{2a^2}{\nu k^3} \right) = 0, \tag{87}$$

$$\frac{\partial}{\partial z} \left(\bar{\rho}\bar{v} + \frac{ka^2}{4\bar{\rho}} + \frac{2a^2}{\nu k^3} \right) + \frac{\partial}{\partial x} \left(\frac{\bar{\rho}^2}{q} + \bar{\rho}\bar{v}^2 + \frac{k^2 a^2}{4\bar{\rho}} + \frac{\bar{v}ka^2}{2\bar{\rho}} + \frac{4\bar{v}a^2}{\nu k^3} + \frac{a^2}{\nu k^2} \right) = 0, \tag{88}$$

$$\begin{aligned} & \frac{\partial}{\partial z} \left(\bar{\rho}\bar{v}^2 + \frac{2\bar{\rho}^2}{q} + \frac{k^2 a^2}{4\bar{\rho}} + \frac{k\bar{v}a^2}{2\bar{\rho}} + \frac{4a^2}{\nu k^2} + \frac{4\bar{v}a^2}{\nu k^3} \right) + \frac{\partial}{\partial x} \left(\bar{\rho}\bar{v}^3 + \frac{4\bar{v}\bar{\rho}^2}{q} + \frac{ka^2}{q} + \frac{k^3 a^2}{4\bar{\rho}} \right. \\ & \left. + \frac{3\bar{v}k^2 a^2}{4\bar{\rho}} + \frac{3\bar{v}^2 ka^2}{4\bar{\rho}} + \frac{6\bar{v}a^2}{\nu k^2} + \frac{6\bar{v}^2 a^2}{\nu k^3} + \frac{2a^2}{\nu k} \right) = 0 \end{aligned} \tag{89}$$

for the (slowly varying) amplitude a , wavenumber k , and means $\bar{\rho}$ and \bar{v} of the modulated Stokes wave [12].

The modulation Equation (87) is that, for optical power conservation, Equation (88) is momentum conservation, and (89) is energy conservation. The modulation Equation (86)

is the equation for conservation of waves, $k_z + \omega_x = 0$, on noting that the x derivative term is just the dispersion relation (77). In this regard, it should be noted that the dispersion relation for the Stokes' wave from which the modulation equations are calculated has the carrier waves' phase shift term $2\bar{\rho}/q$ added [35,36], as explained above,

$$\omega = k\bar{v} + \frac{1}{2}k^2 + \frac{2\bar{\rho}}{q} + \frac{4\bar{\rho}}{vk^2} - \frac{k^2a^2}{8\bar{\rho}^2} - \frac{3a^2}{vk^2\bar{\rho}}. \quad (90)$$

Figure 2d shows that, in the TDSW regime, the KdV-type nematic bore structure of Figure 2a–c has disappeared, leaving a dominant resonant wavetrain which is linked to the intermediate level u_i by a negative polarity solitary wave [26]. As discussed above, this link between the resonant wavetrain and the intermediate level can be approximated by a Whitham shock, a jump in the modulation equation variables [36,48], so that the Whitham shock links the resonant wavetrain with the level u_i behind, in a similar manner to a gas dynamic shock wave links two compressible flow states [12]. Let us denote the amplitude, wavenumber, mean level and mean phase gradient of the resonant wavetrain by $a_r, k_r, \bar{\rho}_r,$ and $\bar{v}_r,$ respectively. Matching the Whitham shock velocity U_s to the Stokes' wave velocity (90), as these are co-propagating, gives

$$U_s = \bar{v}_r + \frac{1}{2}k_r + \frac{2\bar{\rho}_r}{qk_r} + \frac{4\bar{\rho}_r}{vk_r^3} - \frac{k_r a_r^2}{8\bar{\rho}_r^2} - \frac{3a_r^2}{vk_r^3\bar{\rho}_r}. \quad (91)$$

Ahead of the Whitham shock, there is the resonant wavetrain, and behind it is a flat shelf, the intermediate level, which is a wavetrain of zero amplitude. The mass, momentum, and energy conservation Equations (87)–(89) then give the jump conditions

$$\begin{aligned} U_s(\bar{\rho}_r - \rho_i) &= \bar{\rho}_r\bar{v}_r + \frac{k_r a_r^2}{4\bar{\rho}_r} + \frac{2a_r^2}{vk_r^3} - \rho_i v_i, \\ U_s\left(\bar{\rho}_r\bar{v}_r + \frac{k_r a_r^2}{4\bar{\rho}_r} + \frac{2a_r^2}{vk_r^3} - \rho_i v_i\right) &= \frac{\bar{\rho}_r^2}{q} + \bar{\rho}_r\bar{v}_r^2 + \frac{k_r^2 a_r^2}{4\bar{\rho}_r} + \frac{\bar{v}_r k_r a_r^2}{2\bar{\rho}_r} + \frac{4\bar{v}_r a_r^2}{vk_r^3} \\ &+ \frac{a_r^2}{vk_r^2} - \frac{\rho_i^2}{q} - \rho_i v_i^2, \end{aligned} \quad (92)$$

$$\begin{aligned} U_s\left(\bar{\rho}_r\bar{v}_r^2 + \frac{2\bar{\rho}_r^2}{q} + \frac{k_r^2 a_r^2}{4\bar{\rho}_r} + \frac{k_r\bar{v}_r a_r^2}{2\bar{\rho}_r} + \frac{4a_r^2}{vk_r^2} + \frac{4\bar{v}_r a_r^2}{vk_r^3} - \rho_i v_i^2 - \frac{2\rho_i^2}{q}\right) &= \bar{\rho}_r\bar{v}_r^3 + \frac{4\bar{v}_r\bar{\rho}_r^2}{q} \\ &+ \frac{k_r a_r^2}{q} + \frac{k_r^3 a_r^2}{4\bar{\rho}_r} + \frac{3\bar{v}_r k_r^2 a_r^2}{4\bar{\rho}_r} + \frac{3\bar{v}_r^2 k_r a_r^2}{4\bar{\rho}_r} + \frac{6\bar{v}_r a_r^2}{vk_r^2} + \frac{6\bar{v}_r^2 a_r^2}{vk_r^3} + \frac{2a_r^2}{vk_r} - \rho_i v_i^3 - \frac{4v_i\rho_i^2}{q} \end{aligned} \quad (93)$$

across the Whitham shock. Together with the resonance condition (91), these form four equations for the five unknowns $U_s, a_r, k_r, \bar{\rho}_r,$ and $\bar{v}_r,$ noting that ρ_i and v_i are given by (24) and (25), respectively. The final equation is obtained by assuming that the Riemann invariant R_- (22) is conserved through the resonant wavetrain and its lead partial DSW, which is valid for a full DSW [19,50]. This then determines the mean of the resonant phase gradient \bar{v}_r [36]. This Riemann invariant condition gives

$$\bar{v}_r = 2\sqrt{\frac{2}{q}}(\sqrt{\bar{\rho}_r} - \sqrt{\rho_+}) = 2\sqrt{\frac{2}{q}}(\sqrt{\bar{\rho}_r} - u_+). \quad (94)$$

The above nematic Whitham modulation equation jump conditions (92)–(93) with (94) can be solved numerically for $U_s, a_r, k_r,$ and $\bar{\rho}_r$ using Newton's method. The full details for this numerical solution of the Whitham shock jump conditions can be found in Reference [36]. Figure 8 shows comparisons for the Whitham shock velocity from the nonlocal to local limits, the optical power increasing, as given by the jump conditions and full numerical solutions of the nematic Equations (11) and (12). The values of the level ahead u_+ were chosen to lie in the TDSW regime; see Figure 3. It can be seen that there is excellent agreement between the theoretical and numerical solutions from high nonlocality, ν large, down to $\nu = O(10)$. As for the lead solitary wave amplitude comparison of Figure 4,

there is little change in the Whitham shock velocity as the nonlocality parameter ν varies by an order of magnitude, with only a small increase in the velocity. There is a small, increasing deviation between the theoretical and numerical values towards $\nu = 20$. This is due to the onset on the VDSW regime for which u vanishes at a point, a vacuum point [35,36]. Once the vacuum point is reached, $|u|$ cannot decrease further, so that the Whitham shock jump conditions need to be modified [36]. This will not be pursued further here.

For a fixed level ahead u_+ , as the nonlocality parameter ν decreases (optical power increases), the nematic DSW evolves from CDSW to TDSW type; see Figure 3. The borderline between the CDSW and TDSW regimes can be determined from the Whitham shock jump conditions (92)–(93) and the resonance condition (91) based on the following condition. For a fixed nonlocality parameter ν , as the level ahead u_+ increases, it is found that the Whitham shock velocity becomes greater than the linear group velocity

$$c_g = \bar{v}_r + k_r - \frac{8\bar{\rho}_r}{\nu k_r^3} \tag{95}$$

of the resonant wavetrain. This is unphysical as this would mean that the resonant wave-train could not form. Figure 3 shows this theoretical bound between the CDSW and TDSW regimes as a red line. It can be seen that the agreement with numerical solutions is excellent over the entire range of ν , even for jump heights $u_- - u_+$, which are not small.

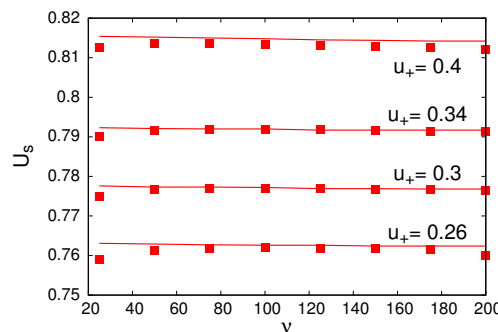


Figure 8. Comparison between the Whitham shock velocity U_s given by the modulation equation jump conditions (92)–(93) with (94) and numerical solutions of the nematic Equations (11) and (12) in the TDSW regime. Solution of jump conditions: red (full) line; numerical solution: red boxes. Here, $u_- = 1.0$ and $q = 2$.

As ν decreases, it would be expected that the high nonlocality modulation Equations (86)–(89) cease to be applicable. The Whitham modulation equations for the nematic equations in the local limit, ν small, were calculated based on the equivalent of the Stokes’ wave expansions (74)–(77) and (78)–(81), expanding in ν rather than $1/\nu$. However, these were found not to give solutions in good agreement with numerical solutions. This is expected as Figures 3 and 4 show that the nematic DSW is highly nonlocal down to very small values of ν , which are unphysical, as discussed at the end of Section 3.

7. RNLS and NLS DSW Regimes

The KdV approximation (44) gives that the DSW changes from KdV to NLS type at $\nu = q^2 / (4u_+^2)$ due to the change in sign of the coefficient of the third derivative, as discussed above, and as shown in Figure 3. It should be noted that numerical solutions do not show a distinct change in DSW type, but a transition from a KdV-type DSW to an NLS-type DSW, as seen in Figure 2d,e and as shown by the two regimes RNLS and NLS type in Figure 3. The TDSW regime is characterized by a negative polarity solitary wave connecting the resonant wavetrain to the intermediate level, as in Figure 2d. As the nonlocality ν decreases, the beam power increases, and the height of this solitary wave decreases, resulting in the RNLS regime which consists of a Whitham shock connecting a resonant wavetrain to the intermediate level u_i . Ahead of the resonant wavetrain is a partial NLS-type DSW

which connects to the level ahead u_+ ; see Figure 2e. As ν decreases further, the resonant wavetrain shrinks, and the partial DSW becomes a full NLS DSW with solitary waves at its trailing edge and linear waves at its leading edge, resulting in an NLS DSW for sufficiently small ν ; see Figure 3b. In this limit, the NLS DSW alone links the intermediate level to the level ahead. As ν decreases in the RNLS regime, the waves at the trailing edge of the partial DSW evolve from weakly nonlinear Stokes waves to fully nonlinear periodic waves, and then solitary waves in the NLS DSW regime.

The intermediate RNLS state, illustrated in Figure 2e, consists of a resonant wavetrain with the height of the negative polarity solitary wave at the Whitham shock negligible. To compare the KdV-NLS DSW boundary $\nu = q^2 / (4u_+^2)$ with numerical solutions, the choice of the height of this solitary wave being 5×10^{-3} above u_i was chosen for the onset of the RNLS regime in numerical solutions. It can be seen that there is good agreement for this regime boundary for u_+ close to u_- , but there is increasing disagreement as u_+ decreases. This is expected as the reductive nematic eKdV Equation (42) was derived under the assumption that $|u_- - u_+|$ is small.

8. Conclusions

The structure of the nematic DSW (dispersive shock wave) solution of the defocusing nematic equations governing the propagation of an optical beam through a cell filled with nematic liquid crystals has been investigated using a combination of numerical solutions of the equations governing the beam, consisting of an NLS-type equation for the optical beam and an elliptic medium response equation, and solutions of the governing nematic equations using Whitham modulation theory and/or asymptotic solutions. In contrast to previous work [34–36], the evolution of the DSW structure was studied as the power of the optical beam varied, from the experimental low power for which the nematic response is nonlocal to high power for which the response is local. As the beam power varies, it was found that the nematic DSW transitions between six regimes, four of which were studied in previous work [34–36]. The two NLS-type DSWs do not exist in the low power regime studied in this previous work. However, the experimental verification of these high power DSW types is questionable as the powers required for their existence are unrealistic due to the possible excessive medium heating the high beam powers would cause. Excellent agreement was found between numerical solutions and analytical solutions for the four physically relevant DSW regimes, the PDSW, RDSW, CDSW, and TDSW regimes displayed in Figure 2a–d. In particular, the analytical theory gives good agreement for the boundaries between the existence regions for five of the DSW types as the nonlocality parameter ν varies, the exception being the boundary between the PDSW and RDSW regimes.

It has been found that the details of the nematic DSW, for instance, its lead wave amplitude and velocity and the amplitude of the associated resonant radiation, are well approximated by the nematic equations in the high nonlocality limit, the nonlocality parameter ν large, as the DSW transitions to the local limit. This holds for the PDSW, RDSW, CDSW and TDSW regimes with the nonlocality parameter ν ranging from $O(100)$ to $O(1)$. As the analysis of the nematic DSW is much easier in the high nonlocality limit based on asymptotic analyses with $\nu \gg 1$, this is an important result for future analysis of the nematic DSW in its various regimes and over its nonlocality range.

There are still a number of issues which could be addressed by future work. An outstanding issue is the correct determination of resonance between the nematic DSW and diffractive radiation. In contrast to the high nonlocality limit with ν large [34–36], as ν decreases from the high to the low nonlocality limit, the beam power increases, and the resonance condition used in previous work in the RDSW and CDSW regimes that the velocity of the lead solitary wave of the DSW matches the linear phase velocity of the resonant waves does not agree with numerical solutions. The theoretical transition from the PDSW regime for high nonlocality to the RDSW regime due to the onset of resonance as ν decreases occurs for $\nu = O(1)$, while numerical solutions show the transition for $\nu = O(100)$ to $O(10)$. As noted in previous work [36], and in contrast with other work

on resonant DSWs, not only is the lead wave of the DSW in resonance with diffractive radiation, but the whole modulated periodic wave which forms the DSW is in resonance. However, even this observation does not yield the correct resonance condition for the RDSW regime as the nonlocality parameter ν decreases below the highly nonlocal limit. The correct resonance condition between the DSW and diffractive radiation requires further study. This should be an important general issue for all resonant DSWs beyond the specific application to nematic liquid crystals.

Author Contributions: Conceptualization, S.B., D.J.F., T.P.H., C.H., T.R.M. and N.F.S.; methodology, S.B., D.J.F., T.P.H., C.H., T.R.M. and N.F.S.; software, S.B., T.R.M. and N.F.S.; validation, S.B., D.J.F., T.P.H., C.H., T.R.M. and N.F.S.; methodology, S.B., D.J.F., T.P.H., C.H., T.R.M. and N.F.S.; formal analysis, S.B., D.J.F., T.P.H., C.H., T.R.M. and N.F.S.; methodology, S.B., D.J.F., T.P.H., C.H., T.R.M. and N.F.S.; investigation, S.B., D.J.F., T.P.H., C.H., T.R.M. and N.F.S.; methodology, S.B., D.J.F., T.P.H., C.H., T.R.M. and N.F.S.; writing—S.B., D.J.F., T.P.H., C.H., T.R.M. and N.F.S.; methodology, S.B., D.J.F., T.P.H., C.H., T.R.M. and N.F.S.; writing—review and editing, S.B., D.J.F., T.P.H., C.H., T.R.M. and N.F.S.; methodology, S.B., D.J.F., T.P.H., C.H., T.R.M. and N.F.S.; project administration, N.F.S. All authors have read and agreed to the published version of the manuscript.

Funding: This research received no external funding.

Data Availability Statement: There is no experimental data resulting from this research. The numerical data is available on request from the authors.

Acknowledgments: Saleh Baqer thanks the research sector of Kuwait University for a Research Initiation Grant (RIG) given during the preparation of the paper.

Conflicts of Interest: The authors declare no conflict of interest.

References

1. Khoo, I.C. *Liquid Crystals: Physical Properties and Nonlinear Optical Phenomena*; Wiley: New York, NY, USA, 1995.
2. Peccianti, M.; Assanto, G. Nematicons. *Phys. Rep.* **2012**, *516*, 147–208. [CrossRef]
3. Assanto, G. Nematicons: Reorientational solitons from optics to photonics. *Liq. Cryst. Rev.* **2018**, *6*, 170–194. [CrossRef]
4. Conti, C.; Peccianti, M.; Assanto, G. Route to nonlocality and observation of accessible solitons. *Phys. Rev. Lett.* **2003**, *91*, 073901. [CrossRef] [PubMed]
5. Assanto, G.; Smyth, N.F. Self-confined light waves in nematic liquid crystals. *Phys. D* **2020**, *402*, 132182. [CrossRef]
6. Peccianti, M.; Assanto, G.; Luca, A.D.; Umeton, C.; Khoo, I.C. Electrically assisted self-confinement and waveguiding in planar nematic liquid crystal cells. *Appl. Phys. Lett.* **2000**, *77*, 7–9. [CrossRef]
7. Peccianti, M.; Assanto, G. Signal readdressing by steering of spatial solitons in bulk nematic liquid crystals. *Opt. Lett.* **2001**, *26*, 1690–1692. [CrossRef]
8. Assanto, G.; Peccianti, M. Spatial solitons in nematic liquid crystals. *IEEE J. Quantum Electron.* **2003**, *39*, 13–21. [CrossRef]
9. Piccardi, A.; Alberucci, A.; Bertolozzo, U.; Residori, S.; Assanto, G. Readdressable interconnects with spatial soliton waveguides in liquid crystal light valves. *IEEE Photon. Technol. Lett.* **2010**, *22*, 694–696. [CrossRef]
10. Karimi, N.; Virkki, M.; Alberucci, A.; Buchnev, O.; Kauranen, M.; Priimagi, A.; Assanto, G. Molding optical waveguides with nematicons. *Adv. Opt. Mater. Commun.* **2017**, *5*, 1700199. [CrossRef]
11. Assanto, G.; Minzoni, A.A.; Smyth, N.F. Light self-localization in nematic liquid crystals: Modelling solitons in nonlocal reorientational media. *J. Nonlin. Opt. Phys. Mater.* **2009**, *18*, 657–691. [CrossRef]
12. Whitham, G.B. *Linear and Nonlinear Waves*; J. Wiley and Sons: New York, NY, USA, 1974.
13. Russell, J.S. *Report of the Fourteen Meeting of the British Association for the Advancement of Science, Report on Waves*; The British Association for the Advancement of Science: London, UK, September 1844; pp. 311–390.
14. Hooper, C.G.; Ruiz, P.D.; Huntley, J.M.; Khusnutdinova, K.R. Undular bores generated by fracture. *Phys. Rev. E* **2021**, submitted.
15. Davydov, A.S. *Solitons in Molecular Systems*, 2nd ed.; Kluwer Academic Publishers: Dordrecht, The Netherlands, 1991.
16. Tlidi, M.; Staliunas, K.; Panajotov, K.; Vladimirov, A.G.; Clerc, M.G. Localized structures in dissipative media: From optics to plant ecology. *Phil. Trans. R. Soc. A* **2014**, *372*, 20140101. [CrossRef] [PubMed]
17. Kivshar, Y.S.; Agrawal, G.P. *Optical Solitons. From Fibers to Photonic Crystals*; Academic Press: San Diego, CA, USA, 2003.
18. Ablowitz, M.J. *Nonlinear Dispersive Waves. Asymptotic Analysis and Solitons*; Cambridge University Press: Cambridge, UK, 2011.
19. El, G.A.; Hofer, M.A. Dispersive shock waves and modulation theory. *Phys. D* **2016**, *333*, 11–65. [CrossRef]
20. Whitham, G.B. A general approach to linear and non-linear dispersive waves using a Lagrangian. *J. Fluid Mech.* **1965**, *22*, 273–283. [CrossRef]
21. Whitham, G.B. Non-linear dispersive waves. *Proc. Roy. Soc. Lond. A* **1965**, *283*, 238–261.
22. Whitham, G.B. Variational methods and applications to water waves. *Proc. Roy. Soc. Lond. A* **1967**, *299*, 6–25.

23. Gurevich, A.V.; Pitaevskii, L.P. Nonstationary structure of a collisionless shock wave. *Sov. Phys. JETP* **1974**, *33*, 291–297.
24. Fornberg, B.; Whitham, G.B. Numerical and theoretical study of certain non-linear wave phenomena. *Phil. Trans. Roy. Soc. Lond. Ser. A Math. Phys. Sci.* **1978**, *289*, 373–404.
25. Flaschka, H.; Forest, M.G.; McLaughlin, D.W. Multiphase averaging and the inverse spectral solution of the Korteweg-de Vries equation. *Comm. Pure Appl. Math.* **1980**, *33*, 739–784. [CrossRef]
26. Sprenger, P.; Hofer, M.A. Shock waves in dispersive hydrodynamics with nonconvex dispersion. *SIAM J. Appl. Math.* **2017**, *77*, 26–50. [CrossRef]
27. Hofer, M.A.; Smyth, N.F.; Sprenger, P. Modulation theory solution for nonlinearly resonant, fifth-order Korteweg-de Vries, nonclassical, travelling dispersive shock waves. *Stud. Appl. Math.* **2019**, *142*, 219–240. [CrossRef]
28. Kawahara, T. Oscillatory solitary waves in dispersive media. *J. Phys. Soc. Jpn.* **1972**, *33*, 260–264. [CrossRef]
29. Conforti, M.; Trillo, S. Dispersive wave emission from wave breaking. *Opt. Lett.* **2013**, *38*, 3815–3818. [CrossRef] [PubMed]
30. Conforti, M.; Trillo, S. Radiative effects driven by shock waves in cavity-less four-wave mixing combs. *Opt. Lett.* **2014**, *39*, 5760–5763. [CrossRef]
31. Conforti, M.; Trillo, S.; Mussot, A.; Kudlinski, A. Parametric excitation of multiple resonant radiations from localized wavepackets. *Sci. Rep.* **2015**, *5*, 1–5. [CrossRef] [PubMed]
32. Malaguti, S.; Conforti, M.; Trillo, S. Dispersive radiation induced by shock waves in passive resonators. *Opt. Lett.* **2014**, *39*, 5626–5629. [CrossRef]
33. Piccardi, A.; Alberucci, A.; Tabiryan, N.; Assanto, G. Dark nematicons. *Opt. Lett.* **2011**, *36*, 1356–1358. [CrossRef]
34. Smyth, N.F. Dispersive shock waves in nematic liquid crystals. *Phys. D* **2016**, *333*, 301–309. [CrossRef]
35. El, G.A.; Smyth, N.F. Radiating dispersive shock waves in non-local optical media. *Proc. Roy. Soc. Lond. A* **2016**, *472*, 20150633. [CrossRef]
36. Baqer, S.; Smyth, N.F. Modulation theory and resonant regimes for dispersive shock waves in nematic liquid crystals. *Phys. D* **2020**, *403*, 132334. [CrossRef]
37. El, G.A.; Geogjaev, V.V.; Gurevich, A.V.; Krylov, A.L. Decay of an initial discontinuity in the defocusing NLS hydrodynamics. *Phys. D* **1995**, *87*, 186–192. [CrossRef]
38. Marchant, T.R.; Smyth, N.F. The initial-boundary problem for the Korteweg-de Vries equation on the negative quarter-plane. *Proc. Roy. Soc. Lond. A* **2002**, *458*, 857–871. [CrossRef]
39. García-Reimbert, C.; Minzoni, A.A.; Smyth, N.F.; Worthy, A.L. Large-amplitude nematicon propagation in a liquid crystal with local response. *J. Opt. Soc. Am. B* **2006**, *23*, 2551–2558. [CrossRef]
40. Assanto, G.; Minzoni, A.A.; Peccianti, M.; Smyth, N.F. Optical solitary waves escaping a wide trapping potential in nematic liquid crystals: Modulation theory. *Phys. Rev. A* **2009**, *79*, 033837. [CrossRef]
41. Izdebskaya, Y.; Krolikowski, W.; Smyth, N.F.; Assanto, G. Vortex stabilization by means of spatial solitons in nonlocal media. *J. Opt.* **2016**, *18*, 054006. [CrossRef]
42. Ghofraniha, N.; Conti, C.; Ruocco, G.; Trillo, S. Shocks in nonlocal media. *Phys. Rev. Lett.* **2007**, *99*, 043903. [CrossRef] [PubMed]
43. Kamchatnov, A.M. Whitham theory for perturbed Korteweg-de Vries equation. *Phys. D* **2016**, *333*, 99–106. [CrossRef]
44. Chan, T.F.; Kerkhoven, T. Fourier methods with extended stability intervals for KdV. *SIAM J. Numer. Anal.* **1985**, *22*, 441–454. [CrossRef]
45. Trefethen, L.N. *Spectral Methods in MATLAB*; SIAM: Philadelphia, PA, USA, 2000.
46. Baqer, S. Dispersive Hydrodynamics in a Non-Local Non-Linear Medium. Ph.D. Thesis, University of Edinburgh, Edinburgh, UK, 2020.
47. Marchant, T.R.; Smyth, N.F. An undular bore solution for the higher-order Korteweg-de Vries equation. *J. Phys. A Math. Gen.* **2006**, *39*, L563–569. [CrossRef]
48. Sprenger, P.; Hofer, M.A. Discontinuous shock solutions of the Whitham modulation equations and traveling wave solutions of higher order dispersive nonlinear wave equations. *Nonlinearity* **2020**, *33*, 3268–3302. [CrossRef]
49. Smyth, N.F. Modulation theory solution for resonant flow over topography. *Proc. Roy. Soc. Lond. A* **1987**, *409*, 79–97.
50. El, G.A. Resolution of a shock in hyperbolic systems modified by weak dispersion. *Chaos* **2005**, *15*, 037103. [CrossRef] [PubMed]
51. Horikis, T.P. Small-amplitude defocusing nematicons. *J. Phys. A* **2015**, *48*, 02FT01. [CrossRef]
52. Kodama, Y.; Taniuti, T. Higher order approximation in the reductive perturbation method. I. The weakly dispersive system. *J. Phys. Soc. Jpn.* **1978**, *45*, 298–310. [CrossRef]
53. Marchant, T.R.; Smyth, N.F. The extended Korteweg-de Vries equation and the resonant flow of a fluid over topography. *J. Fluid Mech.* **1990**, *221*, 263–288. [CrossRef]
54. Laudyn, U.A.; Kwaśny, M.; Sala, F.A.; Karpierz, M.A.; Smyth, N.F.; Assanto, G. Curved optical solitons subject to transverse acceleration in reorientational soft matter. *Nat. Sci. Rep.* **2017**, *7*, 12385. [CrossRef]
55. Congy, T.; El, G.A.; Hofer, M.A. Interaction of linear modulated waves and unsteady dispersive hydrodynamic states with application to shallow water waves. *J. Fluid Mech.* **2019**, *875*, 1145–1174. [CrossRef]
56. El, G.A.; Khamis, E.G.; Tovbis, A. Dam break problem for the focusing nonlinear Schrödinger equation and the generation of rogue waves. *Nonlinearity* **2016**, *29*, 2798–2836. [CrossRef]
57. Marchant, T.R.; Smyth, N.F. Approximate techniques for dispersive shock waves in nonlinear media. *J. Nonlin. Opt. Phys. Mater.* **2012**, *21*, 1250035. [CrossRef]

58. Marchant, T.R. Asymptotic solitons of the extended Korteweg-de Vries equation. *Phys. Rev. E* **1999**, *59*, 3745–3748. [CrossRef]
59. Gelfand, I.M.; Fomin, S.V. *Calculus of Variations*; Prentice-Hall: Englewood Cliffs, NJ, USA, 1963.

Article

Discrete Nonlinear Schrödinger Systems for Periodic Media with Nonlocal Nonlinearity: The Case of Nematic Liquid Crystals

Panayotis Panayotaros

Depto. Matemáticas y Mecánica, IIMAS, Universidad Nacional Autónoma de México, Apdo. Postal 20–726, Cd. México 01000, Mexico; panos@mym.iimas.unam.mx

Abstract: We study properties of an infinite system of discrete nonlinear Schrödinger equations that is equivalent to a coupled Schrödinger-elliptic differential equation with periodic coefficients. The differential equation was derived as a model for laser beam propagation in optical waveguide arrays in a nematic liquid crystal substrate and can be relevant to related systems with nonlocal nonlinearities. The infinite system is obtained by expanding the relevant physical quantities in a Wannier function basis associated to a periodic Schrödinger operator appearing in the problem. We show that the model can describe stable beams, and we estimate the optical power at different length scales. The main result of the paper is the Hamiltonian structure of the infinite system, assuming that the Wannier functions are real. We also give an explicit construction of real Wannier functions, and examine translation invariance properties of the linear part of the system in the Wannier basis.

Keywords: optical waveguides; nonlocal media; nematic liquid crystals; Wannier functions

Citation: Panayotaros, P. Discrete nonlinear Schrödinger systems for periodic thermal media: The case of nematic liquid crystals. *Appl. Sci.* **2021**, *11*, 4420. <https://doi.org/10.3390/app11104420>

Academic Editor: Gaetano Assanto

Received: 17 February 2021

Accepted: 20 April 2021

Published: 13 May 2021

Publisher's Note: MDPI stays neutral with regard to jurisdictional claims in published maps and institutional affiliations.



Copyright: © 2021 by the authors. Licensee MDPI, Basel, Switzerland. This article is an open access article distributed under the terms and conditions of the Creative Commons Attribution (CC BY) license (<https://creativecommons.org/licenses/by/4.0/>).

1. Introduction

We study properties of an infinite system of discrete nonlinear Schrödinger (DNLS) equations that is equivalent to a coupled Schrödinger-elliptic system of partial differential equations with periodic coefficients. The system was derived in [1] as a model for the propagation of laser light in nematic liquid crystal substrates with a periodic structure in one of the directions normal to the optical axis. The model was originally motivated by experimental studies of such waveguide systems [2–4] and leads to extensions of a nonlocal DNLS equation of Fratalocchi and Assanto [5,6].

The Fratalocchi-Assanto equation has a nonlocal nonlinearity that leads to new effects when compared to the cubic power DNLS model studied commonly in photonics and atomic physics [7]. These effects include non-monotonic amplitude profiles of static (breather) solutions, additional internal modes in the linearization around breathers [8,9], and enhanced mobility of traveling localized solutions [10]. On the other hand, the mathematical justification of the Fratalocchi-Assanto model, in particular the question of how well it approximates the partial differential equations with periodic coefficients used to describe the underlying physics, is less studied. The present paper is a step in studying this problem.

Schrödinger-elliptic systems of differential equations with a similar nonlocal structure in the nonlinear term arise in a variety of contexts. Examples from physics include Bose-Einstein condensates [11], thermal media [12], and matter-wave microwave systems [13]. The recent review [14] includes further examples describing laser beams in liquid crystals [5,15–17]. A related area of application of such models concerns thermo-optical interactions induced by beams in liquid crystals [18–20]. The combination of nonlocal nonlinearity and spatial periodicity or more general inhomogeneity, and the analysis of relevant equations is therefore a problem of wider interest.

The Schrödinger-elliptic differential equation we study describes the coupling of the laser field amplitude to the nematic crystal director angle. The derivation uses approximations of the coupled Oseen-Frank-Maxwell system for a linearly polarized beam [1]. The periodicity of the medium in the direction transverse to the propagation of the laser beam leads to an elliptic (Poisson-like) equation with periodic coefficients. Our approach is to expand the laser field and director angle in a Wannier function basis. The system is subsequently written as an infinite system of coupled DNLS equations for the Wannier mode amplitudes. The Wannier functions we use are defined in terms of a periodic Schrödinger operator appearing in the elliptic equation [1]. Note that the Wannier functions are integer translates of an infinite set of localized functions with an increasing degree of oscillation. Thus Wannier mode amplitudes give information on both the location and the spatial scale of images. Wannier and the related Bloch functions are a standard tool in the analysis of periodic Schrödinger operators [21–24], and related linear problems in theoretical physics, e.g., solid state physics [25].

Wannier functions are increasingly used in the study of nonlinear waves in inhomogeneous media. The use of Wannier functions for deriving discrete Schrödinger equations for nonlinear wave systems with periodic coefficients was first proposed in [26] for the periodic Gross-Pitaevski equation (NLS with periodic potential). The Wannier expansion has been used to justify the approximation of this equation by the DNLS equation in the tight binding approximation limit for the potential term in [23,27]. Related systems where the theory applies are described in [11,12]. In the present problem the Wannier basis leads to a heuristic derivation of the model of [6] and also allows us to derive more general DNLS-type equations and systems that include additional inter- and intra-band Wannier mode interactions [1]. However, the Wannier approach does not immediately justify truncation to the lowest band because the linear part does not have the band gaps assumed in [23,26,27]. Thus the question of justifying the derivation of finite systems of (possibly a few) DNLS equations from the infinite system requires some additional analysis, and also motivates a better understanding of the structure of the infinite system.

A first result of the paper is an outline of the global existence theory, that is the boundedness of a suitable norm of the solutions. This type of result is a mathematical way to describe the absence of catastrophic self-focusing (beam collapse) and the possibility of stable localized beams [28]. The result also implies an estimate for the energy (optical power) at different length scales and provides a heuristic justification of truncation to a finite number of DNLS systems, corresponding to Wannier modes of the first bands.

The main result of the paper is a proof that the infinite system resulting from the Wannier basis expansion is a Hamiltonian system. This fact implies the Hamiltonian structure of the finite band truncations and can be useful in analyzing discrete soliton structures, using for instance methods from [8,9]. The proof assumes that the Wannier functions are real, and we subsequently give examples of an explicit construction of real Wannier functions in terms of explicit Bloch functions.

We also examine some features of the linear part of the problem, in particular we show that it is diagonalized by the trigonometric functions. This observation implies that the dispersion relation and the coupling between the modes can be computed with relative ease, and that the linear part of the problem is homogenized in the Wannier basis, i.e., is effectively a translation invariant [29,30]. This latter property is an additional motivation for further developing Bloch-Wannier analysis in nonlinear wave equations.

The paper is organized as follows. In Section 2 we outline the global existence theory for the coupled Schrödinger-elliptic system and show that the system in the Wannier basis is Hamiltonian. In Section 3 we discuss the construction of real Wannier functions. We also discuss translation invariance properties of the linear part of the system. In Section 4 we discuss some questions for further work.

2. Hamiltonian Structure of Periodic Nematicon Equations

We consider the system of equations (“nematicon equations”)

$$\partial_z u = \frac{1}{2}i\partial_y^2 u + \frac{1}{2}\beta i\psi u \tag{1}$$

$$-\partial_y^2 \psi + V(y)\psi + g^2 \psi = \alpha |u(y)|^2, \tag{2}$$

with α, β, g^2 positive constants, and V b -periodic and positive.

The complex amplitude u describes the electric field amplitude of a linearly polarized laser beam through a nematic liquid crystal sample, while ψ describes the director angle deviation of the liquid crystal due to the laser beam. The geometry of the problem is indicated in Figures 1 and 2, see also [3,6]. In Figure 1 we show a vertical direction x , and the laser beam propagation axis z . The y -axis is perpendicular to the plane of the figure. The laser beam electric field is polarized along the x -axis, while the angle ψ is on the x, z plane. The device (medium) is periodic along the y -axis. The periodicity can be imposed by an external electric field that is also along the x -axis, see Figure 2. We also simplify the problem mathematically by ignoring the dependence of u and ψ in x . Boundary effects in the directions transverse to the beam are also ignored. Equations (1) and (2) were derived in [1] from Maxwell’s equations coupled to the Oseen-Frank equations for the director field [16,31]. Schrödinger operator $-\partial_y^2 + V$. Similar equations with constant coefficients have been studied widely in the context of optical solitons in liquid crystals (“nematicons”) and other nonlocal media [5,14–17].

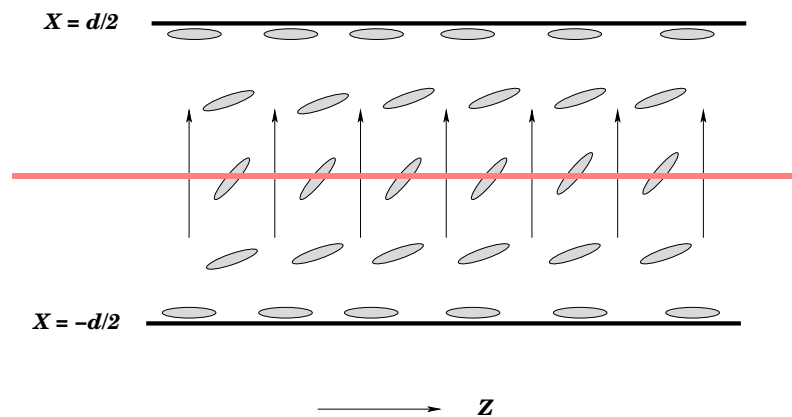


Figure 1. View of vertical (x) and optical (z) directions. The laser and external electric fields have only vertical components, indicated by the arrow. The red line crossing the sample represents the laser beam, $u(y, x, z)$ is the electric field amplitude of the beam. The nematic director (shaded ovaloids) is assumed lie on the x, z plane. The angle $\psi(y, x, z)$ is the deviation (from the z -axis) produced by the laser beam. The second horizontal direction (y -axis) is perpendicular to the plane of the figure. In (1), (2) we simplify the mathematical problem by ignoring the dependence of u and ψ on the vertical variable x . Possible effects of the vertical boundaries of the sample are also ignored.

In model (1), (2) the transverse periodicity of the medium is captured by the b -periodic function V , and our study involves the analysis of the periodic Schrödinger operator $-\partial^2 + V$. More detailed models [1] involve more complicated operators with periodic coefficients in the second equation. An example is the operator considered in [3]. The simplification used here captures the fact that the periodicity of the medium appears in the nonlinear term of the beam Equation (1).

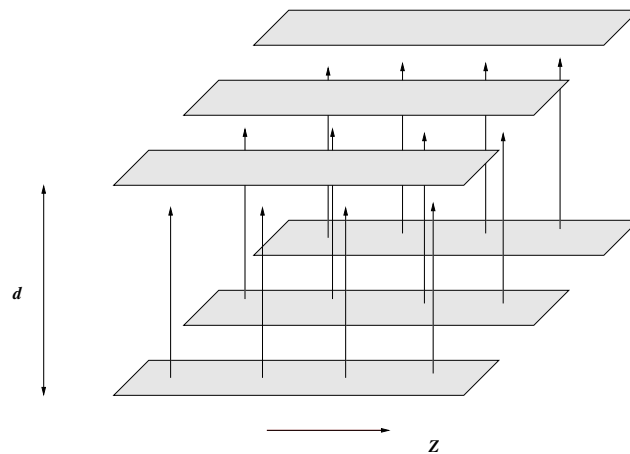


Figure 2. The periodicity of the device (or medium) in the horizontal direction (y -axis) is due to a vertical electric field applied externally. The parallel stripes represent capacitors that apply a voltage that is uniform along the beam propagation direction (z -axis), and periodic along the y -axis, see [3,6]. The dependence on the vertical direction is not included in model (1), (2). Horizontal boundaries are also ignored.

Equation (2) is written in the abstract form $A + V$, with $A = -\partial_y^2 + g^2$. Assuming $V \in L^\infty(\mathbb{R}; \mathbb{R})$, and non-negative we have that $G = (A + V)^{-1}$ is bounded symmetric operator in $L^2(\mathbb{R}; \mathbb{R})$, and we can write $\|Gf\|_{L^2} \leq C\|f\|_{L^2}, \forall f \in L^2$. Also G maps $L^2(\mathbb{R}; \mathbb{R})$ to $H^2(\mathbb{R}; \mathbb{R})$. see e.g., [31], Lemmas 2.1, 2.2.

The local and global existence theory for the initial value problem of system (1), (2) follows from standard arguments and similar to the one in 2-D in [31–33]. This theory implies that the solution avoids catastrophic nonlinear collapse in finite length, see [28]. This is an important feature of nonlinear beam propagation in nematic liquid crystals and related nonlocal media, and is a prerequisite for the existence of stable nonlinearly focused beams [17], see [33] for mathematical aspects.

The main ingredient of the global existence theory is the conservation of the Hamiltonian of the system (1), (2)

$$H = \int_{\mathbb{R}} \left(\frac{1}{2} |u_y|^2 - \frac{\alpha\beta}{4} G(|u|^2) |u|^2 \right), \tag{3}$$

and of the (optical) power $P = \int_{\mathbb{R}} |u|^2$, the squared L^2 -norm of u . We use the notation $\|f\|_{L^p} = \left(\int_{\mathbb{R}} |f|^p \right)^{1/p}, \|f\|_{L^\infty} = \text{esssup}_{x \in \mathbb{R}} |f(x)|$.

We can use these two conserved quantities to show the boundedness of some simpler quantities. By the Cauchy-Schwarz inequality we have

$$\int_{\mathbb{R}} G(|u|^2) |u|^2 \leq \left(\int_{\mathbb{R}} |G(|u|^2)|^2 \right)^{1/2} \left(\int_{\mathbb{R}} |u|^4 \right)^{1/2} \leq \|G(|u|^2)\|_{L^2}^2 \|u\|_{L^4}^2, \tag{4}$$

and using the boundedness of G in L^2 we obtain

$$\int_{\mathbb{R}} G(|u|^2) |u|^2 \leq C^2 \|u\|_{L^4}^4. \tag{5}$$

We use that for all $y \in \mathbb{R}$

$$(u(y))^2 = \int_{-\infty}^y (u^2(s))' ds = \int_{-\infty}^y 2u(s)u'(s) ds, \tag{6}$$

therefore

$$|(u(y))|^2 \leq 2 \int_{-\infty}^y |u(s)u'(s)| ds \leq 2 \int_{\mathbb{R}} |u(s)||u'(s)| ds \leq 2\|u\|_{L^2}\|\partial_y u\|_{L^2}, \tag{7}$$

using the Cauchy-Schwarz inequality. We then have

$$\|u\|_{L^4}^4 \leq \|u\|_{L^\infty}^2 \int_{\mathbb{R}} |u|^2 \leq 2\|u_y\|_{L^2}\|u\|_{L^2}^3, \tag{8}$$

and by (5) we bound the quartic part of the Hamiltonian as

$$\int_{\mathbb{R}} G(|u|^2)|u|^2 \leq 2C^2\|\partial_y u\|_{L^2}\|u\|_{L^2}^3. \tag{9}$$

Then

$$4H \geq 2\|u_y\|_{L^2}^2 - 2\alpha\beta C^2\|u_y\|_{L^2}\|u\|_{L^2}^3 = 2\|u_y\|_{L^2}^2 - 2\alpha\beta C^2 P^{3/2}\|u_y\|_{L^2}, \tag{10}$$

with P the power, a constant. The conservation of H and (10) imply that $\|u_y\|_{L^2}$ must remain bounded for all $z \in \mathbb{R}$.

Also, $\int_{\mathbb{R}} V|u|^2 \leq \|V\|_{L^\infty}P$, thus we have a bound

$$H_2 := \int_{\mathbb{R}} (|u_y|^2 + V|u|^2 + |u|^2) \leq C_0 \tag{11}$$

for all $z \in \mathbb{R}$, with C_0 depending on H and P at $z = 0$.

We now consider an equivalent discrete system using expansions in Wannier functions. We also examine some consequences of the Hamiltonian structure of system (1), (2) and of the bound (11).

We start by defining the Wannier functions associated to the Schrödinger operator $-\partial_y^2 + V(y)$, with V b -periodic, see [21,22]. Bounded solutions $\phi_{n,k}$ (Bloch functions) and eigenvalues $E_{n,k}$ of the periodic Schrödinger equation satisfy

$$-\partial_y^2 \phi_{n,k} + V(y)\phi_{n,k} = E_{n,k}\phi_{n,k}, \quad n \in \mathbb{N}, \quad k \in \mathbb{R}, \tag{12}$$

where

$$\phi_{n,k}(y) = v_{n,k}(y)e^{iky}, \quad \text{with} \quad v_{n,k}(y+b) = v_{n,k}(y), \tag{13}$$

for all $y \in \mathbb{R}, n \in \mathbb{N}, k \in \mathbb{R}$. By $V > 0$ we have $E_{n,k} > 0$, furthermore

$$E_{n,k+\frac{2\pi}{b}} = E_{n,k}, \quad \phi_{n,k+\frac{2\pi}{b}}(y) = \phi_{n,k}(y), \tag{14}$$

for all $n \in \mathbb{N}, k, y \in \mathbb{R}$. Then we can consider k in any interval of length $2\pi/b$. The index n is referred to as band index (or number). For any fixed k in an interval of length $2\pi/b$, $E_{n,k}$ is the n -th largest eigenvalue of (12) with boundary conditions $\phi_{n,k}(y+b) = e^{ikb}\phi_{n,k}(y)$, implied by (13).

Also, by (12), (13), the b -periodic functions $v_{n,k}$ satisfy

$$-(\partial_y + ik)^2 v_{n,k} + V(y)v_{n,k} = E_{n,k}v_{n,k}, \tag{15}$$

thus for any k fixed, n labels the eigenvalues $E_{n,k}$ in an increasing order. This equation can be also be used to compute the $v_{n,k}, E_{n,k}$ numerically for each $k \in [0, 2\pi/b)$.

For $n \in \mathbb{N}, y \in \mathbb{R}$, we consider the Fourier coefficients

$$w_n^m(y) = \sqrt{\frac{b}{2\pi}} \int_{-\frac{\pi}{b}}^{\frac{\pi}{b}} \phi_{n,k}(y)e^{-imbk} dk, \quad m \in \mathbb{Z}, \tag{16}$$

of $\phi_{n,\cdot}(y)$, and we also have the inversion formula

$$\phi_{n,k}(y) = \sqrt{\frac{b}{2\pi}} \sum_{m \in \mathbb{Z}} w_n^m(y) e^{imbk}, \quad n \in \mathbb{N}, \quad k, x \in \mathbb{R}. \tag{17}$$

The set of functions $w_n^m : \mathbb{R} \rightarrow \mathbb{C}, n \in \mathbb{N}, m \in \mathbb{Z}$ defined by (16) are known as Wannier functions [21,22,25]. Note that the Bloch functions are not unique. One of the basic results is that we can define the Bloch functions so that the Wannier functions form an orthonormal basis for $L^2(\mathbb{R}; \mathbb{C})$ [23,24]. We discuss the construction of Bloch and Wannier functions in the next section.

Another property of the Wannier functions is that, by (16), (13),

$$w_n^{m+p}(y) = w_n^m(y - pb), \quad \forall n \in \mathbb{N}, \quad m, p \in \mathbb{Z}, \quad y \in \mathbb{R}. \tag{18}$$

Thus, fixing n , the function w_n^m is a translation of the function w_n^0 by mb .

We use expansions of ψ and u in Wannier functions w_n^m as

$$\psi(y, z) = \sum_{n \in \mathbb{N}} \sum_{m \in \mathbb{Z}} c_{n,m}(z) w_n^m(y), \tag{19}$$

$$u(y, z) = \sum_{n \in \mathbb{N}} \sum_{m \in \mathbb{Z}} u_{n,m}(z) w_n^m(y). \tag{20}$$

By the orthonormality of the Wannier basis, the coefficients $c_{n,m}, u_{n,m}$ are obtained from the physical quantities ψ, u by

$$c_{n,m}(z) = \int_{\mathbb{R}} \psi(y, z) w_n^{m*}(y) dy, \quad u_{n,m}(z) = \int_{\mathbb{R}} u(y, z) w_n^{m*}(y) dy. \tag{21}$$

The Wannier functions and the integrals must be evaluated numerically (or approximately).

Note that the definition w_n^0 and the regularity of the $\phi_{n,k}$ in k can also lead to strong localization of the w_n^0 in y , see [23,24,34] and the discussion of the next section. The decay of w_n^m is more pronounced for larger oscillation V and for the first n . Numerical examples are shown in [1]. For rapidly decaying Wannier functions, the decay of the coefficients of $c_{n,m}, u_{n,m}$ in m reflect the decay of the spatial profile of ψ, u respectively.

We can also use the orthonormality of the Bloch and Wannier functions to derive a bound on the optical power of each energy band. Let

$$u(y, z) = \sum_{n \in \mathbb{N}} \int_{-\frac{\pi}{b}}^{\frac{\pi}{b}} \hat{c}_{n,k}(z) \phi_{n,k}(y) dk. \tag{22}$$

By

$$\int_{\mathbb{R}} \phi_{n,k}(y) \phi_{n',k'}^*(y) dy = \delta_{n,n'} \delta(k - k') \tag{23}$$

and (12) we have that H_2 of (11) satisfies

$$H_2 = \int_{\mathbb{R}} (-u_{yy} + Vu + u)u^* = \sum_{n \in \mathbb{N}} \int_{-\frac{\pi}{b}}^{\frac{\pi}{b}} (1 + E_{n,k}) |\hat{c}_{n,k}|^2 dk. \tag{24}$$

Let $\varepsilon_n = \min_{k \in [0, 2\pi/b)} E_{n,k}$. We have $\varepsilon_n > 0, \forall n \in \mathbb{N}$. Then

$$H_2 \geq \sum_{n \in \mathbb{N}} (1 + \varepsilon_n) \int_{-\frac{\pi}{b}}^{\frac{\pi}{b}} |\hat{c}_{n,k}|^2 dk. \tag{25}$$

By the orthonormality of the Bloch and Wannier functions for the n -th band and (20), (22) we have

$$\int_{-\frac{\pi}{b}}^{\frac{\pi}{b}} |\hat{c}_{n,k}|^2 = \sum_{m \in \mathbb{Z}} |u_{n,m}|^2. \tag{26}$$

Combining with (25), (11) we have

$$\sum_{n \in \mathbb{N}} (1 + \varepsilon_n) \sum_{m \in \mathbb{Z}} |u_{n,m}|^2 \leq C_0, \tag{27}$$

therefore

$$\sum_{m \in \mathbb{Z}} |u_{n,m}|^2 \leq (1 + \varepsilon_n)^{-1} C_0, \tag{28}$$

for all $n \in \mathbb{N}$. For large n we have $\varepsilon_n \sim n^2$, more precisely, there exist $c, C > 0$ such that $cn^2 \leq \varepsilon_n \leq Cn^2, \forall n \in \mathbb{N}$. We discuss this estimate in the next section. Therefore

$$\sum_{m \in \mathbb{Z}} |u_{n,m}|^2 \leq (1 + cn^2)^{-1} C_0, \tag{29}$$

for all $n \in \mathbb{N}$.

This bound gives us the optical power in the higher band components, e.g., we can estimate number of modes needed to have a given high percentage of the power in the lowest band modes. This is a heuristic justification of using a finite system where $n \in \{1, \dots, N\}$, i.e., a truncation to the Wannier modes of a finite, possibly large, set of bands. Note that (29) does not give us however an estimate for the difference between solutions of the full and truncated systems. This question will be examined in future work.

Equations (1) and (2) in the Wannier basis, see [1], are

$$\begin{aligned} \frac{du_{n',m'}}{dz} &= \frac{1}{2}i \sum_{n \in \mathbb{N}} \sum_{m \in \mathbb{Z}} D_{n,\bar{n}'}^{m,\bar{m}'} u_{n,m} \\ &+ \frac{1}{2}i\alpha\beta \sum_{n_1, n_2, n_3 \in \mathbb{N}} \sum_{m_1, m_2, m_3 \in \mathbb{Z}} V_{n_1, n_2, n_3, n'}^{m_1, m_2, m_3, m'} u_{n_1, m_1} u_{n_2, m_2}^* u_{n_3, m_3}, \end{aligned} \tag{30}$$

where

$$D_{n,\bar{n}'}^{m,\bar{m}'} = \int_{\mathbb{R}} (w_n^m)'(y) w_{n'}^{m'}(y) dy, \tag{31}$$

and

$$V_{n_1, n_2, n_3, n'}^{m_1, m_2, m_3, m'} = \sum_{n \in \mathbb{N}} \sum_{m \in \mathbb{Z}} G_{n, n'}^{m, m'} I_{n_1, \bar{n}_2, \bar{n}'}^{m_1, \bar{m}_2, \bar{m}'} I_{n, n_3, \bar{n}'}^{m, m_3, \bar{m}'}, \tag{32}$$

with

$$G_{n, n'}^{m, m'} = \frac{b}{2\pi} \delta_{n, n'} \left(\int_{-\pi/b}^{\pi/b} \frac{e^{i(m-m')bk}}{E_{n',k} + g^2} dk \right), \tag{33}$$

$$I_{n_1, \bar{n}_2, \bar{n}'}^{m_1, \bar{m}_2, \bar{m}'} = \int_{\mathbb{R}} w_{n_1}^{m_1}(y) w_{\bar{n}_2}^{m_2^*}(y) w_{\bar{n}'}^{m'}(y) dy, \quad I_{n, n_3, \bar{n}'}^{m, m_3, \bar{m}'} = \int_{\mathbb{R}} w_n^m(y) w_{n_3}^{m_3}(y) w_{\bar{n}'}^{m'}(y) dy. \tag{34}$$

System (30) was obtained in [1], and we describe the steps in the Appendix A. To show that it is a Hamiltonian system we compare (30) to Hamilton's equations with the Hamiltonian H of (3) expressed in the Wannier basis.

By (11) and (31)

$$H = -\frac{1}{2} \sum_{n, n' \in \mathbb{N}} \sum_{m, m' \in \mathbb{Z}} D_{n,\bar{n}'}^{m,\bar{m}'} u_{n,m} u_{n',m'}^* - \frac{\beta}{4} \sum_{n, n_3, n_4 \in \mathbb{N}} \sum_{m, m_3, m_4 \in \mathbb{Z}} I_{n, n_3, \bar{n}_4}^{m, m_3, \bar{m}_4} c_{n,m} u_{n_3, m_3} u_{n_4, m_4}^* \tag{35}$$

and by (33)

$$\begin{aligned}
 H &= -\frac{1}{2} \sum_{n,n' \in \mathbb{N}} \sum_{m,m' \in \mathbb{Z}} D_{n,\bar{n}'}^{m,\bar{m}'} u_{n,m} u_{n',m'}^* \\
 &- \frac{\alpha\beta}{4} \sum_{n_1,n_2,n_3,n_4 \in \mathbb{N}} \sum_{n_1,n_2,m_3,m_4 \in \mathbb{Z}} \Lambda_{n_1,n_2,n_3,n_4}^{m_1,m_2,m_3,m_4} u_{n_1,m_1} u_{n_2,m_2}^* u_{n_3,m_3} u_{n_4,m_4}^* \tag{36}
 \end{aligned}$$

with

$$\Lambda_{n_1,n_2,n_3,n_4}^{m_1,m_2,m_3,m_4} = \sum_{n,n' \in \mathbb{N}} \sum_{m,m' \in \mathbb{Z}} G_{n,n'}^{m,m'} I_{n_1,\bar{n}_2,\bar{n}'}^{m_1,\bar{m}_2,\bar{m}'} I_{n,n_3,\bar{n}_4}^{m,m_3,\bar{m}_4}. \tag{37}$$

We show that Hamilton’s equations for (36) coincide with (30), provided the Wannier basis functions are real.

We first see that the symmetry of G implies that the coefficients $G_{n,n'}^{m,m'}$ of (33) satisfy $G_{n,n'}^{m,m'} = (G_{n',n}^{m',m})^*$, for all $n, n' \in \mathbb{N}, m, m' \in \mathbb{Z}$.

We use the double index notation $j = (n, m)$, i.e., (19), (20) are written as

$$\psi = \sum_j c_j w_j, \quad u = \sum_j u_j w_j \tag{38}$$

with summation over $j = (n, m) \in \mathbb{N} \times \mathbb{Z}$. Then $G_{n,n'}^{m,m'} = G_{j,j'}$ with $j = (n, m), j' = (n', m')$.

Let $g_{j,j'} = \int_{\mathbb{R}} (Gw_{j'}) w_j^*$. We will show that $G_{j,j} = g_{j,j}$ and that the symmetry of G implies $g_{j,j'} = g_{j',j}^*$.

We write (2) as $\psi = Gv, v = |u|^2$, and by (38), $v = \sum_{j'} v_{j'} w_{j'}$ we have

$$c_j = \int_{\mathbb{R}} \psi w_j^* = \int_{\mathbb{R}} (Gv) w_j^* = \sum_{j'} \left(\int_{\mathbb{R}} (Gw_{j'}) w_j^* \right) v_{j'} = \sum_{j'} g_{j,j'} v_{j'}. \tag{39}$$

Then

$$c_j = \sum_{j'} g_{j,j'} v_{j'} = \sum_{j'} g_{j,j'} \left(\int_{\mathbb{R}} |u|^2 w_{j'}^* \right) = \sum_{j'} g_{j,j'} \sum_{j_1,j_2} u_{j_1} u_{j_2}^* \int_{\mathbb{R}} w_{j_1} w_{j_2}^* w_{j'}^*, \tag{40}$$

or

$$c_j = \sum_{j_1,j_2,j_3} \left(g_{j,j'} \int_{\mathbb{R}} w_{j_1} w_{j_2}^* w_{j'}^* \right) u_{j_1} u_{j_2}^*. \tag{41}$$

By (33) we have $g_{j,j'} = G_{j,j'}, \forall j, j' \in \mathbb{N} \times \mathbb{Z}$.

Symmetry of the real bounded operator G with respect to standard L^2 inner product implies

$$\int_{\mathbb{R}} (Gf) g^* = \int_{\mathbb{R}} f (Gg)^*,$$

for all $f, g \in L^2(\mathbb{R}; \mathbb{C})$, therefore

$$g_{j_1,j_2} = \int_{\mathbb{R}} (Gw_{j_2}) w_{j_1}^* = \int_{\mathbb{R}} w_{j_2} (Gw_{j_1})^* = g_{j_2,j_1}^*, \quad \forall j_1, j_2 \in \mathbb{N} \times \mathbb{Z}. \tag{42}$$

We now examine Hamilton’s equations. We write (36) as $H = h_2 + h_4$ with

$$h_2 = \frac{1}{2} \sum_{j,j'} D_{j,j'} u_j u_{j'}^*, \quad h_4 = -\frac{\alpha\beta}{4} \sum_{j_1,j_2,j_3,j_4} \Lambda_{j_1,j_2,j_3,j_4} u_{j_1} u_{j_2}^* u_{j_3} u_{j_4}^*. \tag{43}$$

Hamilton’s equation is

$$\frac{du_l}{dz} = -i \frac{\partial H}{\partial u_l^*}, \quad l \in \mathbb{N} \times \mathbb{Z}, \tag{44}$$

and we have

$$-i \frac{\partial h_2}{\partial u_l^*} = -i \frac{1}{2} \sum_j D_{j,l} u_j. \tag{45}$$

We have thus recovered the linear part of (30).

For the nonlinear part we have

$$\begin{aligned} -i \frac{\partial h_4}{\partial u_l^*} &= -i \frac{\alpha\beta}{4} \left(\sum_{j_1, j_2, j_3} u_{j_1} \Lambda_{j_1, j_2, j_3, l} u_{j_1} u_{j_2}^* u_{j_3} + \sum_{j_1, j_3, j_4} \Lambda_{j_1, l, j_3, j_4} u_{j_1} u_{j_3}^* u_{j_4}^* \right) \\ &= -i \frac{\alpha\beta}{4} \sum_{j_1, j_2, j_3} \left(\Lambda_{j_1, j_2, j_3, l} + \Lambda_{j_3, l, j_1, j_2} \right) u_{j_1} u_{j_2}^* u_{j_3}. \end{aligned} \tag{46}$$

Let $f = w_{j_1} w_{j_2}^*$, $g = w_{j_3}^* w_l$. We omit the dependence of f, g on the indices for simplicity. Also let $f = \sum_k f_k w_k$, $g = \sum_k g_k w_k$. By (37)

$$\Lambda_{j_1, j_2, j_3, l} = \sum_{k_1, k_2} G_{k_1, k_2} \left(\int_{\mathbb{R}} w_{k_1} g^* \right) \left(\int_{\mathbb{R}} w_{k_2}^* f \right) = \sum_{k_1, k_2} G_{k_1, k_2} g_{k_1}^* f_{k_2}, \tag{47}$$

and

$$\Lambda_{j_3, l, j_1, j_2} = \sum_{k_1, k_2} G_{k_1, k_2} \left(\int_{\mathbb{R}} w_{k_1} w_{j_1} w_{j_2}^* \right) \left(\int_{\mathbb{R}} w_{k_2}^* w_{j_3} w_l^* \right) = \sum_{k_1, k_2} G_{k_1, k_2} f_{k_1}^* g_{k_2}, \tag{48}$$

so that by symmetry of G ,

$$\Lambda_{j_3, l, j_1, j_2} = \sum_{k_1, k_2} G_{k_2, k_1} g_{k_1} f_{k_2}^* = \sum_{k_1, k_2} G_{k_1, k_2}^* g_{k_1} f_{k_2}^*. \tag{49}$$

By (47), (49) we then have

$$\Lambda_{j_3, l, j_1, j_2} = \Lambda_{j_1, j_2, j_3, l}^*. \tag{50}$$

Clearly, the above hold for any double index $j_1, j_2, j_3, l \in \mathbb{N} \times \mathbb{Z}$. If the Wannier functions are real, the coefficients G_{k_1, k_2} and $\Lambda_{j_1, j_2, j_3, j_4}^*$ are real. By (50), (46) yields the nonlinear part of (30). This concludes the argument.

We remark that the Hamiltonian structure of (30) easily implies the Hamiltonian structure of finite band truncations of the (30). The same applies to truncations where we consider a finite set of sites m . It suffices to restrict the summations in (36) to a finite range of n, m , also setting modes outside the desired index range to zero.

Also the Hamiltonian of (36) is invariant under the global phase change $u_{n,m} \mapsto e^{i\phi} u_{n,m}$, for arbitrary real ϕ and all n, m . This fact justifies the terminology coupled DNLS for (30).

As seen in [1], the Wannier expansion leads to a natural extension of the Fratalocchi-Assanto model [6]. The coupled mode approach of [6] can be also extended to describe more degrees of freedom per site [7]. Generally, mode expansions have additional structure when they arise from the solution of some spectral problem. This is the case for Bloch and Wannier functions. This additional structure however requires substantial computational effort, e.g. we need to compute Bloch and Wannier functions and evaluate Wannier overlap integrals. We discuss some of the relevant issues in the next section. We emphasize however that the general structural features of the equations, e.g., Hamiltonian structure, symmetries, form of mode interaction terms, are key. Heuristic simplifications that preserve these features can yield useful models. It is also seems important to be able to justify truncations to a small number of bands. We have at the moment only a partial justification for such truncations, relying on the rate of decay of the power in the higher bands (29).

3. Real Wannier Functions and Dispersive Properties

The Hamiltonian structure of the infinite system for the Wannier coefficients (30) assumed real functions. In this section we describe the construction of real Wannier functions using explicit constructions of the Bloch functions. We also observe that the linear part of (30) will in general couple modes from different bands. This is a main difference between our system and the equations considered in [11,12,26,27]. We show that we can still however diagonalize the system using trigonometric functions. In that sense, the Wannier-Bloch analysis leads to a homogenized, i.e., effectively translation invariant, linear part, see [29,30].

To construct the Wannier functions we examine the Schrödinger equation

$$-\partial_y^2 \Psi + V(y)\Psi = E\Psi, \quad \Psi : \mathbb{R} \rightarrow \mathbb{C} \tag{51}$$

with V nonnegative and b -periodic as a second order ODE with a real parameter $E \in \mathbb{R}$. We assume that V is also piecewise Lipschitz. The spectrum of $-\partial_y^2 + V$ is given by the set of real E for which all solutions of (51) are bounded, see e.g., [24,35]. The equations for the real and imaginary parts of Ψ decouple, and all complex valued solutions are of the form $A\Psi_1(\cdot; E) + B\Psi_2(\cdot; E)$, $A, B \in \mathbb{C}$, where $\Psi_1(\cdot; E), \Psi_2(\cdot; E)$ are any two linearly independent real solutions.

We consider solutions $\Psi_1(\cdot; E), \Psi_2(\cdot; E)$ with initial conditions

$$\Psi_1(0; E) = 1, \quad \Psi_1'(0; E) = 0, \tag{52}$$

$$\Psi_2(0; E) = 0, \quad \Psi_2'(0; E) = 1. \tag{53}$$

By the Hamiltonian structure of (51), seen a non-autonomous ODE on the plane, the corresponding solutions are linearly independent, i.e., $[\Psi_1(y; E), \Psi_1'(y; E)], [\Psi_2(y; E), \Psi_2'(y; E)]$ are linearly independent since the (linear) solution map is symplectic, $\forall y \in \mathbb{R}$.

Given $E \in \mathbb{R}$, a solution $\Psi(\cdot; E)$ is bounded if and only if there exists $\lambda \in \mathbb{C}, |\lambda| = 1$, for which

$$\Psi(y + b; E) = \lambda\Psi(y; E), \quad \forall y \in \mathbb{R}, \tag{54}$$

see [21]. Then we must also have

$$\Psi'(y + b; E) = \lambda\Psi'(y; E), \quad \forall y \in \mathbb{R}. \tag{55}$$

Let $\Psi(y; E) = A\Psi_1(y; E) + B\Psi_2(y; E)$ for A, B complex, then (54), (55) at $y = 0$ and (52), (53) imply the system

$$A\Psi_1(b; E) + B\Psi_2(b; E) = \lambda A \tag{56}$$

$$A\Psi_1'(b; E) + B\Psi_2'(b; E) = \lambda B. \tag{57}$$

Then λ must be an eigenvalue of the matrix M defined by

$$M = \begin{pmatrix} \Psi_1(b; E) & \Psi_2(b; E) \\ \Psi_1'(b; E) & \Psi_2'(b; E) \end{pmatrix}. \tag{58}$$

If λ is an eigenvalue of M , and $\lambda = e^{ikb}$, then k and E are related to

$$\mu(E) = \cos kb, \tag{59}$$

where

$$\mu(E) = \frac{\Psi_1(b; E) + \Psi_2'(b; E)}{2}, \tag{60}$$

see [21]. The dependence of μ on the choice of Ψ_1, Ψ_2 , i.e., the initial conditions (52), (53) is suppressed from the notation.

We recall some properties of $\mu(E)$, and the solutions of (59), see [21–24]. The function $\mu(E)$, μ is entire and $\mu'(E) = 0$ implies $|\mu(E)| \geq 1$. Also, $\mu(E) \rightarrow \infty$ as $E \rightarrow -\infty$, and $\mu(E) \rightarrow \cos(b\sqrt{E})$ as $E \rightarrow \infty$. Also $\mu(E) \rightarrow \infty$ as $E \rightarrow -\infty$. For V non-negative μ has no negative critical points and an infinite set of positive critical points that become equidistant.

A band is a maximal connected interval of \mathbb{R} where $\mu(E)$ is monotone and satisfies $|\mu(E)| \leq 1$. By the above, there is an infinite number of bands $B_n, n \in \mathbb{N}$, and a natural way to enumerate them so that points $n < n', E \in B_n, E'$ implies $E_n \leq E_{n'}$, with equality holding for $n = n + 1$ and $E = \max B_n, E' = \min B_{n'}$. Every E satisfying (60) must belong to exactly one band. Also, for every $n \in \mathbb{N}$, and $k \in [0, \pi/b]$, there exists a unique $E \in B_n$ satisfying (60). We denote such $E \in B_n$ by $E_{n,k}$. The large E behavior of $\mu(E)$ also implies that there exist $c, C > 0$ such that $\varepsilon_n = \min B_n$ satisfies $cn^2 \leq \varepsilon_n \leq Cn^2, \forall n \in \mathbb{N}$.

The solutions of (60) can be then parametrized as $E_{n,k}, k \in [0, \pi/b], n \in \mathbb{N}$, and $B_n = [E_{n,\pi/b}, E_{n,0}]$. Also, we let $E(-k, n) = E_{k,n}$ and extend $E_{n,k}$ to $k \in \mathbb{R}$ by $2\pi/b$ -periodicity. This notation is consistent with (60). For V non-negative all bands belong to $\overline{\mathbb{R}^+}$. By the implicit function theorem, given $n \in \mathbb{N}, E_{n,k}$ is real analytic for $k \in (0, \pi/b)$, and is continuous in $[0, \pi/b]$. The even and $2\pi/b$ -periodic extension of $E_{n,k}$ to real k is continuous in \mathbb{R} , and real analytic at all points outside the lattice $\mathbb{Z}\frac{\pi}{b}$, for all $n \in \mathbb{N}$. Regularity of $E_{n,k}$ at points $\mathbb{Z}\frac{\pi}{b}$ for given n follows under gap conditions for the edges of the band B_n .

Consider now $E = E_{n,k}$ as above a solution of (60) for some $n \in \mathbb{N}, k \in [0, \pi/b]$, and the corresponding real solutions $\Psi_1(\cdot; E), \Psi_2(\cdot; E)$. Solving (56), (57) we have

$$\frac{A}{B} = \frac{\Psi_2(b; E)}{\lambda - \Psi_1(b; E)}, \tag{61}$$

and we obtain

$$\Psi(y; E) = A \left(\Psi_1(y; E) + \frac{\Psi_2(b; E)}{\lambda - \Psi_1(b; E)} \Psi_2(y; E) \right), \tag{62}$$

with $\lambda = e^{ikb}, E = E_{n,k}, n \in \mathbb{N}, k \in (0, \pi/b)$. The expression can be extended to the endpoints $k = 0, \pi/b$, under conditions we discuss below. Also, the complex coefficient A is free, e.g., it can be also chosen to normalize $\Psi(y; E)$. In general it may depend on n, k , and we write $A = A_{n,k}$.

Denote $\Psi(\cdot; E) = \Psi(\cdot; E_{n,k})$ by $\Psi_{n,k}, n \in \mathbb{N}, k \in [0, \pi/b]$. Clearly $\Psi_{n,k}^*$ is also a solution of (51). We then let

$$\phi_{n,k} = \begin{cases} \Psi_{n,k} & \text{if } 0 < k < \frac{\pi}{b}, \\ \Psi_{n,-k}^* & \text{if } -\frac{\pi}{b} < k < 0. \end{cases} \tag{63}$$

The functions $\phi_{n,k}$ are extended by $2\pi/b$ -periodicity for $k \in \mathbb{R} \setminus \mathbb{Z}\frac{\pi}{b}$ and are Bloch functions, see (12), (13), (14).

We check that the corresponding Wannier functions are real. By (18), it suffices to show that the w_n^0 are real. By (16)

$$w_n^0(y) = \sqrt{\frac{b}{2\pi}} \int_{-\frac{\pi}{b}}^{\frac{\pi}{b}} \phi_{n,k}(y) dk, \tag{64}$$

and by (63)

$$\int_{-\frac{\pi}{b}}^{\frac{\pi}{b}} \phi_{n,k}(y) dk = \int_{-\frac{\pi}{b}}^0 \Psi_{n,-k}^*(y) dk + \int_0^{\frac{\pi}{b}} \Psi_{n,k}(y) dk = 2\text{Re} \int_0^{\frac{\pi}{b}} \Psi_{n,k}(y) dk, \tag{65}$$

$\forall y \in \mathbb{R}$. It is assumed that the last integral is well defined.

We now give a condition that makes the above construction well defined, leading to $w_n^0 \in L^2(\mathbb{R}, \mathbb{R})$, for all $n \in \mathbb{N}$. In particular, assume that the limits

$$\lim_{k \rightarrow 0^+} \frac{dE_{n,k}}{dk}, \quad \lim_{k \rightarrow \pi/b^-} \frac{dE_{n,k}}{dk}$$

exist (and are finite). Then the corresponding limits of the fraction $\Psi_2(b; E)/(\lambda - \Psi_1(b; E))$ also exist, and $\Psi_{n,k}$ given by the right hand side of (62), with $A = 1$, is well defined for all $n \in \mathbb{N}, k \in [0, \pi/b]$. We further see that the $\Psi_{n,\cdot}(\cdot)$ are continuous in $[0, \pi/b] \times \mathbb{R}, \forall n \in \mathbb{N}$. Defining $\phi_{n,k}$ by (63), the integrals in (64), (65) are finite for all $y \in \mathbb{R}$. It follows that $\phi_{n,\cdot}(y) \in L^2([-\pi/b, \pi/b]; \mathbb{C})$, for all $n \in \mathbb{N}, y \in \mathbb{R}$. Then by Percival and (18) we see that

$$\int_{\mathbb{R}} |w_n^0(y)|^2 dy = 2\pi \int_0^b \left(\sqrt{\frac{b}{2\pi}} \int_{-\frac{\pi}{b}}^{\frac{\pi}{b}} \phi_{n,k}(y) dk \right) dy,$$

i.e., finite, for all n . Thus the Wannier functions constructed this way are square-summable. Normalized Wannier functions are obtained by choosing a suitable coefficient $A_{n,k} = A_n$ for each $n \in \mathbb{N}$.

Note that the condition we used is always satisfied if both $E_{n,0}, E_{n,\pi/b}$ belong to the boundary of the spectrum for some n . In such band gap situations, $E_{n,\cdot}$ is real analytic in \mathbb{R} , and we obtain an exponentially decaying Wannier function w_n^0 [23,24].

The above suggest that several qualitative features of the Wannier functions can be deduced by theoretical arguments. The main input is information on the energy band structure. This information is obtained by solving (59) numerically. The function $\mu(E)$ must be computed numerically from (60). The functions $\Psi_1(y; E), \Psi_2(y; E)$ are computed by numerical integration of (51) in the interval $y \in [0, b]$ for different values of E , using the initial conditions (52), (53) respectively. Explicit expressions for the $\Psi_1(b; E), \Psi_2(b; E)$ are known for a piece-wise constant potential V with two steps, see [1,23,36], but are cumbersome in the general case. This calculation also yields $E_{n,k}, k \in [-\pi/b, \pi/b]$, for the lowest n , numerical plots can be found in several sources, see e.g., [1,26].

Wannier functions are obtained numerically from (62)–(64), see [1,23,26] for some examples indicating the decay of the Wannier functions (for small n) as V is varied. The evaluation of mode interaction coefficients (33), (34) also uses quadrature, see [1]. The main difficulty here is the large number of coefficients, and the combinatorial nature of their enumeration. At this stage we need some efficient cut-off criteria, and we typically opt for some heuristic truncation to a few mode interactions, e.g., with a few nearest neighbors, justified by the decay of Wannier functions. This part of the analysis is still not as developed. In the case where we consider truncation to the first band modes, the main question is distinguishing between a power (on-site-only) and a nonlocal nonlinearity [6], see [1] for some results. As we already mentioned the two models have properties the can distinguish them [8–10]. The possibility of long range linear mode interactions, e.g., as in [37], was also considered. It would be desirable to have a similar study for a model with two or three bands, inter-band mode interactions could be a more important feature of the problem.

We now examine the linear part of the nematic system (1), (2). Generally the Wannier modes of different bands interact, and we want to examine the effect of these interactions for finite band truncations of the general discrete system (A8).

In what follows we will consider expansions in real Wannier functions and use the Hamiltonian structure of the linear systems. The linear coefficients of (31), (35) are then $D_{n,\bar{n}'}^{m,m'} = D_{n,n'}^{m,m'}$ with

$$\begin{aligned} D_{n,n'}^{m,m'} &= \int_{\mathbb{R}} (w_n^m)''(y) w_{n'}^{m'}(y) dy \\ &= \int_{\mathbb{R}} (w_n^0)''(y - mb) w_{n'}^0(y - m'b) dy \\ &= \int_{\mathbb{R}} (w_n^0)''(\tilde{y}) w_{n'}^0(\tilde{y} - (m - m')b) d\tilde{y}. \end{aligned} \tag{66}$$

Let $D_{n_1,n_2}(m) = D_{n_1,n_2}^{0,m}$, then by (66) we have the symmetries

$$D_{n_1,n_2}^{m_1,m_2} = D_{n_1,n_2}(m_1 - m_2) = D_{n_2,n_1}(m_2 - m_1) = D_{n_2,n_1}^{m_2,m_1}, \tag{67}$$

for all $n_1, n_2 \in \mathbb{N}, m_1, m_2 \in \mathbb{Z}$. Linear interaction coefficients for $n_1 = n_2 = n$ depend on $|m_1 - m_2|$. In general, the linear interactions between bands $n_1 \neq n_2$ do not vanish.

The linear coefficients $D_{n_1, n_2}^{m_1, m_2}$ are contrasted to those of the periodic or perturbed periodic Schrödinger equation

$$\partial_z u = \frac{1}{2} i \partial_y^2 u + \frac{1}{2} i [V(y) + \tilde{V}(y)] u, \tag{68}$$

with \tilde{V} a perturbation of the b -periodic potential V used to define the Wannier functions. For $\tilde{V} \equiv 0$ the Hamiltonian is

$$h_{2,V} = \frac{1}{2} \int_{\mathbb{R}} u (-\partial_y^2 + V) u^*, \tag{69}$$

and we use expansion in the Bloch functions and (12), (13) and the definition of the Wannier functions to compute

$$h_{2,V} = \frac{1}{2} \sqrt{\frac{b}{2\pi}} \sum_{n \in \mathbb{N}} \sum_{m_1, m_2 \in \mathbb{Z}} \hat{E}_n(m_1 - m_2) u_{n, m_1} u_{n, m_2}^*, \tag{70}$$

with

$$\hat{E}_n(m) = \sqrt{\frac{b}{2\pi}} \int_{-\frac{\pi}{b}}^{\frac{\pi}{b}} E_{n,k} e^{-imbk} dk, \quad m \in \mathbb{Z}. \tag{71}$$

Also, $E_{n,k}$ real and even in k , implies $\hat{E}_n(-m) = \hat{E}_n^*(m) = \hat{E}_n(m)$, for all $n \in \mathbb{N}, m \in \mathbb{Z}$. The interaction between different bands therefore vanishes.

The effect of the perturbation \tilde{V} is described adding to the Hamiltonian the part

$$h_{\tilde{V}} = \frac{1}{2} \int_{\mathbb{R}} u \tilde{V} u^*. \tag{72}$$

We have

$$h_{\tilde{V}} = \frac{1}{2} \sum_{n_1, n_2 \in \mathbb{N}} \sum_{m_1, m_2 \in \mathbb{Z}} \tilde{V}_{n_1, n_2}^{m_1, m_2} u_{n_1, m_1} u_{n_2, m_2}^*, \tag{73}$$

with

$$\tilde{V}_{n_1, n_2}^{m_1, m_2} = \int_{\mathbb{R}} w_{n_1}^{m_1}(y) \tilde{V}(y) w_{n_2}^{m_2}(y) dy. \tag{74}$$

The coefficients will in general couple modes from different bands. In the case where \tilde{V} is also b -periodic the $\tilde{V}_{n_1, n_2}^{m_1, m_2}$ have the symmetries that are similar to the ones in (67), i.e., $\tilde{V}_{n_1, n_2}^{m_1, m_2} = \tilde{V}_{n_2, n_1}^{m_2, m_1} = \tilde{V}_{n_1, n_2}^{0, m_1 - m_2}$ and will also couple modes from different bands. In the case where $V + \tilde{V}$ is periodic a new set of Wannier functions may be defined so that the new bands decouple.

We remark that the Hamiltonian of the linear part of is denoted by h_2 , see (43). Clearly, $h_2 = h_{2,V} - h_V$, with the notation of (70), (73). Thus the coefficients $D_{n_1, n_2}^{m_1, m_2}$ of (66) can be expressed in terms of the $\hat{E}_n(m), V_{n_1, n_2}^{m_1, m_2}$ of (71), (74), as

$$D_{n_1, n_2}^{m_1, m_2} = -\sqrt{\frac{b}{2\pi}} \delta_{n_1, n_2} \hat{E}_{n_1}(m_1 - m_2) - V_{n_1, n_2}^{m_1, m_2}. \tag{75}$$

(In the case $n_1 \neq n_2$, the first term vanishes.) Comparing (66), (75) we thus see that can then avoid computation of the derivative of the Wannier functions at the cost of computing the Fourier transform of $E_{n,k}$.

Consider now a truncation of the general discrete system (A8) to the first N bands. The linear part is

$$\frac{du_{j,m}}{dz} = \frac{i}{2} \sum_{n_1=1}^N \sum_{m_1 \in \mathbb{Z}} u_{n_1, m_1} D_{n_1, j}^{m_1, m} = \frac{i}{2} \sum_{n_1=1}^N \sum_{m_1 \in \mathbb{Z}} D_{n_1, j}(m_1 - m) u_{n_1, m_1}. \tag{76}$$

To find the dispersion relation we look for solutions $u_{j,m} = A_j e^{-i(mb\kappa + \omega_\kappa z)}$, $j \in \{1, \dots, N\}$, $m \in \mathbb{Z}$, $\kappa \in \mathbb{R}$. Then (76) becomes

$$\omega_\kappa A_j = -\frac{1}{2} \sum_{n=1}^N \left(\sum_{l \in \mathbb{Z}} D_{n,j}(l) e^{-ilb\kappa} \right) A_n, \quad j = 1, \dots, N. \tag{77}$$

Thus ω_κ is an eigenvalue of the matrix T_κ defined by

$$T_\kappa(j, n) = -\frac{1}{2} \sum_{l \in \mathbb{Z}} D_{n,j}(l) e^{-ilb\kappa}, \quad j, n \in \{1, \dots, N\}. \tag{78}$$

For instance, truncation up to the second band yields

$$\omega_\kappa = \frac{1}{2} \left(T_\kappa(1, 1) + T_\kappa(2, 2) \pm \sqrt{(T_\kappa(1, 1) - T_\kappa(2, 2))^2 + 4T_\kappa(1, 2)T_\kappa(2, 1)} \right), \tag{79}$$

$\kappa \in \mathbb{R}$.

By the symmetries (67) T_κ is Hermitian, $\forall \kappa \in \mathbb{R}$, so that the eigenvalues ω_κ are real.

Note that the solutions $u_{j,m}$ and T_κ are 2π -periodic in κ so that we may consider only $\kappa \in [0, 2\pi)$. Varying $\kappa \in [0, 2\pi)$ for each of the N eigenvalues $\omega_{\kappa,j}$, $j = 1, \dots, N$ of T_κ will produce N intervals.

We finally note that substitution of (31), (67) into (78), and use of (17) leads to somewhat simpler expressions that involve the Bloch functions

$$T_\kappa(j, n) = \frac{1}{2} \sqrt{\frac{b}{2\pi}} \int_{\mathbb{R}} (w_n^0)''(y) \phi_{j,\kappa}^*(y) dy = -\frac{1}{2} \sqrt{\frac{b}{2\pi}} \int_{\mathbb{R}} w_n^0(y) (\phi_{j,\kappa}^*)''(y) dy. \tag{80}$$

The linear part of the evolution equation is therefore diagonalized by plane wave (trigonometric) solutions, and is thus effectively translation invariant in the Wannier basis. This is expected as the periodicity of the medium is absorbed in the nonlinear term. The range of the $\omega_{\kappa,j}$, $\kappa \in [0, 2\pi)$, $j = 1, \dots, N$, will produce N intervals that must be computed numerically. These intervals may overlap or have gaps, although in the limit $N \rightarrow \infty$ we expect that their union is the positive real axis, i.e., the spectrum of $-\partial_y^2$. The computation of these intervals involves the computation of linear mode interaction coefficients and will be considered in future work.

4. Discussion

We have examined some properties of a coupled Schrödinger-elliptic system modeling optical waveguide arrays in a nematic liquid crystal substrate. The system is studied by first passing to an equivalent infinite system of discrete describing the interaction of Wannier mode amplitudes of the relevant physical quantities [1]. The Wannier basis functions are defined in terms of a periodic Schrödinger operator appearing in the system and must be computed numerically. The Wannier mode amplitudes are related to the observed quantities by quadrature formulas (21) that may be evaluated numerically or using approximations. The Wannier basis approach leads to the derivation of systems of discrete nonlinear Schrödinger (DNLS) equations by truncation to the mode amplitudes of the first bands of the periodic Schrödinger operator. We have shown that these systems are Hamiltonian. The proof uses the reality of Wannier functions, and we have also described an explicit construction of real Wannier functions. Finally we show that the linear part of the system of discrete equations is diagonalized by (trigonometric) plane waves.

Bloch-Wannier analysis is a classical subject in theoretical physics, with well-known applications in classical and quantum mechanics [24,25]. Recently it is increasingly applied to the study of nonlinear waves in inhomogeneous media [23,26], and in the theory of homogenization [29,30]. The paper considers a problem in nonlinear waves where the periodicity appears in the nonlinear interaction. The system includes a natural operator that allows the use of Bloch-Wannier analysis, but differs from the more commonly stud-

ied systems [7] where the linear part of the beam propagation equation is the periodic Schrödinger operator. In that case the band gap structure of the periodic Schrödinger operator allows us to justify the truncation to a model for the lowest band modes through a non-resonance argument [23]. In the present case the the most likely justification of DNLS models will involve truncation to a finite (possibly small) system of DNLS equations. This fact is also suggested by experimental results of [3]. Note that [3] consider a more complicated periodic operator in the director field equation that also includes the second (vertical) direction of the plane perpendicular to the optical axis. The present paper uses a simplification of the director field equation and takes advantage of the more developed Bloch analysis of the periodic Schrödinger operator. The idea is that the nonlinear effect of the transverse periodicity is already present in the simpler version. In addition, the more tractable Wannier-Bloch analysis of the simpler problem has allowed us to derive multi-band DNLS systems and to analyze their structure. This a first towards further analysis of such systems, e.g., along the lines of earlier studies of the Fratolocci-Assanto model [8,9]. While the paper considers a problem arising from nonlinear optics in liquid crystals, the combination of nonlocal nonlinearity and periodicity we consider may appear in other areas where similar systems are studied [14,15].

The paper shows that the Wannier basis expansion is an effective tool for elucidating the structural features of simplified DNLS equations. We also saw that the Wannier-Bloch approach requires the numerical computation of several intermediate quantities. For instance, the computation of Wannier functions uses numerically computed Bloch functions and numerical integration over Bloch functions, while the nonlinearity of DNLS systems, as well as the linear interaction between bands also involves the evaluation of Wannier overlap integrals. Possible simplifications may arise for some limits of V [1], and there are general ideas such a eliminating non-resonant interactions [23,26] that can be examined further in this problem. but possibly less practical. Our view is that a good understanding of the structure of the Wannier coupled mode systems may allow us to analyze their dynamical properties without computing everything. It is possible that heuristic simplifications lead to models that capture significant features of the dynamics, and that a better theoretical understanding can bridge the gap between the simplified and fuller models. These questions will be addressed in future work.

Funding: This research received partial funding from a PAPIT IN112119 grant.

Acknowledgments: The author wishes to thank Jose Antonio Velez Perez for helpful discussions, and Gaetano Assanto and Noel Smyth for helpful comments on the manuscript.

Conflicts of Interest: The author declares no conflict of interest.

Appendix A

We present the steps from the Schrödinger system (1), (2) for the variables u, ψ to the infinite system (30) for their Wannier coefficients, see also [1],

We first consider the second nematicon Equation (2). We multiply (2) by $\phi_{n',k'}^*(y)$, integrate over $y \in \mathbb{R}$, and use the Schrödinger Equation (12) to obtain

$$\int_{\mathbb{R}} \psi(y)(E_{n',k'}^* + g^2)\phi_{n',k'}^*(y) dy = \alpha \int_{\mathbb{R}} |u(y)|^2 \phi_{n',k'}^*(y) dy, \tag{A1}$$

hence

$$\int_{\mathbb{R}} \psi(y)\phi_{n',k'}^*(y) dy = \alpha(E_{n',k'} + g^2)^{-1} \int_{\mathbb{R}} |u(y)|^2 \phi_{n',k'}^*(y) dy. \tag{A2}$$

We then multiply (A2) by $e^{imk'b}$ and integrate both sides over $k \in [-\pi/b, \pi/b]$. Interchanging the order of integration in k, y , and using the definition of Wannier functions we obtain that ψ is given by (19) with

$$c_{n,m} = \alpha \sqrt{\frac{b}{2\pi}} \sum_{n_1, n_2 \in \mathbb{N}} \sum_{m_1, m_2 \in \mathbb{Z}} K_{n_1, n_2, n}^{m_1, m_2, m} u_{n_1, m_1} u_{n_2, m_2}^* \tag{A3}$$

where

$$K_{n_1, n_2, n}^{m_1, m_2, m} = \int_{\mathbb{R}} w_{n_1}^{m_1}(y) w_{n_2}^{m_2*}(y) \left\{ \int_{-\pi/b}^{\pi/b} \frac{\phi_{n,k}^*(y) e^{imbk}}{E_{n,k} + g^2} dk \right\} dy. \tag{A4}$$

Expanding $\phi_{n,k}$ in the Wannier basis as in (17) we have

$$\begin{aligned} K_{n_1, n_2, n}^{m_1, m_2, m} &= \sqrt{\frac{b}{2\pi}} \int_{\mathbb{R}} w_{n_1}^{m_1}(y) w_{n_2}^{m_2*}(y) \left\{ \sum_{m' \in \mathbb{Z}} \left(\int_{-\pi/b}^{\pi/b} \frac{e^{i(m-m')bk}}{E_{n,k} + g^2} dk \right) w_n^{m'*}(y) \right\} dy \\ &= \sqrt{\frac{b}{2\pi}} \int_{\mathbb{R}} w_{n_1}^{m_1}(y) w_{n_2}^{m_2*}(y) \left\{ \sum_{n' \in \mathbb{N}} \sum_{m' \in \mathbb{Z}} \delta_{n,n'} \left(\int_{-\pi/b}^{\pi/b} \frac{e^{i(m-m')bk}}{E_{n',k} + g^2} dk \right) w_n^{m'*}(y) \right\} dy \\ &= \sum_{n' \in \mathbb{N}} \sum_{m' \in \mathbb{Z}} \sqrt{\frac{b}{2\pi}} \delta_{n,n'} \left(\int_{-\pi/b}^{\pi/b} \frac{e^{i(m-m')bk}}{E_{n',k} + g^2} dk \right) \int_{\mathbb{R}} w_{n_1}^{m_1}(y) w_{n_2}^{m_2*}(y) w_n^{m'*}(y) dy. \end{aligned} \tag{A5}$$

By (A2), (A5) we then have

$$c_{n,m} = \alpha \sum_{n_1, n_2, n' \in \mathbb{N}} \sum_{m_1, m_2, m' \in \mathbb{Z}} G_{n,n'}^{m,m'} I_{n_1, n_2, n'}^{m_1, m_2, m'} u_{n_1, m_1} u_{n_2, m_2}^* \tag{A6}$$

with

$$G_{n,n'}^{m,m'} = \frac{b}{2\pi} \delta_{n,n'} \left(\int_{-\pi/b}^{\pi/b} \frac{e^{i(m-m')bk}}{E_{n',k} + g^2} dk \right), \quad I_{n_1, n_2, n'}^{m_1, m_2, m'} = \int_{\mathbb{R}} w_{n_1}^{m_1}(y) w_{n_2}^{m_2*}(y) w_n^{m'*}(y) dy. \tag{A7}$$

To expand the first nematicon Equation (1) in coefficients of Wannier functions, we substitute the series expansions (19), (20) into (1), multiply (1) by $w_n^{m'*}(y)$, and integrate over $y \in \mathbb{R}$. We obtain

$$\frac{du_{n',m'}}{dz} = \frac{1}{2} i \sum_{n \in \mathbb{N}} \sum_{m \in \mathbb{Z}} D_{n,n'}^{m,m'} u_{n,m} + \frac{1}{2} i \beta \sum_{n, n_3 \in \mathbb{N}} \sum_{m, m_3 \in \mathbb{Z}} I_{n, n_3, n'}^{m, m_3, m'} c_{n,m} u_{n_3, m_3}. \tag{A8}$$

where

$$D_{n, n'}^{m, m'} = \int_{\mathbb{R}} (w_n^m)''(y) w_n^{m'*}(y) dy, \quad I_{n, n_3, n'}^{m, m_3, m'} = \int_{\mathbb{R}} w_n^m(y) w_{n_3}^{m_3}(y) w_n^{m'*}(y) dy \tag{A9}$$

Substitution of (A3) into (A8) leads to the system

$$\begin{aligned} \frac{du_{n',m'}}{dz} &= \frac{1}{2} i \sum_{n \in \mathbb{N}} \sum_{m \in \mathbb{Z}} D_{n, n'}^{m, m'} u_{n,m} \\ &+ \frac{1}{2} i \alpha \beta \sum_{n_1, n_2, n_3 \in \mathbb{N}} \sum_{m_1, m_2, m_3 \in \mathbb{Z}} V_{n_1, n_2, n_3, n'}^{m_1, m_2, m_3, m'} u_{n_1, m_1} u_{n_2, m_2}^* u_{n_3, m_3}, \end{aligned} \tag{A10}$$

where by (A4), (31), and (A8), (31)

$$V_{n_1, n_2, n_3, n'}^{m_1, m_2, m_3, m'} = \sqrt{\frac{b}{2\pi}} \sum_{n \in \mathbb{N}} \sum_{m \in \mathbb{Z}} K_{n_1, n_2, n}^{m_1, m_2, m} I_{n, n_3, n'}^{m, m_3, m'} = \sum_{n \in \mathbb{N}} \sum_{m \in \mathbb{Z}} G_{n,n'}^{m,m'} I_{n_1, n_2, n'}^{m_1, m_2, m'} I_{n, n_3, n'}^{m, m_3, m'}. \tag{A11}$$

This is the system of (30), with the coefficients (31)–(34).

References

1. Velez Perez, J.A.; Panayotaros, P. Wannier functions and discrete NLS equations for nematicons. *Math. Eng.* **2019**, *1*, 309–326.
2. Fratolocchi, A.; Assanto, G.; Brzdąkiewicz, K.A.; Karpierz, M.A. Discrete propagation and spatial solitons in nematic liquid crystals. *Opt. Lett.* **2004**, *29*, 1530–1532. [CrossRef] [PubMed]
3. Fratolocchi, A.; Assanto, G.; Brzdąkiewicz, K.A.; Karpierz, M.A. Discrete light propagation and self-trapping in liquid crystals. *Opt. Express* **2005**, *13*, 1808–1815. [CrossRef] [PubMed]
4. Rutkowska, K.A.; Assanto, G.; Karpierz, M.A. Discrete light propagation in arrays of liquid crystalline waveguides. In *Nematicons: Spatial Optical Solitons in Nematic Liquid Crystals*; Assanto, G., Ed.; Wiley-Blackwell: Hoboken, NJ, USA, 2012; pp. 255–277.
5. Assanto, G.; Fratolocchi, A.; Peccianti, M. Spatial solitons in nematic liquid crystals: From bulk to discrete. *Opt. Express* **2007**, *15*, 5248–5259. [CrossRef] [PubMed]
6. Fratolocchi, A.; Assanto, G. Discrete light localization in one-dimensional nonlinear lattices with arbitrary nonlocality. *Phys. Rev. E* **2005**, *72*, 066608. [CrossRef] [PubMed]
7. Lederer, F.; Stegeman, G.I.; Christodoulides, D.N.; Assanto, G.; Segev, M.; Silberberg, Y. Discrete solitons in optics. *Phys. Rep.* **2008**, *463*, 1–126. [CrossRef]
8. Ben, R.I.; Cisneros, A.L.; Minzoni, A.A.; Panayotaros, P. Localized solutions for a nonlocal discrete NLS equation. *Phys. Lett. A* **2015**, *379*, 1705–1714. [CrossRef]
9. Ben, R.I.; Borgna, J.P.; Panayotaros, P. Properties of some breather solutions of a nonlocal discrete NLS equation. *Comm. Math. Sci.* **2017**, *15*, 2143–2175. [CrossRef]
10. Kartashov, Y.V.; Vysloukh, V.A.; Torner, L. Soliton modes, stability, and drift in optical lattices with spatially modulated nonlinearity. *Opt. Lett.* **2008**, *33*, 1747–1749. [CrossRef]
11. Abdullaev, F.K.; Brazhnyi, V.A. Solitons in dipolar Bose–Einstein condensates with a trap and barrier potential. *J. Phys. B At. Mol. Opt. Phys.* **2012**, *45*, 085301. [CrossRef]
12. Efreimidis, N.K. Nonlocal lattice solitons in thermal media. *Phys. Rev. A* **2008**, *77*, 063824. [CrossRef]
13. Qin, J.; Dong, G.; Malomed, B.A. Matter-wave—Microwave solitons produced by the local-field effect. *Phys. Rev. Lett.* **2015**, *115*, 023901. [CrossRef]
14. Paredes, A.; Olivier, D.N.; Michinel, H. From optics to dark matter: A review on nonlinear Schrödinger–Poisson systems. *Physica D* **2020**, *403*, 132301. [CrossRef]
15. Assanto, G.; Smyth, N.F. Self-confined light waves in nematic liquid crystals. *Physica D* **2020**, *402*, 132182. [CrossRef]
16. Peccianti, M.; De Rossi, A.; Assanto, G.; De Luca, A.; Umeton, C.; Khoo, I.C. Electrically assisted self-confinement and waveguiding in planar nematic liquid crystal cells. *Appl. Phys. Lett.* **2000**, *77*, 7–9. [CrossRef]
17. Peccianti, M.; Assanto, G. Nematicons. *Phys. Rep.* **2012**, *516*, 147–208. [CrossRef]
18. Assanto, G.; Khan, C.; Smyth, N.F. Multi-hump thermo-reorientational solitary waves in nematic liquid crystals: Modulation theory solutions. *Phys. Rev. A* **2020**, submitted.
19. Laudyn, U.A.; Piccardi, A.; Kwasny, A.; Karpierz, M.A.; Assanto, G. Thermo-optic soliton routing in nematic liquid crystals. *Opt. Lett.* **2018**, *43*, 2296–2299. [CrossRef]
20. Alberucci, A.; Laudyn, U.A.; Piccardi, A.; Kwasny, A.; Klus, B.; Karpierz, M.A.; Assanto, G. Nonlinear continuous-wave optical propagation in nematic liquid crystals: Interplay between reorientational and thermal effects. *Phys. Rev. E* **2017**, *96*, 012703. [CrossRef]
21. Kohn, W. Analytic properties of Bloch waves and Wannier functions. *Phys. Rev.* **1959**, *115*, 809–821. [CrossRef]
22. Kramers, H.A. Das Eigenwertproblem im eindimensionalen periodischen Kraftfelde. *Physica* **1935**, *2*, 483. [CrossRef]
23. Pelinovsky, D.E. *Localization in Periodic Potentials: From Schrödinger Operators to the Gross-Pitaevskii Equation*; Cambridge Univ. Press: Cambridge, UK, 2011.
24. Reed, M.; Simon, B. *Methods of Modern Mathematical Physics IV*; Academic Press: New York, NY, USA, 1978.
25. Ziman, J.M. *Principles of the Theory of Solids*, 2nd ed.; Cambridge Univ. Press: Cambridge, UK, 1972.
26. Alfimov, G.L.; Kevrekidis, P.G.; Konotop, V.V.; Salerno, M. Wannier functions analysis of the nonlinear Schrödinger equation with a periodic potential. *Phys. Rev. E* **2002**, *66*, 046608. [CrossRef] [PubMed]
27. Pelinovsky, D.; Schneider, G. Bounds on the tight-binding approximation for the Gross-Pitaevskii equation with a periodic potential. *J. Diff. Eq.* **2010**, *248*, 837–849. [CrossRef]
28. Fibich, G. *The Nonlinear Schrödinger Equation: Singular Solutions and Optical Collapse*; Springer: New York, NY, USA, 2015.
29. Dohnal, T.; Lamacz, A.; Schweizer, B. Bloch-wave homogenization on large time scales and dispersive effective wave equations. *Multiscale Model. Simul.* **2014**, *12*, 488–513. [CrossRef]
30. Du, Q.; Engquist, B.; Tian, X. Multiscale modeling, homogenization and nonlocal effects: Mathematical and computational issues. *arXiv* **2019**, arXiv:1909.00708v1.
31. Borgna, J.P.; Panayotaros, P.; Rial, D.; Sánchez de la Vega, C. Optical solitons in nematic liquid crystals: Model with saturation effects. *Nonlinearity* **2018**, *31*, 1535. [CrossRef]
32. Borgna, J.P.; Panayotaros, P.; Rial, D.; Sánchez de la Vega, C. Optical solitons in nematic liquid crystals: Large angle model. *Physica D* **2020**, *408*, 132448. [CrossRef]
33. Panayotaros, P.; Marchant, T.R. Solitary waves in nematic liquid crystals. *Physica D* **2014**, *268*, 106–117. [CrossRef]

34. Bruno-Alfonso, A.; Nachbar, D.R. Wannier functions of isolated bands in one-dimensional crystals. *Phys. Rev. B* **2007**, *75*, 115428. [CrossRef]
35. Kapitula, T.; Promislow, K. *Spectral and Dynamical Stability of Nonlinear Waves*; Springer: New York, NY, USA, 2013.
36. Allen, G. Band structures of one-dimensional crystals with square-well potentials. *Phys. Rev.* **1953**, *91*, 531–533. [CrossRef]
37. Fečkan, M.; Rothos, V.M. Travelling waves of discrete nonlinear Schrödinger equations with nonlocal interactions. *Appl. Anal.* **2010**, *89*, 1387–1411. [CrossRef]

Article

Light-Induced Ring Pattern in a Dye-Doped Nematic Liquid Crystal

Marcel G. Clerc ^{1,*}, Gregorio González-Cortés ¹, Paulina I. Hidalgo ², Lucciano A. Letelier ¹,
Mauricio J. Morel ³ and Jorge Vergara ²

¹ Departamento de Física and Millennium Institute for Research in Optics, Facultad de Ciencias Físicas y Matemáticas, Universidad de Chile, Casilla 487-3, Santiago 851, Chile; gregorio.gonzalez@ug.uchile.cl (G.G.-C.); lucciano.letelier@ug.uchile.cl (L.A.L.)

² Departamento de Química Orgánica, Facultad de Ciencias Químicas, Universidad de Concepción, Concepción 129, Chile; pauhidal@udec.cl (P.I.H.); jovergar@udec.cl (J.V.)

³ Departamento de Química y Biología, Facultad de Ciencias Naturales, Universidad de Atacama, Ave. Copayapu, Copiapó 485, Chile; mauricio.morel@uda.cl

* Correspondence: marcel@dfi.uchile.cl; Tel.: +56-2-29784676

Abstract: The use of dye-doped liquid crystals allows the amplification of the coupling of light and liquid crystals. Light can induce the self-organization of the molecular order. The appearance of ring patterns has been observed, which has been associated with phase modulation. However, the morphology and dynamics of the ring patterns are not consistent with self-modulation. Based on an experimental setup with two parallel coherence beams orthogonal to a liquid crystal cell, one of which induces photo-isomerization and the other causes illumination, the formation of ring patterns is studied. To use these two coherent beams, we synthesize methylred methyl ester as a dye-dopant, which is photosensitive only to one of the light beams, and a commercial E7 liquid crystal as a matrix. Based on a mathematical model that accounts for the coupling between the concentration of the *cis*-state and the order parameter, we elucidate the emergence of the rings as forming patterns in an inhomogeneous medium. The bifurcation diagram is analytically characterized. The emergence, propagation of the rings, and the establishment of the ring patterns are in fair agreement with the experimental observations.

Keywords: photo-isomerization in liquid crystals; pattern formation; light-induced phenomena; azo-dye-dopant

Citation: Clerc, M.G.;

González-Cortés, G.; Hidalgo, P.I.;

Letelier, L.A.; Morel, M.J.; Vergara, J.

Light-Induced Ring Pattern in a
Dye-Doped Nematic Liquid Crystal.

Appl. Sci. **2021**, *11*, 5285. [https://](https://doi.org/10.3390/app11115285)

doi.org/10.3390/app11115285

Academic Editor: Gaetano Assanto

Received: 14 May 2021

Accepted: 1 June 2021

Published: 7 June 2021

Publisher's Note: MDPI stays neutral with regard to jurisdictional claims in published maps and institutional affiliations.



Copyright: © 2021 by the authors. Licensee MDPI, Basel, Switzerland. This article is an open access article distributed under the terms and conditions of the Creative Commons Attribution (CC BY) license (<https://creativecommons.org/licenses/by/4.0/>).

1. Introduction

The interaction between light and matter has played a fundamental role in the understanding and characterization from the early stages of research [1]. Likewise, the interaction between light and matter has also been the basis of the development of technological elements such as mirrors, lenses, telescopes, microscopes, lasers, and waveguides, among others. The development of more coherent and monochromatic light sources (lasers) accompanied by materials that present stronger nonlinear responses has allowed the creation of a great variety of devices [2–6]. Liquid crystals are one of the most versatile materials, because of their strong nonlinear response and reorientation capacity through the application of electromagnetic waves and electric and magnetic fields [7–11]. Liquid crystals are a state of matter in which the molecules have a preferential orientation and can have or not have a positional order; this organization is also known as soft matter [7–11]. Indeed, this state of matter shares features of solids and liquids. In particular, fluidity, molecular reorientation, and birefringence are characteristic properties of liquid crystals. One of the most studied types of liquid crystals used in technological applications are nematic liquid crystals (NLC). This state is composed of rod-like organic molecules [7–11]. Because of an intermolecular interaction, these molecules are arranged to have a similar molecular

orientation without positional order for specific temperature ranges. This results in a sharp anisotropy of all their physical properties, especially regarding elastic and optical characteristics. Likewise, the ability to reorient the molecular order has allowed the development of many applications, mainly liquid crystal displays (LCDs) and sensors [12]. The LCD is perhaps the best known liquid crystal application by the public today. However, in most of these applications, the control of molecular reorientation is done through electric fields. LCDs therefore require transparent or reflective electrodes, power sources, and other elements. Another manner of achieving molecular reorientation is to consider the application of electromagnetic waves through the liquid crystal sample [13–17]. However, this type of strategy requires the use of strong electromagnetic fields, which typically need a power on the order of 100 W/cm^2 . For these powers, the nonlinear response of the medium is activated [11,18]. The previous scenario can change radically when one considers the dye-dopant inside the liquid crystal matrix. Indeed, when nematics are doped with azo-dyes, their nonlinear response to opto-electrical perturbations is increased by several orders of magnitude [11,18]. Indeed, azo-dyes mediate the origin of the coupling of the electromagnetic waves with the liquid crystal; when these molecules are irradiated, they present an isomeric transition. This phenomenon is known as the Jánossy effect [19]. This transition is characterized by the fact that the molecule changes from an elongated structure (*trans*-state) to one with a boomerang shape (*cis*-state) when the molecule absorbs a photon. Figure 1 illustrates the typical structure of these molecules.

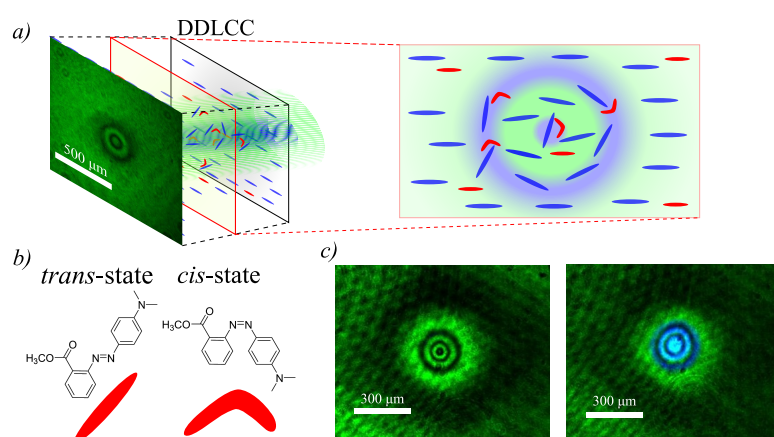


Figure 1. Ring patterns induced by light in a dye-doped liquid crystal cell (DDLCC). (a) Schematic representation of the experimental system. The blue and red bars, respectively, account for the molecules of the liquid crystal and azo-dye. The cell is illuminated by a blue and green beam. The snapshot accounts for the observed ring patterns. A transversal plane in the DDLCC is schematically represented. The areas under higher blue laser irradiation are more disordered, while the zones less illuminated preserve the nematic order. (b) Isomers of the molecule methyl red methyl ester. (c) Two snapshots showing the observed pattern (upper panel) and snapshot with the beam that induces photo-isomerization superimposed (bottom panel).

When a sufficiently intense light beam illuminates a thin film of dye-doped nematic liquid crystal, this can induce molecular disorder, generating a transition from a nematic phase to an isotropic one [20]. This type of transition is characterized by the emergence of a front between phases [20]. These fronts are characterized by being a circular spot that gathers in the center of the beam and spreads outwards and stops in the region where both states are energetically equivalent, Maxwell point. For intermediate light intensities, which do not induce isotropic liquid phase, the emergence of a pattern with a stripe shape has been reported [21,22]. In fact, these patterns correspond to regions that alternate higher and lower orientational molecular order. This phenomenon is understood as a result of the different scales in the transport processes of the concentration of the *cis* state and the orientational order of the liquid crystal. Thin films of liquid crystals without dye-

dopants subjected to strong electromagnetic fields in their cross section exhibit diffraction rings [14,23]. The above phenomenon is associated with phase modulation or autofocusing of light when is diffracted in the NLC. This medium is a good approximation to a Kerr medium [2–6,24], that is, the envelope of the light is under the effect of phase modulation, a cubic term for the envelope and diffraction. Hence, the conjunction of diffraction and phase modulation produces the emergence of diffraction rings. Note that the thickness of the observed rings decreases with the square distance from the center of the light beam. A similar phenomenon is observed in dye-doped liquid crystals when subjected to a coherent light with a moderate and low light intensity [25–27]. Because of the presence of dye-dopants, the nonlinear response can be achieved for light power of a few milliwatts [28]. The emergence of these rings has been associated with phase modulation. However, the morphology and dynamics of the ring patterns are not consistent with that expected for self-modulation rings observed for large intensities of light [14,23]. Furthermore, in this type of description, the dynamical behavior of the *cis* state concentration is passive. In other words, this concentration is enslaved to the system dynamics.

The article aims to elucidate and characterize the origin of the ring patterns observed when illuminating a dye-doped nematic liquid crystal cell with a light beam and planar anchoring. Based on an experimental setup with two parallel coherent beams, one of which induces photo-isomerization and the other the illumination, the formation of ring patterns is studied. Figure 1 illustrates the typical observed ring patterns. This type of setup allows us to separate the induction of the photo-isomerization and the observation of the self-organized patterns. To use these two coherent beams, we have synthesized methyl red methyl ester as dye-dopant, photo sensitive only to one of the light beams, and a commercial E7 (Instec Inc., Boulder, CO, USA) as a liquid crystal matrix. The methylred methyl ester was used as a dye-dopant (cf. Figure 1). Unlike methylred, the methylred methyl ester is more soluble and less viscous in E7 due to the absence of hydrogen bonds from the carboxylic acid group of the methylred. In addition, this structural modification prevents an intramolecular hydrogen bonding interaction with one of the nitrogens of the azo group, causing a faster *cis-trans* isomerization [29]. Theoretically, based on a mathematical model that accounts for the coupling between the concentration of the *cis* state and the order parameter, we elucidate the emergence of the rings as forming patterns in an inhomogeneous medium. The bifurcation diagram is analytically characterized. The emergence, propagation, and establishment of the ring patterns are in fair agreement with the experimental observations.

2. Experimental Observations of the Ring Patterns

The conventional phototropic transition detection is performed by sampling the excitation laser beam and extracting the reorientational order parameter with polarized optical microscopy [19–23,30]. The main inconvenience with those setups arises from the loss of information of the liquid crystal dynamics outside of the central Gaussian illuminated zone. Hence, the impossibility of differentiating between polarization changes in the light filtered out by the analyzer and the absorbed light by the sample. To overcome these difficulties, we developed an experimental setup with two parallel coherent beams applied to the dye-doped liquid crystal sample, which is only photo-sensitive to one beam (excitation beam) while the other is harmless (probing beam).

2.1. Experimental Setup

Figure 2 shows the experimental setup diagram. The dye-doped liquid crystal cell (DDLCC) undergoes a phototropic transition when it is irradiated by a light source in the absorption band of the guest dye [19,31]. We used a concentration of methylred methyl ester 1 wt% as azo-dye guest doping a commercially available E7 NLC (host). The chemical structure and isomers of methylred methyl ester are illustrated in Figure 1c. The absorption spectrum of the methylred methyl ester is depicted in Figure 2b (for details about the chemical synthesis and depuration of the azo-colorant, see Section 2.2).

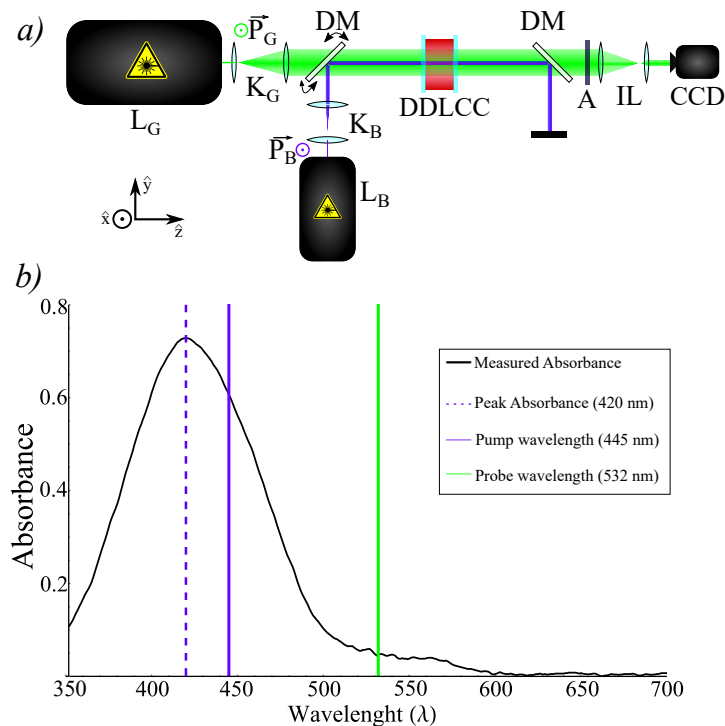


Figure 2. Experimental setup for the dye-doped nematic liquid crystal phototropic transition with a harmless external illumination. (a) A dye-doped liquid crystal cell (DDLCC) is irradiated by a 445 nm blue laser (excitation light beam) L_B and illuminated by a 532 nm green laser (probing light beam) L_G . Two pairs of lenses are placed in a Kepler telescope configuration K_B and K_G to expand the laser beam while preserving the collimation. \vec{P}_B and \vec{P}_G are the polarization of the laser sources. A long-wave pass dichroic mirror DM is used to set both excitation and probing on the same optical line. After the DDLCC, another long-wave pass dichroic mirror is used to filter out the excitation beam. An analyzer in a crossed configuration with respect to \vec{P}_G . A set of imaging optics IL consisting on a $\times 2$ Kepler telescope and a $\times 7$ zoom lens is used to enhance the image captured by the $1/2''$ CCD camera. (b) Absorption spectrum of methyl red methyl ester in dichloromethane 2.0×10^{-5} mol/L. The solid vertical lines account for the wavelength of the exciting and probing light, respectively. Vertical dashed lines account for the absorption maximum.

The mixture was injected into an antiparallel planarly aligned liquid crystal cell with a thickness of $25 \mu\text{m}$ (Instec Inc., Boulder, CO, USA). A 445 nm Cobolt 90 nW Polarized Laser was used as an exciting irradiation source to generate a phototropic transition. The polarization \vec{P}_B was fixed, and the laser power was used as a tuning or bifurcation parameter. Note that the blue laser wavelength was close to the absorbance peak at 420 nm, enabling us to trigger the isomerization and increase the amount of *cis* methyl red methyl ester isomer. There was no relevant temperature change in the DDLCC. The experiment was conducted at room temperature, approximately 20°C . This meant that only an increase of the *cis*-isomer concentration was responsible for a decrease of birefringence on the liquid crystal. A Kepler telescope K_B with a magnification of $\times 1/5$ was used to change the waist of the blue laser. The orientational molecular order in the dye-doped liquid crystal interacted with the blue light, making blue light sampling unsuitable for scanning the optical response of the liquid crystal sample.

To uncouple the excitation and probing fields, we provided illumination with a 532 nm Verdi V-2 polarized green laser as a probing light. Indeed, the absorbance at 532 nm is negligible for methyl red methyl ester, as seen in Figure 2. Both the green laser polarization \vec{P}_G and its intensity were set fixed. A Kepler telescope with a magnification of $\times 2$ was used to expand the beam and obtain a more homogeneous illumination. A long-pass dichroic mirror DM (cutoff wavelength at 500 nm) was mounted in a pitch-yaw kinematic mount to

control the reflection angle and thus the position of the blue laser on the DDLCC. A second dichroic mirror was used to filter out the excitation light from the optical path to the 1/2" CCD camera. To record the images, a set of illumination optics was used to enhance the image quality. A first pair of lenses in a Kepler telescope configuration with an optical zoom of $\times 2$ and a secondary zoom lens with a magnification of $\times 7$ was used. This system allowed us to achieve diffractionless recordings on the elements in the DDLCC plane, ensuring no diffractive rings on the images were recorded. Likewise, we displaced the liquid crystal cell parallel to the optical axis with respect to the dichroic mirrors, and no changes were observed in the ring patterns. This guaranteed that the observed phenomenon was not diffractive in nature. Figure 1b shows the probing illumination field in the upper panel, and the lower panel shows both the excitation and probing fields obtained by the CCD camera, respectively. The dynamical behavior of the order parameter could not be completely sampled only by measuring the excitation field. A set of imaging lenses was used to enhance the recorded images. In particular, we used a $\times 2$ magnification telescope coupled with a zoom lens and density filters. Notice that both excitation and probe illuminations were collimated when reaching the DDLCC. Thus, diffractive effects induced by changes in the position along the optical axis of the DDLCC were negligible. This meant that the position of the DDLCC was not a parameter of the experiment. The dynamics of the *cis* concentration and nematic order parameter did not depend on the cell position along the z axis, which was the axis of light propagation on the dye-doped liquid crystal cell.

2.2. Synthesis and Preparation of Dye-Dopant and Liquid Crystal Mixture

Dye-dopant: The methylred methyl ester was obtained from a Fischer–Spier esterification between methyl red (Sigma-Aldrich Inc., St. Louis, MO, USA) and methanol (Merck). The methanol was used as a reagent and solvent at reflux for 6 h with sulfuric acid (Merck) as a catalyst [32]. The final compound was characterized by Fourier Transform Infrared Spectroscopy, and the purity was confirmed by thin layer chromatography. The absorption spectrum of methyl red methyl ester was measured by employing a Spectroquant Pharo 300 spectrometer with a 1 cm optical path quartz cuvette in dichloromethane (Merck) solutions. The absorption spectrum is reported in Figure 2b).

Mixture preparation: The 1 wt% mixture was prepared by weighing each component and dissolving them separately into dichloromethane. The solutions were combined and homogenized by sonicating for 5 min. The solvent was removed by slow evaporation at room temperature.

2.3. Light-Induced Ring Patterns

When the dye-doped liquid crystal cell was illuminated with a probing light, the monitoring CCD camera showed a homogeneous dark greenish color throughout the cell, as illustrated in the snapshot of Figure 3b at t_0 . When applying the blue light beam, we observed that the illuminated area immediately began to transmit more light. Figure 3a illustrates how the total transmitted intensity measured in the green channel of the CCD camera (ΔI_g) evolved over time with respect to the transmitted light without the blue light beam ($I_{g,0}$). The temporal evolution of the detected light intensity was characterized by growth and subsequent saturation. Figure 3a shows two regions in which the growth (region I) and saturation region (II) could be distinguished. In order to describe the growth and saturation process, we modeled it using the following expression: $\Delta I_g(t)/I_{g,0} = A(1 - e^{-t/\tau})$, where $A = 2.79$ and $\tau = 55.71$ s. Namely, the establishment of the stationary ring pattern required a time period on the order of one minute.

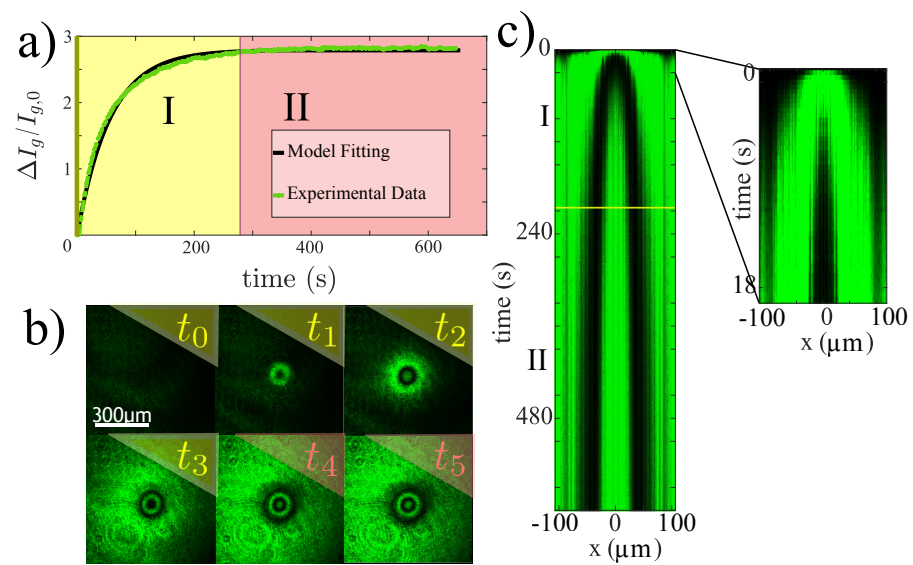


Figure 3. Experimental ring pattern emergence induced by a blue light (with a 445 nm wavelength) applied to a dye-doped liquid crystal cell, E7 NLC with azo-dye methyl red methyl ester at a concentration of 1 wt%. (a) Temporal evolution of transmitted total intensity, measured in the green channel of the CCD camera (ΔI_g) with respect to the transmitted light without the blue light beam ($I_{g,0}$). The points were obtained experimentally, and the continuous curve was acquired using the expression $\Delta I_g(t)/I_{g,0} = A(1 - e^{-t/\tau})$, where $A = 2.79$ and $\tau = 55.71$ s. Painted areas I and II account for the growth and saturation regions, respectively. (b) Temporal sequence of snapshots in the ring pattern formation process ($t_0 = 0$ s, $t_1 = 1$ s, $t_2 = 5$ s, $t_3 = 84$ s, $t_4 = 360$ s, and $t_5 = 570$ s). (c) Spatiotemporal diagram evolution of a diameter cut section.

When the blue light was applied, a region of light green with a darker center emerged; as time elapsed, this dark spot became a propagative ring. Note that the lightened region continued to grow, becoming even larger than the waist of the blue laser. Figure 1b compares the light green region to the waist size of the blue laser. As time continued to elapse, the dark ring continued to move away from the center, and a new dark spot emerged in the center, which then became a new dark ring. Figure 3b summarizes the temporal sequence of snapshots in the ring pattern formation process. In order to determine the process of spot emergence and ring propagation, we consider the spatiotemporal evolution of a diameter cut section. Figure 3c illustrates the observed spatiotemporal diagram evolution. From this chart, we see how the dark rings emerge, spread, and stop.

When we applied low powers of the blue laser (few mW, cf. Figure 4), the system did not show the formation of ring patterns, and we only observed the emergence of a light green spot. As the power was increased, this light green spot increased in size. With powers close to 40 mW, we began to observe the emergence of a dark spot in the center of the illuminated region (see Figure 4). Physically, we interpreted this region as a region of greater orientational disorder due to the consideration of the dye-doped liquid crystal sample between crossed polarizers. When we further increased the power of the blue laser, we observed the emergence of the first ring. Figure 4 shows the observed equilibrium ring. As the power increased, the diameter of the equilibrium ring grew. For powers close to 70 mW, we observed the emergence of a ring with a dark spot in the center as a state of equilibrium. As the power of the blue laser continued to increase, we observed that the central dark spot grew, and at a higher power, it became unstable, generating a new ring. Figure 4 summarizes the equilibria found for different blue laser powers.

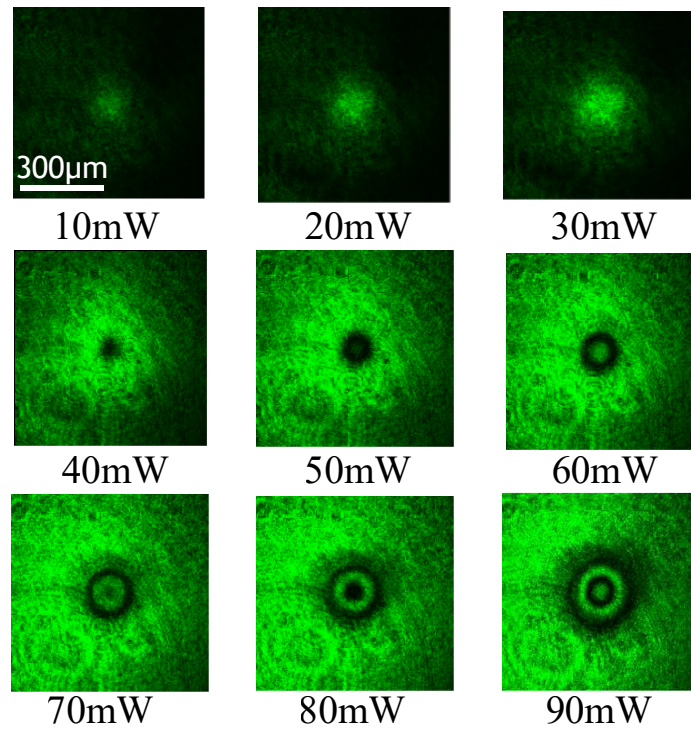


Figure 4. Equilibria ring patterns were experimentally observed for different powers of the blue light beam. After a long period of evolution, snapshots were observed for different powers, as denoted in the lower part of each snapshot.

3. Mathematical Modeling for Photo-Isomerization in Dye-Doped Liquid Crystals

Nematic liquid crystals are formed by rod-shaped molecules that—in a temperature range—can present an orientational rather than positional order. Then, the dynamics of the NLC can be described by a scalar order parameter $S(\vec{r}; t)$ that accounts for the alignment of the molecules along a given direction [7–9], defined by

$$S(\vec{r}; t) \equiv \frac{3\langle \cos^2 \theta \rangle - 1}{2}, \quad (1)$$

where the brackets $\langle \cdot \rangle$ mean the spatial average in a microscopic element volume at position \vec{r} and time t , and θ is the angle between the molecules and the local preferred direction [7–9]. Thus, S accounts for the dispersion of the molecules with respect to their average direction. The scalar order parameter for a perfectly aligned nematic phase is $S = 1$, and that for an isotropic phase is $S = 0$. Note that a negative and large S shows that the molecules are oriented, but the choice of the current orientation does not coincide with the molecular average orientation. Close to a phase transition, Landau conjectured that the free energy can be written as a polynomial expansion of the order parameter [33]. Based on this type of approach, in the Landau–de Gennes theory, the transition between a nematic and an isotropic liquid state in a thin film is described by the dimensionless equation [7]

$$\partial_t S(r_{\perp}, t) = -AS + BS^2 - S^3 + \nabla^2 S, \quad (2)$$

where r_{\perp} accounts for the transversal coordinate of the liquid crystal layer and A is the bifurcation parameter, which is proportional to the difference between the current and critical temperature. Note that for large values of A , the isotropic state is favored in comparison to the nematic state. B is a parameter that characterizes the size of the region of coexistence between the nematic and isotropic liquid state. The third and fourth terms on the right-hand side account for the nonlinear response of the medium and the spatial coupling of the order parameter, respectively. This coupling is diffusive in nature. Namely,

the flow of the order parameter is proportional to its gradient. This model predicts that the nematic and the isotropic liquid transition is of a subcritical nature. On the other hand, the concentration of molecules in the *cis*-state $C(\vec{r}, t)$ at position \vec{r} in time t satisfies a relaxation and diffusion equation of the form [19]

$$\partial_t C = -\lambda[C - C_0(I)] + \delta \nabla^2 C, \quad (3)$$

where λ is the decay rate related to the transition from a *cis* to *trans* state by thermal relaxation. $C_0(I)$ is the equilibrium concentration of molecules in the *cis* state that is proportional to the total intensity of the incident light I . Indeed, $C_0(I) \equiv \gamma I / (1 + \eta I)$, where γ and η are dimensional parameters [19]. δ is the diffusion coefficient of the concentration of the *cis* state. As a result of the propagation of light, the intensity of the light has the following form:

$$I = I_0 e^{-r_{\perp}^2 / w^2}, \quad (4)$$

where w and I_0 are the light beam waist and the light intensity at the beam's center, respectively.

As we have mentioned, the incorporation of dye-dopants increases the nonlinear response of liquid crystals under the excitation of external fields [11,18–20,34]. Since the dye-dopant is not a liquid crystal and may even be immiscible, its excessive inclusion can prevent the mixture from being a liquid crystal; thus, a dye-dopant should be used in small amounts. We note that one of the reasons for considering methyl red methyl ester is that it is more miscible in E7 than other dopants; for example, methyl red. To describe the dynamics of the photo-isomerization process in the dye-doped nematic layer with planar anchoring, let us consider the concentration of molecules in the *cis*-state $C(\vec{r}_{\perp}, t)$ and the scalar order parameter $S(\vec{r}_{\perp}, t)$, which satisfy the dimensionless rate equations [21,22]

$$\begin{aligned} \partial_t C &= -\lambda[C - C_0(I) + \alpha S] + \delta \nabla^2 C + D \nabla^2 S, \\ \partial_t S &= -(A + \beta C)S + BS^2 - S^3 + \nabla^2 S + D \nabla^2 C. \end{aligned} \quad (5)$$

The α parameter accounts for the reduction of the *cis*-state concentration when the liquid crystal molecules are more aligned (larger S) because the dye-dopants tend to be oriented in the direction of the molecules (transition from *cis* to *trans*) [19]. Indeed, the liquid crystal matrix tends to make the dye-dopants orient and stretch in the direction of the molecular order. The parameter β stands for the entropic effect of the photo-isomerization process; that is, by increasing the concentration of the *cis* molecules, the disordered or non-oriented state is favored. Then, the linear term in S must decrease if the dye-dopant concentration increases. The parameter D accounts for the mutual transport process; namely, a gradient in the dopant concentration induces the propagation of the order parameter [35].

In the limit of the large-scale separation between the order parameter S and the concentration of the *cis*-state ($\lambda \gg 1$) and for small α and intensity I , the *cis*-state concentration satisfies

$$C = C_0(I) \approx \gamma I = \gamma I_0 e^{-r_{\perp}^2 / w^2}. \quad (6)$$

Therefore, the *cis*-state concentration acquires a Gaussian profile. Using this expression in the equation of the order parameter, S satisfies the Landau–De-Gennes model for the nematic to isotropic transition induced by photo-isomerization [20]. Indeed, the bifurcation parameter $A(I) \equiv A + \beta \gamma I$ is controlled by the light intensity profile. When the sample is not illuminated, the system is in a NLC phase (S_+). When the sample is illuminated, the light can induce front propagation from the isotropic (S_{IS}) to the nematic phase [20].

3.1. Adiabatic Elimination and Effective Model

To determine the dynamics described by Equation (5), one can consider the adiabatic elimination of the *cis*-state concentration [36]. Indeed, by assuming that the temporal evolution of the *cis*-state concentration is rapid compared to the dynamics of the order

parameter—i.e., $\lambda \gg 1$ —and by using Neumann series, one can approach, in a dominant order, the *cis* concentration by

$$C \simeq C_0(I) - \alpha S + \frac{D - \alpha\delta}{\lambda} \nabla^2 S. \tag{7}$$

Introducing this expression in the equation for the order parameter S , at a dominant order, we obtain

$$\begin{aligned} \partial_t S &= -[A + \beta C_0(I)]S + (B - \alpha\beta)S^2 - S^3 + (1 - D\alpha)\nabla^2 S \\ &+ \frac{D(D - \alpha\delta)}{\lambda} \nabla^4 S + \frac{\beta}{\lambda} (D - \delta\alpha)S\nabla^2 S + D\nabla^2 C_0(I). \end{aligned} \tag{8}$$

Renormalizing the space $\vec{r} = \vec{r}'[\lambda/D(\delta\alpha - D)]^{1/4}$, the effective model reads

$$\partial_t S = -\tilde{A}S + \tilde{B}S^2 - S^3 - \nu\nabla^2 S - \nabla^4 S + bS\nabla^2 S + \tilde{\eta}, \tag{9}$$

where

$$\tilde{A}(\vec{r}') \equiv A + \beta C_0(I(\vec{r}')), \tag{10}$$

$$\tilde{B} \equiv (B - \alpha\beta), \tag{11}$$

$$\nu \equiv D\alpha - 1\sqrt{\frac{\lambda}{D(\delta\alpha - D)}}, \tag{12}$$

$$b \equiv \frac{\beta(D - \delta\alpha)}{\sqrt{\lambda D(\delta\alpha - D)}}, \tag{13}$$

$$\tilde{\eta}(\vec{r}') \equiv D\sqrt{\frac{\lambda}{D(\delta\alpha - D)}}\nabla^2 C_0(I). \tag{14}$$

The model in Equation (9) corresponds to a non variational Swift–Hohenberg-type equation [37,38]. This model has been used to study patterns [39,40], localized, stationary [37,41], and propagative structures [42,43], and spatiotemporal chaotic extended [40] and localized structures [44]. These phenomena have been studied in different contexts ranging from physics and chemistry to biology. The physical origin of the formation of spatial structures is due to the anti-diffusion coefficient ($\nu > 0$), which represents the different scales of the transport processes of the *cis* order and state parameter, which introduces an intrinsic characteristic scale: the Turing mechanism [45]. Namely, by having two transport processes with different scales, the system cannot propagate the order parameter and the *cis*-state homogeneously; thus, it self-organizes, forming patterns.

3.2. Homogeneous Illumination and Bifurcation Diagram

Considering a spatially homogeneous illumination—that is, C_0 is a constant—the parameters that characterize the nematic and isotropic liquid transition are renormalized and independent of the space. The effective model has the form

$$\partial_t S = -\tilde{A}S + \tilde{B}S^2 - S^3 - \nu\nabla^2 S - \nabla^4 S + bS\nabla^2 S. \tag{15}$$

The homogeneous phases of this model have the form $S_0 = 0$ and

$$S_{\pm} = \frac{\tilde{B} \pm \sqrt{\tilde{B}^2 - 4\tilde{A}}}{2}, \tag{16}$$

where S_0 and S_{\pm} account for the liquid isotropic and nematic phase. For high temperatures—i.e., a large \tilde{A} —it is expected that the only stable state is the isotropic liquid phase S_0 . When decreasing \tilde{A} , the system presents a coexistence between the isotropic and nematic phase for $\tilde{A} = A_{sn} \equiv \tilde{B}^2/4$. This bifurcation occurs due to the emergence of two new equilibria:

the saddle-node bifurcation causes the emergence of a stable nematic state (S_+) and an unstable state (S_-). Figure 5 shows the bifurcation diagram of the model in Equation (15). As \tilde{A} continues to decrease, the isotropic liquid state S_0 is as favorable as the nematic phase S_+ for $A = A_M \equiv 2\tilde{B}^2/9$ —the Maxwell point [46]. Then, a flat wall between these two phase states at this critical point is characterized by being motionless. When further decreasing \tilde{A} , the isotropic liquid phase presents a spatial instability. We can study this instability by linearizing Equation (15) around the isotropic liquid state $S_0 = 0$, and considering the ansatz $S(\vec{r}, t) = S' e^{i\vec{k}\vec{r} + i\sigma t}$, we obtain the growth rate equation:

$$\sigma = -\tilde{A} + \nu\vec{k}^2 - \tilde{k}^4, \tag{17}$$

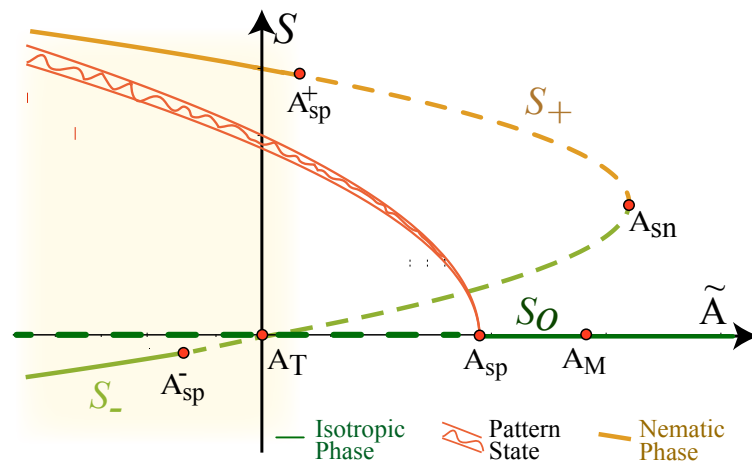


Figure 5. Schematic representation of the bifurcation diagram of the effective model in Equation (15) with constant coefficients. The order parameter S as a function of the bifurcation parameter \tilde{A} . S_0 , S_+ , and S_- account for the isotropic liquid and nematic phases, respectively. The continuous and dashed lines account for stable and unstable states respectively. A_{sn} , A_M , and A_T are the critical points that account for the emergence of the nematic phase; both phases are equally favored, with a transcritical bifurcation of the isotropic liquid phase. A_{sp} , A_{sp}^+ , and A_{sp}^- account for the spatial instabilities of the homogeneous phases. The painted area shows the region of coexistence between the periodic state and the homogeneous state. The decorated curve explains the amplitude of the patterns.

The instability condition is $d\sigma(k_c)/dk = 0$ and $\sigma(k_c) = 0$. The first condition determines the critical length $k_c = \sqrt{\tilde{k}^2} \equiv \sqrt{\nu/2}$, and the second defines the critical relation of the parameters for the spatial instability, which has the form $\tilde{A} = A_{sp} \equiv \nu^2/4$. Weakly nonlinear analysis shows that this instability is of a supercritical nature for a small \tilde{B} . Thus, despite the fact that the linear term is positive, $0 < \tilde{A} < A_{sp}$, the isotropic liquid state is unstable. For $\tilde{A} = A_T \equiv 0$, the system presents a transcritical bifurcation between unstable states.

To study the stability of the nematic phase, we use a similar strategy as in the study of the spatial stability of the isotropic liquid phase. Let us consider the linear perturbation $S = S_{\pm} + \chi$, where χ is a small variable that satisfies the equation

$$\partial_t \chi = (-\tilde{A} + 2\tilde{B} - 3S_{\pm}^2)\chi - (\nu + bS_{\pm})\nabla^2 \chi - \nabla^4 \chi. \tag{18}$$

Introducing the ansatz $\chi(\vec{r}, t) = \chi' e^{i\vec{k}\vec{r} + i\sigma t}$ in the above equation, we obtain

$$\sigma = -\tilde{A} + 2\tilde{B} - 3S_{\pm}^2 + (\nu + bS_{\pm})\tilde{k}^2 - \tilde{k}^4. \tag{19}$$

Imposing the spatial instability conditions, we obtain $k_c = \sqrt{\tilde{k}^2} = \sqrt{(\nu + bS_{\pm})/2}$ and

$$2\tilde{A} + \tilde{B}S_{\pm} = -\frac{(\nu + bS_{\pm})^2}{4}. \tag{20}$$

From this expression, we obtain two critical conditions for spatial instability A_{sp}^+ and A_{sp}^- corresponding to each of the nematic states (see Figure 5). Therefore, the effective model predicts a region of coexistence between a pattern state and a nematic phase. Figure 5 shows this region of coexistence with a painted area.

3.3. Light-Induced Ring Pattern

Figure 5 summarizes the different behaviors presented by the model in Equation (15). From this chart, we conclude that the system has a coexistence region between the nematic state and the pattern. Note that this pattern alternates between areas of higher and lower orientation order [21,22]. This affects the sample's refractive index; therefore, if a light beam passes through the sample in a patterned state, one expects to observe interference fringes. As the light intensity increases, the bifurcation parameter \tilde{A} grows. Then, if one considers a light intensity with a Gaussian profile, the parameter $\tilde{A}(I)$ is characterized by being inhomogeneous, with a bell-like shape. Thus, if the cell is in a nematic phase when the sample is illuminated, the central part of the light beam can induce the cell to leave the coexistence region, and only the pattern will be stable. For this type of region, we would expect to find that the illuminated area shows patterns because the central area of the light beam is circular, and for a small-waist beam, one would expect to see ring-like patterns. Figure 6 shows the typical equilibrium ring pattern observed numerically for the model Equation (9). All numerical simulations presented are obtained by considering finite differences coded with the Runge–Kutta order-4 algorithm.

If the system is not illuminated, $I_0 = 0$, the uniform nematic phase is the equilibrium of the system. By illuminating the system with a low intensity, we found numerically that there was a slight decrease in the reorientation order and an increase in the *cis* concentration in the central part of the Gaussian (cf. Figure 7). As the intensity I_0 increased, the size of the central spot showed greater orientation disorder; that is, the order parameter S decreased in the central zone as I_0 increased. Note that the spot of the orientational disorder was smaller than the waist of the Gaussian forcing. As I_0 increased in the central zone, the parameter of order S approached zero (isotropic liquid). When it hit zero, it generated a new dynamical behavior; the central point expanded, creating a ring. The origin of the clearing out of the central zone was due to the fact that the order parameter S became negative. This could be interpreted as two ordered regions separated by a circular interface of the disordered state. A dark ring in Figure 7 represents this region. As I_0 increased further, the ring continued to expand. By further increasing the intensity of the Gaussian forcing, we observed the emergence of a new central spot surrounded by a ring. Note that for this parameter region, when beginning with a uniform nematic state and applying Gaussian forcing, a central spot of disorder state initially emerged that expanded, forming a ring that continued to propagate; later, another central spot of disorder state emerged, and finally the ring pattern stopped and remained in a stationary state. Experimentally, we observed a similar behavior to that observed numerically (see Figure 3). As the intensity of the Gaussian forcing I_0 increased further, new central spots emerged, which became new rings of disordered states (see Figure 7). The waist of the light beam limits the above process. This process is similar to the experimental process (see Figure 3).

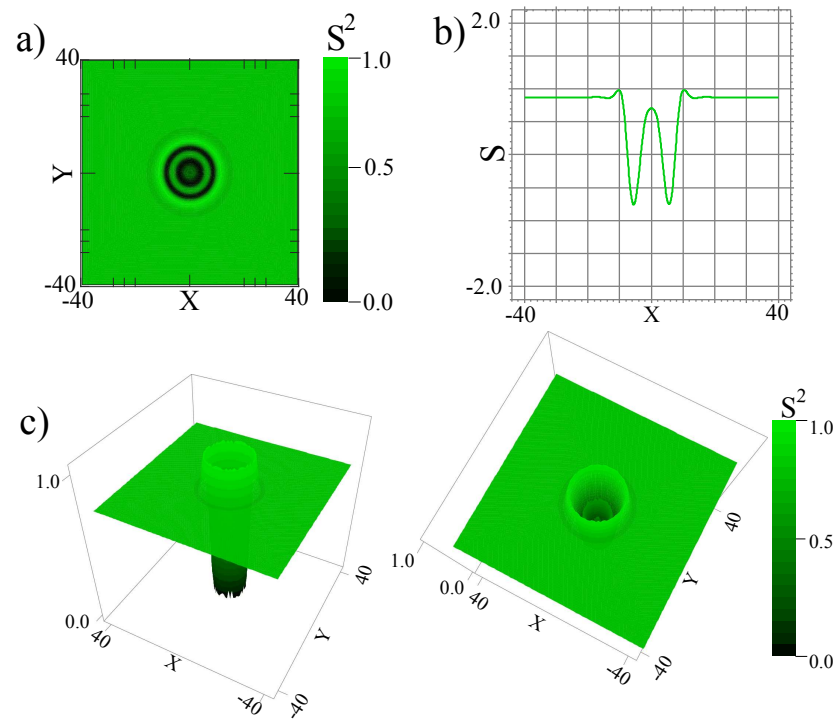


Figure 6. Numerical stationary ring pattern in a dye-doped nematic liquid crystal using the effective model in Equation (9) for $\tilde{A} = -0.5$, $\tilde{B} = 0.3$, $\nu = 1.05$, $b = 0.1$, $I_0 = 1.45$, and $w = 4$. (a) Contour plot of the squared order parameter S . (b) Profile of the cut of the order parameter S in the diameter of the ring pattern. (c) Surface plot of the squared order parameter S .

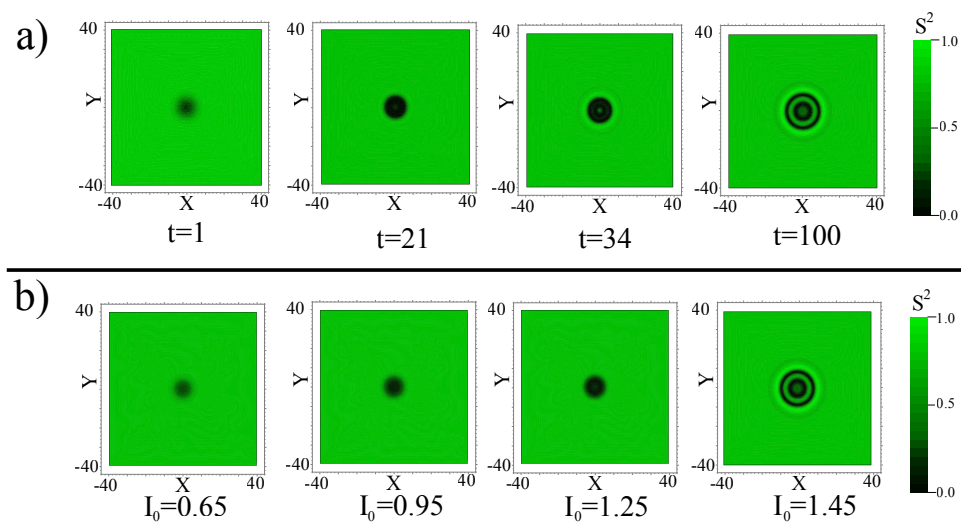


Figure 7. Numerical light-induced ring pattern in a dye-doped nematic liquid crystal using the model in Equation (9). (a) Temporal evolution of ring pattern using the effective model in Equation (9) for $\tilde{A} = -0.5$, $\tilde{B} = 0.3$, $\nu = 1.05$, $b = 0.1$, $I_0 = 1.45$, and $w = 4$. (b) Equilibrium of ring patterns numerically obtained for a different forcing strength I_0 , and the other parameters are $\tilde{A} = -0.5$, $\tilde{B} = 0.3$, $\nu = 1.05$, $b = 0.1$, and $w = 4$.

In brief, the effective model in Equation (9) described the dynamics of the light-induced ring pattern in a dye-doped nematic liquid crystal well in qualitative terms.

4. Discussion

The emergence of ring patterns from an illuminated dye-doped nematic liquid crystal cell was initially attributed to the phase modulation of the diffractive light [27]. The light diffraction process is mathematically described by the nonlinear Schrödinger equation, which corresponds to the paraxial equation with a nonlinear correction associated with phase modulation. A local disturbance of the homogeneous state is characterized by the emergence of propagative rings towards the outside of the disturbance; these propagative rings are concentric with different thicknesses and decay with the square of the distance. In turn, the outer ring generates the emergence of outer rings with an increasingly smaller thickness. This type of pattern is similar to those reported for liquid crystal samples subjected to intense light rays [23]. The morphology of the ring pattern and the exhibited dynamics are different from those observed experimentally in the dye-doped nematic liquid crystal sample (see Figures 3 and 4).

The patterns found may allow manipulable interferometric patterns for light rays outside the absorption range of the dye-dopant. To illustrate the manipulability of the ring patterns, we adjusted the pitch and yaw of the dichroic mirror. Figure 8 schematizes the modification of the dichroic mirror, the effect on the light beam, and the observed ring patterns. Then, the light beam inside the doped liquid crystal sample could be shifted. Experimentally, we observed from the ring pattern in equilibrium that it moved almost rigidly. Figure 8b shows the light path scheme used and the ring patterns observed at the points marked on the path by discs. Likewise, it is important to note that the previous results showed that an interference mechanism does not cause the observed ring patterns. Note that the ring patterns caused by phase modulation were deformed with the angle of incidence [14], which is different from the observations in our setup (see Figure 8).

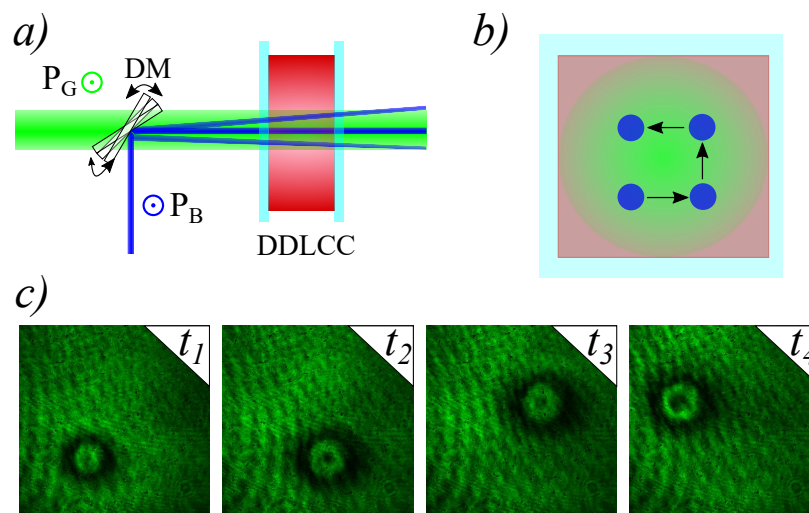


Figure 8. Manipulable ring patterns induced by illumination on a dye-doped liquid crystal sample. (a) Schematic representation of the mechanism for applying the light beam to the dye-doped liquid crystal sample. (b) Schematic representation of the path made by the light beam by adjusting the pitch and yaw of the dichroic mirror. (c) Snapshots of ring patterns observed at different times ($t_1 < t_2 < t_3 < t_4$).

5. Conclusions

Experimentally and theoretically, we have elucidated and characterized the origin of the ring patterns observed in a dye-doped nematic liquid crystal cell with planar anchoring under a light beam in the absorption band of the dye-dopant. To shed light onto the effect of the coherent excitation beam, we designed an experimental setup that considered two parallel beams—exciting and probing light—in which the probing light was monitored.

Based on a mathematical model that accounted for the coupling between the concentration of the *cis*-state and the orientational order parameter, we established the emergence of the rings as forming patterns in an inhomogeneous medium. Namely, the origin of the formation of pattern rings is due to the different scales and transport mechanisms of the concentration of the *cis*-state and the orientational order parameter. The formation of spatial structures induced by light can open up new applications such as the harnessing of diffraction gratings, masks, and irises. Work in this direction is in progress.

Author Contributions: Conceptualization, M.G.C. and G.G.-C.; methodology, G.G.-C., P.I.H., M.J.M. and J.V.; numerical analysis, L.A.L.; validation, G.G.-C. and L.A.L.; formal analysis, M.G.C. and L.A.L.; writing—original draft preparation, M.G.C.; improvement and verification of the manuscript, all authors. All authors have read and agreed to the published version of the manuscript.

Funding: This research was funded by FONDECYT grant number 1210353, the National Agency for Research and Development (ANID) Scholarship Program Becas Doctorado Nacional 2017211716, and ANID–Millennium Science Initiative Program-ICN17_012.

Institutional Review Board Statement: Not applicable.

Informed Consent Statement: Not applicable.

Acknowledgments: The authors acknowledge the fruitful discussions with Raouf Barboza.

Conflicts of Interest: The authors declare no conflict of interest.


References

- Newton, I. *Opticks, or, a Treatise of the Reflections, Refractions, Inflections & Colours of Light*; Sam. Smith and Benj. Walford, Printers to the Royal Society: London, UK, 1704.
- Boyd, R.W. *Nonlinear Optics*; Academic Press: San Diego, CA, USA, 2003.
- Shen, Y.R. *The Principles of Nonlinear Optics*; Wiley-Interscience: New York, NY, USA, 1984.
- Mills, D.L. *Nonlinear Optics: Basic Concepts*; Springer Science & Business Media: Berlin/Heidelberg, Germany, 2012.
- New, G. *Introduction to Nonlinear Optics*; Cambridge University Press: Cambridge, UK, 2011.
- Lugiato, L.; Prati, F.; Brambilla, M. *Nonlinear Optical Systems*; Cambridge University Press: Cambridge, UK, 2015.
- De Gennes, P.G.; Prost, J. *The Physics of Liquid Crystals*, 2nd ed.; Oxford Science Publications, Clarendon Press: Oxford, UK, 1993.
- Chandrasekhar, S. *Liquid Crystal*; Cambridge University Press: New York, NY, USA, 1992.
- Oswald, P.; Pieranski, P. *Nematic and Cholesteric Liquid Crystals*; CRC Press: Boca Raton, FL, USA, 2005.
- Vertogen, G.; de Jeu, W.H. *Thermotropic Liquid Crystals, Fundamentals*; Springer Science & Business Media: Berlin/Heidelberg, Germany, 2012.
- Khoo, I.C. *Liquid Crystals*; John Wiley & Sons: Hoboken, NJ, USA, 2007.
- Takatoh, K.; Sakamoto, M.; Hasegawa, R.; Koden, M.; Itoh, N.; Hasegawa, M. *Alignment Technology and Applications of Liquid Crystal Devices*; CRC Press: Abingdon, UK, 2005.
- Zel'Dovich, B.Y.; Pilipetskii, N.F.; Sukhov, A.V.; Tabiryan, N.V. Giant Optical Nonlinearity in the Mesophase of a Nematic Liquid Crystal. *JETP Lett.* **1980**, *31*, 263–267.
- Zolot'ko, A.S.; Kitaeva, V.F.; Sobolev, N.K.N.; Chillag, L. The effect of an optical field on the nematic phase of the liquid crystal OCBP. *JETP Lett.* **1980**, *32*, 158–162.
- Zolot'ko, A.S.; Kitaeva, V.F.; Sobolev, N.N.; Sukhorukov, A.P. Self-focusing of laser radiation in the course of the Fréedericksz transition in the nematic phase of a liquid crystal. *Zh. Eksp. Teor. Fiz.* **1981**, *81*, 933–941.
- Durbin, S.D.; Arakelian, S.M.; Shen, Y.R. Optical-field-induced birefringence and Freedericksz transition in a nematic liquid crystal. *Phys. Rev. Lett.* **1981**, *47*, 1411–1414. [CrossRef]
- Frissen, B.J.; Palffy-Muhoray, P. Electric-field-induced twist and bend Freedericksz transitions in nematic liquid crystals. *Phys. Rev. A* **1989**, *39*, 1513–1518. [CrossRef]
- Khoo, I.C. Nonlinear optics of liquid crystalline materials. *Phys. Rep.* **2009**, *471*, 221–267. [CrossRef]
- Jánossy, I.; Szabados, L. Photoisomerization of azo-dyes in nematic liquid crystals. *J. Nonlinear Opt. Phys.* **1998**, *7*, 539–551. [CrossRef]
- Odent, V.; Clerc, M.G.; Falcón, C.; Bortolozzo, U.; Louvergneaux, E.; Residori, S. Photo-isomerization fronts in dye-doped nematic liquid crystals. *Opt. Lett.* **2014**, *39*, 1861–1864. [CrossRef]
- Andrade-Silva, I.; Bortolozzo, U.; Clerc, M.G.; González-Cortés, G.; Residori, S.; Wilson, M. Spontaneous light-induced Turing patterns in a dye-doped twisted nematic layer. *Sci. Rep.* **2018**, *8*, 1–8. [CrossRef]
- Andrade-Silva, I.; Bortolozzo, U.; Castillo-Pinto, C.; Clerc, M.G.; González-Cortés, G.; Residori, S.; Wilson, M. Dissipative structures induced by photoisomerization in a dye-doped nematic liquid crystal layer. *Phil. Trans. R. Soc. A* **2018**, *376*, 20170382. [CrossRef]

23. Durbin, S.D.; Arakelian, S.M.; Shen, Y.R. Laser-induced diffraction rings from a nematic-liquid-crystal film. *Opt. Lett.* **1981**, *6*, 411–413. [CrossRef]
24. Assanto, G. *Nematicons: Spatial Optical Solitons in Nematic Liquid Crystals*; John Wiley & Sons: Hoboken, NJ, USA, 2012.
25. Barnik, M.I.; Zolot'ko, A.S.; Kitaeva, V.F. Interaction of light with a dye-doped nematic liquid crystal. *J. Exp. Theor. Phys.* **1997**, *84*, 1122–1130. [CrossRef]
26. Deng, L.; He, K.; Su, W.; Sun, H.; Wang, R.; Zhang, H.; Liu, H.K. Optical limiting performances of the methyl-red-dye-doped nematic liquid crystal films. *Mater. Devices Syst. Disp. Lighting* **2002**, *4918*, 79–89.
27. Li, H.; Wang, J.; Wang, C.; Zeng, P.; Cai, P.; Pan, Y.; Yang, Y. Off-resonant nonlinear optical refraction properties of azo dye doped nematic liquid crystals. *Opt. Mater. Express* **2016**, *6*, 459–465. [CrossRef]
28. Serak, S.V.; Tabiryany, N.V.; Assanto, G. Nematicons in azobenzene liquid crystals. *Mol. Cryst. Liq. Cryst.* **2012**, *559*, 202–213. [CrossRef]
29. Park, H.S.; Oh, K.S.; Kim, K.S.; Chang, T.; Spiegel, D.R. Change of internal hydrogen bonding of methyl red upon photoisomerization monitored by Forced Rayleigh Scattering. *J. Phys. Chem. B* **1999**, *103*, 2355–2360. [CrossRef]
30. Castillo-Pinto, C.; Clerc, M.G.; González-Cortés, G. Extended stable equilibrium invaded by an unstable state. *Sci. Rep.* **2019**, *9*, 1–8. [CrossRef] [PubMed]
31. Kosa, T.; Sukhomlinova, L.; Su, L.; Taheri, B.; White, T.J.; Bunning, T.J. Light-induced liquid crystallinity. *Nature* **2012**, *485*, 347–349. [CrossRef]
32. Kahl, D.J.; Hutchings, K.M.; Lisabeth, E.M.; Haak, A.J.; Leipprandt, J.R.; Dexheimer, T.; Khanna, D.; Tsou, P.S.; Campbell, P.L.; Fox, D.A.; et al. 5-Aryl-1,3,4-oxadiazol-2-ylthioalkanoic Acids: A Highly Potent New Class of Inhibitors of Rho/Myocardin-Related Transcription Factor (MRTF)/Serum Response Factor (SRF)-Mediated Gene Transcription as Potential Antifibrotic Agents for Scleroderma. *J. Med. Chem.* **2019**, *62*, 4350–4369. [CrossRef]
33. Landau, L.D.; Lifshitz, E.M. *Statistical Physics (Course of Theoretical Physics, Volume 5)*; Pergamon Press: New York, NY, USA, 1993.
34. Sasaki, T.; Ikeda, T. Photochemical switching of polarization in ferroelectric liquid crystals: Effect of structure of host FLCs. *Ferroelectrics* **1993**, *149*, 343–351. [CrossRef]
35. Bechhoefer, J.; Simon, A.J.; Libchaber, A.; Oswald, P. Destabilization of a flat nematic-isotropic interface. *Phys. Rev. A* **1989**, *40*, 2042–2056. [CrossRef] [PubMed]
36. Haken, H. *Synergetics: Introduction and Advanced Topics*; Springer: Berlin/Heidelberg, Germany, 1977.
37. Clerc, M.G.; Petrossian, A.; Residori, S. Bouncing localized structures in a liquid-crystal light-valve experiment. *Phys. Rev. E* **2005**, *71*, 015205. [CrossRef]
38. Kozyreff, G.; Tlidi, M. Nonvariational real Swift-Hohenberg equation for biological, chemical, and optical systems. *Chaos* **2007**, *17*, 037103. [CrossRef] [PubMed]
39. Kozyreff, G.; Chapman, S.J.; Tlidi, M. Interaction of two modulational instabilities in a semiconductor resonator. *Phys. Rev. E* **2003**, *68*, 015201. [CrossRef] [PubMed]
40. Clerc, M.G.; Verschueren, N. Quasiperiodicity route to spatiotemporal chaos in one-dimensional pattern-forming systems. *Phys. Rev. E* **2013**, *88*, 052916. [CrossRef]
41. Burke, J.; Dawes, J.H. Localized states in an extended Swift-Hohenberg equation. *SIAM J. Appl. Dyn. Syst.* **2012**, *11*, 261–284. [CrossRef]
42. Alvarez-Socorro, A.J.; Clerc, M.G.; Tlidi, M. Spontaneous motion of localized structures induced by parity symmetry breaking transition. *Chaos* **2018**, *28*, 053119. [CrossRef]
43. Houghton, S.M.; Knobloch, E. Swift-Hohenberg equation with broken cubic-quintic nonlinearity. *Phys. Rev. E* **2011**, *84*, 016204. [CrossRef]
44. Verschueren, N.; Bortolozzo, U.; Clerc, M.G.; Residori, S. Spatiotemporal chaotic localized state in liquid crystal light valve experiments with optical feedback. *Phys. Rev. Lett.* **2013**, *110*, 104101. [CrossRef]
45. Turing, A.M. The chemical basis of morphogenesis. *Philos. Trans. R. Soc. B* **1952**, *237*, 37–72.
46. Goldstein, R.E.; Gunaratne, G.H.; Gil, L.; Couillet, P. Hydrodynamic and interfacial patterns with broken space-time symmetry. *Phys. Rev. A* **1991**, *43*, 6700–6721. [CrossRef] [PubMed]

Review

Unique Features of Nonlocally Nonlinear Systems with Oscillatory Responses

Guo Liang ^{1,2} , Jinlong Liu ^{1,3}, Wei Hu ¹ and Qi Guo ^{1,*}

¹ Guangdong Provincial Key Laboratory of Nanophotonic Functional Materials and Devices, South China Normal University, Guangzhou 510631, China; liangguo0916@163.com (G.L.); liujldragon@163.com (J.L.); huwei@scnu.edu.cn (W.H.)

² School of Physics and Electrical Information, Shangqiu Normal University, Shangqiu 476000, China

³ College of Science, South China Agriculture University, Guangzhou 510642, China

* Correspondence: guoq@scnu.edu.cn

Abstract: We review the recent investigation of a new form of nonlocally nonlinear system with oscillatory responses. The system has various new features, such as the nonlocality-controllable transition of self-focusing and self-defocusing nonlinearities, a unique modulational instability and new forms of solitons. We also discuss the propagation of the optical beam in a nematic liquid crystal with negative dielectric anisotropy and demonstrate theoretically that propagation can be modelled by the system.

Keywords: nonlocally nonlinear systems; oscillatory responses; nematic liquid crystal

PACS: 42.65.Jx; 42.65.Tg; 42.70.Df; 42.65.Ky

Citation: Liang, G.; Liu, J.; Hu, W.; Guo, Q. Unique Features of Nonlocally Nonlinear Systems with Oscillatory Responses. *Appl. Sci.* **2022**, *12*, 2386. <https://doi.org/10.3390/app12052386>

Academic Editors: Gaetano Assanto and Noel F. Smyth

Received: 26 August 2021

Accepted: 8 February 2022

Published: 25 February 2022

Publisher's Note: MDPI stays neutral with regard to jurisdictional claims in published maps and institutional affiliations.



Copyright: © 2022 by the authors. Licensee MDPI, Basel, Switzerland. This article is an open access article distributed under the terms and conditions of the Creative Commons Attribution (CC BY) license (<https://creativecommons.org/licenses/by/4.0/>).

1. Introduction

The optical Kerr effect (OKE), a phenomenon that refers to the dependence of the refractive index on the optical intensity, is one of the most important effects in nonlinear optics [1,2]. The physical mechanism of OKE includes molecular reorientation, thermal nonlinearity, photorefractive effect, electronic contribution and electrostriction, etc. No matter what the physical mechanism is, the caused refractive index can always be phenomenologically represented as $n(\mathbf{r}, z, t) = n_0(\mathbf{r}, z) + n_{nl}(\mathbf{r}, z, t)$, with n_0 and n_{nl} being, respectively, the linear refractive index and nonlinear refractive index (NRI). If NRI at a certain point in space is not determined solely by the optical intensity at that point but also depends on its vicinity, nonlinearity is spatially nonlocal [3–5]. Mathematically, NRI can be expressed as an integral of a kernel function (also called the response function) and an optical intensity [3]. The media of nonlocal nonlinearity are referred to as nonlocally nonlinear media [6–9], which ranges from nematic liquid crystal (NLC) with positive dielectric anisotropy [10–14], lead glass [15], nonlinear ion gas [16], photorefractive crystal [17], dipolar Bose–Einstein condensate [18] and so on. For the physical systems mentioned above, response functions are positive definite, for example, the exponential-decay response function for the (1 + 1)-dimensional case [19] and the zeroth-order modified Bessel function for the (1 + 2)-dimensional infinite case [10,20].

In fact, there is the other kind of response function without positive definiteness: the sine-oscillation function, brought out in the study of quadratic solitons by the formal equivalence in mathematics between quadratic and nonlocal solitons [21,22]. This kind of sine-oscillation function was also obtained in a system of coupled Gross–Pitaevskii–Poisson equations [23], which govern the evolutions for matter-wave components and the microwave magnetic field in atomic Bose–Einstein condensates. Recently, we investigated the nonlocally nonlinear system with oscillatory responses [24–32] and found various new features such as the nonlocality-controllable transitions between focusing and defocusing

nonlinearities, unique modulational instabilities (MI) and new kinds of solitons. The nonlocally nonlinear system with oscillatory responses can model the propagation of optical beams in NLC with negative dielectric anisotropy.

In this review article, we provide a brief overview of unique features of nonlocally nonlinear system with oscillatory responses, including its mathematical model, the treatment of the model and the nonlocality-controllable transition between focusing and defocusing nonlinearities in Section 2, the short-term and long-term MI properties in Section 3, different kind of soliton solutions in Section 4 and a special algorithm for finding soliton solutions in Section 5. In Section 6, we discuss the nonlinearity characteristic of NLC with negative dielectric anisotropy and show that it can be modeled by the nonlinear system with oscillatory responses.

2. Nonlocality-Controllable Kerr Nonlinearities

The model we considered is the dimensionless system in the form of [27,28]

$$i\frac{\partial u}{\partial z} + \frac{1}{2}\nabla_D^2 u + \Delta n u = 0, \tag{1}$$

$$w_m^2 \nabla_D^2 \Delta n + \Delta n - s|u|^2 = 0. \tag{2}$$

The equations are the coupled equations for a dimensionless optical beam $u(\mathbf{r}, z)$ and its (dimensionless) induced NRI $\Delta n(\mathbf{r}, z)$, where \mathbf{r} is D -dimensional transverse coordinate vectors ($D = 1$ or 2), ∇_D^2 is the D -dimensional transverse Laplacian operator, $s(= \pm 1)$ is the sign of Kerr coefficient and w_m is the nonlinear characteristic length. We will show in Section 6 that the model, Equation (1) plus (2), can describe the evolutions of optical beams in the NLC with negative dielectric anisotropy. However, the model discussed extensively before is the following [3,5]:

$$w_m^2 \nabla_D^2 \Delta n - \Delta n + s|u|^2 = 0, \tag{3}$$

of which the second term has different signs from that of Equation (2). It is such a difference in the signs that makes the two nonlinear systems described by Equations (2) and (3) exhibit utterly different features.

Although the NRI described by Equation (2) in an infinite space can also be expressed by the following convolution:

$$\Delta n(\mathbf{r}, z) = sR_D \otimes |u|^2, \tag{4}$$

similarly to the case of Equation (3) [3,5], the D -dimensional response function R_D is completely different. When $D = 1$, the response takes the sin-oscillatory function as [27]

$$R_1 = \frac{1}{2w_m} \sin\left(\frac{|x|}{w_m}\right). \tag{5}$$

While, when $D = 2$ [28], the response function is expressed by the following:

$$R_2 = \frac{1}{4w_m^2} Y_0\left(\frac{r}{w_m}\right) \tag{6}$$

with Y_0 being the zeroth order Bessel function of the second kind. Substituting Equation (4) into Equation (1) yields a nonlocally nonlinear Schrödinger equation in the form of

$$i\frac{\partial u}{\partial z} + \frac{1}{2}\nabla_D^2 u + suR_D \otimes |u|^2 = 0. \tag{7}$$

We can glimpse at the self-focusing and self-defocusing property of the nonlinear system described by Equation (7) from two limits where $w_m = 0$ and $w_m \rightarrow \infty$. When $w_m = 0$, Equation (2) is reduced to $\Delta n = s|u|^2$. Clearly, the focusing nonlinearity occurs

for $s = 1$ and the defocusing nonlinearity does for $s = -1$. When $w_m \rightarrow \infty$, Equation (2) changes to $w_m^2 \nabla_D^2 \Delta n = s|u|^2$, which models the focusing nonlinearity in lead glass for $s = -1$ [15] and the defocusing nonlinearity for $s = 1$. Therefore, the nonlinearities reverse if w_m proceeds from 0 to ∞ for both cases of $s = \pm 1$. This indicates that the self-focusing and self-defocusing property of the nonlinear system described by Equation (7) depends on the degree of nonlocality, which is defined by $\sigma = w_m/w$ with w being the beam width [27]. In contrast, for the nonlinear system given by Equation (3), the self-focusing and self-defocusing property is different. In the case where $s = 1$, Equation (3) is reduced to $\Delta n = |u|^2$ when $w_m = 0$, and to $w_m^2 \nabla_D^2 \Delta n = -|u|^2$ when $w_m \rightarrow \infty$. Under the two limits, the system (3) exhibits both self-focusing nonlinearity: that is, the local self-focusing nonlinearity when $w_m = 0$ and the (thermally induced) nonlocal self-focusing nonlinearity in lead glass $w_m \rightarrow \infty$ [15]. Conversely, in the case where $s = -1$, the self-defocusing nonlinearity exists for the two limits of w_m . Therefore, no nonlinearities transition can take place in the nonlinear system given by Equation (3).

The dependence of the self-focusing and self-defocusing property on the degree of nonlocality can be obtained by both the variational approach and by numerical simulations. The Lagrangian density of the system described by Equation (7) is the following: [33,34]

$$\mathcal{L} = \frac{i}{2} \left(u^* \frac{\partial u}{\partial z} - u \frac{\partial u^*}{\partial z} \right) - \frac{1}{2} |\nabla_D u|^2 + \frac{s}{2} |u|^2 (R_D \otimes |u|^2). \tag{8}$$

We introduce a trial Gaussian beam:

$$u(\mathbf{r}, z) = A(z) \exp[i\alpha(z)] \exp \left[-\frac{r^2}{2w(z)^2} + ic(z)r^2 \right], \tag{9}$$

where all meanings of parameters A, α and c can be found in Ref. [28]. According to the standard procedure of variational approach [33,34], we obtain the evolution of the beam width w [28]:

$$\frac{d^2 w}{dz^2} = \frac{1}{w^3} - \frac{2sP_0}{\pi^D} N_D(w, w_m), \tag{10}$$

where $P_0 = \int_{-\infty}^{+\infty} |u(\mathbf{r}, z)|^2 d^D \mathbf{r} = \pi^{D/2} A^2 w^D$ is the input power, and the mathematical expression of N_D can be found in Ref. [28]. By assuming $w|_{z=0} = w_0 = 1$ and $dw/dz|_{z=0} = 0$, Equation (10) can be solved:

$$z = \int_1^w \frac{dw_2}{\sqrt{1 - 1/w_2^2 - (4sP_0/\pi^D) \int_1^{w_2} N_D(w_1, \sigma_0) dw_1}}, \tag{11}$$

where $\sigma_0 = w_m/w_0|_{w_0=1} = w_m$. For linear propagations of the input Gaussian beam, the beam width $w_0 = 1$ is widened to be $w(z) = \sqrt{1 + z^2}$ [35]. If the beam is in a focusing state, its width is $w(z) < \sqrt{1 + z^2}$, while in a defocusing state it is $w(z) > \sqrt{1 + z^2}$. Therefore, when nonlinearities transit between focusing and defocusing as the degree of nonlocality changes, by replacing w with $\sqrt{1 + z^2}$ in Equation (11) transition point σ_c can be obtained as

$$z = \int_1^{\sqrt{1+z^2}} \frac{dw_2}{\sqrt{1 - 1/w_2^2 - (4sP_0/\pi^D) \int_1^{w_2} N_D(w_1, \sigma_c) dw_1}}. \tag{12}$$

Equation (12) provides an implicit function of the critical degree of nonlocality σ_c on z, P_0, s and D . For a given s, D and P_0 , the function $\sigma_c(z)$ can be obtained by numerically solving the integral Equation (12) at different propagation distances z , which is shown in Figure 1.

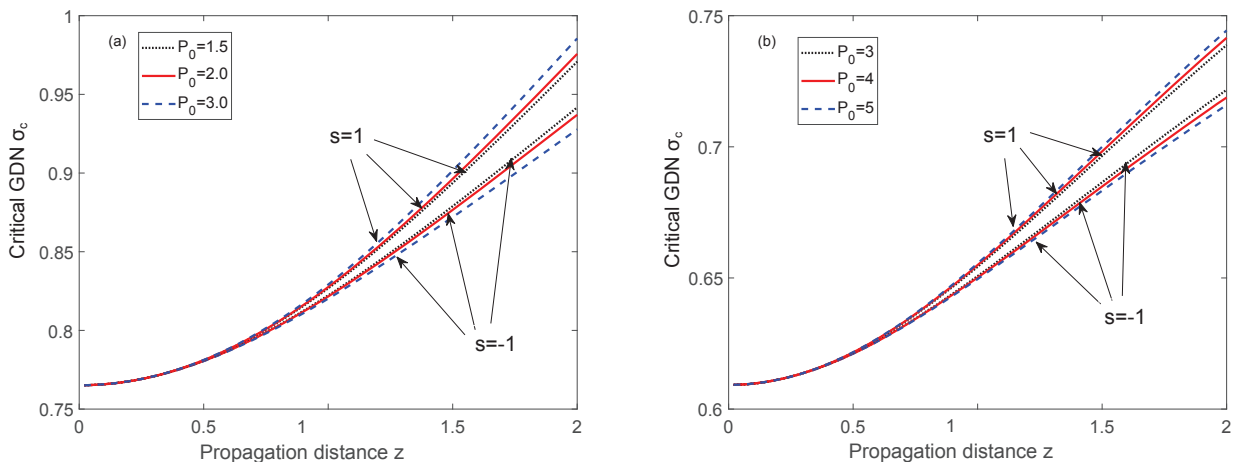


Figure 1. Critical degree of nonlocality σ_c as the function of propagation distance z . (a) $D = 1$, (b) $D = 2$. All data of the curves are numerically obtained from Equation (12) (After Ref. [28]).

At the specific distance $z = 1$, the critical degree of nonlocality for the $(1 + 1)$ - and $(1 + 2)$ -dimensional cases can be obtained from Equation (12) in that $\sigma_c|_{z=1} = 0.82$ and $\sigma_c|_{z=1} = 0.63$, respectively. The dependence of beam width on the degree of nonlocality is given in Figure 2. For the case of $s = -1$, optical beams experience self-defocusing nonlinearity when $\sigma_0 < \sigma_c$, and self-focusing nonlinearity when $\sigma_0 > \sigma_c$. The case of $s = 1$ is on the contrary. Figure 3 shows the evolutions of the optical beam for different degree of nonlocality in two cases of $s = 1$ and $s = -1$, where the degree-of-nonlocality-dependence self-focusing and self-defocusing effects can be obviously observed.

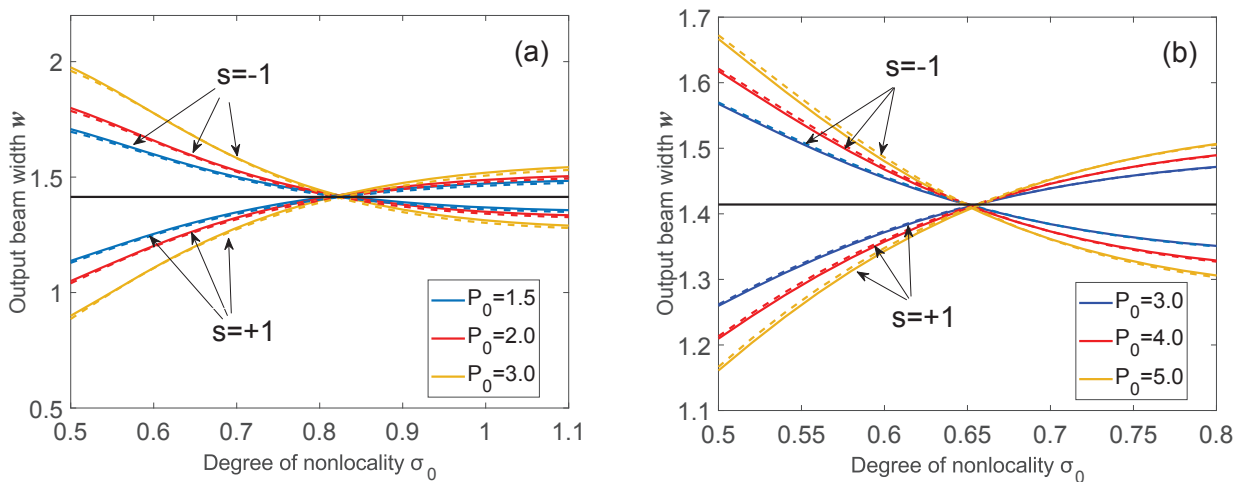


Figure 2. Beam widths at $z = 1$ as the function of σ_0 for different input powers. (a) $D = 1$, (b) $D = 2$. Solid color curves represent the numerical simulation results, agreeing well with the variational results denoted by dashed color curves. For comparison, the output beam width at $z = 1$ in the linear case is also plotted by the horizontal solid straight line (After Ref. [28]).

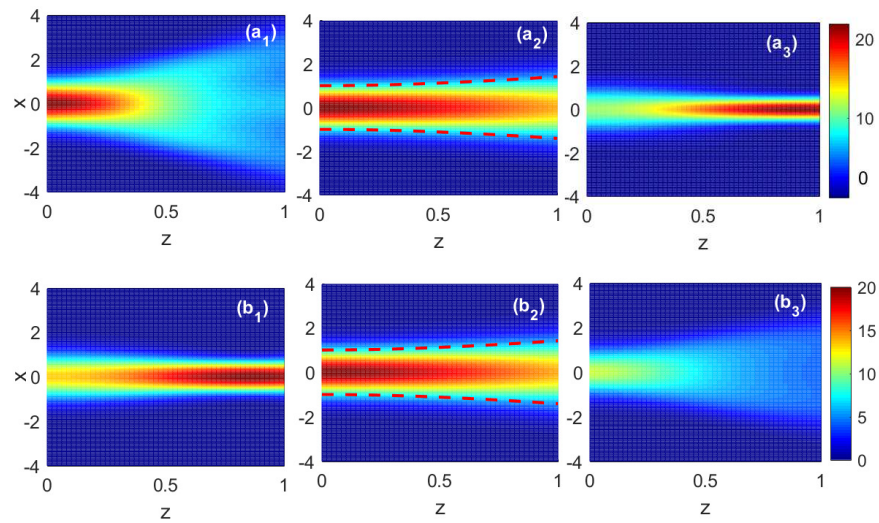


Figure 3. Evolutions of optical beams for both $s = -1$ ($\mathbf{a}_1, \mathbf{a}_3$) and $s = 1$ ($\mathbf{b}_1, \mathbf{b}_3$). $\sigma_0 = 0.45$ in ($\mathbf{a}_1, \mathbf{b}_1$), whereas $\sigma_0 = 1.2$ in ($\mathbf{a}_3, \mathbf{b}_3$). The linear evolutions are displayed in ($\mathbf{a}_2, \mathbf{b}_2$) for comparison (After Ref. [27]).

3. Unique Modulational Instability

In this section, we briefly review the modulational instabilities (MI) of the (1 + 1)-dimensional nonlocally nonlinear system (7) with oscillatory response (5). The evolution of perturbations we investigated includes two processes: short-term evolution and long-term evolution. During the short-term evolution of MI, the perturbation is small enough so that the linear analysis on the NNLSE (7) is valid [31]. However, after the optical field evolves for long term, the increasing perturbation is not much lower than the amplitude of plane wave, and the linear approximation method is not applicable, and the nonlinear evolution of MI should be considered: that is, the long-term evolution of MI [32].

3.1. Short-Term Evolution of MI

According to the standard procedure [36], we add a random perturbation ψ ($|\psi(x, z)|^2 \ll I_0$) on the plane wave:

$$u(x, z) = \left[I_0^{1/2} + \psi(x, z) \right] \exp \left[i2\pi s I_0 \tilde{R}(0)z \right], \tag{13}$$

where $\tilde{R}(0) = \tilde{R}(k_x)|_{k_x=0}$ and $\tilde{R}(k_x)$ represents the Fourier transform of the response function (5). After calculations, the gain coefficient of perturbation is obtained as follows [31]:

$$g = \text{Re} \left[2|k_x| \left(\frac{sI_0}{1 - w_m^2 k_x^2} - \frac{k_x^2}{4} \right)^{1/2} \right], \tag{14}$$

which only exists when $sI_0 / (1 - w_m^2 k_x^2) > k_x^2 / 4$. When $s = -1$, MI occurs when the following is the case:

$$1 < w_m^2 k_x^2 < \frac{1}{2} \left(1 + 16w_m^2 I_0 \right)^{1/2} + \frac{1}{2}, \tag{15}$$

which is shown Figure 4. When $s = 1$ and the light intensity is small enough to meet the following condition:

$$0 < I_0 \leq \frac{1}{16w_m^2}, \tag{16}$$

there are two MI gain bands, as shown in Figure 5, at each side of the origin.

$$\begin{cases} 0 < w_m^2 k_x^2 < \frac{1}{2} - \frac{1}{2}(1 - 16w_m^2 I_0)^{1/2}, \\ 1 > w_m^2 k_x^2 > \frac{1}{2} + \frac{1}{2}(1 - 16w_m^2 I_0)^{1/2}. \end{cases} \quad (17)$$

Furthermore, after I_0 exceeds the critical value of $1/16w_m^2$, the MI gain bands combine into one as follows:

$$0 < w_m^2 k_x^2 < 1, \quad (18)$$

which is shown Figure 5. MI in the nonlocally nonlinear system with oscillatory responses is found to have two unique properties. First, MI exists both when the Kerr coefficient is positive and when it is negative. Second, the maximum gain points of MI do not shift with light intensity. The physical mechanism behind the properties of MI has been revealed by utilizing the theory of four-wave mixing in Ref. [31].

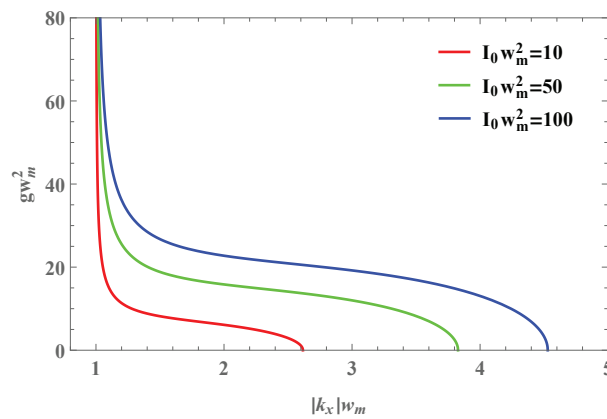


Figure 4. Gain spectra of MI under different values of I_0 when $s = -1$.

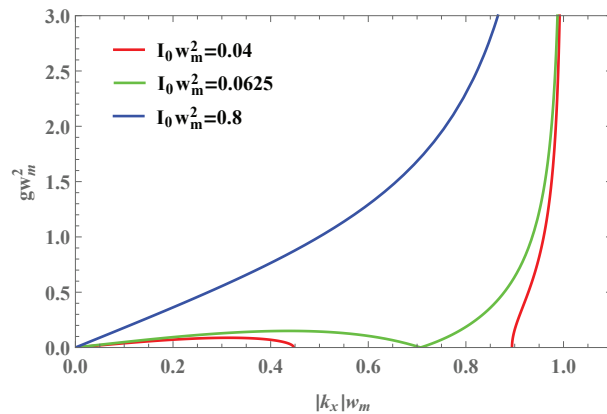


Figure 5. Gain spectra of MI under different values of I_0 when $s = 1$.

3.2. Long-Term Evolution of MI

To show the long-term evolution of MI, we take an infinite plane wave with perturbation [32]:

$$u(x, z)|_{z=0} = 1 + 10^{-4} \cos(k_x x), \quad (19)$$

as the initial input of Equation (7) with $s = -1$ and $D = 1$, where the first term, the second term and k_x represent plane wave, perturbation and frequency of perturbation, respectively. In the following numerical simulation, we assume that $w_m = 1$ and $I_0 = 1$. Then, MI appears in the range of $1 < |k_x| < 1.61$. $|k_x| = 1$ is the singular point at which the gain coefficient g is infinite and $|k_x| = 1.61$ is the cutoff point. The nonlinear evolutionary process of initial input (19) of different perturbation frequencies is shown in Figure 6. In the short-term evolution, the curve of intensity obtained through linear processing

is consistent with the numerical simulation, which means that linear approximation is applicable. However, in long-term evolution, the results obtained by linear approximation gradually deviated from numerical simulations. Additionally, the perturbation of the frequency close to the singular point increases more quickly to a larger peak; by contrast, the perturbation of the frequency close to the cutoff point presents a slower growth of a lower peak. The reason why the numerical simulations deviate from the analytical result is that, during the nonlinear evolutions of perturbation higher-order, harmonic waves appear. In this case, the linear approximation of perturbation is not appropriate, and harmonic waves with higher frequencies should be taken into account.

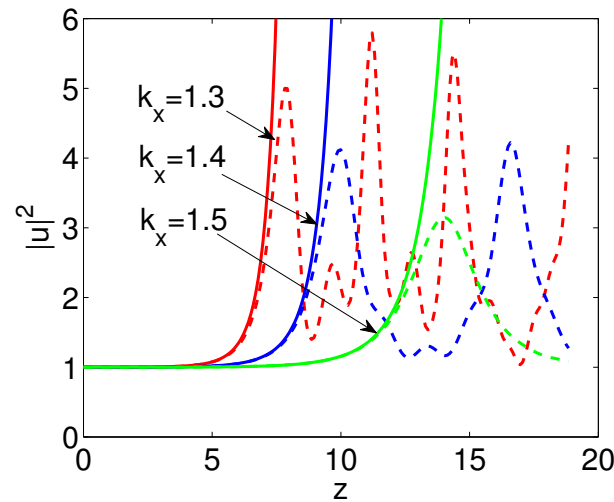


Figure 6. Evolution of the optical field at $x = 0$ under input condition (19) when $w_m = 1$ (solid line: analytical results obtained through linear approximation method; dashed line: results attained through simulation) (After Ref. [32]).

We can obtain the stable solution of induced MI by considering the input modulated wave to be composed of harmonics with various frequencies:

$$u(x, z) = \sum_{n=-\infty}^{+\infty} A_n(z) \exp(ik_x nx).$$

For stable solutions, the amplitudes A_n of various harmonic do not vary with propagation distance z ; then, we assume $A_n = a_n \exp(i\beta z)$. Substitution into Equation (7) with $D = 1$ and $s = -1$ yields the following:

$$-\beta a_n - \frac{1}{2} a_n k_x^2 n^2 + s \sum_{m=-\infty}^{+\infty} a_m I_{n-m}(z) \frac{1}{1 - w_m^2 k_x^2 (n - m)^2} = 0. \tag{20}$$

If only the first harmonic is taken into account, the analytical solution to Equation (20) can be obtained as

$$u(x, z) = \left[\sqrt{\frac{\left(\frac{1}{1-w_m^2 k_x^2} - \frac{k_x^2}{4}\right)(1-w_m^2 k_x^2)}{2}} + \sqrt{\frac{\left(\frac{1}{1-w_m^2 k_x^2} + \frac{k_x^2}{4}\right)(1-w_m^2 k_x^2)}{4}} \cos(k_x x) \right] \exp \left[-i \left(\frac{1}{1-w_m^2 k_x^2} + 1 + \frac{k_x^2}{4} \right) z \right]. \tag{21}$$

By using $u(x, 0)$ as the initial conditions, the evolution of stable solution is displayed in Figure 7. As shown in the figure, only the solutions when the modulation frequency is near the cutoff frequency are able to be stably propagated, while the ones when the modulation

frequency departs from the cutoff frequency will fluctuate greatly during propagations; in this case, an increased number of harmonics should be considered. In this case, it is impossible to obtain the analytical solution, and the numerical method is required in order to solve Equation (20) [32].

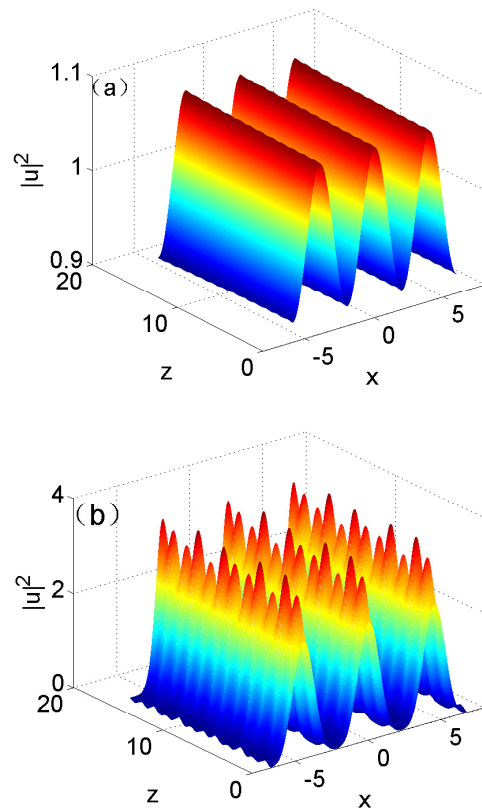


Figure 7. Evolution of stable solution when $w_m = 1$ at different modulation frequencies: (a) $k_x = 1.6$; (b) $k_x = 1.4$ (After Ref. [32]).

4. Characteristics of Solitons

The MI of the nonlocally nonlinear system (7) always exists for cases of $s = \pm 1$ [31]. In consequence, due to the MI [36], the dark solitons [27,37] in self-defocusing sides of such a nonlocally nonlinear system are unstable [27], while the bright solitons existing in self-focusing sides can propagate stably. Concretely, in the case of $s = -1$, self-focusing and self-defocusing nonlinearities are, respectively, exhibited in high ($\sigma_0 > \sigma_c$) and low ($\sigma_0 < \sigma_c$) ranges of the degree of nonlocality, while in the case of $s = 1$, the self-focusing and self-defocusing properties are on the contrary. In the following, we will review our works on the bright solitons in the self-focusing sides of such a system described by Equation (7) in cases of $s = \pm 1$. In addition to fundamental solitons [27,28], there are new kinds of solitons including the in-phase and out-of-phase bound-state solitons [29] and multi-peak (more than four peaks) solitons [30] in the nonlocally nonlinear system with oscillatory responses.

The variational approach is used to obtain the approximate solutions of bright solitons, including the fundamental solitons [28] and Hermite–Gaussian-type multi-peak solitons [30]. The variational results have been confirmed by the numerical ones. We used the imaginary time evolution method to iterate the fundamental solitons [27,28] and the in-phase and out-of-phase bound-state solitons [29]. To iterate the multi-peak solitons with arbitrary peak numbers [30], we specifically developed a perturbation-iteration method [38].

4.1. Fundamental Solitons

Integrating Equation (10) once yields $\frac{1}{2} \left(\frac{dw}{dz} \right)^2 + V_D(w) = 0$, where $V_D(w)$ is the equivalent potential in the form of [28]

$$V_D(w) = - \int_1^w \left[\frac{1}{w_1^3} - \frac{2sP_0}{\pi^D} N_D(w_1, \sigma_0) \right] dw_1. \tag{22}$$

The soliton solutions correspond to the extremum points of the equivalent potential [28,33]; therefore, by allowing $\partial_w V_D = 0$ the critical power of the solitons can be obtained as

$$P_c = \frac{\pi^D}{2sN_D(1, \sigma_0)}. \tag{23}$$

It should be noted that, in Equation (23), the critical power P_c must be positive, which requires $N_D > 0$ for $s = 1$ and $N_D < 0$ for $s = -1$. Furthermore, the solitons are stable at the minimum points of $V_D(w)$, then we have:

$$\left. \frac{d^2 V_D}{dw^2} \right|_{w=1, P_0=P_c} > 0. \tag{24}$$

From Equation (24), the existence ranges of the degree of nonlocality σ_0 for the solitons can be determined, which depend on the values of D and the sign of s . When $D = 1$, the solitons exist if $\sigma_0 \in [0, 0.76]$ for $s = 1$ and $[1.05, +\infty)$ for $s = -1$. When $D = 2$, the existence ranges of σ_0 are $[0.33, 0.61]$ for $s = 1$ and $[0.90, +\infty)$ for $s = -1$. These variational results agree well with the numerical ones, which are given in the following.

In order to numerically iterate the soliton solution, we assume $u(x, z) = u(x) \exp(i\lambda z)$. Substitution of the solution into Equations (1) and (2) yields the following:

$$\frac{1}{2} \frac{d^2 u}{dx^2} - \lambda u + \Delta n u = 0, \tag{25}$$

$$w_m^2 \frac{d^2 \Delta n}{dx^2} + \Delta n - s u^2 = 0. \tag{26}$$

By the imaginary-time method, the solitons can be numerically found in higher ranges of the degree of nonlocality, $\sigma_0 \in [1.05, +\infty)$ for $D = 1$ and $\sigma_0 \in [1.11, +\infty)$ for $D = 2$ in the case of $s = -1$. These ranges of σ_0 are all within the self-focusing sides of such a nonlinear system and agree well with the variational results. The bright solitons have two abnormal properties. The first one is the negative propagation constants, while it is the opposite of the cases in local nonlinear media [39] and nonlocally nonlinear media with the positively defining attenuating response functions [3]. The other is the negative slope of the $P_c(\lambda)$ (P_c and λ being the critical power and the propagation constant), as shown in Figure 8. By means of linear stability analysis, all solitons are shown to be stable [27]. This means that the stability criterion obeys an anti-Vakhitov–Kolokolov stability criterion [40], which is also obeyed by the in-phase and out-of-phase bound-state solitons and the multi-peak solitons reviewed in the next two sections. However, in nonlocally nonlinear media with the positively defining attenuating response functions, stable solitons should comply with the Vakhitov–Kolokolov criterion [9]. We have noticed that the evolutions for matter-wave components and the microwave magnetic field in the atomic Bose–Einstein condensates can also be governed by the mathematical model of Equation (1) plus (2) with $s = -1$ in some specific conditions [23,41,42], and in such a system, bright solitons are obtained in strongly nonlocal cases.

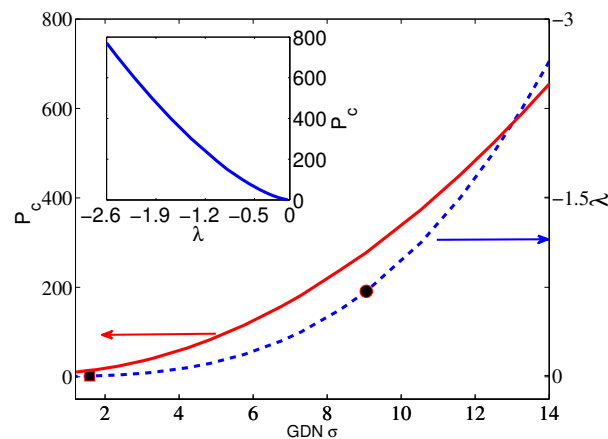


Figure 8. Critical power P_c and the soliton propagation constant λ versus the degree of nonlocality σ . The inset shows P_c versus λ . All plots are for $D = 1$. The obtained solitons are stable (After Ref. [27]).

Although what Equations (25) and (26) determine are the solitons of the nonlocally nonlinear system (7), the coupled equations with $s = 1$ are formally the same as the model governing parametric spatial solitary waves in quadratic nonlinear materials [21,22,43]. The fundamental and the second harmonic waves are mathematically equivalent to the paraxial beam and its induced NRI [21]. Esbensen et al. employed the formal equivalence between two distinct physical systems to investigate the stabilities of solitons and found that the solitons are all unstable. However, it should be noted that equivalence is limited only to the solitary waves, while their dynamic properties, such as the stability, are completely different. In quadratic nonlinear materials, there is the energy and phase exchange between the fundamental and the second harmonic waves. Therefore, for the second harmonic wave, its z -dependant evolution should be taken into account, which is not the case for the NRI shown in Equation (2). Detailed discussions on this point can be found in Ref. [10]. Our group also made some improvements on the issue of quadratic solitons [24–26]. We found that the boundary confinement of media can support stable solitons [24]. Furthermore, the fundamental waves even can be multipole solitons [25], the existence of which depends closely on the sample size and the degree of nonlocality. If nonlocality is fixed and the sample size is varied, soliton width varies piecewise and approximately periodically [26].

4.2. In-Phase and Out-of-Phase Bound-State Solitons

In the case of $s = 1$, the nonlinear system exhibits self-focusing nonlinearity in lower ranges of degree of nonlocality, that is, $\sigma_0 < \sigma_c$. In these ranges, we obtained bright solitons with complicated structures, which are the in-phase bound-state solitons when $\sigma_0 \in [0.28, 0.78]$ and the out-of-phase bound-state solitons when $\sigma_0 \in [0.38, 0.78]$ [29]. The in-phase bound-state soliton, shown in Figure 9, owns the symmetrical profile and the nonzero central value. On the other hand, the out-of-phase bound-state soliton, shown in Figure 10, owns the antisymmetrical profile and the zero central value. When the degree of nonlocality decreases, the in-phase bound-state soliton approaches the sech profile shown in Figure 9, and the out-of-phase bound-state soliton tends toward the first-order Hermite–Gaussian profile shown in Figure 10. The above-mentioned abnormal properties in the previous section, that is, the negative propagation constants and the negative slope of the power-propagation constant (the so-called anti-Vakhitov–Kolokolov stability criterion), also exist for bound-state solitons, which is shown in Figure 11a. Furthermore, it can be found from Figure 11b that the power-propagation constant diagrams are the same for both the in-phase and the out-of-phase bound-state solitons. In other words, we can say that two forms of bound-state solitons form degenerate modes.

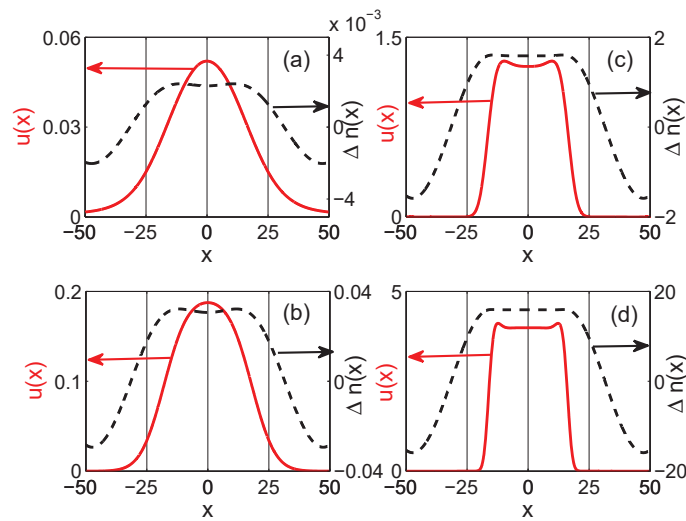


Figure 9. Profiles of in-phase bound-state solitons (solid red lines) and their induced NRI (dashed black lines) for the case that $s = 1$. (a) $\sigma_0 = 0.472$, (b) $\sigma_0 = 0.700$, (c) $\sigma_0 = 0.773$ and (d) $\sigma_0 = 0.778$. The obtained solitons are stable (After Ref. [29]).

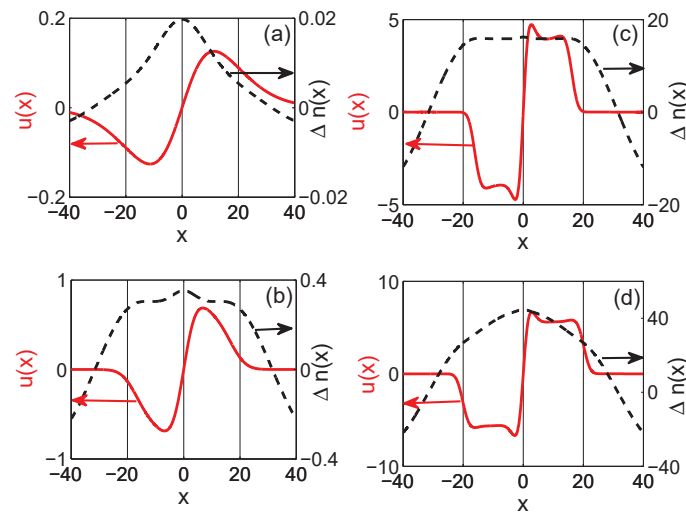


Figure 10. Profile of out-of-phase bound-state solitons (solid red lines) and the induced NRI (dashed black lines) for the case that $s = 1$. (a) $\sigma_0 = 0.453$, (b) $\sigma_0 = 0.731$, (c) $\sigma_0 = 0.777$ and (d) $\sigma_0 = 0.778$. The obtained solitons are stable (After Ref. [29]).

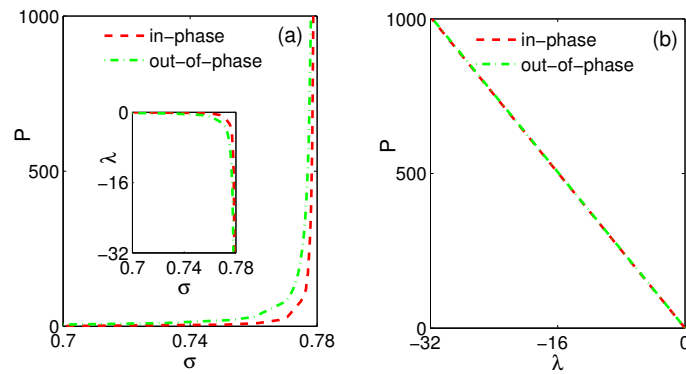


Figure 11. (a) Power P and propagation constant λ vs. the degree of nonlocality σ ; (b) power P vs. propagation constant λ of the in-phase and out-of-phase bound-state solitons for the case that $s = 1$. The obtained solitons are stable (After Ref. [29]).

4.3. Multi-Peak Solitons

The Hermite–Gaussian soliton solutions with multi-peaks in fact have been discussed in nonlocally nonlinear media with positively-definiting attenuating response functions [44,45]. However, the upper thresholds of the peak number of the stable solitons in nonlocally nonlinear media are different, which closely depend on the response function of media. For instance, in the nonlocal system with the Gaussian response, the multi-peak solitons with any peak number [4] are stable [44]. In nematic liquid crystals with positive dielectric anisotropy, the response function is an exponential decay one for the (1 + 1) case, and the peak-number of the solitons supported is only less than five [44]. In the nonlocally nonlinear system with oscillatory responses described by Equations (1) and (2), we found the upper thresholds of the peak number of the stable solitons are five and four in the cases of $s = -1$ and 1 , respectively [30].

The variational approach can be applied to find solitons and discuss their stabilities. The Hermite–Gaussian solitons of the (1 + 1)-dimensional NNLSE (7) are of the following profiles:

$$u_n = \left(\frac{P_{nc} \sqrt{2n+1}}{2^n n! \sqrt{\pi}} \right)^{1/2} H_n(\sqrt{2n+1}x) \exp \left[-\frac{(2n+1)x^2}{2} \right]. \tag{27}$$

The critical power is obtained as follows:

$$P_{nc} = \frac{(2n+1)(\sqrt{\pi}2^n n!)^2}{sN^{(n)}(1, \sigma_0)}, \tag{28}$$

where function $N^{(n)}$ is the N_n given in Ref. [30]. The degree of nonlocality range within which HG solitons exist is obtained by the variational approach, which is summarized in Table 1, where the numerical results are also given for a comparison.

Table 1. The ranges of σ_0 within which the HG-type solitons exist.

		$n = 0$	$n = 1$	$n = 2$	$n \geq 3$
$s = -1$	variational	(1.05, +∞)	(1.06, +∞)	(1.06, +∞)	(1.06, +∞)
	numerical	(1.05, +∞)	(1.05, +∞)	(1.05, +∞)	(1.05, +∞)
$s = +1$	variational	(0, 0.77)	(0.38, 0.79)	(0.39, 0.79)	(0.39, 0.79)
	numerical	(0.05, 0.78)	(0.38, 0.78)	(0.39, 0.78)	(0.40, 0.78)

Note: self-focusing nonlinearity is exhibited when $\sigma_0 \in (\sigma_c, +\infty)$ for $s = -1$, and $[0, \sigma_c]$ for $s = 1$ (for example, $\sigma_c|_{z=1} = 0.82$).

Multi-peak solitons can be numerically obtained for two cases of $s = \pm 1$, which are shown in Figures 12 and 13, respectively. Clearly, the multi-peak solitons in the case of $s = -1$ exhibit Hermite–Gaussian structures and are in good agreement with numerical ones. While, the profiles of solitons in the case of $s = 1$ deviate from the Hermite–Gaussian form, especially when σ_0 becomes large. Likely, for multi-peak solitons, the propagation constants and the slope of the power-propagation constant are both negative, which is shown in Figure 14. By linear stability analyses, the ranges of the degree of nonlocality σ_0 within which the stable multi-peak solitons exist are summarized in Table 2.

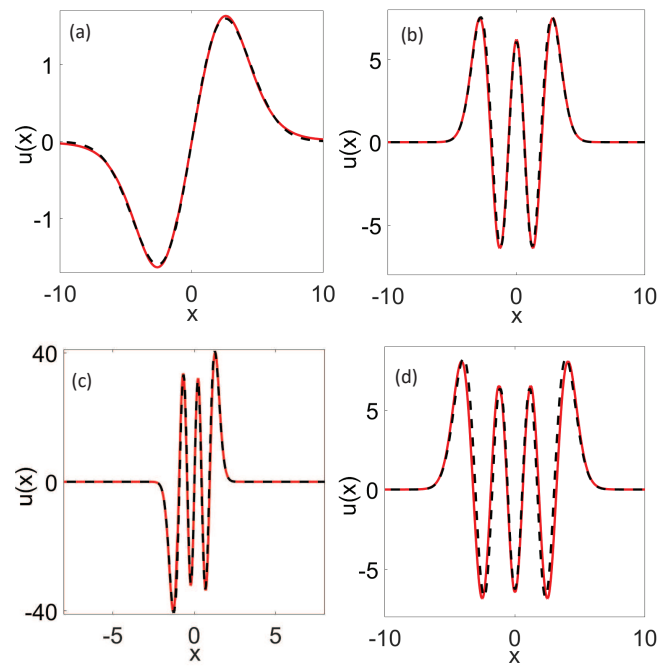


Figure 12. Profiles of the numerical multi-peak solitons $u(x)$ (the solid red curves) for $s = -1$ and $w_m = 5$. (a–d) for $n = 1, 4, 5, 6$ and $\sigma_0 = 1.13, 1.43, 3.52, 1.08$, respectively. The variational results (the dashed black curves) with the same parameters are also given for comparison. Soliton in (b) is stable, while the ones in the other three figures are unstable.

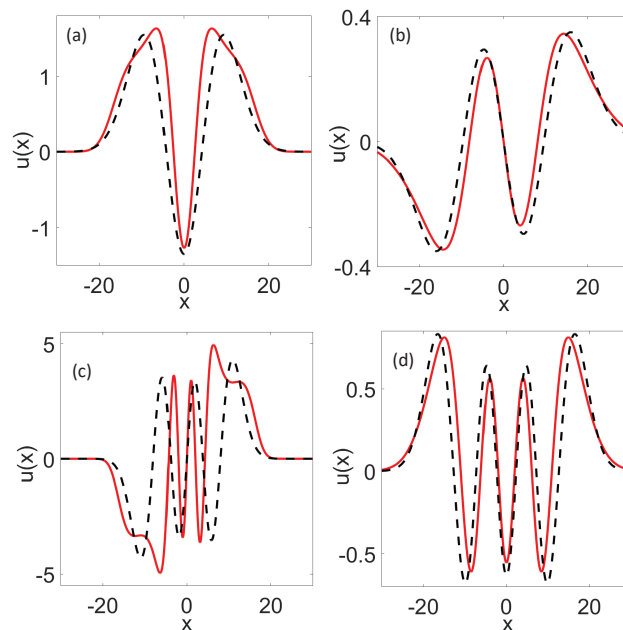


Figure 13. Profiles of the numerical multi-peak solitons $u(x)$ (the solid red curves) for $s = 1$ and $w_m = 10$. (a–d) for $n = 2, 3, 5, 6$ and $\sigma_0 = 0.74, 0.48, 0.75, 0.51$, respectively. The corresponding numerical results are denoted in the same manner as in Figure 5. Soliton in (b) is stable, while the ones in the other three figures are unstable.

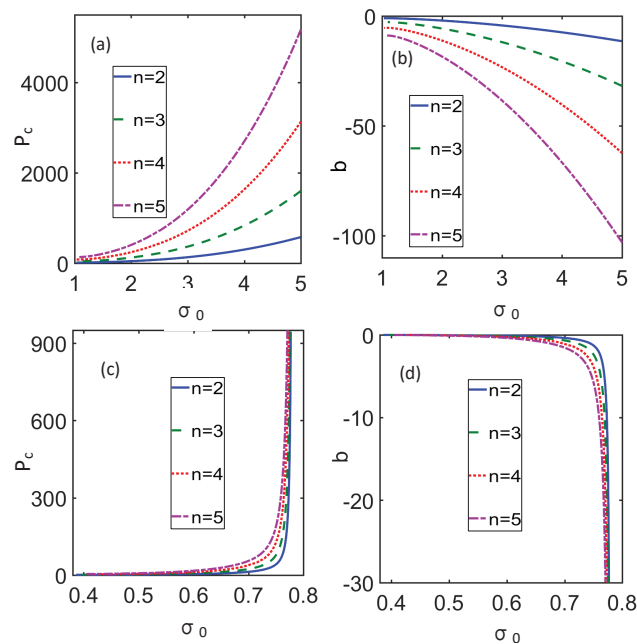


Figure 14. Dependencies of the power P_c on the degree of nonlocality σ_0 (a,c) and the propagation constant b on the degree of nonlocality σ_0 (b,d) for the multi-peak solitons. (a,b) and (c,d) for $s = -1$ and $s = 1$, respectively.)

Table 2. The ranges of σ_0 within which the HG-type solitons are stable.

	$n = 0$	$n = 1$	$n = 2$	$n = 3$	$n = 4$	$n \geq 5$
$s = -1$	(1.05, $+\infty$)	(1.41, $+\infty$)	(1.10, $+\infty$)	(1.10, $+\infty$)	(1.10, 1.61)	no
$s = 1$	(0.05, 0.78)	(0.38, 0.78)	(0.42, 0.45)	(0.48, 0.49)	no	no

5. Perturbation-Iteration Method

In the nonlocally nonlinear system with oscillatory responses governed by Equation (7), the Hermite–Gauss-like solitons with arbitrary peak numbers are hardly obtained by the usual numerical algorithms such as the Newton-conjugate-gradient method. Therefore, we developed a special numerical method by which we called the perturbation-iteration method to solve this problem [38]. The key idea behind the perturbation-iteration method is to treat the NNLSE as a perturbed model of the harmonic oscillator, and soliton solutions can be obtained by perturbation theory in quantum mechanics [46]. The procedure for the perturbation-iteration method is briefly reviewed. Substituting the following soliton solutions:

$$u_n(x, z) = \sqrt{A_n} \psi_n(x) \exp(-i\beta_n z) \quad (n = 0, 1, 2, 3, \dots) \tag{29}$$

into the NNLSE (7) yields the following:

$$\left[-\frac{1}{2} \frac{d^2}{dx^2} - A_n \int_{-\infty}^{\infty} R(x - \xi) \psi_n^2(\xi) d\xi \right] \psi_n(x) = \beta_n \psi_n(x), \tag{30}$$

where A_n is a coefficient related to the power of soliton, $\psi_n(x)$ and β_n are, respectively, the transverse distribution and propagation constant of soliton and n is the order of soliton. We can treat Equation (30) as a perturbed model of the harmonic oscillator:

$$\left[-\frac{1}{2} \frac{d^2}{dx^2} + \frac{1}{2\mu^4} x^2 + f_n(x) \right] \psi_n(x) = E_n \psi_n(x), \tag{31}$$

where $\psi_n(x)$ and E_n are, respectively, eigenfunctions and eigenvalues, $f_n(x)$ is the perturbation compared to the potential of the harmonic oscillator. Starting from the perturbed

model of the harmonic oscillator, we determine the “minimum” perturbation, then use the formal expression of infinite-order perturbation expansions to numerically calculate the eigenfunctions and eigenvalues of the perturbed model and iterate this perturbation to obtain multippeak solitons with enough high accuracy.

This form of perturbation-iteration method developed for the (1 + 1)-dimensional NNLSE also has been extended to the (1 + 2)-case [47]. In fact, the method we developed might also be extended to the numerical integration of the Schrödinger equations in any type of potentials.

6. Optical Beams in NLC with Negative Dielectric Anisotropy

6.1. Evolution Equation for Optical Beams in NLC

The physical mechanism of nonlinearity in NLC is the optically induced molecular reorientation and nonlocality comes from the interactions between NLC molecules [3]. We consider the propagation of optical beams in the sample cell of NLC shown in Figure 15. NLC molecules exhibit anisotropy in both the low-frequency domain and the optical frequency domain, which is expressed by ϵ_a^{rf} ($= \epsilon_{\parallel} - \epsilon_{\perp}$) and ϵ_a^{op} ($= n_{\parallel}^2 - n_{\perp}^2$), respectively. Anisotropy ϵ_a^{rf} can be either positive [10,48] or negative [48,49], while ϵ_a^{op} is always positive.

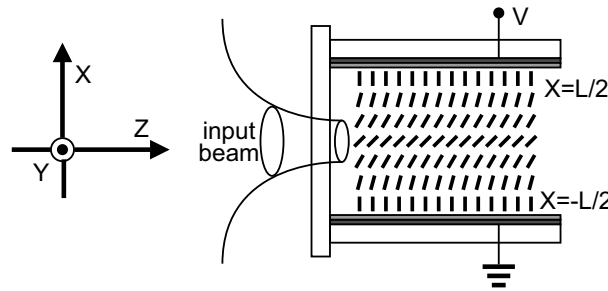


Figure 15. X-Z cross-section of the planar cell of the NLC with negative dielectric anisotropy, and the cell can be considered invariant along Y. Two pieces of glasses sandwich NLC. Polymer coatings provide molecules anchoring $\theta|_{X=L/2} = \theta|_{X=-L/2} = \pi/2$ at the boundaries, and ITO films allow for the application of low frequency bias. An optical beam propagating inside the cell along Z induces an index perturbation.

When an external low-frequency electrical field $\vec{E}_{rf} = E_{rf}\vec{e}_X$ and an optical field $\vec{E}_{op} = E_{op}\vec{e}_X$ are present, the molecular director \vec{n} expressed by $\vec{n}(\theta) = (\sin \theta, 0, \cos \theta)$ (θ is the tilt angle between \vec{n} and z) will be reorientated. NLC molecules approach the equilibrium state when the three torques are balanced, i.e., $\vec{\Gamma}_{op} + \vec{\Gamma}_{lf} + \vec{\Gamma}_{el} = 0$, where $\vec{\Gamma}_{op}$, $\vec{\Gamma}_{lf}$ and $\vec{\Gamma}_{el}$ are the optical field-induced torque, low-frequency electrical field induced torque and the elastic torque, respectively. Using the one-constant approximation [48], we can have the following:

$$\vec{\Gamma}_{el} = K\nabla^2\theta\vec{e}_Y,$$

where K is the NLC average elastic constant. We can also obtain the following [48]:

$$\begin{aligned} \vec{\Gamma}_{lf} &= \vec{D}_{rf} \times \vec{E}_{rf} = \epsilon_0\epsilon_a^{rf} \sin \theta \cos \theta E_{rf}^2 \vec{e}_Y, \\ \vec{\Gamma}_{op} &= \langle \vec{D}_{op} \times \vec{E}_{op} \rangle = \frac{1}{2}\epsilon_0\epsilon_a^{op} \sin \theta \cos \theta |E_{op}|^2 \vec{e}_Y, \end{aligned}$$

where $\vec{D}_{rf} = \epsilon_0\epsilon_{\perp}\vec{E}_{rf} + \epsilon_0\epsilon_a^{rf}(\vec{n} \cdot \vec{E}_{rf})\vec{n}$ and $\vec{D}_{op} = \epsilon_0n_{\perp}^2\vec{E}_{op} + \epsilon_0\epsilon_a^{op}(\vec{n} \cdot \vec{E}_{op})\vec{n}$ are the electric displacements, and $\langle \rangle$ denotes the time average.

In the absence of light, from the balance of torques of $\vec{\Gamma}_{el}$ and $\vec{\Gamma}_{lf}$, the pretilt angle $\hat{\theta}$ produced by the low-frequency electric field \vec{E}_{rf} can be determined, which is the only function of X [48]

$$2K \frac{d^2 \hat{\theta}}{dX^2} + \epsilon_0 \epsilon_a^{rf} E_{rf}^2 \sin(2\hat{\theta}) = 0. \tag{32}$$

If $\epsilon_a^{rf} > 0$ (the NLC with positive dielectric anisotropy), $d^2 \hat{\theta} / dX^2 < 0$, which indicates that the angle at the center ($X = 0$) of the cell $\theta_0 (= \hat{\theta}|_{X=0})$ is at the maximum and decreases as it proceeds closer to the boundaries. The opposite happens for the case that $\epsilon_a^{rf} < 0$ (the NLC with negative dielectric anisotropy), the angle at the center of the cell θ_0 is at the minimum and increases as it approaches the boundaries. As a result, NLC molecules should be anchored at the boundaries in a manner where $\theta|_{X=L/2} = \theta|_{X=-L/2} = 0$ for the positive dielectric anisotropy, as was observed in Refs. [3,10,50], and where $\theta|_{X=L/2} = \theta|_{X=-L/2} = \pi/2$, as shown in Figure 15, for negative dielectric anisotropy. In addition, the dependence of θ_0 on low-frequency voltage $V_{rf} (\approx E_{rf}L)$ is different for the NLC with positive and the negative dielectric anisotropy, when V_{rf} is higher than the Fréedericks threshold $V_{fr} = \pi \sqrt{K/\epsilon_0 |\epsilon_a^{rf}|}$. For the NLC with positive dielectric anisotropy [51], $\theta_0 \approx (\pi/2) \left[1 - (V_{fr}/V_{rf})^3 \right]$, and for the NLC with negative dielectric anisotropy, we have the following

$$\theta_0 \approx (\pi/2) \left(V_{fr}/V_{rf} \right)^3. \tag{33}$$

Although the molecule anchoring at the boundaries is different, the physical processes for both the positive and the negative are the same. Following the procedure to deal with the propagation of optical beams in an NLC with positive dielectric anisotropy [3,10,50], we obtained the equations for that in the NLC with negative dielectric anisotropy and found that the two cases can be uniformly expressed. In the presence of an externally applied (low-frequency) electric field E_{rf} , the propagation of the slowly varying envelope Φ of the optical field linearly polarized along the X -direction (the extraordinary light) and propagating along the Z -direction in the NLC-cell can be described by the following system:

$$2ik \frac{\partial \Phi}{\partial Z} + \nabla_{XY}^2 \Phi + k_0^2 \epsilon_a^{op} \left[\sin^2 \theta - \sin^2 \theta_0 \right] \Phi = 0, \tag{34}$$

$$2K \left(\frac{\partial^2 \theta}{\partial Z^2} + \nabla_{XY}^2 \theta \right) + \epsilon_0 \left(\epsilon_a^{rf} E_{rf}^2 + \epsilon_a^{op} \frac{|\Phi|^2}{2} \right) \sin(2\theta) = 0, \tag{35}$$

where $k = k_0 n_0$ with k_0 being the vacuum wavenumber and n_0 being the (linear) refractive index of the extraordinary light. Although it looks the same in form for both cases, Equation (35) is in fact different for either the positive or the negative cases because the sign of ϵ_a^{rf} is different. The term $\partial_Z^2 \theta$ in Equation (35) was proven to be negligible compared to $\nabla_{XY}^2 \theta$ [50]. Furthermore, we can write $\theta = \hat{\theta} + (\hat{\theta}/\theta_0)\Psi$, where Ψ represents optically induced angle perturbation. By simple substitution into Equation (35), we have the following:

$$2K \frac{\hat{\theta}}{\theta_0} \nabla_{\perp}^2 \Psi + \frac{4K}{\theta_0} \frac{\partial \hat{\theta}}{\partial x} \frac{\partial \Psi}{\partial x} - \epsilon_0 \epsilon_a^{rf} E_{rf}^2 \sin(2\hat{\theta}) \left[1 - \cos\left(2\frac{\hat{\theta}}{\theta_0}\Psi\right) + \frac{\Psi}{\theta_0} - \cot(2\hat{\theta})\sin\left(2\frac{\hat{\theta}}{\theta_0}\Psi\right) \right] + \epsilon_0 \epsilon_a^{op} \frac{|\Phi|^2}{2} \left[\sin(2\hat{\theta})\cos\left(2\frac{\hat{\theta}}{\theta_0}\Psi\right) + \cos(2\hat{\theta})\sin\left(2\frac{\hat{\theta}}{\theta_0}\Psi\right) \right] = 0, \tag{36}$$

which is the exact result after direct substitution without any approximation. Supposing that the beam width is far smaller than cell thickness L and noting that $\hat{\theta} \approx \theta_0$ and $\partial_x \hat{\theta} \approx 0$ in the middle of the cell, we can simplify Equation (36) into the following form:

$$\nabla_{XY}^2 \Psi - \frac{\epsilon_0 \epsilon_a^{rf} E_{rf}^2 \sin(2\theta_0) [1 - 2\theta_0 \cot(2\theta_0)]}{2K\theta_0} \Psi + \epsilon_0 \epsilon_a^{op} \frac{\sin(2\theta_0)}{4K} |\Phi|^2 = 0, \tag{37}$$

where we also made such an assumption of $\epsilon_a^{op} |\Phi|^2 / 2 \ll \epsilon_a^{rf} E_{rf}^2$ [3]. Multiplied by $\theta_0 \epsilon_a^{op} / E_{rf}^2 \epsilon_0 \epsilon_a^{rf} n_0 [1 - 2\theta_0 \cot(2\theta_0)]$, the equation can be re-expressed as follows:

$$\text{sgn}(\epsilon_a^{rf}) W_{mL}^2 \nabla_{XY}^2 n_{nl} - n_{nl} + n_2 |\Phi|^2 = 0, \tag{38}$$

where

$$n_{nl} = \frac{\epsilon_a^{op} \sin(2\theta_0) \Psi}{2n_0}, \tag{39}$$

$$n_2 = \frac{(\epsilon_a^{op})^2 \theta_0 \sin(2\theta_0)}{4n_0 \epsilon_a^{rf} E_{rf}^2 [1 - 2\theta_0 \cot(2\theta_0)]}, \tag{40}$$

$$W_{mL} = \frac{1}{E_{rf}} \left(\frac{2\theta_0 K}{\epsilon_0 |\epsilon_a^{rf}| \sin(2\theta_0) [1 - 2\theta_0 \cot(2\theta_0)]} \right)^{1/2}, \tag{41}$$

are the NRI, the Kerr coefficient and the nonlinear characteristic length for the NLC. When $W_{mL} \rightarrow 0$, Equation (38) above will be reduced to $n_{nl} = n_2 |\Phi|^2$ for the local limit [39]. Therefore, our definition of n_2 in Equation (40) can guarantee that its expression form is consistent when the degree of nonlocality transitions from the nonlocal case to the local case. On the other hand, the propagation equation for optical beams, Equation (34), is simplified as

$$i \frac{\partial \Phi}{\partial Z} + \frac{1}{2k} \nabla_{XY}^2 \Phi + k_0 n_{nl} \Phi = 0. \tag{42}$$

When $\epsilon_a^{rf} > 0$, the Kerr coefficient n_2 given by Equation (40) is positive, and Equation (38) becomes $W_{mL}^2 \nabla_{XY}^2 n_{nl} - n_{nl} + n_2 |\Phi|^2 = 0$. This equation is that of the molecular reorientation for NLC with positive dielectric anisotropy and has been discussed extensively [3,10,19,20,50–52]. For the NLC with negative dielectric anisotropy, however, $\epsilon_a^{rf} < 0$, the Kerr coefficient n_2 is negative, and Equation (38) becomes $W_{mL}^2 \nabla_{XY}^2 n_{nl} + n_{nl} - n_2 |\Phi|^2 = 0$, which has been rarely investigated so far. In this case ($\epsilon_a^{rf} < 0$), by the introduction of the dimensionless transform $u = \Phi / \Phi_0$, $\Delta n = n_{nl} / N_{L0}$, $x(y) = X(Y) / W_0$, $z = Z / kW_0^2$, and $w_m = W_{mL} / W_0$, where $\Phi_0 = \sqrt{n_0 / |n_2|} / kW_0$, $N_{L0} = 1 / k_0^2 W_0^2 n_0$, and W_0 is the beam width in Lab coordinate system, Equations (42) and (38) can be transformed as the dimensionless form $i \partial_z u + (1/2) \nabla_{xy}^2 u + \Delta n u = 0$ and $w_m^2 \nabla_{xy}^2 \Delta n + \Delta n + |u|^2 = 0$, which does be Equations (1) and (2) with $s = -1$.

6.2. Optical Nonlinearities of NLC with Negative Dielectric Anisotropy

By substitution of Equation (33) and $E_{rf} \approx V_{rf} / L$, the nonlinear characteristic length W_{mL} given by Equation (41) for the NLC with negative dielectric anisotropy is reduced to the following:

$$W_{mL} = \frac{L}{\pi^{4/3}} \sqrt{\frac{\gamma^{5/3}}{\sin \gamma - \gamma \cos \gamma}}, \tag{43}$$

where $\gamma = \pi^4 K^{3/2} / [\epsilon_0 (-\epsilon_a^{rf})]^{3/2} V_{rf}^3$. W_{mL} is, obviously, the function of the cell thickness L , the bias voltage V_{rf} and the material parameters of the NLC. By setting $dW_{mL}(V_{rf}) / dV_{rf} = 0$, we obtain $\gamma_{min} = 2.35$ at which W_{mL} / L takes the minimum 0.29, which does not depend on the material parameters of the NLC and is confirmed in Figure 16. Since model Equations (42) and (38) are obtained with the assumption that the beam width in the lab coordinate system, W_0 , is far smaller than NLC thickness L , we can assume that $W_0 = 0.1L$ so that the weakest degree of nonlocality $\sigma_{min} [= (W_{mL})_{min} / W_0]$ is 2.9,

and the degree of nonlocality $\sigma_0 (= W_{mL}/W_0)$ is always higher than σ_c (for an example, $\sigma_c|_{z=1} = 0.63$ for the (1 + 2)-dimensional case). Therefore, the NLC with negative dielectric anisotropy can only behave with self-focusing nonlinearity, and the transition from the self-focusing to the self-defocusing when σ_0 decreases across the critical point σ_c , which was predicted by the system of Equations (1) and (2) with $s = -1$, cannot be observed in the system of Equations (38) and (42) for the negative dielectric anisotropy, because the condition $\sigma_0 < \sigma_c$ cannot be realized in such a NLC. We also numerically investigated the propagation of the optical beam in the NLC with negative dielectric anisotropy described by Equations (34) and (35) without simplification and found that the beam can always sample the self-focusing nonlinearity indeed [53]. Consequently, the nonlinear refractive index due to reorientation in the pure NLC is always self-focusing, despite the sign of the anisotropy in the low-frequency domain.

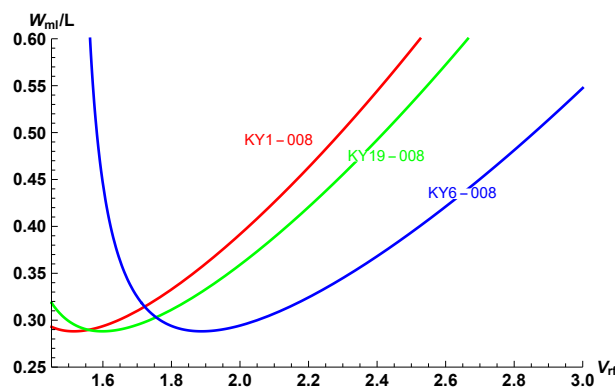


Figure 16. Dependence of W_{mL}/L on bias voltage V_{rf} for different NLC samples. The values of ϵ_a^{rf} are -5.9 , -5.3 and -3.8 for KY1-008, KY19-008 and KY6-008-type NLCs, respectively. $K = 1 \times 10^{-11} N$ for all materials.

It is a well-known fact [54–56] that only dark solitons can exist in nonlocally nonlinear media with the positively defining attenuating response and the negative Kerr coefficient ($n_2 < 0$) described by Equations (1) and (3) for $s = -1$, no matter how much the degree of nonlocality is. However, as discussed above, the nonlocally nonlinear system of Equations (1) and (2) with $s = -1$, that is, Equations (42) and (38) for the NLC with negative dielectric anisotropy, can exhibit self-focusing nonlinearity in high ranges of the degree of nonlocality ($\sigma_0 > \sigma_c$) and support the bright solitons. It is the unique feature of a nonlocally nonlinear system with oscillatory responses. By the relation of the input optical power between the Lab coordinate system $P_0^{(Lab)}$ and the dimensionless system P_0

$$P_0^{(Lab)} = \frac{k}{\omega\mu_0} \iint |\Phi|^2 dXdY = n_0 \sqrt{\frac{\epsilon_0}{\mu_0}} \Phi_0^2 W_0^2 \iint |u|^2 dx dy = \sqrt{\frac{\epsilon_0}{\mu_0}} \frac{1}{(-n_2)k_0^2} P_0,$$

we can have the theoretical value of the critical power P_{tc} via the variational result, i.e., Equation (23) for $s = -1$:

$$P_{tc} = \sqrt{\frac{\epsilon_0}{\mu_0}} \frac{1}{(-n_2)k_0^2} P_c|_{s=-1} = \sqrt{\frac{\epsilon_0}{\mu_0}} \frac{4n_0\epsilon_a^{rf} V_{rf}^2 [1 - 2\theta_0 \cot(2\theta_0)]}{(2\pi/\lambda)^2 L^2 (\epsilon_a^{op})^2 \theta_0 \sin(2\theta_0)} \frac{\pi^2}{2N_2(1, \sigma_0)}, \quad (44)$$

where $n_0 = n_{\parallel}n_{\perp} / \sqrt{n_{\parallel}^2 \cos^2 \theta_0 + n_{\perp}^2 \sin^2 \theta_0}$, and $N_2(1, \sigma_0) = \frac{\pi}{16\sigma_0^2} \left[\frac{1}{\sigma_0^2} \exp(-\frac{1}{2\sigma_0^2}) \text{Ei}(\frac{1}{2\sigma_0^2}) - 2 \right]$ with Ei being the exponential integral function [28]. By using the parameters for the NLC KY19-008 [57], $K = 1 \times 10^{-11} N$, $\epsilon_a^{op} = 0.74106$, $\epsilon_a^{rf} = -5.3$, $L = 80 \mu\text{m}$, and beam parameters including $\lambda = 532 \text{ nm}$ and $W_0 = 4 \mu\text{m}$, we obtain $P_{tc} \approx 6.37 \text{ mW}$ when voltage bias $V_{rf} \approx 3.4 \text{ V}$ is applied.

7. Conclusions

We reviewed recent research on the nonlocally nonlinear system with oscillatory responses. This nonlinear system exhibits various new features, such as the nonlocality-controllable transitions of nonlinearities, unique modulational instabilities and new kinds of solitons. The unique features of nonlocally nonlinear system come from oscillatory responses without positive definiteness, which are quite different from the positively defining attenuating ones discussed so far. In particular, in nonlocally nonlinear media with oscillatory responses, we theoretically predicted that bright solitons can exist even when the Kerr coefficient is negative, where only dark solitons were supposed to exist if the response functions are positively defining and attenuating. We find that oscillatory responses can describe the interaction between the optical beam and the nematic liquid crystal with negative dielectric anisotropy, although self-defocusing nonlinearity cannot be exhibited in such a nematic liquid crystal. These new and unexpected behaviors found in the nonlocally nonlinear system with oscillatory responses are of significance at a fundamental level, especially for the relevance between the nonlocality and the focusing-defocusing nonlinearities, which appears to be promising for tailoring optical properties in materials.

Author Contributions: Writing—original draft preparation, writing—review and editing, G.L.; conceptualization, methodology, W.H.; formal analysis, J.L.; conceptualization, methodology, supervision, project administration, Q.G. All authors have read and agreed to the published version of the manuscript.

Funding: This research was supported by the Natural Science Foundation of Guangdong Province of China (No. 2021A1515012214) and the Science and Technology Program of Guangzhou (No. 2019050001).

Acknowledgments: The authors would like to express the thanks to Ying Xiang (Guangdong University of Technology) for his useful and careful discussions on the issues of nematic liquid crystals.

Conflicts of Interest: The authors declare no conflict of interest.

References

1. Shen, Y.R. *Principles of Nonlinear Optics*; Wiley: New York, NY, USA, 1984.
2. Boyd, R.W. *Nonlinear Optics*; Academic Press: Amsterdam, The Netherlands, 2008.
3. Assanto, G. *Nematicons: Spatial Optical Solitons in Nematic Liquid Crystals*; John Wiley & Sons, Inc.: Hoboken, NJ, USA, 2013.
4. Snyder, A.W.; Mitchell, D.J. Accessible Solitons. *Science* **1997**, *276*, 1538. [CrossRef]
5. Guo, Q.; Lu, D.; Deng, D. Nonlocal spatial optical solitons. In *Advances in Nonlinear Optics*; Chen, X., Zhang, G., Zeng, H., Guo, Q., Shen, W., Eds.; De Gruyter: Berlin, Germany, 2015; Chapter 4, pp. 227–305.
6. Peccianti, M.; Assanto, G. Nematicons. *Phys. Rep.* **2012**, *516*, 147. [CrossRef]
7. Królikowski, W.; Bang, O.; Nikolov, N.I.; Neshev, D.; Wyller, J.; Rasmussen, J.J.; Edmundson, D. Modulational instability, solitons and beam propagation in spatially nonlocal nonlinear media. *J. Opt. B Quantum Semiclass. Opt.* **2004**, *6*, S288. [CrossRef]
8. Guo, Q. Nonlocal spatial solitons and their interactions. In *Optical Transmission, Switching, and Subsystems*; SPIE: Bellingham, WA, USA, 2004; Volume 5281, pp. 581–594.
9. Królikowski, W.; Bang, O.; Briedis, D.; Dreischuh, A.; Edmundson, D.; Luther-Davies, B.; Neshev, D.; Nikolov, N.; Petersen, D.E.; Rasmussen, J.J. Nonlocal solitons. In *Nonlinear Optics Applications*; SPIE: Warsaw, Poland, 2005; Volume 5949, pp. 76–85.
10. Conti, C.; Peccianti, M.; Assanto, G. Route to nonlocality and observation of accessible solitons. *Phys. Rev. Lett.* **2003**, *91*, 073901. [CrossRef]
11. Conti, C.; Peccianti, M.; Assanto, G. Observation of optical spatial solitons in a highly nonlocal medium. *Phys. Rev. Lett.* **2004**, *92*, 113902. [CrossRef]
12. Piccardi, A.; Alberucci, A.; Buchnev, O.; Kaczmarek, M.; Khoo, I.C.; Assanto, G. Frequency-controlled deflection of spatial solitons in nematic liquid crystals. *Appl. Phys. Lett.* **2012**, *101*, 081112. [CrossRef]
13. Piccardi, A.; Alberucci, A.; Buchnev, O.; Kaczmarek, M.; Khoo, I.C.; Assanto, G. Frequency-controlled routing of self-confined beams in nematic liquid crystals. *Mol. Cryst. Liq. Cryst.* **2013**, *573*, 26. [CrossRef]
14. Laudyn, U.; Kwasny, M.; Karpierz, M.; Assanto, G. Electro-optic quenching of nematicon fluctuations. *Opt. Lett.* **2019**, *44*, 167. [CrossRef]
15. Rotschild, C.; Cohen, O.; Manela, O.; Segev, M.; Carmon, T. Solitons in nonlinear media with an infinite range of nonlocality: First observation of coherent elliptic solitons and of vortex-ring solitons. *Phys. Rev. Lett.* **2005**, *95*, 213904. [CrossRef]

16. Suter, D.; Blasberg, T. Stabilization of transverse solitary waves by a nonlocal response of the nonlinear medium. *Phys. Rev. A* **1993**, *48*, 4583. [CrossRef]
17. Segev, M.; Crosignani, B.; Yariv, A.; Fischer, B. Spatial solitons in photorefractive media. *Phys. Rev. Lett.* **1992**, *68*, 923. [CrossRef] [PubMed]
18. Parola, A.; Salasnich, L.; Reatto, L. Structure and stability of bosonic clouds: Alkali-metal atoms with negative scattering length. *Phys. Rev. A* **1998**, *57*, R3180. [CrossRef]
19. Rasmussen, P.D.; Bang, O.; Krolikowski, W. Theory of nonlocal soliton interaction in nematic liquid crystals. *Phys. Rev. E* **2005**, *72*, 066611. [CrossRef] [PubMed]
20. Hu, W.; Zhang, T.; Guo, Q.; Xuan, L.; Lan, S. Nonlocality-controlled interaction of spatial solitons in nematic liquid crystals. *Appl. Phys. Lett.* **2006**, *89*, 071111. [CrossRef]
21. Nikolov, N.I.; Neshev, D.; Bang, O.; Krolikowski, W.Z. Quadratic solitons as nonlocal solitons. *Phys. Rev. E* **2003**, *68*, 036614. [CrossRef] [PubMed]
22. Esbensen, B.K.; Bache, M.; Krolikowski, W.; Bang, O. Quadratic solitons for negative effective second-harmonic diffraction as nonlocal solitons with periodic nonlocal response function. *Phys. Rev. A* **2012**, *86*, 023849. [CrossRef]
23. Qin, J.; Dong, G.; Malomed, B.A. Hybrid matter-wave-microwave solitons produced by the local-field effect. *Phys. Rev. Lett.* **2015**, *115*, 023901. [CrossRef]
24. Wang, J.; Li, Y.; Guo, Q.; Hu, W. Stabilization of nonlocal solitons by boundary conditions. *Opt. Lett.* **2014**, *39*, 405. [CrossRef]
25. Wang, J.; Ma, Z.; Li, Y.; Lu, D.; Guo, Q.; Hu, W. Stable quadratic solitons consisting of fundamental waves and oscillatory second harmonics subject to boundary confinement. *Phys. Rev. A* **2015**, *91*, 033801. [CrossRef]
26. Zheng, Y.; Gao, Y.; Wang, J.; Lv, F.; Lu, D.; Hu, W. Bright nonlocal quadratic solitons induced by boundary confinement. *Phys. Rev. A* **2017**, *95*, 013808. [CrossRef]
27. Liang, G.; Hong, W.; Luo, T.; Wang, J.; Li, Y.; Guo, Q.; Hu, W.; Christodoulides, D.N. Transition between self-focusing and self-defocusing in a nonlocally nonlinear system. *Phys. Rev. A* **2019**, *99*, 063808. [CrossRef]
28. Liang, G.; Dang, D.; Li, W.; Li, H.; Guo, Q. Nonlocality-controllable Kerr-nonlinearity in nonlocally nonlinear system with oscillatory responses. *New J. Phys.* **2020**, *22*, 073204. [CrossRef]
29. Liang, G.; Hong, W.; Guo, Q. Spatial solitons with complicated structure in nonlocal nonlinear media. *Opt. Express.* **2016**, *24*, 28784. [CrossRef] [PubMed]
30. Zhong, L.; Dang, D.; Li, W.; Ren, Z.; Guo, Q. Multi-peak solitons in nonlocal nonlinear system with sine-oscillation response. *Commun. Nonlinear Sci.* **2022**, *109*, 106322. [CrossRef]
31. Wang, Z.; Guo, Q.; Hong, W.; Hu, W. Modulational instability in nonlocal Kerr media with a sine-oscillatory response. *Opt. Commun.* **2017**, *394*, 31. [CrossRef]
32. Guan, J.; Ren, Z.; Guo, Q. Stable solution of induced modulation instability. *Sci. Rep.* **2020**, *10*, 10081. [CrossRef]
33. Anderson, D. Variational approach to nonlinear pulse propagation in optical fibers. *Phys. Rev. A* **1983**, *27*, 3135. [CrossRef]
34. Guo, Q.; Luo, B.; Chi, S. Optical beams in sub-strongly non-local nonlinear media: A variational solution. *Opt. Commun.* **2006**, *259*, 336. [CrossRef]
35. Haus, H.A. *Waves and Fields in Optoelectronics*; Prentice-Hall: Englewood Cliffs, NJ, USA, 1984.
36. Agrawal, G.P. *Nonlinear Fiber Optics*, 4th ed.; Academic: San Diego, CA, USA, 2007.
37. Hu, Y.; Lou, S. Analytical descriptions of dark and gray solitons in nonlocal nonlinear media. *Commun. Theor. Phys.* **2015**, *64*, 665. [CrossRef]
38. Hong, W.; Tian, B.; Li, R.; Guo, Q.; Hu, W. Perturbation-iteration method for multi-peak solitons in nonlocal nonlinear media. *J. Opt. Soc. Am. B* **2018**, *35*, 317. [CrossRef]
39. Kivshar, Y.S.; Agrawal, G.P. *Optical Solitons: From Fibers to Photonic Crystals*; Academic Press Inc.: Cambridge, MA, USA, 2003.
40. Sakaguchi, H.; Malomed, B.A. Solitons in combined linear and nonlinear lattice potentials. *Phys. Rev. A* **2010**, *81*, 013624. [CrossRef]
41. Qin, J.; Dong, G.; Malomed, B.A. Stable giant vortex annuli in microwave-coupled atomic condensates. *Phys. Rev. A* **2016**, *94*, 053611. [CrossRef]
42. Qin, J.; Liang, Z.; Malomed, B.A.; Dong, G. Tail-free self-accelerating solitons and vortices. *Phys. Rev. A* **2019**, *99*, 023610. [CrossRef]
43. Buryak, A.V.; Kivshar, Y.S. Solitons due to second harmonic generation. *Phys. Lett. A* **1995**, *197*, 407. [CrossRef]
44. Xu, Z.; Kartashov, Y.V.; Torner, L. Upper threshold for stability of multipole-mode solitons in nonlocal nonlinear media. *Opt. Lett.* **2005**, *30*, 3171. [CrossRef]
45. Dong, L.; Ye, F. Stability of multipole-mode solitons in thermal nonlinear media. *Phys. Rev. A* **2010**, *81*, 013815. [CrossRef]
46. Ouyang, S.; Guo, Q.; Hu, W. Perturbative analysis of generally nonlocal spatial optical solitons. *Phys. Rev. E* **2006**, *74*, 036622. [CrossRef]
47. Tian, B.; Guo, Q.; Hong, W.; Hu, W. Extension of the perturbation-iteration method to (1 + 2)-dimensional case. *Optik* **2019**, *192*, 162909. [CrossRef]
48. Khoo, I.C. *Liquid Crystals: Physical Properties and Nonlinear Optical Phenomena*; Wiley: New York, NY, USA, 1995.
49. Schiekkel, M.F.; Fahrenschon, K. Deformation of nematic liquid crystals with vertical orientation in electrical fields. *Appl. Phys. Lett.* **1971**, *19*, 391. [CrossRef]

50. Peccianti, M.; Conti, C.; Assanto, G.; De Luca, A.; Umeton, C. Nonlocal optical propagation in nonlinear nematic liquid crystals. *J. Nonlinear Opt. Phys. Mater.* **2003**, *12*, 525. [CrossRef]
51. Peccianti, M.; Conti, C.; Assanto, G. Interplay between nonlocality and nonlinearity in nematic liquid crystals. *Opt. Lett.* **2005**, *30*, 415. [CrossRef] [PubMed]
52. Assanto, G.; Peccianti, M. Spatial solitons in Nematic liquid crystals. *IEEE J. Quantum Electron.* **2003**, *39*, 13. [CrossRef]
53. Zhang, Y. Numerical Research on Modulation Instability of Nematic Liquid Crystals with Negative Dielectric Anisotropy. Master's Dissertation, South China Normal University, Guangzhou, China, 2005. (In Chinese)
54. Krolikowski, W.; Bang, O. Solitons in nonlocal nonlinear media: Exact solutions. *Phys. Rev. E* **2000**, *63*, 016610. [CrossRef]
55. Kong, Q.; Wang, Q.; Bang, O.; Krolikowski, W. Analytical theory of dark nonlocal solitons. *Opt. Lett.* **2010**, *35*, 2152. [CrossRef] [PubMed]
56. Conti, C.; Fratilocchi, A.; Peccianti, M.; Ruocco, G.; Trillo, S. Observation of a gradient catastrophe generating solitons. *Phys. Rev. Lett.* **2009**, *102*, 083902. [CrossRef] [PubMed]
57. Wang, J.; Chen, J.; Liu, J.; Li, Y.; Guo, Q.; Hu, W.; Xuan, L. Nematicons in liquid crystals with negative dielectric anisotropy. *arXiv* **2018**, arXiv:1403.2154v2.

Review

Light Propagation in Confined Nematic Liquid Crystals and Device Applications

Antonio d'Alessandro *  and Rita Asquini 

Centre of Nanotechnologies Applied to Engineering–CNIS, Department of Information Engineering, Electronics and Telecommunications, Sapienza University of Rome, 00185 Roma, Italy; rita.asquini@uniroma1.it
* Correspondence: antonio.dalessandro@uniroma1.it

Abstract: Liquid crystals are interesting linear and nonlinear optical materials used to make a wide variety of devices beyond flat panel displays. Liquid crystalline materials can be used either as core or as cladding of switchable/reconfigurable waveguides with either an electrical or an optical control or both. In this paper, materials and main device structures of liquid crystals confined in different waveguide geometries are presented using different substrate materials, such as silicon, soda lime or borosilicate glass and polydimethylsiloxane. Modelling of the behaviour of liquid crystal nanometric molecular reorientation and related refractive index distribution under both low-frequency electric and intense optical fields is reported considering optical anisotropy of liquid crystals. A few examples of integrated optic devices based on waveguides using liquid crystalline materials as core for optical switching and filtering are reviewed. Reported results indicate that low-power control signals represent a significant feature of photonic devices based on light propagation in liquid crystals, with performance, which are competitive with analogous integrated optic devices based on other materials for optical communications and optical sensing systems.

Keywords: liquid crystals; optical waveguides; optoelectronics; integrated optics; electro-optics; nonlinear optics

Citation: d'Alessandro, A.; Asquini, R. Light Propagation in Confined Nematic Liquid Crystals and Device Applications. *Appl. Sci.* **2021**, *11*, 8713. <https://doi.org/10.3390/app11188713>

Academic Editor: Andrés Márquez

Received: 23 August 2021
Accepted: 15 September 2021
Published: 18 September 2021

Publisher's Note: MDPI stays neutral with regard to jurisdictional claims in published maps and institutional affiliations.



Copyright: © 2021 by the authors. Licensee MDPI, Basel, Switzerland. This article is an open access article distributed under the terms and conditions of the Creative Commons Attribution (CC BY) license (<https://creativecommons.org/licenses/by/4.0/>).

1. Introduction

It is well known that the most important application of liquid crystals (LCs) nowadays is flat panel displays (FPD), which is a very mature industry. Recently, other FPD technologies, such as OLED and micro-LED, are competing with LC-FPD in many applications. However, LCs are excellent materials for light phase modulation which cannot be achieved by OLED and micro-LED. Indeed, many photonic devices/systems and applications based on LC modulations are developing.

Liquid crystalline materials used for most applications are usually made of mixtures of different compounds to optimize their electro-optical performance. LC molecules, made of ring systems, linking groups, substituents and terminal groups as sketched in Figure 1, are designed in order to optimize LC physical and optical properties.

LCs have low optical losses from UV to IR with scattering decreasing as $\lambda^{-2.34}$ [1] gaining interest for guide wave devices [2,3]. LC have been demonstrated as effective materials to make both electrically [4] and optically [5] controlled cores for switchable and reconfigurable waveguides to be used at the wavelength of 1.55 μm in optical communications for their attractive optical properties. The efficient electro-optical effect with the additional advantage of negligible electrical current absorption and the nonlinear optical properties allow very low power consumption without appreciable energy dissipation. Linear optical properties stimulated the study and development of LC-based waveguides [6–15].

Nonlinear optical properties fostered intense research activity on the development of solitonic propagation in LC with many potential applications [16–22]. Photonic bandgap structures obtained by infiltrating LC in hollow optical fibres, the so-called photonic LC

fibres, were also intensely studied, generating another broad research line [23–27]. The light characteristics make LC-based photonic devices interesting potential candidates for both datacom and optofluidic applications [28–32]. LC propagation properties were also interestingly investigated to generate optical vortices [33,34], which may result in an important breakthrough in the development of optical tweezers, high-order quantum entanglement and novel nonlinear optic effects with competing nonlinearities [35,36]. Another interesting effect of light propagation in LC is related to all-optical angular control of the molecular alignment in LC films due to light and matter angular momentum conservation [37,38].

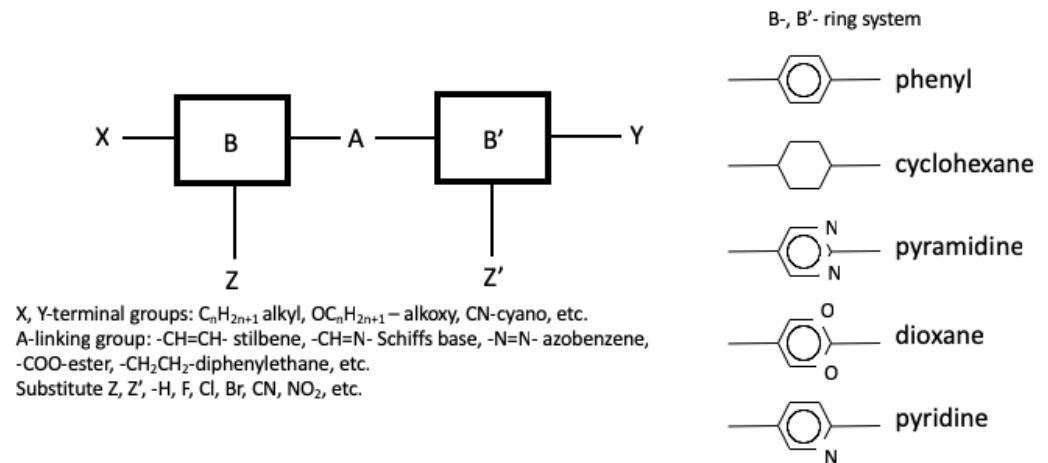


Figure 1. Schematic molecular structure of thermotropic LCs.

More recently, LC-based optical sources were demonstrated to envision full integration of optical functionalities in a single chip using liquid crystalline materials. OLEDs were reported by employing liquid-crystalline host matrix in the emission layer [39]. Lasers were demonstrated by means of a novel approach to generate actively Q-switched laser pulses based on an integrated waveguide chip and an LC cell in the deformed helix ferroelectric (DHF) mode, able to behave like an active Q-switch modulator under a wide range of repetition frequencies [40]. Vertical cavity surface-emitting laser, including LC as a tuning medium, was also reported [41].

Despite the many interesting optical properties of LCs, it is no small undertaking to make waveguiding devices in which input and output signals can be coupled in and out by using standard optical fibres. In this paper, a review of proposed devices is presented to make optical switches and filters based on propagation properties of nematic LCs in which a signal is transmitted between two standard single mode fibres. Such devices can be integrated in many systems for several applications such as communications and sensor microsystems. In Section 2, materials and main device structures of LCs confined in different waveguide geometries are presented by focusing on fabrication issues. Section 3 reports on modelling for designing guide wave LC devices and simulations of their operation. Section 4 shows some examples of optical switches and tunable filters in which light beams are confined in oriented nematic LC channels. Section 5 reports some perspective conclusions on further research development of LC-based guided wave devices.

2. Materials and LC Waveguide Structures

LC materials can be used either to make a core of optical waveguides, in which light beams can be confined, or to make a cladding [42]. In both cases tunable or reconfigurable optical channels can be obtained by exploiting the LC electro-optic effect. LCs can be infiltrated by capillarity in different confined geometries of optical waveguides [8–10] or optical fibres [43].

2.1. Nematic LC Confined in SiO₂/Si V-grooves

A channel waveguide can be obtained by infiltrating a nematic LC in a SiO₂/Si groove as shown in Figure 2a. The ITO layer and the n-Si substrate act as electrodes to apply an external electric field. A silicon V-groove is made by exploiting anisotropic etching of silicon. Typical groove width ranges from 5 to 15 μm. A native thermal oxide SiO₂, obtained in an oven at about 1100 °C acts as a low index cladding, considering that a nematic LC has a refractive index higher than 1.45. The V-groove is fabricated by means of a micromachining process whose details are described in ref [44].

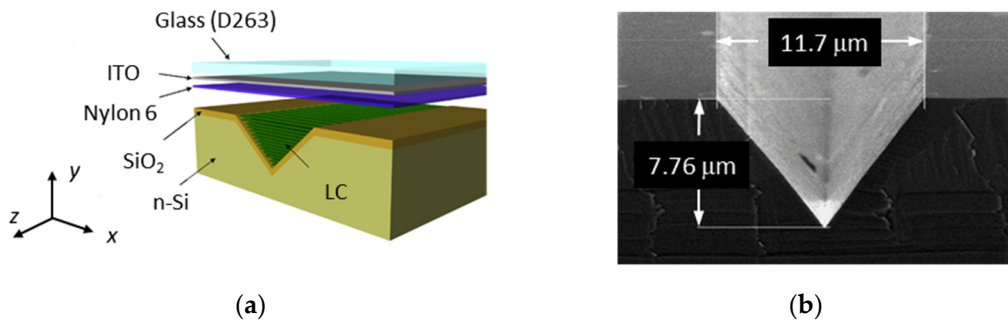


Figure 2. Optical waveguide made of LC infiltrated in a SiO₂/Si V-groove: (a) Three-dimensional exploded schematic, showing the orientation of the nematic LC molecules along the V-groove; (b) Electron microscope scanning of a SiO₂/Si V-groove.

Figure 2b shows a scanning electron microscope picture of the V-groove in which smoothness of SiO₂/Si surfaces is able to minimize defects in the embedded LC molecules, consequently attenuating light scattering in the final LC waveguide.

The etching of Si creates a V-groove with an angle $\alpha = 54.7^\circ$ using (100) Si wafer as schematically shown in Figure 3a. A glass cover of 0.5 mm is then placed on top of the V-groove [4]. A D263 borosilicate glass substrate is used with a refractive index $n_{D263} = 1.516$ (at the wavelength $\lambda = 1.55 \mu\text{m}$) intermediate between the values of the extraordinary and the ordinary refractive index of the LC used, such as E7 ($n_e = 1.69, n_o = 1.5$ at wavelength $\lambda = 1.55 \mu\text{m}$), which allows the creation of an optical switch [4]. A thin film of Nylon 6 is spanned and rubbed on top of the ITO film, to align the LC along the groove. Nematic LC E7 in the isotropic phase is infiltrated in the covered V-groove by capillarity in vacuum at 80 °C and then cooled down to the room temperature. Figure 3b shows the orientation of nematic LC molecules, whose tilt angle θ is controlled by the applied voltage between the ITO and n-Si.

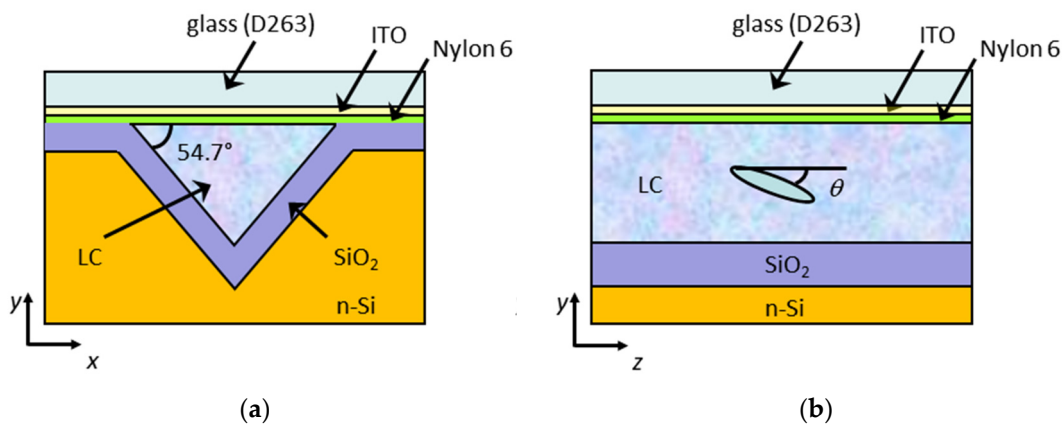


Figure 3. Schematic images of an LC waveguide in SiO₂/Si groove: (a) cross-section indicating the etching angle of the Si groove; (b) longitudinal section showing the orientation of the nematic LC molecules under applied electric field between ITO and n-Si.

Light is coupled to LC waveguides in Si/SiO₂ grooves, referred to as LCW (Liquid Crystal Waveguide), by fibre butt-coupling, as shown in Figure 4. Since LC-NOA61 interface was used, total coupling losses, including input and output, of 4.5 dB or better were measured, as a result of minimization of LC molecular random orientation representing a source of light scattering at the input and output faces of the LCW, which determined higher coupling losses in previous samples without LC-NOA61 interface [45]. Propagation losses resulted to be about 6 dB/cm which can be further lowered by using photoalignment techniques, able to improve the optical quality of the LCW [46,47].

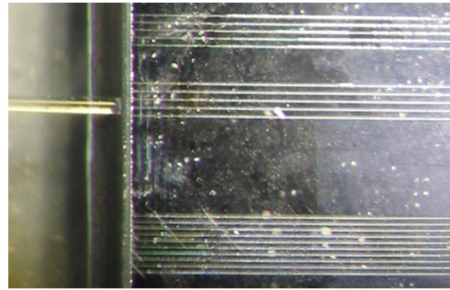


Figure 4. Picture of a single-mode optical fiber which is butt-coupled to a chip, including a set of LC waveguides on SiO₂/Si grooves. Waveguide width is 8–12 μm .

2.2. Nematic LC in PDMS Waveguides

Optical waveguides can be made by infiltrating a nematic LC in polydimethylsiloxane (PDMS) channels by capillarity. Such waveguides are referred as LC:PDMS waveguides. Use of PDMS is motivated since it is a material often used for microfluidic applications with high optical quality [48]. PDMS is optical transparent, with low surface energy in the range of 20–23 mJ/m^2 at 20 °C [49], low dielectric constant in the range of 2.32–2.40 [50] and Young's modulus, which is between 0.57 MPa and 3.7 MPa [51], and thermally and optically enabled polymerization. PDMS is also reliable for soft lithographic fabrication of many microfluidic and micro-optical devices [52].

Flexibility is another attractive feature of PDMS which is effectively used in robotics, automation, consumer electronics and in novel applications, such as health care and biomedical technologies. PDMS is used in optical interconnections for datacom applications to replace metallic connections whose performance in terms of bit rate are very low and suffer problems related to high heat dissipation [53].

PDMS channels to be filled with a nematic LC are fabricated by the cast and moulding technique involving several technological phases as shown in Figure 5 and described in ref. [31].

The PDMS channels are filled with a nematic LC by capillarity which results in homeotropically alignment as shown in Figure 6a. Homeotropic alignment of LC is due to the hydrophobic characteristic of the PDMS inner surface. A fabricate sample including LC:PDMS waveguides with widths of 8, 10 and 15 μm is reported in Figure 6b. The optical characterization to check the LC alignment in the LC:PDMS waveguides is performed using a polarized microscope. Polarized light is transmitted through the channels, revealing the homeotropic arrangement of the LC molecules. Such orientation of the LC is proven by the black part in the central region for the waveguides indicating that polarization of input light is not changed when transmitted through the LC and is stopped by the crossed analyser, as it can be observed in Figure 6c. Light leaks through the edges of the waveguides because of the optical retardation induced by the LC molecules homeotropically aligned on the vertical sides of the PDMS channels.

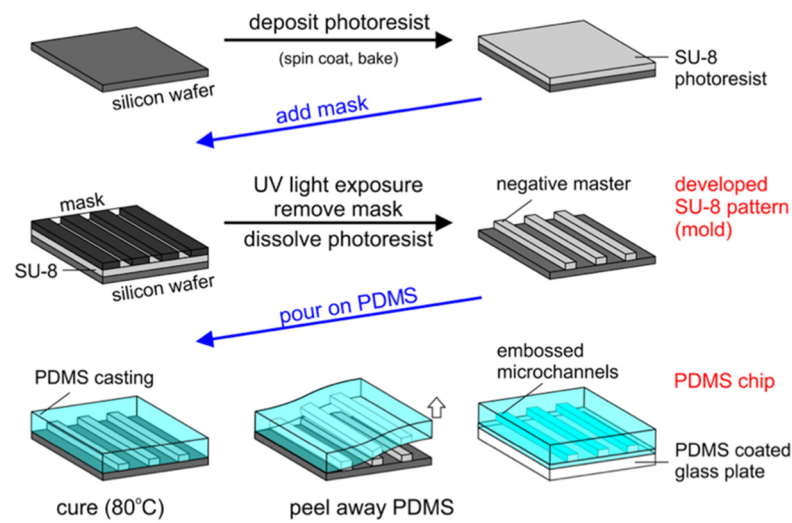


Figure 5. Technological phases to make PDMS microchannels used obtain LC:PDMS waveguides.

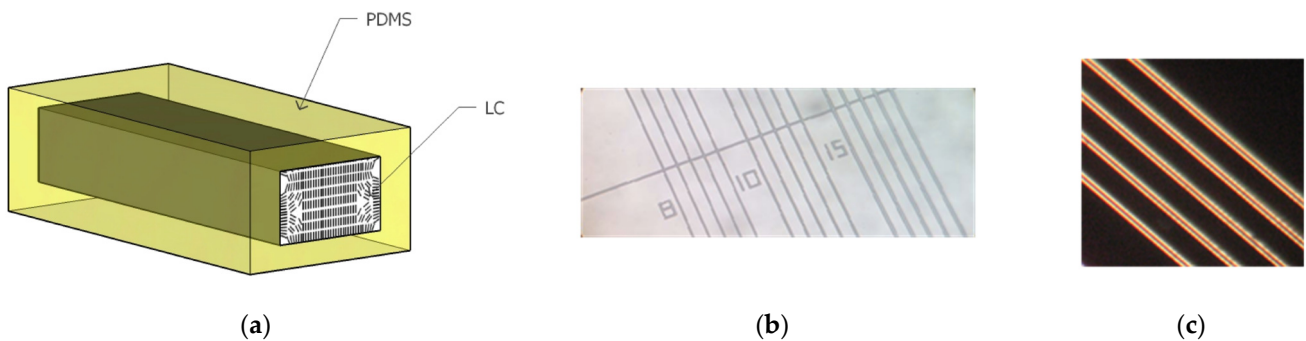


Figure 6. LC:PDMS waveguides: (a) oriented LC molecules inside the PDMS channel; (b) PDMS chip with optical waveguides with widths of 8, 10 and 15 μm ; (c) image of LC:PDMS waveguides with a width of 10 μm observed under the microscope in transmission.

LC molecular orientation inside the PDMS channel induces a refractive index distribution which determines polarization-independent light propagation [31]. Green laser light at a wavelength of 532 nm and red light using an He-Ne laser source at a wavelength of 632.8 nm were efficiently fibre butt-coupled to the LC:PDMS waveguide as shown in Figure 7a. Propagation in the C-band was also studied using a tunable laser source between 1510 nm and 1590 nm. Light transmission versus polarization orientation was measured using a set-up including a polarization controller, consisting of a half-wave plate between two quarter-wave plates, an optical power meter and a polarizer at the output of the waveguide. It has been observed that light polarization does not vary as it propagates along the LC:PDMS channel for any polarization at the input. A polarization differential loss of only 0.3 dB, as shown in Figure 7b, was measured with propagation losses of about 8 dB/cm.

It is possible to control LC:PDMS waveguides by means of coplanar electrodes. Preliminary measurements show that LC molecules can be switched by applying a square voltage of 1 kHz with an amplitude of about 2 V. In this case, only change of modal propagation was affected without a substantial light transmission of light, since the core refractive index remains above the PDMS refractive index. By choosing a PDMS with a refractive index intermediate between the ordinary and the extraordinary refractive of the LC, light modulation or switching is possible.

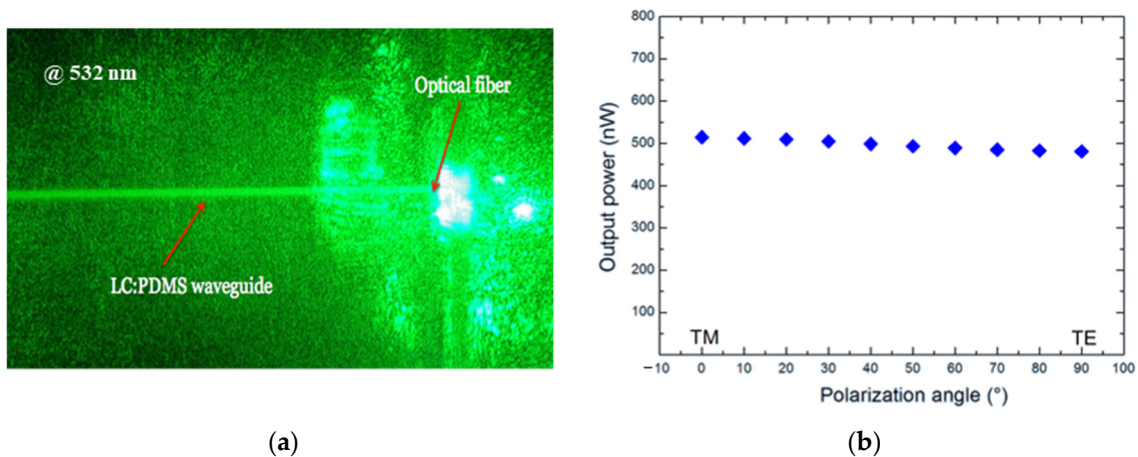


Figure 7. Propagation properties of an LC:PDMS waveguide with a width of 15 μm : (a) green laser light (wavelength = 532 nm) beam butt-coupled by using a single mode optical fiber of 125 μm ; (b) output power versus polarization at a wavelength of 1550 nm.

3. Modelling of Light Propagation in Nematic LC Waveguides

Light propagation in LC waveguides is affected by the LC molecular orientation represented by a unity vector referred to as director \mathbf{n} , as shown in Figure 8. Typical dimensions are a few nanometres along the molecular axis and about 1 nm in the perpendicular direction. Locally, a refractive index n_{\parallel} along the molecular axis and a refractive index n_{\perp} perpendicular to the molecular axis are defined. In the bulk LC, an extraordinary refractive index n_e and an ordinary refractive index n_o are defined along and perpendicularly to the director \mathbf{n} , respectively, showing a birefringence ranging between 0.15 and 0.5, depending on the chemical compounds and wavelengths.

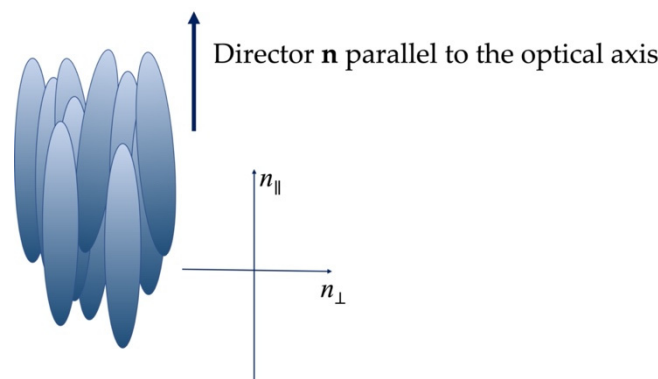


Figure 8. Molecular director \mathbf{n} and refractive index at the molecular level.

The optical anisotropy and the molecular orientation of the LC molecules induce the refractive index spatial distribution $n_{LC}(x,y)$ in the LCW determined by the electric field E_{ac} related to the ac voltage applied to the electrodes and the optical electric field E_{opt} of the propagating light beam when its intensity is relatively high. The electric field dependence enables both an electro-optic and an all-optical control. The LC molecular orientation is the result of the balance between the electric torques and the elastic restoring torque when an electric field is applied. The deformation pattern affected by the elastic torque is the result of a combination of three basic deformations, which are splay, twist and bend.

The orientation of the LC is imposed by the minimum of the free energy F given by:

$$F = F_{el} - F_{diel} - F_{opt} \quad (1)$$

in which F_{el} is the elastic term, F_{diel} is the dielectric term and F_{opt} is the optical term related to the electric field of the optical beam propagating in the LC.

The Oseen–Frank theory indicates that the elastic energy is given by [54]:

$$F_{el} = \frac{1}{2} \iiint [k_{11}(\nabla \cdot \mathbf{n})^2 + k_{22}(\mathbf{n} \cdot \nabla \times \mathbf{n})^2 + k_{33}(\mathbf{n} \times \nabla \times \mathbf{n})^2] dv \quad (2)$$

where k_{11} , k_{22} and k_{33} are the elastic constants corresponding to the splay, twist and bend, respectively, in which v is the volume. The dielectric energy is given by:

$$F_{diel} = \frac{1}{2} \iiint [\varepsilon_0 \varepsilon_{\perp,ac} |E_{ac}|^2 + \varepsilon_0 \Delta \varepsilon_{ac} (E_{ac} \cdot \mathbf{n})^2] dv \quad (3)$$

where ε_0 is the dielectric permittivity in vacuum, $\varepsilon_{\perp,ac}$ is the dielectric permittivity perpendicular to the optical axis, $\Delta \varepsilon_{ac}$ is the dielectric anisotropy, and E_{ac} is the applied electric field at low frequency. The optical term of the energy is given by:

$$F_{opt} = \frac{1}{2} \iiint [\varepsilon_0 \varepsilon_{\perp,opt} |E_{opt}|^2 + \varepsilon_0 \Delta \varepsilon_{opt} (E_{opt} \cdot \mathbf{n})^2] dv \quad (4)$$

where ε_0 is the dielectric permittivity in vacuum, $\varepsilon_{\perp,opt}$ is the dielectric permittivity perpendicular to the optical axis, $\Delta \varepsilon_{opt}$ is the dielectric anisotropy, and E_{opt} is the electric field at the optical frequencies. The minimum of F is determined by solving the Euler–Lagrange equation coupled with the solution of the Poisson equation for the distribution of the electric potential Φ in the LC structure:

$$\nabla \cdot [\varepsilon_{\perp,ac} \nabla \Phi + \Delta \varepsilon_{ac} (\nabla \Phi \cdot \mathbf{n}) \mathbf{n}] = 0 \quad (5)$$

The resulting output is the spatial distribution of the LC director orientation, from which the refractive index profile can be obtained. Figure 9 shows the typical refractive index distribution for an LCW in a SiO₂/Si groove with an upper width of 10 μm without (Figure 9a) and with an intense optical power of 25 mW at 1550 nm (Figure 9b). The possibility to have a refractive index distribution allows to design any optical device, and this is more crucial in LC waveguide-based integrated optic devices. The advantage of this model is that we do not make any hypothesis or simplification of the director and electric potential distributions. Therefore, this fully consistent model can be used for any type of geometry, either two- or three-dimensional, provided the boundary conditions are correctly stated. Alternatively, a study of the molecular director distribution can be obtained by means of Monte Carlo simulation techniques [55,56], also taking into account the external applied ac field [57].

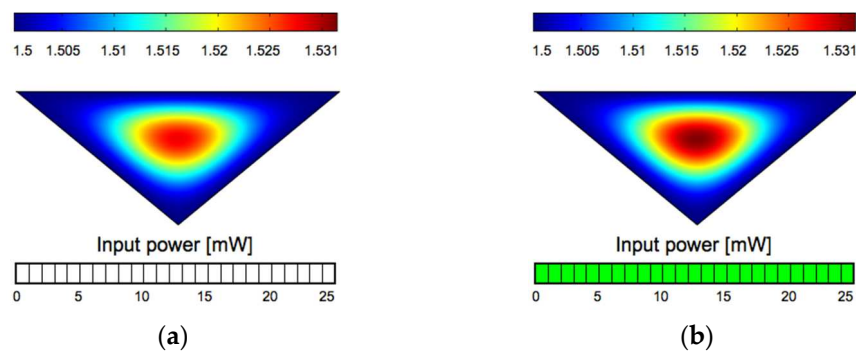


Figure 9. Computed all-optical dependence of the refractive index distribution in a SiO₂/Si LCW with upper width of 10 μm: (a) without input optical signal; (b) with input optical signal.

After computing the refractive index distribution, the beam propagation method can be used to simulate light propagation in LC waveguides, allowing design of photonic devices [58–60]. Figure 10 shows a typical contour map of the fundamental mode (Figure 10a) and a higher order mode (Figure 10b), evaluated at a wavelength of 1550 nm in a 10 μm wide LCW with an applied voltage of 10 V for which 35 modes were found.

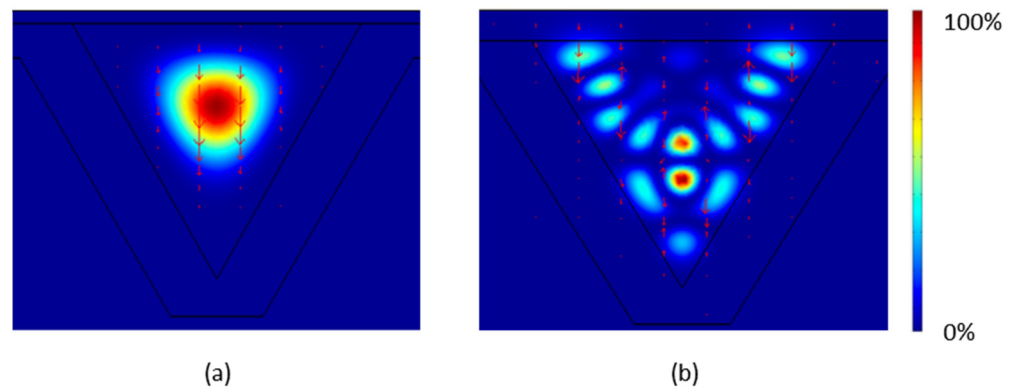


Figure 10. Computed contour map of TM-like propagation of 1550 nm wavelength in a 10 μm wide LCW with applied lines of electric field force (red arrows) for an applied voltage of 10 V: (a) fundamental mode; (b) higher order mode. The color maps show the field intensity distribution.

4. Device Applications

4.1. On-Off Optical Switch and Variable Optical Attenuator

Light propagation can be controlled in a SiO_2/Si LCW by either electrooptic or nonlinear optical effect or both. Since LC molecules can be reoriented along an external electric field, a square wave voltage is applied between the ITO electrode and the n-type Si substrate acting as a second electrode. An ac field is required to avoid electrolysis of the LC. Figure 11 shows the working principle of LCW acting as an on-off switch. A vertically polarized light signal runs into an increasing refractive index of the LC approaching the value of n_e of the LC along the molecular director \mathbf{n} as the voltage increases.

If voltage is not applied, the polarized light beam comes across the ordinary refractive index n_o of the LC, which is lower than the glass refractive index, as shown in Figure 11a. When a voltage is applied, the LC molecules are mostly reoriented perpendicularly to the propagation direction and to the glass plates, and confined light propagates in the LC core, as shown in Figure 11b. In fact, as shown in Figure 12, when a voltage is higher than just 2 V, light starts to propagate, and transmission increases with an on-off extinction ratio (ER) above 40 dB at a voltage of about 8 V, with ER defined as:

$$ER = 10 \log_{10} \frac{P(V) - P_{dark}}{P(0) - P_{dark}} \quad (6)$$

where $P(V)$ is the waveguide output power at voltage V and P_{dark} is the optical power at the photodetector without any input signal. The LCW acts both as an on-off switch and as a variable attenuator for voltages from 2 to 5 V as shown in Figure 12. The switching time is related to reorientation dynamics of the LC in the range of a few ms depending on the viscosity and elastic properties of the LC mixture. The applied voltage controls the number of supported optical modes, which increase as the voltage amplitude increases.

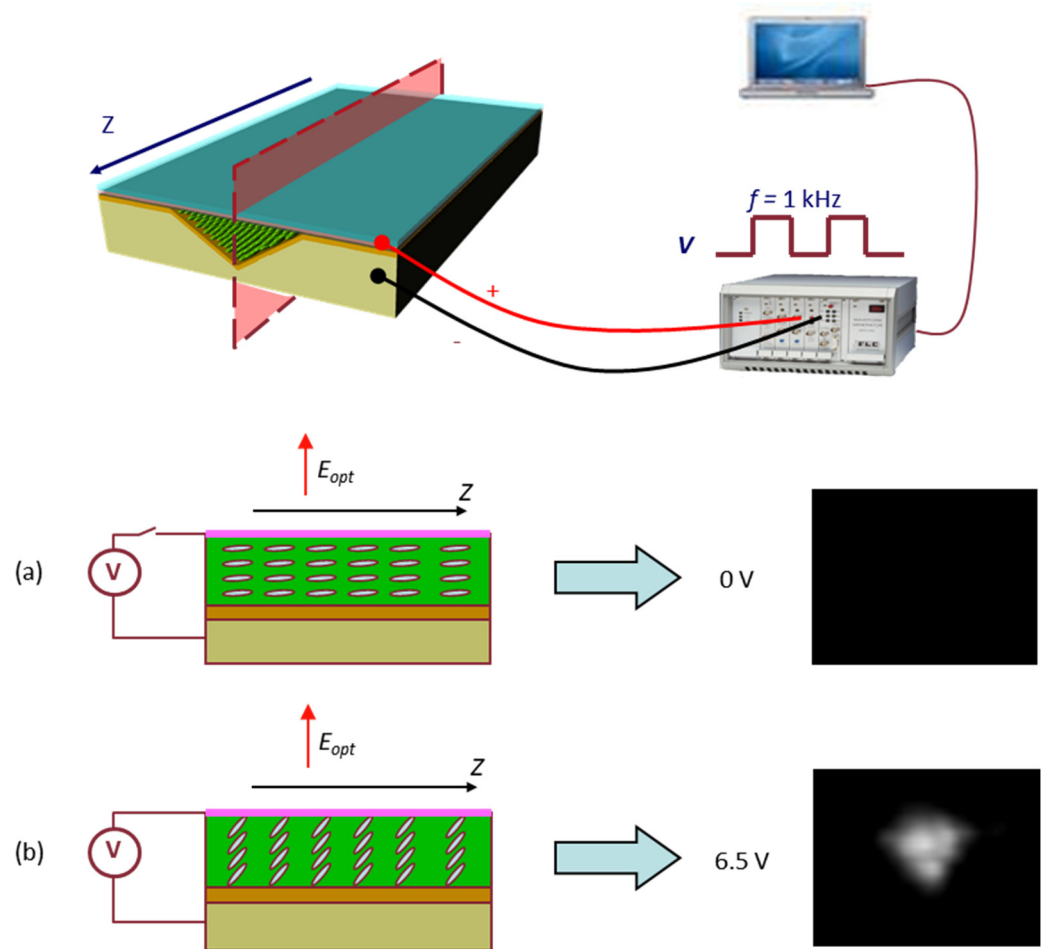


Figure 11. Operation of a SiO₂/Si groove LCW, with an electric field applied between n-Si substrate and an ITO layer: (a) case of no external voltage applied; (b) case of voltage above threshold to tilt LC molecules which allows light propagation. Reprinted with permission from Ref. [4]. Copyright 2010 IEEE.

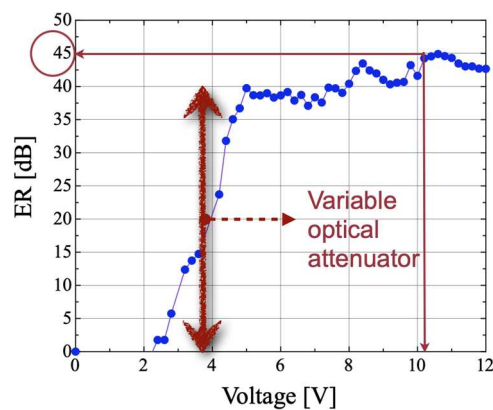


Figure 12. Plot of the extinction ratio (*ER*) as a function of the applied voltage for a SiO₂/Si LCW.

4.2. Electro-Optic Router

An integrated LC guided-wave electro-optic router based on a zero-gap directional coupler structure sketched in Figure 13 has been successfully designed [61] and experimentally demonstrated [62]. The device is made from a thin layer of nematic LC sandwiched between two glass plates to operate as a planar waveguide.

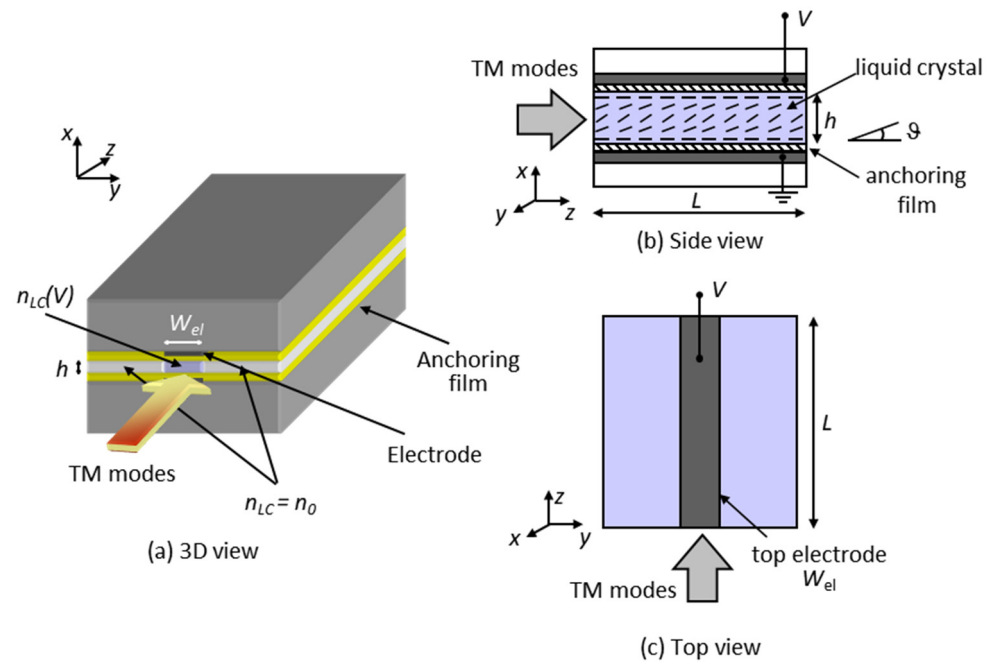


Figure 13. Electro-optic router: (a) three-dimensional view; (b) side view; (c) top view.

The working principle is based on an optical addressing, exploiting the relative wave-vector difference between two copropagating TM-polarized modes. The device works as an adjustable Y junction in a nematic LC, with an input bimodal stem from which two identical single-mode channels depart at a small angle, thus providing two output ports, as illustrated in Figure 14. When it is properly biased, this structure can route an optical signal towards any of the two output ports, switching between them by means of a small voltage modulation over a short propagation distance. In absence of bias, instead, the device does not provide transverse light confinement.

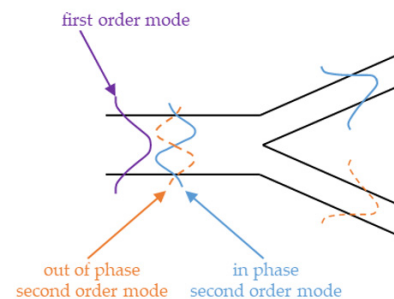


Figure 14. Image of the field distribution due to two superimposed TM guided modes in a 1×2 optical switch encompassing an output Y-junction.

A near infrared switching and signal routing at the wavelength of 1064 nm with a positive uniaxial nematic LC 5CB has been experimentally demonstrated, with modulations of 210 mV for a device length of 160 μm . The balanced superposition of TM_{00} and TM_{01} modes has been excited with a 0.4 mW power beam focused on the waveguide facet. The tilt and offset with respect to the channel axis was carefully adjusted using a $10\times$ microscope. The propagating modes gain a relative phase $\Delta\phi = 2\pi$ after 160 μm , and the output intensity peaks on the same side of the excitation when a bias of $V_l = 0.98$ V is set, as reported in Figure 15a,b, which shows a clear switching for $V = V_h = 1.19$ V. Finally, the transverse intensity profiles acquired in $z = L$ for the two previous cases, reported in Figure 15c, highlight the substantial lateral shift achieved, with a modulation $\Delta V = 210$ mV in 0.16 mm.

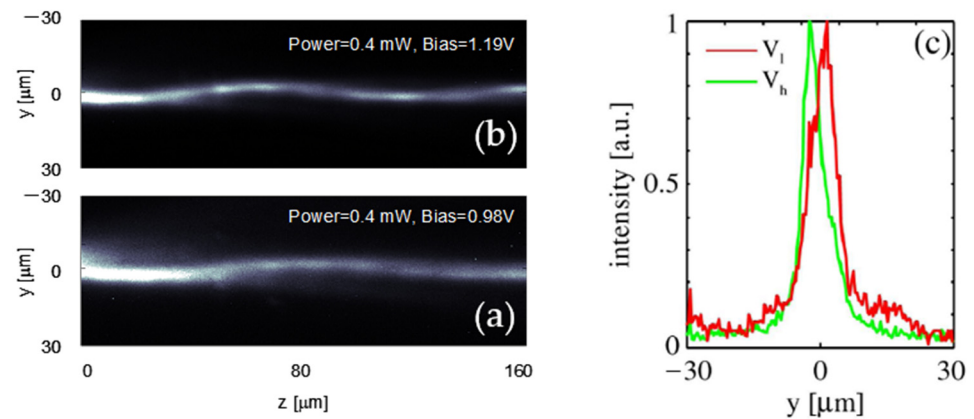


Figure 15. LC guided-wave electro-optic router light propagation in the (y; z) plane: (a) $V = V_l = 0.98$ V; (b) $V = V_h = 1.19$ V; (c) corresponding output intensity distributions.

An optical switch based on the same principle as the previous device has been designed by using a zero-gap directional coupler based on LC:PDMS technology [63]. The coupling condition depends on LC refractive index controlled by in-plane voltage applied to coplanar electrodes. Figure 16a shows the top view of the device, in which two-input single mode optical waveguides are brought together at zero distance between them to form a two-mode region. The $3 \mu\text{m} \times 3 \mu\text{m}$ square cross-section of the bimodal region is reported in Figure 16b, in which coupling occurs because of the interference between the two modes propagating controlled by a voltage applied to coplanar electrodes. Light can be switched to either of the two output waveguides with an extinction ratio higher than 16 dB over a coupling length of 0.5 mm; an applied voltage of just 1.62 V is required to route light to the right-hand output waveguide (Pout 2), while 1.76 V are needed to route light to the left-hand output waveguide (Pout 1). The coupler can also be designed to behave as a demultiplexer for wavelengths 980 nm and 1550 nm by separating them into the two different output ports with a contrast better than 10 dB. Coplanar gold electrodes are used and consist of gold thin films deposited by electroplating, which can switch LC in a PDMS channel by applying only 2.85 V.

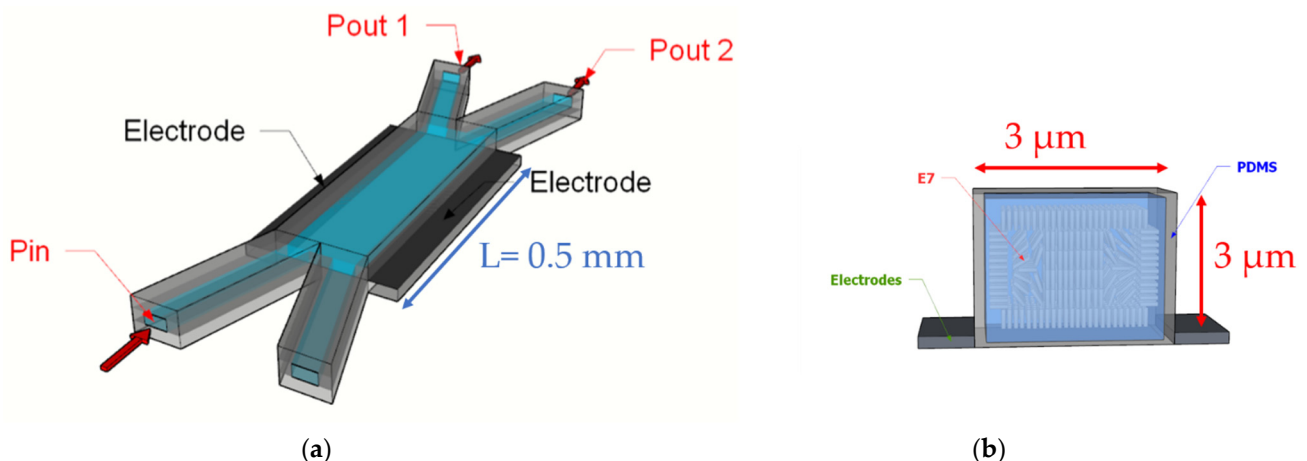


Figure 16. LC:PDMS zero-gap directional coupler switch with bimodal central waveguide and coplanar electrodes: (a) device top view; (b) cross-section of the bimodal LC waveguide.

4.3. Nematic LC Electrically Tunable Bragg Reflectors

Tunable Bragg reflector structures based on an LC waveguide between two glass plates have been demonstrated, where the peak reflection wavelength tuning is driven electro-optically by modifying the LC refractive index [64,65]. Hereinafter, relying on the

same physical model, two possible arrangements of electrodes are reported: a top–bottom electrode disposition and a coplanar electrode configuration. The working principle is based on a refractive index modulation to obtain a Bragg grating along the propagation direction, which allows a wavelength-selective propagation of an optical signal inside the LC layer. Estimation of the reorientation of the LC molecular director has been evaluated as described in Section 2 by considering only an elastic term and an electrostatic term in the expression of F . Coupled mode theory was used for both configurations to evaluate both resonant Bragg wavelength and back-reflected power for TM or TE polarized input light at a specific grating length. A wide wavelength tuning range and a high wavelength selectivity can be achieved in both structures through application of low voltages.

The configuration of the Bragg reflector device based on top–bottom electrodes to obtain an electro-optic distributed feedback waveguide (DFBW) with full adjustability of confinement and Bragg resonance wavelength is shown in Figure 17 [66]. It consists of a planar glass cell with a nematic LC layer and a top–bottom configuration of transparent electrodes allowing an external voltage application. LC molecules are arranged with a planar alignment with the director \mathbf{n} parallel to the propagation direction. Two-dimensional optical confinement of propagating transverse-magnetic TM light polarization is ensured through a graded-index channel by a suitable voltage applied between the comb-shaped top electrode periodic along the propagation direction and the ground plane at the opposite boundary.

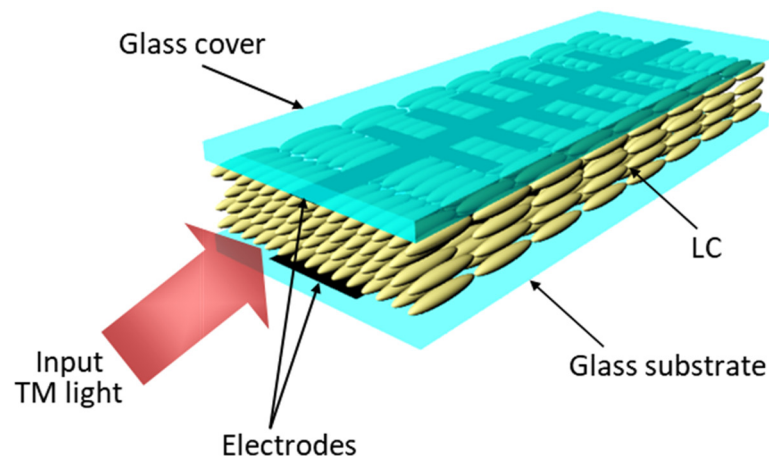


Figure 17. Tunable Bragg reflector with top–bottom electrode configuration with planarly anchored nematic LC.

A Bragg grating can be induced through LC refractive index modulation over a finite propagation distance and for a given operation wavelength to allow a one-dimensional photonic lattice entailing Bragg reflection via distributed feedback. The structure can be optimized in terms of electrode dimensions, periodicity and duty-cycle along the propagation direction and the LC layer thickness to meet the required operation mode as wavelength-selective reflector and tunable drop-multiplexer.

Modulation of the refractive index 100 nm below the top electrode experienced by the TM_{00} mode versus propagation distance or applied voltages from 2 to 3 V (in 0.2 V steps) is reported in Figure 18a. As reported in Figure 18b, a wavelength tuning of 14 nm (1536–1550 nm) is achievable with applied voltages ranging from 2.5 V to 3 V (further details on technology parameters can be found in ref [66]).

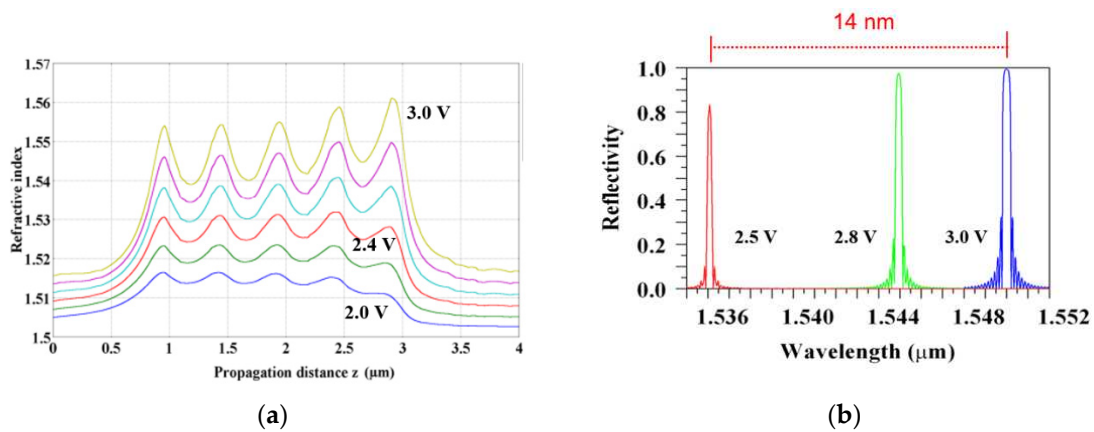


Figure 18. Tuning characteristics of the nematic LC tunable Bragg reflector with top–bottom electrode configuration: (a) refractive index profile modulation along propagation direction for applied voltages between 2 V (bottom line) and 3 V (top line) in 0.2 V steps; (b) normalized grating reflectivity for 2.5 V (red), 2.8 V (green) and 3 V (blue). Reprinted with permission from Ref. [66]. Copyright 2009 OSA.

Another structure of LC tuneable Bragg reflector with a coplanar electrode configuration has been investigated and demonstrated allowing a wavelength tuning range of more than 100 nm in the near infrared with about 10 V applied [67]. Figure 19a is a schematic three-dimensional view of the device.

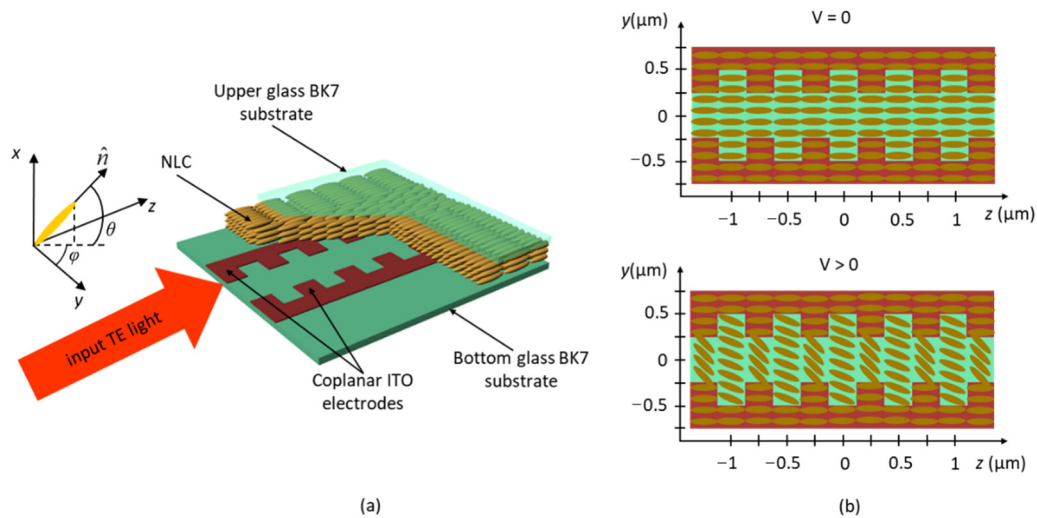


Figure 19. Tunable Bragg reflector with coplanar electrode configuration and planarly anchored nematic LC: (a) three-dimensional view; (b) molecular orientation above the electrodes without ($V = 0$) and with ($V > 0$) applied electric field.

The arrangement is made with a nematic LC planar waveguide restrained between two parallel glass slides. A pair of coplanar comb-shaped 100 nm thick ITO transparent electrodes are deposited and patterned on the inner face of the bottom substrate periodically positioned along the propagation direction. The nematic LC molecules lie with their director aligned along the propagation direction when no voltage is applied, while the field arising when a voltage is applied induces the LC molecular reorientation in the longitudinal plane, resulting in a pure twist deformation that finally leads to a bidimensional optical confinement of the propagating TE polarized beam in the xy plane, as shown in Figure 19b. In Figure 20a, the sinusoidal behaviour of the refractive index modulation achieved along the direction propagation is plotted, corresponding to a phase grating for distributed feedback.

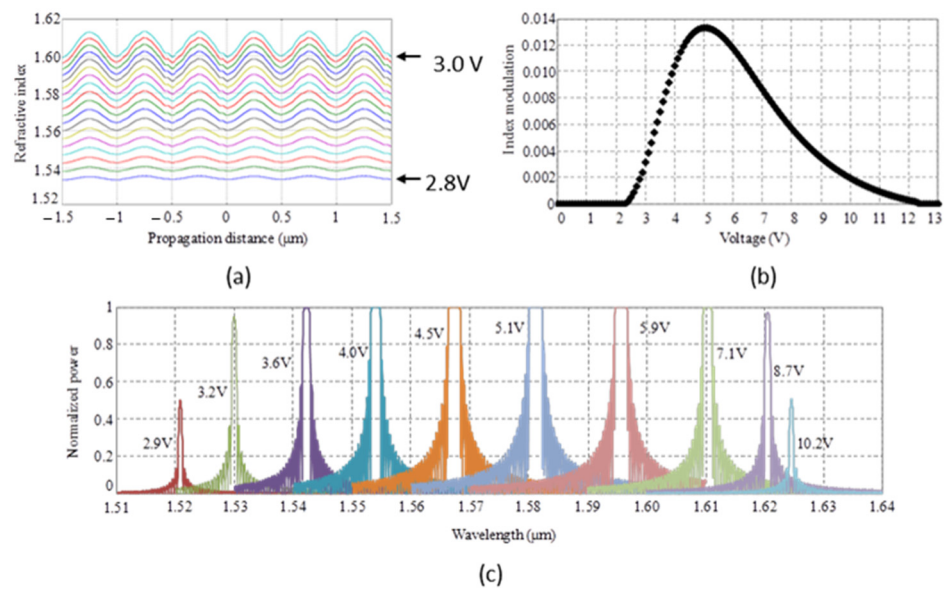


Figure 20. Performance of a tunable Bragg reflector with coplanar electrode configuration: (a) refractive index modulation along the propagation direction for applied voltages between 2.8 V (bottom line) and 3 V (top line); (b) longitudinal modulation versus applied voltage; (c) spectral reflectivity for propagation over 1.5 mm (3000 periods) and for different voltages. Reprinted with permission from Ref. [67]. Copyright 2010 OSA.

The resulting index contrast versus voltage between 0 and 13 V is reported in Figure 20b. The nematic LC reorientation effect is almost negligible up to 2.4 V, leading to little index modulation, but this changes rapidly after this threshold: at $V = 5$ V, the nematic LC molecules are completely reoriented, reaching their maximum twist $\phi = 90^\circ$. Further voltage increase allows LC reorientation which also occurs in the regions that have not yet been completely reoriented, yielding a decrease in modulation. Above 12.4 V, almost all the nematic LC molecules are reoriented parallel to y , and the index contrast is zero.

The back-reflected power (spectral reflectivity) as a function of the resonant wavelength for a device length of 1.5 mm, corresponding to 3000 periods, is reported in Figure 20c. A wide tuning range of 104 nm (1521–1625 nm) can be obtained by varying the applied voltage between 2.9 and 10.2 V, keeping the back-reflection above 50%, with a good spectral selectivity.

5. Conclusions

LC materials can be successfully used beyond the well-known FPD applications. Superb linear and nonlinear optical properties of LC materials have been deeply explored to make a wide range of integrated optic devices. Optical waveguides with an electro-optically or all-optically controlled core enable the development of many integrated optic devices which can be driven by sub-milliwatt signals. Straightforward modelling allows to design simulate several photonic functions, such as switching and filtering and light generation. In this paper, a few examples of photonic devices either for optical switching with extinction ratios over 40 dB, or for optical filtering over 100 nm tuning range have been reported to demonstrate the great LC application potentialities in integrated optics for optical communications and optical sensing systems with low power consumptions. Innovative integrated photonic devices based on LC include combinations of LC with metal nanoparticles for novel sensing systems based on photothermal therapies. Further research could be devoted to the development of integrated optic devices for 3D sensing, augmented reality, terahertz communication and terahertz imaging. The generated vortex beam via q-plates of LCs and vortex gratings could help in studying the interaction of spin-orbital angular momentum for quantum information applications.

Author Contributions: Conceptualization, A.d. and R.A.; methodology, A.d.; software, R.A.; validation, A.d. and R.A.; investigation, A.d. and R.A.; data curation, A.d. and R.A.; writing—original draft preparation, A.d. and R.A.; writing—review and editing, A.d. and R.A.; supervision, A.d. and R.A.; funding acquisition, A.d. and R.A. All authors have read and agreed to the published version of the manuscript.

Funding: This research received no external funding.

Conflicts of Interest: The authors declare no conflict of interest.

References

1. Khoo, I.C. *Liquid Crystals*, 2nd ed.; Wiley: New York, NY, USA, 2007.
2. Zografopoulos, D.C.; Asquini, R.; Kriezis, E.; D'Alessandro, A.; Beccherelli, R. Guided-wave liquid-crystal photonics. *Lab A Chip* **2012**, *12*, 3598–3610. [CrossRef]
3. Beeckman, J.; Neyts, K.; Vanbrabant, P.J.M. Liquid-crystal photonic applications. *Opt. Eng.* **2011**, *50*, 081202. [CrossRef]
4. Donisi, D.; Bellini, B.; Beccherelli, R.; Asquini, R.; Gilardi, G.; Trotta, M.; D'Alessandro, A. A Switchable Liquid-Crystal Optical Channel Waveguide on Silicon. *IEEE J. Quantum Electron.* **2010**, *46*, 762–768. [CrossRef]
5. d'Alessandro, A.; Asquini, R.; Trotta, M.; Gilardi, G.; Beccherelli, R.; Khoo, I.C. All-optical intensity modulation of near infrared light in a liquid crystal channel waveguide. *Appl. Phys. Lett.* **2010**, *97*, 093302. [CrossRef]
6. Neyts, G.K.; Beeckman, J.; Desmet, H. Waveguiding with liquid crystals. *Proc. SPIE* **2007**, *6487*, 64870O.
7. Scalia, G.; Hermann, D.S.; Abbate, G.; Komitov, L.; Mormile, P.; Righini, G.C.; Sirleto, L. Integrated Electro-Optic Switch Based on a Ferroelectric Liquid Crystal Waveguide. *Mol. Cryst. Liq. Cryst.* **1998**, *320*, 321–335. [CrossRef]
8. d'Alessandro, A.; Bellini, B.; Donisi, D.; Beccherelli, R.; Asquini, R. Nematic liquid crystal optical channel waveguides on silicon. *IEEE J. Quant. Electron.* **2006**, *42*, 1084–1090. [CrossRef]
9. Peddireddy, K.; Jampani, V.S.R.; Thutupalli, S.; Herminghaus, S.; Bahr, C.; Muševič, I. Lasing and waveguiding in smectic A liquid crystal optical fibers. *Opt. Express* **2013**, *21*, 30233–30242. [CrossRef]
10. Čančula, M.; Ravnik, M.; Muševič, I.; Žumer, S. Liquid microlenses and waveguides from bulk nematic birefringent profiles. *Opt. Express* **2016**, *19*, 22177–22188. [CrossRef]
11. Xing, Y.; Ako, T.; George, J.P.; Korn, D.; Yu, H.; Verheyen, P.; Pantouvaki, M.; Lepage, G.; Absil, P.; Ruocco Koos, C.; et al. Digitally Controlled Phase Shifter Using an SOI Slot Waveguide with Liquid Crystal Infiltration. *IEEE Photon. Technol. Lett.* **2015**, *27*, 1269–1272. [CrossRef]
12. Wang, T.-J.; Chaung, C.-K.; Li, W.-J.; Chen, T.-J.; Chen, B.-Y. Electrically Tunable Liquid-Crystal-Core Optical Channel Waveguide. *J. Light. Technol.* **2013**, *31*, 3570–3574. [CrossRef]
13. Li, J.; Chu, D. Liquid Crystal-Based Enclosed Coplanar Waveguide Phase Shifter for 54–66 GHz Applications. *Crystals* **2019**, *9*, 650. [CrossRef]
14. Reese, R.; Polat, E.; Tesmer HStrobl, J.; Schuster, C.; Nickel, M.; Granja, A.B.; Jakoby, R.; Maune, H. Liquid Crystal Based Dielectric Waveguide Phase Shifters for Phased Arrays at W-Band. *IEEE Access* **2019**, *7*, 127032–127041. [CrossRef]
15. Tripathi, U.S.; Rastogi, V. Liquid Crystal Based Rib Waveguide. *J. Lightw. Technol.* **2020**, *38*, 4045–4051. [CrossRef]
16. Assanto, G.; Peccianti, M.; Conti, C. Nematicons: Optical Spatial Solitons in Nematic Liquid Crystals. *Opt. Photon-News* **2003**, *14*, 44–48. [CrossRef]
17. Henninot, J.-F.; Blach, J.-F.; Warengem, M. Experimental study of the nonlocality of spatial optical solitons excited in nematic liquid crystal. *J. Opt. A Pure Appl. Opt.* **2007**, *9*, 20–25. [CrossRef]
18. Assanto, G.; Fratalocchi, A.; Peccianti, M. Spatial solitons in nematic liquid crystals. *Opt. Exp.* **2007**, *15*, 5248–5259. [CrossRef]
19. Piccardi, A.; Alberucci, A.; Bertolozzo, U.; Residori, S.; Assanto, G. Soliton gating and switching in liquid crystal light valve. *Appl. Phys. Lett.* **2010**, *96*, 071104. [CrossRef]
20. Piccardi, A.; Trotta, M.; Kwasny, M.; Alberucci, A.; Asquini, R.; Karpierz, M.; D'Alessandro, A.; Assanto, G. Trends and trade-offs in nematicon propagation. *Appl. Phys. A* **2011**, *104*, 805–811. [CrossRef]
21. Jung, P.S.; Krolikowski, W.; Laudyn, U.A.; Trippenbach, M.; Karpierz, M. Supermode spatial optical solitons in liquid crystals with competing nonlinearities. *Phys. Rev. A* **2017**, *95*, 023820. [CrossRef]
22. Aya, S.; Araoka, F. Kinetics of motile solitons in nematic liquid crystals. *Nat. Commun.* **2020**, *11*, 3248. [CrossRef] [PubMed]
23. Du, F.; Lu, Y.-Q.; Wu, S.-T. Electrically tunable liquid-crystal photonic crystal fiber. *Appl. Phys. Lett.* **2004**, *85*, 2181–2183. [CrossRef]
24. Woliński, T.; Ertman, S.; Lesiak, P.; Domański, A.; Czapla, A.; Dąbrowski, R.; Nowinowski-Kruszelnicki, E.; Wójcik, J. Photonic liquid crystal fibers—A new challenge for fiber optics and liquid crystals photonics. *Opto-Electron. Rev.* **2006**, *14*, 329–334. [CrossRef]
25. Lee, C.; Chen, C.; Kao, C.; Yu, C.; Yeh, S.; Cheng, W.; Lin, T. Photo and electrical tunable effects in photonic liquid crystal fiber. *Opt. Express* **2010**, *18*, 2814–2821. [CrossRef] [PubMed]
26. Lorenz, A.; Kitzerow, H.-S. Efficient electro-optic switching in a photonic liquid crystal fiber. *Appl. Phys. Lett.* **2011**, *98*, 241106. [CrossRef]

27. Budaszewski, D.; Chychłowski, M.; Budaszewska, A.; Bartosewicz, B.; Jankiewicz, B.; Wolinski, T. Enhanced efficiency of electric field tunability in photonic liquid crystal fibers doped with gold nanoparticles. *Opt. Express* **2019**, *27*, 14260–14269. [CrossRef] [PubMed]
28. Vasdekis, A.; Cuennet, J.G.; Psaltis, D. Liquid crystal optofluidics. *Proc. SPIE* **2012**, 847507. [CrossRef]
29. De Sio, L.; Romito, M.; Giocondo, M.; Vasdekis, A.; De Luca, A.; Umerton, C. Electro-switchable polydimethylsiloxane-based optofluidics. *Lab A Chip* **2012**, *12*, 3760–3765. [CrossRef]
30. Cuennet, J.G.; Vasdekis, A.E.; Psaltis, D. Optofluidic-tunable color filters and spectroscopy based on liquid-crystal microflows. *Lab Chip* **2013**, *13*, 2721–2726. [CrossRef]
31. d’Alessandro, A.; Martini, L.; Gilardi, G.; Beccherelli, R.; Asquini, R. Polarization-Independent Nematic Liquid Crystal Waveguides for Optofluidic Applications. *IEEE Photonics Technol. Lett.* **2015**, *27*, 1709–1712. [CrossRef]
32. Čopar, S.; Kos, Ž.; Emeršič, T.; Tkalec, U. Microfluidic control over topological states in channel-confined nematic flows. *Nat. Commun.* **2020**, *11*, 59. [CrossRef] [PubMed]
33. Ramaniuk, A.; Jung, P.S.; Christodoulides, D.N.; Krolikowski, W.; Trippenbach, M. Absorption-mediated stabilization of nonlinear propagation of vortex beams in nematic liquid crystals. *Opt. Commun.* **2019**, *451*, 338–344. [CrossRef]
34. Laudyn, U.A.; Kwaśny, M.; Karpierz, M.A.; Assanto, G. Vortex nematicons in planar cells. *Opt. Express* **2020**, *28*, 8282–8290. [CrossRef] [PubMed]
35. Jung, P.S.; Krolikowski, W.; Laudyn, U.A.; Karpierz, M.A.; Trippenbach, M. Semi-analytical approach to supermode spatial solitons formation in nematic liquid crystals. *Opt. Express* **2017**, *25*, 23893–23898. [CrossRef] [PubMed]
36. Ramaniuk, A.; Trippenbach, M.; Jung, P.S.; Christodoulides, D.N.; Krolikowski, W.; Assanto, G. Scalar and vector supermode solitons owing to competing nonlocal nonlinearities. *Opt. Express* **2021**, *29*, 8015–8023. [CrossRef]
37. Piccirillo, B.; Toscano, C.; Vetrano, F.; Santamato, E. Orbital and Spin Photon Angular Momentum Transfer in Liquid Crystals. *Phys. Rev. Lett.* **2001**, *86*, 2285. [CrossRef]
38. Slussarenko, S.; Murauski, A.; Du, T.; Chigrinov, V.; Marrucci, L.; Santamato, E. Tunable liquid crystal q-plates with arbitrary topological charge. *Opt. Express* **2011**, *19*, 4085–4090. [CrossRef] [PubMed]
39. Keum, C.; Liu, S.; Al-Shadeedi, A.; Kaphle, V.; Callens, M.K.; Han, L.; Neyts, K.; Zhao, H.; Gather, M.C.; Bunge, S.D.; et al. Tuning charge carrier transport and optical birefringence in liquid-crystalline thin films: A new design space for organic light-emitting diodes. *Sci. Rep.* **2018**, *8*, 699. [CrossRef]
40. Lei, X.; Wieschendorf, C.; Firth, J.; Ladouceur, F.; Fuerbach, A.; Silvestri, L. Numerical modelling and optimization of actively Q-switched waveguide lasers based on liquid crystal transducers. *Opt. Express* **2019**, *27*, 8777–8791. [CrossRef]
41. Belmonte, C.; Frasunkiewicz, L.; Czystanowski, T.; Thienpont, H.; Beeckman, J.; Neyts, K.; Panajotov, K. Optimization of electrically tunable VCSEL with intracavity nematic liquid crystal. *Opt. Express* **2015**, *23*, 15706–15715. [CrossRef]
42. Pfeifle, J.; Alloatti, L.; Freude, W.; Leuthold, J.; Koos, C. Silicon-organic hybrid phase shifter based on a slot waveguide with a liquid-crystal cladding. *Opt. Express* **2012**, *20*, 15359–15376. [CrossRef]
43. Henninot, J.F.; Debailleul, M.; Asquini, R.; d’Alessandro, A.; Warengem, M. Self-waveguiding in an isotropic channel induced in dye doped nematic liquid crystal and a bent self-waveguide. *J. Opt. A: Pure Appl. Opt.* **2004**, *6*, 315–323. [CrossRef]
44. Bellini, B.; Larchanché, J.-F.; Vilcot, J.-P.; DeCoster, D.; Beccherelli, R.; D’Alessandro, A. Photonic devices based on preferential etching. *Appl. Opt.* **2005**, *44*, 7181–7186. [CrossRef] [PubMed]
45. Bellini, B.; d’Alessandro, A.; Beccherelli, R. A method for butt-coupling optical fibers to liquid crystal planar waveguides. *Opt. Mater.* **2007**, *29*, 1019–1022. [CrossRef]
46. Chigrinov, V.G.; Kozenkov, V.M.; Kwok, H.-S. *Photoalignment of Liquid Crystalline Materials: Physics and Applications*; Wiley: New York, NY, USA, 2008.
47. Schadt, M. Liquid creystal displays, LC materials and LPP photoalignment. *Mol. Cryst. Liq. Cryst.* **2017**, *320*, 253–268. [CrossRef]
48. Duffy, D.C.; McDonald, J.C.; Schueller, O.J.A.; Whitesides, G.M. Rapid Prototyping of Microfluidic Systems in Poly(dimethylsiloxane). *Anal. Chem.* **1998**, *70*, 4974–4984. [CrossRef] [PubMed]
49. Lee, L.-H. Enhancement of surface wettability of adhesive silicone rubber by oxidation. *J. Adhes.* **1972**, *4*, 39–49. [CrossRef]
50. Du, P.; Lin, X.; Zhang, X. Dielectric constants of PDMS nanocomposites using conducting polymer nanowires. In Proceedings of the 16th International Solid-State Sensors, Actuators and Microsystems Conference, Beijing, China, 5–9 June 2011; pp. 645–648.
51. Wang, Z.; Volinsky, A.A.; Gallant, N.D. Crosslinking effect on polydimethylsiloxane elastic modulus measured by custom-built compression instrument. *J. Appl. Polym. Sci.* **2014**, *131*, 41050. [CrossRef]
52. McDonald, J.C.; Duffy, D.C.; Anderson, J.R.; Chiu, D.T.; Wu, H.; Schueller, O.J.; Whitesides, G.M. Fabrication of microfluidic systems in poly(dimethylsiloxane). *Electrophoresis* **2000**, *21*, 27–40. [CrossRef]
53. Missinne, J.; Kalathimekkad, S.; Van Hoe, B.; Bosman, E.; Vanfleteren, J.; Van Steenberge, G. Stretchable optical waveguides. *Opt. Express* **2014**, *22*, 4168–4179. [CrossRef]
54. Yeh, P.; Gu, C. *Optics of Liquid Crystal Displays*; Wiley: New York, NY, USA, 1999.
55. Lebwohl, P.A.; Lasher, G. Nematic-Liquid-Crystal Order—A Monte Carlo Calculation. *Phys. Rev. A* **1972**, *6*, 426–429. [CrossRef]
56. Pasini, P.; Chiccoli, C.; Zannoni, C. *Advances in the Computer Simulations of Liquid Crystals*; Kluwer: Dordrecht, Germany, 2000.
57. D’Alessandro, A.; Asquini, R.; Chiccoli, C.; Pasini, P.; Zannoni, C. Liquid crystal channel waveguides: A computer simulation of the application of transversal external fields. *Mol. Cryst. Liq. Cryst.* **2017**, *649*, 79–85. [CrossRef]

58. d'Alessandro, A.; D'Orazio, A.; Campoli, F.; Petruzzelli, V.; Chessa, G.; Maltese, P. Design of an Ultrashort Directional Coupler with an SSFLC Coupling Layer. *Mol. Cryst. Liq. Cryst.* **1998**, *320*, 355–364. [CrossRef]
59. Asquini, R.; D'Alessandro, A. BPM Analysis of an Integrated Optical Switch using Polymeric Optical Waveguides and SSFLC at 1.55 μm . *Mol. Cryst. Liq. Cryst.* **2002**, *375*, 243–251. [CrossRef]
60. Vanbrabant, P.J.M.; Beeckman, J.; Neyts, K.; James, R.; Fernandez, F.A. A finite element beam propagation method for simulation of liquid crystal devices. *Opt. Express* **2009**, *17*, 10895–10909. [CrossRef] [PubMed]
61. Asquini, R.; Fratalocchi, A.; D'Alessandro, A.; Assanto, G. Electro-optic routing in a nematic liquid-crystal waveguide. *Appl. Opt.* **2005**, *44*, 4136–4143. [CrossRef] [PubMed]
62. Fratalocchi, A.; Asquini, R.; Assanto, G. Integrated electro-optic switch in liquid crystals. *Opt. Express* **2005**, *13*, 32–37. [CrossRef]
63. Asquini, R.; Chiccoli, C.; Pasini, P.; Civita, L.; D'Alessandro, A. Low power photonic devices based on electrically controlled nematic liquid crystals embedded in poly (dimethylsiloxane). *Liq. Cryst.* **2018**, *45*, 2174–2183. [CrossRef]
64. Asquini, R.; Gilardi, G.; D'Alessandro, A.; Assanto, G. Integrated Bragg reflectors in low-index media: Enabling strategies for wavelength tunability in electro-optic liquid crystals. *Opt. Eng.* **2011**, *50*, 71108. [CrossRef]
65. Asquini, R.; D'Alessandro, A. Tunable photonic devices based on liquid crystals and composites. *Proc. SPIE* **2013**, *8828*, 88280T. [CrossRef]
66. Donisi, D.; Asquini, R.; d'Alessandro, A.; Assanto, G. Distributed feedback grating in liquid crystal waveguide: A novel approach. *Opt. Express* **2009**, *17*, 5251–5256. [CrossRef] [PubMed]
67. Gilardi, G.; Asquini, R.; d'Alessandro, A.; Assanto, G. Widely tunable electro-optic distributed Bragg reflector in liquid crystal waveguide. *Opt. Express* **2010**, *18*, 11524–11529. [CrossRef] [PubMed]

Article

Photo-Aligned Nematic Liquid Crystals Enable the Modulation of Thermoplasmonic Heating

Giovanna Palermo^{1,2,*}, Rossella Grillo^{3,4}, Luigia Pezzi^{1,2}, Thomas Bürgi³, Nelson Tabiryan⁵,
Luciano De Sio^{2,6} and Cesare Umeton^{1,*}¹ Department of Physics, University of Calabria, Via P. Bucci, 87036 Rende, Italy; luigia.pezzi@fis.unical.it² CNR NANOTEC—Istituto di Nanotecnologia, UOS Cosenza, 87036 Rende, Italy; luciano.desio@uniroma1.it³ Department of Physical Chemistry, University of Geneva, 41211 Geneva, Switzerland;

rossella.grillo@unirc.it (R.G.); Thomas.Buergi@unige.ch (T.B.)

⁴ DIIES Department, Mediterranean University of Reggio Calabria, Loc. Feo di Vito, 89122 Reggio Calabria, Italy⁵ Beam Engineering for Advanced Measurements Company, 1300 Lee Road, Orlando, FL 32789, USA;

nelson@beamco.com

⁶ Department of Medico-Surgical Sciences and Biotechnologies, Center for Biophotonics, Sapienza University of Rome, Corso Della Repubblica 79, 04100 Latina, Italy

* Correspondence: giovanna.palermo@unical.it (G.P.); cesare.umeton@fis.unical.it (C.U.)

Abstract: We experimentally demonstrate that the plasmonic heat delivered by a single layer of homogeneously distributed gold nanoparticles (AuNPs), immobilized on a glass substrate, can be optically tuned by taking advantage of the properties of an organic layer based on azobenzene and nematic liquid crystal (NLC) molecules. The effect, which exploits the dependence of the NLC refractive index value on the molecular director orientation, is realized using the polarization-dependent, light-induced molecular reorientation of a thin film of photo-aligning material that the NLC is in contact with. The reversibility of the optically induced molecular director reorientation of the NLC enables an active modulation of the plasmonic photo-induced heat.

Keywords: thermoplasmonics; metallic nanoparticles; liquid crystals; reconfigurability; photo-aligning materials

Citation: Palermo, G.; Grillo, R.; Pezzi, L.; Bürgi, T.; Tabiryan, N.; De Sio, L.; Umeton, C. Photo-Aligned Nematic Liquid Crystals Enable the Modulation of Thermoplasmonic Heating. *Appl. Sci.* **2021**, *11*, 6272. <https://doi.org/10.3390/app11146272>

Academic Editor: Gaetano Assanto

Received: 29 May 2021

Accepted: 5 July 2021

Published: 7 July 2021

Publisher's Note: MDPI stays neutral with regard to jurisdictional claims in published maps and institutional affiliations.



Copyright: © 2021 by the authors. Licensee MDPI, Basel, Switzerland. This article is an open access article distributed under the terms and conditions of the Creative Commons Attribution (CC BY) license (<https://creativecommons.org/licenses/by/4.0/>).

1. Introduction

Thermoplasmonics has become one of the most renowned research topics in plasmonics and nano-optics, thanks to the possibility of generating and controlling a great amount of heat at the nanoscale. Thermoplasmonics deals with the heat produced by metallic nanoparticles (NPs) when a radiation with suitable (resonant) wavelength impinges on them [1,2]. Indeed, when the electrons of the conduction band of a metallic NP oscillate coherently with the electric field of the incident radiation, an increase of the absorption in the corresponding frequency range occurs (ω_p) that leads to a rapid rise in the temperature of the NP, followed by a heat dissipation into surrounding media [3,4]. The temperature increase (ΔT) of a single spherical NP can be easily expressed as $\Delta T = Q / (4\pi k_H R_{NP})$, where R_{NP} is the NP radius, k_H is the thermal conductivity of the host medium, and Q is the heat power density. Q depends on the absorption cross-section (σ_{abs}) of the NP, and on the intensity (I) of the incident light through the equation: $Q = \sigma_{abs} I$ [1–4]. For a metallic NP with spherical or rod-like shape, σ_{abs} can be easily calculated using the Mie or Gans theories, respectively, ref. [1–4] while for different geometries more complex theoretical models are required. Nowadays, the thermoplasmonic heating is used in several research fields such as high precision medicine [5–7], electronics [8–10] optics [11–13], biology [14,15], and catalysis [16,17]. All above applications are based on the possibility to finely tune the photo-thermal efficiency of the NPs that can be done by acting on several control parameters such as the intensity of the impinging beam [1–4], the number (N) of involved NPs, and the dielectric function of the surrounding medium ϵ_H [18]. The latter

can be achieved by exploiting the properties of smart and thermo-responsive materials such as thermotropic liquid crystals (LCs). These are organic and anisotropic materials responsive to different external perturbations such as electric, optical and magnetic fields, and temperature variation. LCs have been largely used in various research fields ranging from displays [19–21] to plasmonics [22,23]. Notably, the temperature sensitivity of the optical properties of LCs have been used as a compelling solution to realize novel methodologies for monitoring and controlling the light-induced heat of NPs [24]. In this work, we report and discuss on the realization of a thermoplasmonic-based optical device made of an array of gold nanoparticles (AuNPs) immobilized on a glass substrate and layered with a photo-aligned NLC. This hybrid system, which represents an all-optical thermoplasmonic device, ingeniously realized through the combination of hard-matter (plasmonic NPs) and soft matter (LCs), is characterized in terms of morphological, optical, and thermo-optical properties. It turns out that the thermoplasmonic heating can be easily controlled by controlling the refractive index of the surrounding LC medium, thanks to the presence of the thin surface command layer. Indeed, starting from a single layer of metal NPs the photothermal response can be controlled by varying the intensity in a specific range, but also with the same power of the resonant radiation through subtle control of the refractive index of the surrounding medium, obtainable using the photo-aligning material and liquid crystal. The all-optical thermoplasmonic device forecasts exciting applications in the field of light-driven thermoplasmonics.

2. Materials and Methods

Synthesis of spherical gold nanoparticles: Spherical gold nanoparticles have been prepared according to the conventional Turkevich method [25]. This is the most commonly used approach for the synthesis of size-defined spherical gold nanoparticles through chemical reduction by sodium citrate. Briefly, in a round-bottomed flask, 600 mL of an aqueous solution of tetrachloroauric (III) acid (0.25 mM) were brought to boiling under vigorous magnetic stirring. When the boiling temperature was reached, the gold has been reduced by quickly adding 15 mL of aqueous sodium citrate solution (0.03 M). In about 15 min, the solution colour slowly turned from yellow to deep red, as a result of the full reduction of the gold salt into monodisperse gold nanoparticles with an average diameter of 20 nm. The reaction was then removed from the hot oil bath and allowed to cool down to room temperature overnight.

Functionalization of substrates: The glass substrates were cleaned and hydroxylated with piranha solution (3:1 mixture of sulphuric acid to hydrogen peroxide 30%) for 30 min. Then, the substrates were rinsed several times, first with distilled water and then with milli-Q water before being dried under nitrogen flow. To alter the surface chemistry, the substrates were immersed in a 5% (*v/v*) solution of N-[3-(trimethoxysilyl)propyl] ethylenediamine in ethanol for 30 min and then rinsed with milli-Q water. Excess of water was removed using a stream of nitrogen followed by drying in a furnace at 120 °C for 30 min to assure good silanization.

Gold nanoparticles arrays on planar substrates: Gold nanoparticles were deposited on glass slides by immersing the functionalized substrates in the colloidal solution for two and a half hours. The gold covered substrates were then washed with milli-Q water and dried under a stream of nitrogen.

Deposition of the photoaligning material: PAAD-27 by BeamCo. dissolved in dimethylformamide (C_3H_7NO), which possesses a broad absorption band centered at 415 nm, has been deposited by means of a spin coater (2000 rpm for 30 s). A polarized UV lamp ($\lambda = 395$ nm; $I = 30$ mW/cm²) is used for a suitable time interval (typically 7 min) to reorient the PAAD-27 molecules perpendicularly to its polarization direction. The characteristics average polar anchoring energies of nematic LC on PAAD materials (Beamco., Orlando, FL, USA) are $\approx 10^{-2}$ J/m², a weaker alignment than on polyimide layer [26].

Preparation of the sample cell: The thermotropic nematic liquid crystal (NLC) E7, by Merck has been used. The sample cell was fabricated by gluing together a functionalized

glass slide and the PAAD-27 coated AuNPs monolayer, spaced by 10 μm glass microspheres. The NLC has been then introduced by means of capillary flow. The surface of the glass substrate is covered with a thin organic film, such as polyimide (PI-AL1454 by JSR), using a spin coating (4000 rpm, 60 s) deposition technique. After the deposition of the coating film, a cloth (velvet) with short fibers is moved over the surface to create microgrooves that make the surface unidirectionally anisotropic. The rubbing process induces a specific orientation of the polymer molecules, which is transmitted to the LC molecules anchored on the substrates; moreover, this kind of orientational order propagates in the bulk of the LC molecules via intermolecular forces [27].

Thermographic analysis: The thermographic analysis has been performed by means of a thermocamera (E40 by FLIR), which is characterized by a sensitivity of 0.07 $^{\circ}\text{C}$ and a spatial resolution of 2.72 mrad. The steady-state condition was reached after about 5 min of exposure of the sample cell to a green laser beam ($\lambda = 532 \text{ nm}$)—Verdi G-Series by Coherent, linearly polarized—polarization direction: vertical, $\pm 5^{\circ}$, when no further temperature variations were detected in the limit of the thermo-camera sensitivity.

3. Results and Discussion

AuNPs monolayers on glass substrates have been prepared by following the procedure described in the Materials and Methods section. The samples were then characterized by performing a morphological analysis by means of an Atomic Force Microscope (AFM). Figure 1a shows a representative AFM image of uniformly distributed AuNPs with an average diameter of about 20 nm. The inset of Figure 1a shows a photo of the realized sample, which exhibits a distinctive pinkish color associated with the presence of well-dispersed AuNPs. Indeed, the spectral response of the sample (Figure 1b) shows the typical absorption peak of spherical AuNPs centered at the wavelength $\lambda_{LPR} = 522 \text{ nm}$, corresponding to the localized plasmon resonance of the AuNPs [1,2]. Figure 1c shows the absorption spectrum of the photoaligning material PAAD-27 (by BeamCo), dissolved in dimethylformamide, which possesses a broad absorption band centered at 420 nm. PAAD-27 is an azo-based material that is used to promote planar alignment of nematic liquid crystals (NLC); its optical and all-optical properties have been reported elsewhere [28,29].

The AuNPs monolayer has been then covered with the PAAD-27 material (see Materials and Methods section): the absorbance of the obtained sample (AuNPs + PAAD 27) is reported in Figure 1d (green curve). The absorption peak of AuNPs is significantly red shifted, from 522 nm to 544 nm. In general, when metallic nanoparticles are immersed in a large refractive index medium, the resonance is shifted toward longer wavelengths [30]. In fact, the shift observed in Figure 1d is related to a change in the refractive index n of the surrounding medium: from the air value ($n_{air} = 1$) to the PAAD-27 value ($n_{PAAD} = 1.73$). This behavior well agrees with the Mie theory [31], which provides an analytical solution of Maxwell's equations used to calculate the scattering and the absorption of electromagnetic radiation due to a spherical and isolated metallic NP. Figure 2a sketches the AuNPs monolayer on glass substrate before (top-left) and after the deposition of the PAAD-27 (top-right), whose molecules are randomly aligned. When the sample is illuminated with a polarized UV light (10 min, 2.7 J/cm²), a PAAD-27 molecular alignment is induced, which turns out to be perpendicular to the light polarization direction. In fact, when PAAD-27 molecules are optically activated by a light beam whose polarization direction is parallel to their absorption oscillators, they become excited and relax several times with a random alignment; this process results in a new orientation of the PAAD molecules with respect to the initial one, with a consequent excess of molecules in the direction in which the absorbing oscillators are perpendicular to the polarization of the incident radiation. It is a consequence of this process that the PAAD-27 alignment direction can be easily modified by changing the polarization direction of the incident UV light beam. Figure 2b highlights that once the sample is exposed to polarized UV radiation, a further red shift of the plasmonic band is observed with respect to the position registered for the sample in which the AuNPs are covered by amorphous (not aligned) PAAD-27; this further red shift of about 16 nm

can be attributed to the change of the refractive index of the medium surrounding the AuNPs, following the alignment of the PAAD-27 molecules. Finally, we have observed that there is no difference in the shift of the plasmonic band of the sample covered with a PAAD-27 layer when this is acted on by radiations with different (orthogonal) polarizations (blue and magenta curves of Figure 2b). This result points out that the plasmonic response of the AuNPs is not substantially affected by the actual in-plane orientation of the PAAD-27 molecules.

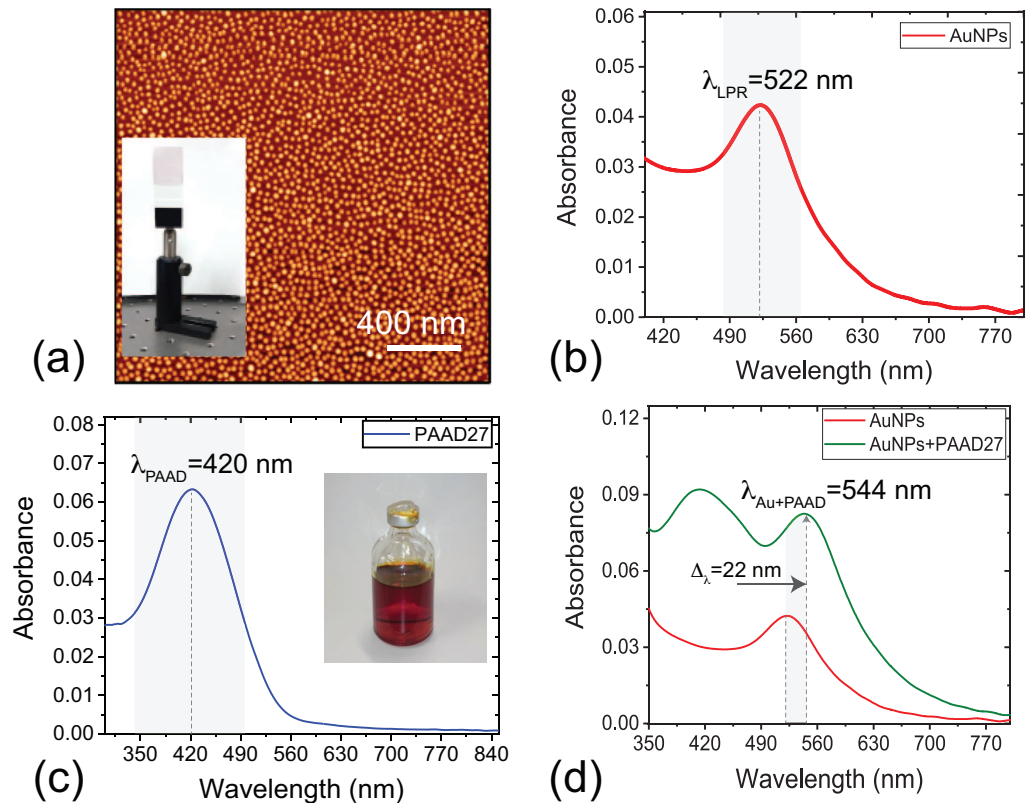


Figure 1. (a) AFM image of the AuNPs monolayer on a glass substrate. In the inset, a photograph of the sample. Spectral response of the AuNPs monolayer surrounded by (b) air and (c) PAAD-27; In the inset, a photograph of the photo-aligning material. (d) Absorbance response of the AuNPs monolayer covered by the PAAD-27.

A very interesting behavior is observed when monitoring the photothermal response of the sample. The thermo-optical setup used for the experiments is sketched in Figure 2c: A CW green laser ($\lambda = 532$ nm, spot size 2.25 ± 0.22 mm), impinges perpendicularly onto the sample and excites simultaneously the plasmonic band of the irradiated AuNPs, with a consequent increase (ΔT) of the macroscopic temperature of the sample with respect to the environment temperature (T_0). In general, to calculate the temperature variation at a point r from a single NP, it is necessary to solve the heat transfer equation [4], where the solution results are:

$$\Delta T(r) = \frac{QR_{NP}^3}{3rk_H} \quad (1)$$

where Q is the heat production due to the Joule effect, R_{NP} is the NP radius and K_H is the thermal conductivity of the host medium. Thus, by illuminating a macroscopic surface region of the AuNPs layer with a laser spot w in radius, a considerable number of AuNPs are acted on by the light; in this case, as a matter of fact, the temperature increase has to be calculated by adding the contribution of all the irradiated AuNPs as specified in this formula [18]:

$$\Delta T(r) = 2\pi\omega n_{NP} \frac{V_{NP} \text{Im}(\chi_{NP})}{2\lambda k_H \sqrt{\epsilon_H}} \left| \frac{3\epsilon_H}{2\epsilon_H + \epsilon_{NP}} \right|^2 I \quad (2)$$

where n_{NP} is the AuNPs surface density, V_{NP} is the average AuNP volume, k_H is the thermal conductivity of the host medium, χ_{NP} is the AuNPs dielectric permeability, ϵ_{NP} and ϵ_H are the AuNPs and host medium dielectric permittivity, respectively. From Equation (2), it is evident that the temperature variation exhibits a strong enhancement under the Frölich condition, in which the quantity $|2\epsilon_H + \epsilon_{NP}|$ assumes a minimum value, a condition that occurs if $\text{Re}[\epsilon_{NP}(\omega)] = -2\epsilon_H$ [32]. Equation (2) shows also that the temperature variation ΔT varies linearly with the intensity of the pump beam (I), used to excite the resonance of the AuNPs, and strongly depends on the optical and thermal characteristics of the medium that hosts the AuNPs, expressed by ϵ_H and k_H , respectively. This behavior was experimentally demonstrated by illuminating the AuNPs with different pump beam intensities I and by monitoring the maximum induced ΔT for each I value. By monitoring the temperature values T_{max} of the central pixel of each hot-spot of the thermographic images (Figure 2c), which corresponds to the warmest point, we plotted the temperature variation $\Delta T = T_{max} - T_0$ versus the impinging intensity I . Successively, we repeated the photothermal experiments (Figure 2d) by fixing the intensity range ($I = 0.05 - 1.2 \text{ W/cm}^2$) for the cases of AuNPs monolayer in air (red sphere) and covered by the PAAD-27 molecules before (green sphere) and after exposure to UV light of two different polarization directions (blue and magenta spheres). As predicted by Equation (2), the behavior of ΔT as a function of I can be easily fitted with a linear curve. For the maximum I considered we acquire a ΔT of about $(3.2 \pm 0.3) \text{ }^\circ\text{C}$ for the AuNPs monolayer in air, $(32.6 \pm 0.3) \text{ }^\circ\text{C}$ for the sample where AuNPs are covered by PAAD-27, and of about $(49.0 \pm 0.3) \text{ }^\circ\text{C}$ and $(38.0 \pm 0.3) \text{ }^\circ\text{C}$ for AuNPs-PAAD-27 samples acted on by UV light with two different polarization directions. The differences in the measured ΔT values acquired for the four different cases is related to the variation of the AuNPs plasmonic band induced by changes in the characteristics of the host medium surrounding the AuNPs. In particular, Figure 2b shows that in the case of not aligned PAAD-27, there is an increase of the sample absorbance, and this is also observed when the PAAD-27 molecules are aligned. However, in this latter case, the difference in the temperature variations are not due to a change in the sample absorbance but to a different value of k_H in the two cases: as a matter of fact, the observation that the plasmonic band does not change for the two different alignment conditions indicates that no variations occur in the refractive index of the PAAD-27, which corresponds to no variation in the Frölich condition. Therefore, a prediction of the sample temperature variation goes through a determination of the k_H value of the medium hosting the AuNPs, which is made of glass and PAAD-27 layer. We can say that the PAAD-27 alignment induces a reversible and repeatable thermal anisotropy due to an induced change in the thermal conductivity value of the PAAD-27, which turns out to be different for the two different polarization directions of the resonant impinging light. As demonstrated in a previous work [18], we are able to calculate the thermal conductivity value by detecting variations of sample temperature as a function of the laser intensity; thus, we can determine the thermal anisotropy of the PAAD-27 layer using Equations (1) and (2). Following the procedure illustrated in [18], the k_H values of the PAAD-27 in the three cases are measured as: $0.77 \text{ W}(\text{ }^\circ\text{ m})^{-1}$ for the amorphous PAAD-27, $0.32 \text{ W}(\text{ }^\circ\text{ m})^{-1}$ for the E_x aligned PAAD-27 and $0.40 \text{ W}(\text{ }^\circ\text{ m})^{-1}$ for the E_y aligned PAAD-27. These results confirm that it is possible to modulate the thermal behavior of PAAD-27 material by means of polarized light. As mentioned above, PAAD-27 can be used to align liquid crystals; for this reason, we have studied the behavior of a sample of AuNPs + PAAD-27 modified by adding a nematic liquid crystal (NLC, see Materials and Methods section) to investigate how a variation of the optical properties of the new medium (represented now by PAAD-27 plus NLC) surrounding the AuNPs, determines variations of the thermal efficiency of the whole system that are not related to a change in the value of the thermal conductivity k_H of some of its components.

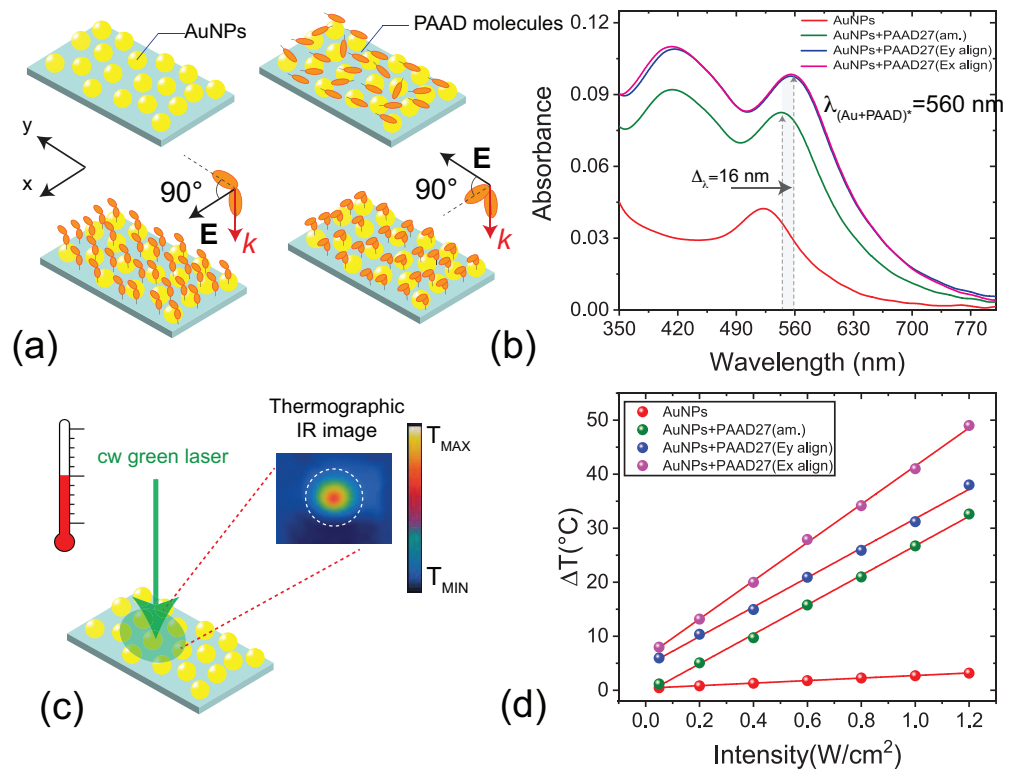


Figure 2. (a) Sketch of the AuNPs monolayer on a glass substrate before (top, left) and after the deposition of the PAAD-27 material (top, right); orientation of the PAAD-27 molecules after the exposure to UV radiation for two different polarizations (bottom). (b) Absorbance response of the AuNPs monolayer in the air (red curve), after the deposition of the PAAD-27—before (green curve) and after the exposure to polarized UV radiation with different polarizations (blue and magenta curves); (c) Sketch of the photothermal measurement. (d) Photo-thermal response of the AuNPs monolayer in air and after the deposition and alignment of the PAAD-27.

A sketch of the photo-alignment process of the NLC molecules is reported in Figure 3a. Two limit cases are considered for the configuration of the NLC director as determined by the PAAD-27 photalignment: a planar one, in which the directions of the molecular director on the two sides of the cell are parallel to each other, and a twisted one, in which these directions are perpendicular to each other; details on cell fabrication are reported in the Materials and Methods section. Figure 3b shows polarized optical microscope (POM) images of the photo-exposed area of the sample. The original planar aligned area is outside the red circled zone, while inside, there is a twisted aligned area after it has been exposed to an external light source for 7 min ($\lambda_{max} = 405 \text{ nm}$; $I = 30 \text{ mW}/\text{cm}^2$). The spectral response of the sample shows a decrease of the absorbance in the plasmonic band and a blue shift with respect to the AuNPs+PAAD-27 sample (Figure 3c). This behavior can be ascribed to a reduction of the effective refractive index that the AuNPs monolayer sees in the surrounding medium in both (planar and twisted) alignment configurations due to the presence of the NLC. As a consequence, the corresponding temperature variation results are lower with respect to the sample with PAAD-27 alone (Figure 3d) but still totally tunable in a given range. In fact, the ΔT obtained at the maximum intensity of the impinging light are about $(13.0 \pm 0.3) ^{\circ}\text{C}$ for the planar cell and $(28.2 \pm 0.3) ^{\circ}\text{C}$ for the twisted cell. Interestingly, all intermediate temperature variations highlighted in Figure 3d by the yellow region can be obtained by continuously varying the polarization of the aligning UV light which reorients the PAAD-27 and therefore the NLC director from the planar to twisted cases.

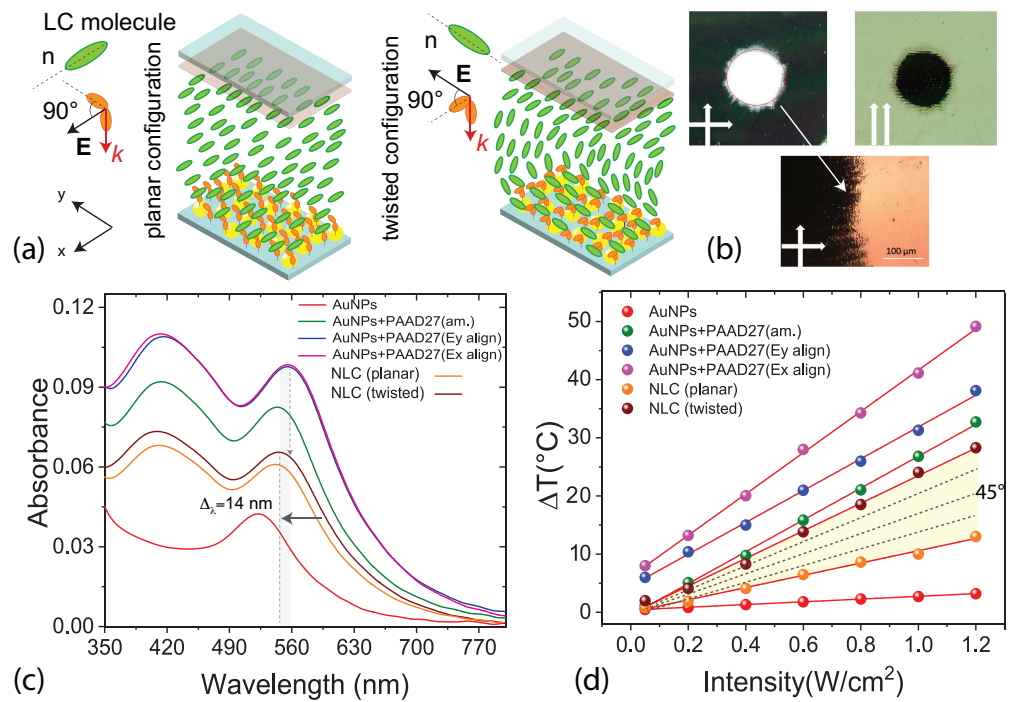


Figure 3. (a) Sketch of the AuNPs+PAAD-27+NLC cell in planar and twisted configuration. (b) POM view of the planar (left and right images, outside the red circle) and twist (left and right images, inside the red circle) alignment along with a high magnification of the transition zone (from planar to twist, bottom photo) of the sample. Left and right images have been acquired between crossed and parallel polarizers, respectively. (c) Absorbance of the AuNPs monolayer in air, covered by PAAD-27 and with NLC; (d) Photo-thermal response of the sample in air and after the deposition and alignment of PAAD-27 and the infiltration and photo-alignment of NLC.

As we can see in Table 1, the combination of an AuNPs layer with a photoaligning material as PAAD-27, demonstrates the potential response of the system to the change of the refractive index of the surrounding medium. From the linear fit of the temperature variation ΔT as a function of the intensity of the pump beam, it is possible to calculate the Sensitivity (α) of the system, defined as $\Delta T/\Delta I$, representing the slope of the linear fit. This parameter can help to better understand the performance of the proposed device; just an example: the highest thermal response is obtained in the case of AuNPs + PAAD-27 Ex aligned characterized by a sensitivity of $(35.38 \pm 0.41) \text{ }^\circ\text{C m}^2/\text{W}$; if, on the other hand, it is necessary to have greater control of the temperature in a very precise range and for a specific intensity range of the pump beam, the choice of inserting the liquid crystal in the system produces a higher thermal variation range if compared to the case of the PAAD-27 alone.

Table 1. Maximum temperature variation ΔT of the samples and the corresponding Sensitivity.

Sample	$\Delta T = T_{max} - T_0$ [$^\circ\text{C}$]	α : Sensitivity ($\Delta T/\Delta I$) [$^\circ\text{C m}^2/\text{W}$]
AuNPs	3.2 ± 0.3	2.35 ± 0.02
AuNPs + PAAD-27 amorphous	32.6 ± 0.3	9.43 ± 0.07
AuNPs + PAAD-27 Ex align.	49.0 ± 0.3	35.38 ± 0.41
AuNPs + PAAD-27 Ey. Align.	38.0 ± 0.3	27.26 ± 0.53
AuNPs + PAAD-27 + NLC (planar)	13.0 ± 0.3	10.95 ± 0.33
AuNPs + PAAD-27 + NLC (twisted)	28.2 ± 0.3	20.63 ± 0.43

4. Conclusions

We proved that: (a) by exploiting a photo-aligning material (PAAD-27) alone it is possible to modify the photo-thermal efficiency of a monolayer of gold nanoparticles (AuNPs); (b) the photo-aligning material, as driven by a polarized UV light, can be exploited to reorient the director of NLC molecules used as host medium of an AuNPs monolayer; this director reorientation induces a modification of the effective refractive index of the NLC as seen by the AuNPs; in turn, this variation affects the photothermal response of the monolayer of AuNPs. In particular, for the maximum intensity considered ($I = 1.2 \text{ W/cm}^2$) a ΔT of about $(3.2 \pm 0.3) \text{ }^\circ\text{C}$ is detected for the AuNPs monolayer in air, $(32.6 \pm 0.3) \text{ }^\circ\text{C}$ for the sample where AuNPs are covered by PAAD-27, and of about $(49.0 \pm 0.3) \text{ }^\circ\text{C}$ and $(38.0 \pm 0.3) \text{ }^\circ\text{C}$ for AuNPs-PAAD-27 samples acted on by UV light of two different polarization directions. The presence of the PAAD-27 leads to a modulation of the photo thermal response whose photo-thermal range extension can be maximized using the PAAD-27 as photoaligning layer for NLC. In this case the ΔT obtained at the maximum intensity of the impinging light are about $(13.0 \pm 0.3) \text{ }^\circ\text{C}$ for the planar cell and $(28.2 \pm 0.3) \text{ }^\circ\text{C}$ for the twisted cell. In conclusion, we have shown that a particular interaction of light with nematic liquid crystals, mediated by a photo-aligning material, can be exploited to control an effect of thermoplasmonic heating. Indeed, by simply varying the polarization direction of the UV light that drives the reorientation of the NLC director (by means of photosensitive PAAD-27 molecules), it is possible to control in a simple and fast way the heat produced at the nanoscale by a monolayer of gold nanoparticles.

Author Contributions: G.P., L.D.S. and C.U. conceived the idea. G.P. fabricated and fully characterized the samples. R.G. and T.B. fabricated and characterized the metallic nanostructures. L.P. conceived and carried out the theoretical work. N.T. fabricated and characterized the photo aligning material. T.B., N.T. and C.U. supervised the work. G.P. and L.D.S. and C.U. prepared and wrote the manuscript with input from all authors. All authors reviewed the manuscript. All authors have read and agreed to the published version of the manuscript.

Funding: Not applicable.

Institutional Review Board Statement: Not applicable.

Informed Consent Statement: Not applicable.

Data Availability Statement: The data that support the findings of this study are available within the article.

Acknowledgments: This research has been supported by the "AIM: Attraction and International Mobility", PON R&I 2014-2020 Calabria.

Conflicts of Interest: The authors declare no conflict of interest.

References

- Baffou, G.; Quidant, R. Thermo-plasmonics: Using metallic nanostructures as nano-sources of heat. *Laser Photonics Rev.* **2013**, *7*, 171–187. [CrossRef]
- Baffou, G.; Quidant, R. Thermoplasmonics. In *World Scientific Handbook of Metamaterials and Plasmonics: Volume 4: Recent Progress in the Field of Nanoplasmonics*; World Scientific: Singapore, 2018; pp. 379–407.
- Baffou, G.; Cichos, F.; Quidant, R. Applications and challenges of thermoplasmonics. *Nat. Mater.* **2020**, *19*, 946–958. [CrossRef] [PubMed]
- Govorov, A.O.; Richardson, H.H. Generating heat with metal nanoparticles. *Nano Today* **2007**, *2*, 30–38. [CrossRef]
- Lal, S.; Clare, S.E.; Halas, N.J. Nanoshell-enabled photothermal cancer therapy: Impending clinical impact. *Acc. Chem. Res.* **2008**, *41*, 1842–1851. [CrossRef] [PubMed]
- Huang, X.; Jain, P.K.; El-Sayed, I.H.; El-Sayed, M.A. Plasmonic photothermal therapy (PPTT) using gold nanoparticles. *Lasers Med. Sci.* **2008**, *23*, 217–228. [CrossRef]
- Guglielmelli, A.; Rosa, P.; Contardi, M.; Prato, M.; Mangino, G.; Miglietta, S.; Petrozza, V.; Pani, R.; Calogero, A.; Athanassiou, A.; et al. Biomimetic keratin gold nanoparticle-mediated in vitro photothermal therapy on glioblastoma multiforme. *Nanomedicine* **2020**, *16*, 121–138. [CrossRef]
- Tordera, D.; Zhao, D.; Volkov, A.V.; Crispin, X.; Jonsson, M.P. Thermoplasmonic semitransparent nanohole electrodes. *Nano Lett.* **2017**, *17*, 3145–3151. [CrossRef]

9. Agarwal, D. Engineering Phonon, Photon, Electron and Plasmon Interactions in Silicon-Metal Nanocavities for Silicon Photonics and Thermoplasmonics. Ph.D. Thesis, University of Pennsylvania, Philadelphia, PA, USA, 2016.
10. Wang, S.; Komvopoulos, K. Effect of material optical properties on thermo-plasmonics of heat-assisted magnetic recording devices. *J. Appl. Phys.* **2018**, *124*, 185109. [CrossRef]
11. Pierini, F.; Guglielmelli, A.; Urbanek, O.; Nakielski, P.; Pezzi, L.; Buda, R.; Lanzi, M.; Kowalewski, T.A.; De Sio, L. Thermoplasmonic-Activated Hydrogel Based Dynamic Light Attenuator. *Adv. Opt. Mater.* **2020**, *8*, 2000324. [CrossRef]
12. Lio, G.E.; Ferraro, A.; Ritacco, T.; Aceti, D.M.; De Luca, A.; Giocondo, M.; Caputo, R. Leveraging on ENZ Metamaterials to Achieve 2D and 3D Hyper-Resolution in Two-Photon Direct Laser Writing. *Adv. Mater.* **2021**, *33*, 2008644. [CrossRef]
13. Cunha, J.; Guo, T.L.; Koya, A.N.; Toma, A.; Prato, M.; Della Valle, G.; Alabastri, A.; Proietti Zaccaria, R. Photoinduced Temperature Gradients in Sub-Wavelength Plasmonic Structures: The Thermoplasmonics of Nanocones. *Adv. Opt. Mater.* **2020**, *8*, 2000568. [CrossRef]
14. Zhu, M.; Baffou, G.; Meyerbrcker, N.; Polleux, J. Micropatterning thermoplasmonic gold nanoarrays to manipulate cell adhesion. *ACS Nano* **2012**, *6*, 7227–7233. [CrossRef]
15. Shen, W.; Black, N.; Kalies, S.; Mazur, E. Impulse generated by laser-irradiated nanostructures in water and its effects on cell poration. *Plasmon. Biol. Med. Int. Soc. Opt. Photonics* **2021**, *11661*, 116610C.
16. Naldoni, A.; Kudyshev, Z.A.; Mascaretti, L.; Sarmah, S.P.; Rej, S.; Froning, J.P.; Tomanec, O.; Yoo, J.E.; Wang, D.; Kment, S.; et al. Solar thermoplasmonic nanofurnace for high-temperature heterogeneous catalysis. *Nano Lett.* **2020**, *20*, 3663–3672. [CrossRef]
17. Chehadi, Z.; Girardon, J.S.; Capron, M.; Dumeignil, F.; Jradi, S. Thermoplasmonic-induced energy-efficient catalytic oxidation of glycerol over gold supported catalysts using visible light at ambient temperature. *Appl. Catal. A Gen.* **2019**, *572*, 9–14. [CrossRef]
18. Pezzi, L.; Palermo, G.; Veltri, A.; Cataldi, U.; Bürgi, T.; Ritacco, T.; Giocondo, M.; Umeton, C.; De Luca, A. Photo-thermal study of a layer of randomly distributed gold nanoparticles: From nano-localization to macro-scale effects. *J. Phys. D Appl. Phys.* **2017**, *50*, 435302. [CrossRef]
19. Saupe, A. On molecular structure and physical properties of thermotropic liquid crystals. *Mol. Cryst. Liq. Cryst.* **1969**, *7*, 59–74. [CrossRef]
20. Khoo, I.C. *Liquid Crystals*; John Wiley & Sons: Hoboken, NJ, USA, 2007; Volume 64.
21. de Gennes, P.; Prost, J. *The Physics of Liquid Crystals*; Oxford University Press: Oxford, UK, 1993; Volume 83.
22. Khoo, I.C. Nonlinear optics, active plasmonics and metamaterials with liquid crystals. *Prog. Quantum Electron.* **2014**, *38*, 77–117. [CrossRef]
23. Si, G.; Zhao, Y.; Leong, E.S.P.; Liu, Y.J. Liquid-crystal-enabled active plasmonics: A review. *Materials* **2014**, *7*, 1296–1317. [CrossRef] [PubMed]
24. Palermo, G.; Sio, L.D.; Placido, T.; Comparelli, R.; Curri, M.L.; Bartolino, R.; Umeton, C. Plasmonic thermometer based on thermotropic liquid crystals. *Mol. Cryst. Liq. Cryst.* **2015**, *614*, 93–99. [CrossRef]
25. Kimling, J.; Maier, M.; Okenve, B.; Kotaidis, V.; Ballot, H.; Plech, A. Turkevich method for gold nanoparticle synthesis revisited. *J. Phys. Chem. B* **2006**, *110*, 15700–15707. [CrossRef] [PubMed]
26. Perivolari, E.; D'Alessandro, G.; Apostolopoulos, V.; Brouckaert, N.; Heiser, T.; Kaczmarek, M. Two-dimensional snapshot measurement of surface variation of anchoring in liquid crystal cells. *Taylor Francis Liq. Cryst.* **2021**, *1*, 1–11.
27. Stöhr, J.; Samant, M.G.; Cossy-Favre, A.; Diaz, J.; Momoi, Y.; Odahara, S.; Nagata, T. Microscopic origin of liquid crystal alignment on rubbed polymer surfaces. *ACS Macromol.* **1998**, *6*, 1942–1946. [CrossRef]
28. Serak, S.V.; Bunning, T.J.; Tabiryan, N.V. Ultrafast photoalignment: Recording a lens in a nanosecond. *Crystals* **2017**, *7*, 338. [CrossRef]
29. Kimball, B.R.; Steeves, D.M.; Hoke, L.; Osgood, R.M.; Carlson, J.; Belton, L.; Tabiryan, N.V.; Rersisyan, S.R.; Serak, S.V.; Hrozhyk, U.A.; et al. *Advances in Anisotropic Materials for Optical Switching*; Technical Report; Massachusetts Inst of Tech Lexington Lincoln Lab: Lexington, MA, USA, 2010.
30. Grillo, R.; Beutel, D.; Cataldi, U.; Rockstuhl, C.; Bürgi, T. Self-Assembled Arrays of Gold Nanorod-Decorated Dielectric Microspheres with a Magnetic Dipole Response in the Visible Range for Perfect Lensing and Cloaking Applications. *ACS Appl. Nano Mater.* **2020**, *3*, 6108–6117. [CrossRef]
31. Fu, Q.; Sun, W. Mie theory for light scattering by a spherical particle in an absorbing medium. *Appl. Opt.* **2001**, *40*, 1354–1361. [CrossRef] [PubMed]
32. Pezzi, L.; De Sio, L.; Veltri, A.; Placido, T.; Palermo, G.; Comparelli, R.; Curri, M.L.; Agostiano, A.; Tabiryan, N.; Umeton, C. Photo-thermal effects in gold nanoparticles dispersed in thermotropic nematic liquid crystals. *Phys. Chem. Chem. Phys.* **2015**, *17*, 20281–20287. [CrossRef] [PubMed]

MDPI
St. Alban-Anlage 66
4052 Basel
Switzerland
Tel. +41 61 683 77 34
Fax +41 61 302 89 18
www.mdpi.com

Applied Sciences Editorial Office
E-mail: applsci@mdpi.com
www.mdpi.com/journal/applsci



MDPI
St. Alban-Anlage 66
4052 Basel
Switzerland
Tel: +41 61 683 77 34
www.mdpi.com



ISBN 978-3-0365-5123-4